Spanwise rotating convection in an ideal gas

Dissertation

for the award of the degree

"Doctor rerum naturalium" (Dr.rer.nat.)

of the Georg-August-Universität Göttingen

within the doctoral program Physik

of the Georg-August University School of Science (GAUSS)

submitted by

Kevin Lüdemann

from Rotenburg (Wümme)

Göttingen 2023

Thesis Committee:

Prof. Dr. Andreas Tilgner, *Geophysikalische Strömungsmechanik, Institut für Astrophysik und Geophysik Göttingen*

Prof. Dr. Michael Wilczek, *Theoretische Physik I, Fakultät für Mathematik, Physik und Informatik Bayreuth*

Prof. Dr. Martin Rein, *Institut für Aeordynamik und Strömungstechnik (IAS), Deutsches Zentrum für Luft- und Raumfahrt e.V. (DLR) Göttingen*

Members of the Examination Board:

Reviewer:

Prof. Dr. Andreas Tilgner, *Geophysikalische Strömungsmechanik, Institut für Astrophysik und Geophysik Göttingen*

Second Reviewer:

Prof. Dr. Michael Wilczek, *Theoretische Physik I, Fakultät für Mathematik, Physik und Informatik Bayreuth*

Further members of the Examination Board:

Prof. Dr. Martin Rein, *Institut für Aeordynamik und Strömungstechnik (IAS), Deutsches Zentrum für Luft- und Raumfahrt e.V. (DLR) Göttingen*

PD. Dr. Olga Shishkina, *Theory of Turbulent Convection, Max Planck Institute for Dynamics and Self-Organization Göttingen*

Prof. Dr. Ansgar Reiners, *Stellare und planetare Astrophysik, Institut für Astrophysik und Geophysik Göttingen*

PD. Dr. Salvatore R. Manmana, *Institut für Theoretische Physik, Universität Göttingen*

Date of the oral examination: 02.06.2023

Contents

List of Figures

List of Symbols

Constants	Description
d	Height (vertical) with units m
L	Length (horizontal) with units m
$\mathbf{g} = g\hat{z}$	Gravitational acceleration with units $\mathrm{m\,s^{-1}}$
$\boldsymbol{\Omega} = \Omega\hat{y}$	Global rate of rotation with units $\mathrm{s^{-1}}$
k	Thermal conductivity with units $\mathrm{W\,m^{-1}\,K^{-1}}$
μ	Dynamic viscosity with units $\mathrm{Pa\,s = kg\,m^{-1}\,s^{-1}}$
c_P, c_V	Specific heat capacities at fixed pressure, Volume with units $\mathrm{J\,K^{-1}\,kg^{-1}}$
$R = c_P - c_V$	Universal gas constant with units $\mathrm{J\,K^{-1}\,kg^{-1}}$
$\gamma = \frac{c_P}{c_V}$	Adiabatic index or ratio of heat capacities
$n = \frac{c_V}{c_P - c_V}$	Polytropic index
ρ_0	Density on upper boundary with units $\mathrm{kgm^{-3}}$
$\kappa_0 = \frac{k}{\rho c_P}$	Thermal diffusivity with units $\mathrm{m^2\,s^{-1}}$
$\nu_0 = \frac{\mu}{\rho}$	Kinematic viscosity with units $\mathrm{m^2\,s^{-1}}$
α_0	Thermal expansion coefficient with units $\mathrm{K^{-1}}$
$\Delta T = T(z=0) - T(z=1)$	Prescribed temperature difference with units K
$c_0 = \sqrt{\gamma R T_0}$	Ideal gas Speed of sound with units $\mathrm{m\,s^{-1}}$
$\Delta T_{\mathrm{ad}} = \frac{gd}{c_P}$	Adiabatic temperature gradient
$\mathcal{D} = \frac{\alpha_0 g d}{c_P} = (\gamma - 1)\,d/H_0$	Dissipation number
Γ, ϵ	Half vorticity, rate of strain

Units	Description
t_{diff}	Thermal diffusion time d^2/κ_0
v_{diff}	Thermal diffusion velocity d/t_{diff}
$t_{\text{free fall}}$	Free fall time $\frac{d}{V_{\text{free fall}}}$
$V_{\text{free fall}}$	Free fall velocity $\sqrt{\alpha_0 g \Delta T d}$
t_{rot}	Rotation time Ω^{-1}

Variable	Description
t	Time, with unit t_{diff}
$\mathbf{r}$	Euclidean Space, with unit d, sometimes radial vector
$\hat{x}, \hat{y}, \hat{z}$	Euclidean direction vectors
$\underline{\underline{A}}$	Matrix, rank two tensor
i, j, k	Indices for space coordinates x, y, z
ε_u	Energy dissipation rate for kinetic energy
ε_θ	Energy dissipation rate for the thermal energy
$()_0$	Index 0 indicates variable at top boundary
$()_*$	Index $*$ indicates a superadiabatic variable
$()_{\text{2D}}, ()_{\text{3D}}$	Index 2D and 3D for variables of 2D or 3D simulations only
$()_{\text{BL}}, ()_{\text{bulk}}$	Indices are boundary layer or bulk
$\mathbf{v}$	Velocity, with units v_{diff}
T	Temperature, with units $\frac{T-T_0}{\Delta T}$
T_s	Background temperature profile
θ	temperature perturbations from background
ρ	Density, with units ρ_0
ρ_s	Density background field
P	Pressure
$\mathcal{V}, \mathcal{A}, \mathcal{T}$	Volume, area and time
Φ_{viscouse}	Viscous heating term
τ_{ij}	Stress tensor
$\mathbf{q}$	Heat flux
$\mathbf{k}$	Wave vector
$\beta = \frac{\Gamma}{\epsilon}$	Ellipticity
N	Number of points

Symbol	Description
$\mathrm{Pr} = \frac{\nu_0}{\kappa_0}$	Prandtl number
$\mathrm{Ra} = \frac{d^3 g \alpha_0 \Delta T}{\nu_0 \kappa_0}$	Rayleigh number
$\mathrm{Ek} = \frac{\nu_0}{d^2 \Omega}$	Ekman number
d/H_0	Number of density scale heights
$H_0 = \frac{\gamma R T_0}{g} = \frac{\gamma (\gamma-1) c_V T_0}{g}$	Adiabatic scale height
$\Delta T / T_0$	Number of temperature "scale heights"
$\frac{\Delta T_{\mathrm{ad}}}{\Delta T} = (\gamma - 1)\, T_0 / \Delta T\, d / H_0$	Temperature ratio
$\mathrm{Nu} = \frac{1}{\mathcal{A}} \int_{\mathcal{A}} \boldsymbol{\nabla} T\vert_{z=0,1} \mathrm{d}\mathcal{A}$	Nusselt number
$E_{\mathrm{kin}} = \frac{1}{\mathcal{V}} \int_{\mathcal{V}} \frac{1}{2} \rho \mathbf{v}^2 \mathrm{d}\mathcal{V}$	Kinetic energy density
$\mathrm{Pe} = \frac{vd}{\kappa_0} = \sqrt{\frac{1}{\mathcal{V}} \int_{\mathcal{V}} \mathbf{v}^2 \mathrm{d}\mathcal{V}}$	Péclet number
$\mathrm{Re} = \frac{vd}{\nu_0} = \mathrm{Pe}/\mathrm{Pr}$	Reynolds number
$\mathrm{Ro} = \frac{v}{d\Omega} = \mathrm{Re}\mathrm{Ek}$	Rossby number
$\frac{\langle v_y^2 \rangle}{\langle v_x^2 + v_z^2 \rangle}$	Anisotropy, ratio of energies
$v_{max} = max(\mathbf{v})$	Maximum velocity
ε_{ijk}	Levi-Civita symbol
$\partial_i = \frac{\partial}{\partial_i}$	Partial derivative short hand
$\nabla_\perp$	Gradient perpendicular to the wall i.e. $\nabla_\perp \rho\vert_z = \partial_z \rho$
$\nabla_\parallel$	Derivative parallel to a wall i.e. at $z=0$ ∂_x and ∂_y
$\boldsymbol{\nabla}, \boldsymbol{\nabla}\cdot, \boldsymbol{\nabla}^2$	Gradient, divergence, Laplace operators
$\mathcal{R}, \mathcal{I}$	Real and imaginary part
2D, 3D	Two-dimensional, three-dimensional
δ_{ij}	Kronecker delta
CPU, GPU	Central and graphics processing units
L2	Level 2 cache of a processor
SM	Streaming multiprocessor of a GPU
HS	Halo size for finite difference computation

1 What is this work about

Earth's atmosphere has been, and continues to be a source of wonders, followed by scientific discoveries. It is one of the two most influential systems determining our weather and climate. The other system, Earth's oceans, is also investigated with measurements, numerical and laboratory experiments, but it is very different to the atmosphere. The water it consists of can be considered incompressible and therefore the equations governing its dynamic can be vastly simplified. It is important to acknowledge that the oceans have their own type of complexity because it is a convecting system with two diffusive properties, adding new layers of complexity which could only recently be investigated experimentally for example by Rosenthal, Lüdemann, and Tilgner, 2022.

In contrast to that, the system investigated in this work has to be considered compressible since all planets of the solar system have an atmosphere consisting of a gas with large density changes across the depth. The phenomenon to be investigated here is convection under the influence of rotation, specifically spanwise rotation, meaning equator regions. Convection refers to a fluid driven by buoyancy from a density gradient, due to for example temperature, or salinity changes. The most prominent example is called Rayleigh-Bénard convection and consists of two vertically bounding surfaces, where the bottom one is heated and the top one cooled, leading to an unstable density distribution. The most obvious and visually pleasing example for compressible convection is the outer atmosphere of Jupiter. It consists of multi coloured bands moving east- and west-wards. These winds in the bands, also called zonal wind or zonal flow, are thought to be a result of either the sloping surfaces or, the compressibility. Compressibility is what this work will focus on.

Maybe more interesting from a geophysics perspective, Earth's outer liquid core can also be considered compressible since it has varying iron content. Earth's liquid core is even less well studied than Jupiter, since a few probes already investigated it and some even descended into its atmosphere. No such study was performed for Earth's core, as well as no experimental studies could be performed, even though a few experiments were set out to study its dynamo action.

This is exactly where this theoretical and numerical study is most effective. As with
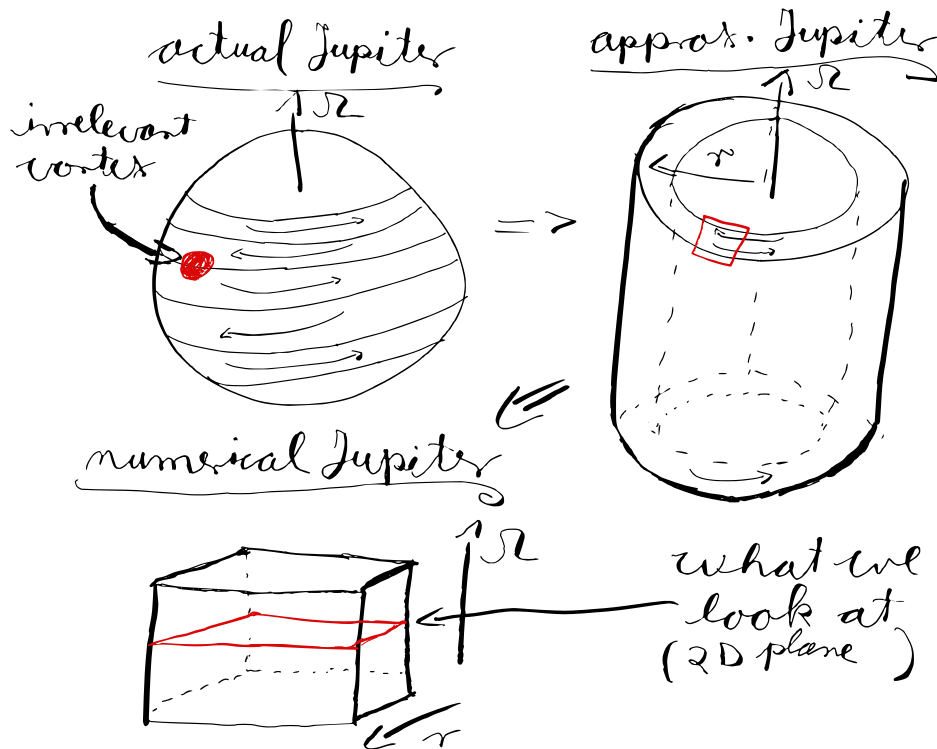
Figure 1.1: Shown are the simplifications applied to the real world system of Jupiter's atmosphere compared with the numerical approach. The banded structure with east and west winds visible on Jupiter are translated into a cylinder to remove one of the curvatures and the sloping vertical boundaries. A second step removes the second curvature as well and also reduces the 3D problem into a 2D one while keeping the axis of rotation Ω perpendicular to the axis of gravity $\mathbf{r}$. This is a model for the equator region.

every theoretical study, we simplify the system in order to remove unwanted effects. The simplifications applied are sketched in Figure 1.1. Shown is a sketch of Jupiter in the top left with its bands and approximated wind directions marked by arrows. The so called "red spot", which is a vortex, is irrelevant and ignored. Sloping boundaries are removed leading to a description with two rotating cylinders in the top right. Ultimately, a small cutout of the cylinder removes the second curvature as well, and we arrive at the studied geometry in the bottom left. Some simulations will only use a 2D plane, which is marked red in the bottom left box. The axis of rotation is marked with Ω and

the direction gravity is acting on is the radial direction $\hat{r}$, which is perpendicular to the axis of rotation in the final geometry. This models the equator region of, for example Jupiter.

Rotating convection, where the axis of gravity and rotation are parallel, has been investigated by many researchers before and a good summary can be found in the articles by Rouhi et al., 2021 and Ecke and Shishkina, 2023. An axis of rotation perpendicular to the axis of gravity has received less attention.

Some recent experiments started exploring this specific geometry for two reasons. First, this geometry offers the possibility to artificially increase the gravitational acceleration by using a centrifuge, meaning centrifugal acceleration substitutes the gravitational one. This was done with water, which is an incompressible liquid, by Jiang et al., 2020. The second reason is that a centrifuge can be used to compress a gas to achieve large density changes across the domain which was done by Menaut et al., 2019. The last experiment is the one that inspired this work including the geometry.

Others have already performed some numerical investigations with different simplifications, like Hardenberg et al., 2015 who investigated incompressible liquids with zonal flow properties. Again, others investigated a similar geometry and found zonal flow for different types of boundaries, done by Poel et al., 2014, and for different aspect ratios, done by Wang et al., 2020. Both of these used an incompressible liquid and a simplification of a 2D flow, removing the velocity along the axis of rotation. Similarly Verhoeven and Stellmach, 2014 investigated this system with an approximation for the compressibility. The problems with this approximation, the so called anelastic approximation, has also been investigated earlier by Verhoeven, Wiesehöfer, and Stellmach, 2015 and Verhoeven and Glatzmaier, 2018. For that reason, this work will use the fully compressible ideal gas without other approximations.

This work will investigate under which conditions a 2D flow, without the velocity parallel to the axis of rotation, is actually applicable as well as investigate fully compressible flow similarly to what Tilgner, 2011 did. The basic equations as well as the geometry and numerical set up is explained in Chapter 2. This is followed by an investigation of the geometry for incompressible liquids to find the regime where the 2D approximation is applicable in Chapter 3. Afterwards, the incompressible liquid is substituted with an ideal gas and a comparison between 2D and 3D flow without the Coriolis force is performed in Chapter 4. Finally, the influence of the Coriolis fore is investigated in Chapter 5.

2 What tools are being used

The tools are related to basic equations and numerical techniques. This chapter is designed to put the reader onto an even playing ground with regard to basics that are required for the later investigations. Further chapters will build on these basics and extend them. Additionally, some information is considered vital to the reproducibility of the results but is too detailed to be expanded upon in the main part of this thesis. Those details are mostly regarding the numerics and programming specifics and can be found in the appendix. Feel free to skip the middle part of the thesis and read the appendix before moving to the results but it is not required for understanding the physics.

This chapter starts with introducing the geometry and some scales of the problem in chapter 2.1. Afterwards, these scales and others are used to make the equations of motion for both the incompressible as well as the ideal gas case dimensionless in Section 2.2. Finally, the numerics of solving the equations of motion are discussed in Section 2.3.

2.1 Geometry and actual system

The systems explained in the introduction have a specific geometry regarding the direction of gravity and the axis of rotation. This geometry is generalized in the Figure 2.1, where the axis of rotation is parallel to the y-direction and the axis gravity is acting along is antiparallel to the z-direction. We will use an aspect ratio of one half $L/d = 0.5$ for the most part in order to be close to the experiment done by Menaut et al., 2019 in a centrifuge. This means that the horizontal width of the cell L is half of the vertical height d. The bottom and top of the domain have a fixed temperature stylized by "red" and "blue" colour as well as the labels "T hot" at the bottom and "T cold" at the top. This is the well known Rayleigh-Bénard configuration. If you think of the y-axis as a center shaft to which the geometry is attached, you can imagine the centrifuge. Here,
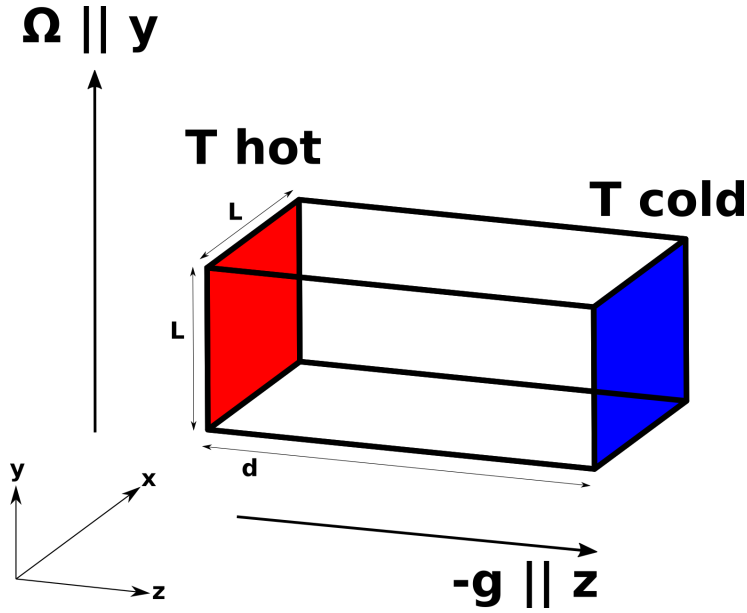
Figure 2.1: Shown is the geometry of most of the simulations with an aspect ratio of $L/d = 0.5$. The axis of rotation is the y-direction and the direction of gravitational acceleration is antiparallel to the z-direction. The vertical height has length d and the horizontal width has length L. The top and bottom surfaces have a constant temperature in the Rayleigh-Bénard configuration while the walls are insulating. This volume will either be filled with an incompressible liquid or an ideal gas.

both the rate of rotation and the gravitational acceleration can be set independently of each other, which is not possible in the experiment, where the centrifugal acceleration is needed as an effective gravitational acceleration. This contrast is also the reason why the centrifugal acceleration is neglected here since it would only change the gravitational effects. A more mathematical explanation can be seen by calculating the centrifugal acceleration $\boldsymbol{\Omega} \times \boldsymbol{\Omega} \times \mathbf{r} = -\Omega^2 (\hat{x} + \hat{z})$. The x-component is neglected since the length L in the x-direction is considered small compared with the circumference of a full cylinder annulus. This is a simplification, which was done in order to remove the distance to the axis of rotation as a parameter. The results presented here assume a distant axis of rotation, which also allows us to ignore the effects of curvature. A faithful recreation of the experiment would need both accelerations in order to capture the full physics.

Some simulations will use a higher aspect ratio of two $L/d = 2$, where the width L is twice the height d and the remaining parameters stays the same. This higher aspect ratio is still considered to comply with the simplification of removing the centrifugal

acceleration. These simulations are run as a comparison to earlier work done by Tilgner, 2011, which are full 3D simulations. The comparison is used as a validation and to see how different compressible 2D simulations are compared with the 3D ones. Additionally, the aspect ratio two $L/d = 2$ simulations will be used to study zonal flow in this geometry.

2.2 Equations of motion

The motion of a fluid can be described by a set of equations for the density ρ, the velocity $\mathbf{v}$, and the temperature field T, which are conservation equations for the mass, momentum, and internal energy. A good description of these equations, their derivations, and conservative properties can be found in Kundu and Cohen, 2001, wherein Chapters 2.13 and 2.14 of the book contain most of the information. Also, further information on rotating frames of reference as well as the description of an ideal gas and the Newtonian stress tensor can be found there. Here, a short overview of the necessary equations and physical properties will suffice.

The local and temporal change in density is described by the continuity equation

$$\partial_t \rho + \boldsymbol{\nabla} \cdot (\rho \mathbf{v}) = 0, \tag{2.1}$$

which corresponds to the conservation of mass. The changes in the velocity fields are described by the Navier-Stokes equation in a rotating frame of reference with the Coriolis and the buoyancy force

$$\rho \left(\partial_t v_j + (v_i \partial_i) v_j + 2\Omega_k v_i \varepsilon_{kij} \right) = \rho g_j + \partial_i \tau_{ij}, \tag{2.2}$$

which describes the conservation of momentum. It is necessary to use the continuity equation to see the conservation properties and form it into $\partial_t (\rho \mathbf{v})$, which is the momentum description of this equation. A velocity description is easier to integrate, which is why we use it here without loss of generality. The stress tensor for Newtonian fluids $\tau_{ij} = -\left(P + \frac{2}{3}\mu \boldsymbol{\nabla} \cdot \mathbf{v}\right) \delta_{ij} + 2\mu e_{ij}$, where $e_{ij} = \frac{1}{2} \left(\partial_j v_i + \partial_i v_j\right)$, and with μ the dynamic viscosity can be rewritten into a more familiar form and inserted into the equation. This calculation results in the familiar form of the Navier-Stokes equation if μ is considered a constant

$$\rho \left(\partial_t \mathbf{v} + (\mathbf{v} \cdot \boldsymbol{\nabla}) \mathbf{v} + 2\boldsymbol{\Omega} \times \mathbf{v} \right) = -\boldsymbol{\nabla} P + \mu \left(\boldsymbol{\nabla}^2 \mathbf{v} + \frac{1}{3} \boldsymbol{\nabla} (\boldsymbol{\nabla} \cdot \mathbf{v}) \right) + \rho \mathbf{g}. \tag{2.3}$$

Here, the dynamic viscosity $\mu = \rho\nu$ is the product of density and kinematic viscosity ν and the vector of gravitational acceleration is $\mathbf{g} = -g\hat{z}$.

The final equation describes the conservation of internal energy

$$\rho\left(\partial_t e + (\mathbf{v} \cdot \boldsymbol{\nabla})\,e\right) = -\boldsymbol{\nabla} \cdot \mathbf{q} - P\left(\boldsymbol{\nabla} \cdot \mathbf{v}\right) + \Phi_{\text{viscous}}. \tag{2.4}$$

The internal energy of an ideal gas $e = c_V T$ can be expressed in terms of the temperature and the constant specific heat capacity for fixed volume. Similarly, the heat flux $\mathbf{q} = -k\boldsymbol{\nabla}T$ obeys the Fourier law, is also dependent on the temperature, and the constant thermal conductivity $k = c_P \rho \kappa$. The thermal conductivity can be calculated with the density, the specific heat capacity at constant pressure c_P, and the thermal diffusivity κ. Finally, the viscous heating $\Phi_{\text{viscous}} = 2\mu\left(e_{ij} - \frac{1}{3}\delta_{ij}\boldsymbol{\nabla} \cdot \vec{v}\right)^2$ describes the energy transport from kinetic to thermal energy due to viscous dissipation and has the inverse sign of the viscous dissipation in the Navier-Stokes equation. Substituting these expressions, dividing by $c_V\rho$, and setting $\gamma = c_P/c_V$ results in the temperature advection diffusion equation with viscous heating

$$\partial_t T + (\mathbf{v} \cdot \boldsymbol{\nabla})\,T = \gamma\kappa\boldsymbol{\nabla}^2 T - \frac{P\boldsymbol{\nabla} \cdot \mathbf{v}}{\rho c_V} + \frac{2\mu}{\rho c_V}\left(e_{ij} - \frac{1}{3}\delta_{ij}\boldsymbol{\nabla} \cdot \mathbf{v}\right)^2. \tag{2.5}$$

One more simplification can be applied, which will become interesting for the boundary conditions. The temperature will be split into background state T_s and deviations θ

$$T = \theta + T_s \tag{2.6}$$

without any assumption about their relative sizes. The background state is considered constant in time and changes only with height. This allows us to calculate the equation for the temperature deviations

$$\partial_t\theta + (\mathbf{v} \cdot \boldsymbol{\nabla})\,\theta + v_z\partial_z T_s = \gamma\kappa\boldsymbol{\nabla}^2\left(\theta + T_s\right) - \frac{P\boldsymbol{\nabla} \cdot \mathbf{v}}{\rho c_V} + \frac{2\mu}{\rho c_V}\left(e_{ij} - \frac{1}{3}\delta_{ij}\boldsymbol{\nabla} \cdot \mathbf{v}\right)^2. \tag{2.7}$$

The form of the temperature background will be calculated in Section 2.2.3.

These equations are in the most general form required for this work. We will be considering two specific cases and calculate the dimensionless equations for those. The first is the Boussinesq case for an incompressible liquid in Section 2.2.1 and second is the ideal gas case in Section 2.2.2.

2.2.1 Boussinesq Approximation

The Equations (2.1), (2.3), and (2.5) can be simplified for an incompressible fluid. Therefore, the density is considered a constant in addition to μ and k. A constant density

would remove the buoyancy as a force from the Navier-Stokes equation. Therefore, the Navier-Stokes equation will retain small density fluctuations only in the buoyancy term. This approximation is widely used and called the "Boussinesq approximation". A more detailed description can be found in Chapter 4.18 of the book by Kundu and Cohen, 2001. It also goes into more detail about the applicability of this approximation to moderately compressible liquids.

In the Boussinesq approximation, the density fields is considered constant with small fluctuations

$$\rho\left(\mathbf{r}, t\right) = \rho_0 + \rho'\left(\mathbf{r}, t\right). \tag{2.8}$$

Only the buoyancy term retains the density fluctuations, which are approximated to depend linearly on the temperature

$$\rho = \rho_0 \left(1 - \alpha_0 \left(T - T_0\right)\right). \tag{2.9}$$

Here, T_0 is the temperature on the top boundary, ρ_0 is the reference density on the top boundary, and α_0 is the thermal expansion coefficient also at the top boundary. The thermal expansion coefficient can be seen as part of the Taylor expansion of the density close to T_0 with $\frac{1}{\rho}\partial\rho/\partial T = -\alpha$. A more physical meaning of the expansion coefficient will be explained in more detail in Section 2.2.2. The top boundary is chosen, and the index 0 kept in order to be consistent with the ideal gas description. In fact, there is no difference in the thermal expansion coefficient α, the kinematic viscosity ν, or the thermal diffusivity κ between the top and bottom boundaries due to the lack of density stratification. The product $\alpha_0\Delta T$ is small compared to one, with ΔT being the temperature difference between top and bottom boundary.

Due to this approximation, the continuity Equation (2.1) simplifies to

$$\boldsymbol{\nabla} \cdot \mathbf{v} = 0. \tag{2.10}$$

This equation can be used to compute an equation for the pressure by taking the divergence of the Navier-Stokes equation leading to a Poisson equation for the pressure. No equation of state is needed for this approximation since the density lost its freedom.

The Navier-Stokes equation (2.3) simplifies to

$$\partial_t \mathbf{v} + \left(\mathbf{v} \cdot \boldsymbol{\nabla}\right) \mathbf{v} = -\boldsymbol{\nabla} \frac{p}{\rho_0} + \nu_0 \boldsymbol{\nabla}^2 \mathbf{v} - 2\boldsymbol{\Omega} \times \mathbf{v} + \alpha_0 \left(T - T_0\right) \mathbf{g}. \tag{2.11}$$

Here, we used $\nu_0 = \frac{\mu}{\rho_0}$ to substitute the kinematic viscosity and retained the temperature dependent part of the density in the buoyancy term. The term $\frac{\rho_0 + \rho'}{\rho_0}\mathbf{g}$ has one

constant from a gradient field, which can be added to the pressure gradient without loss of generality. This is the reason for substituting the pressure field P with a compensated pressure p. The temperature equation (2.5) simplifies to

$$\partial_t T + (\mathbf{v} \cdot \boldsymbol{\nabla}) T = \kappa_0 \boldsymbol{\nabla}^2 T. \tag{2.12}$$

It is time to strip these equations off their dimensions. All dimensionless variables are indicated by $'$. To that end, we will calculate times in units of the thermal diffusion time $t = t' \frac{d^2}{\kappa_0}$, length in units of the height of the container $r = r'd$, and velocities in units of the thermal diffusion time and the height $\mathbf{v} = \mathbf{v}' \frac{d}{\kappa_0}$. The temperature will be expressed in terms of reference temperature at the top boundary and the temperature difference between top and bottom $T = T' \Delta T + T_0$. Furthermore, the split of the temperature shown in Equation (2.6) can be handled in the same manner. The Coriolis term will be scaled with the global rate of rotation Ω and the whole term can be rewritten

$$2\boldsymbol{\Omega} \times \mathbf{v} = 2\Omega \hat{y} \times \mathbf{v} \tag{2.13}$$

using the geometry discussed in Chapter 2.1.

Inserting these scales into Equations (2.10), (2.11), and (2.12) will leave the continuity equation unchanged. Dropping all $'$ for simplicity, the Navier-Stokes and temperature equation will look like this

$$\partial_t \mathbf{v} + (\mathbf{v} \cdot \boldsymbol{\nabla}) \mathbf{v} = -\boldsymbol{\nabla} p + \mathrm{Pr} \boldsymbol{\nabla}^2 \mathbf{v} - 2\frac{\mathrm{Pr}}{\mathrm{Ek}} \hat{y} \times \mathbf{v} + \mathrm{RaPr} T \hat{z}, \tag{2.14}$$

$$\partial_t T + (\mathbf{v} \cdot \boldsymbol{\nabla}) T = \boldsymbol{\nabla}^2 T. \tag{2.15}$$

The resulting three parameters are

$$\text{the Rayleigh number } \mathrm{Ra} = \frac{g\alpha_0 \Delta T d^3}{\kappa_0 \nu_0}, \tag{2.16}$$

$$\text{the Prandtl number } \mathrm{Pr} = \frac{\nu_0}{\kappa_0}, \tag{2.17}$$

$$\text{the Ekman number } \mathrm{Ek} = \frac{\nu_0}{\Omega d^2}. \tag{2.18}$$

Easiest to understand is the Prandtl number, which is a measure for the type of fluid. As a rough estimate, it is usually assumed that air has $\mathrm{Pr} \approx 0.7$, water has about $\mathrm{Pr} \approx 7$, liquid metals like mercury have about $\mathrm{Pr} \approx 0.07$ or lower, some oils like motor oil have $\mathrm{Pr} \approx 70$, and Earths mantle has a number as high as $\mathrm{Pr} \approx 10^{25}$. This number will be set to $\mathrm{Pr} = 0.7$ for the majority of the simulations presented here.

Next is the Rayleigh number, which is a measure for strength of buoyancy compared to the diffusive forces. Usually, there is a critical value in the Rayleigh number after

which active transport sets in. This value is called the critical Rayleigh number Ra_c. It depends on the boundary conditions and other forces, which results in vastly varying values. Many calculated values for the critical Rayleigh number can be found in the book from Chandrasekhar, 1961. It's relevance to this work will be discussed in Chapter 5.1. Some rough numbers range from $\mathrm{Ra} \approx 10^7$ for Earth's mantle, $\mathrm{Ra} \approx 10^{30}$ for Earth's liquid core, and $\mathrm{Ra} \approx 10^{22}$ for the troposphere. Some laboratory experiment done at sea level with water, a cell with dimensions $L = d = 0.20\,\mathrm{cm}$, and a temperature difference of $\Delta T = 10\,\mathrm{K}$ has a Rayleigh number of about $\mathrm{Ra} \approx 10^9$. Numerically it is not easy to reach these high numbers. Usually, simulating three-dimensional convection with Rayleigh numbers of up to $\mathrm{Ra} = 10^8$ is considered to be achievable. Two dimensional simulation can reach higher numbers due to the reduced computational effort.

Finally, the Ekman number is a measure for the strength of the Coriolis force compared to viscose forces. It is usually a small number because it scales inversely with the global rate of rotation. Some rough estimates are $\mathrm{Ek} \approx 10^{-8}$ for Earth's troposphere and $\mathrm{Ek} \approx 10^{-14}$ for Earth's liquid core. Again, numerically $\mathrm{Ek} = 10^{-6}$ is considered achievable. The reasons for these numerical limitations will be explained in Section 2.3.4.

2.2.2 Ideal gas

The simplifications of the Boussinesq description allowed us to compute all variables without the need for an equation of state. In fact, the pressure variable is only needed to fulfill Equation (2.10), meaning that the velocity field is free of divergences. Many experimental and numerical studies have shown that the Boussinesq approximation is applicable to a wide variety of problems. Especially liquids like water or oils but also gases like air without stratification can be approximated with the Boussinesq approximation.

This also means that a physical equation of state is required if stratification effects are considered to be important. It will provide us with a physical link between the thermodynamic variables and allows us to close the full Equations of motion (2.1), (2.3), and (2.5). The simplest and most useful equation of state is the ideal gas law

$$P = R\rho T, \tag{2.19}$$

which links the pressure P to the density ρ and temperature T, with the gas constant $R = c_P - c_V$ and the specific heats at constant pressure c_P, and constant volume c_V. Many gases at reasonable temperatures and pressures like air at ambient temperature

and ground level pressures can be approximated with this equation of state.

The gas is assumed to be monatomic, which sets the adiabatic index $\gamma = c_P/c_V = \frac{5}{3} \approx 1.66$ close to the value for air $\gamma = 1.4$.

Another important parameter is the volume expansion coefficient, which was constant in the Boussinesq case is now temperature dependent

$$\alpha = -\frac{1}{\rho}\left(\frac{\partial \rho}{\partial T}\right)_P = \frac{1}{T}. \tag{2.20}$$

This relation can be calculated using the Equation of state (2.19). We set it to the value $\alpha_0 = \frac{1}{T_0}$, since the temperature of the top boundary is assumed to be fixed. The same applies to the speed of sound

$$c = \sqrt{\left(\frac{\partial p}{\partial \rho}\right)_S} = \sqrt{\gamma RT}. \tag{2.21}$$

The index S indicates that the derivative is calculated at constant entropy. Using the top boundary again, allows us to fix the speed of sound $c_0 = \sqrt{\gamma RT_0}$.

Further interesting parameters include the adiabatic temperature gradient $\partial_z T_{ad} = -\frac{g}{c_P}$ and the isothermal scale height $H = \frac{\gamma RT}{g}$, which will also be calculated at the top boundary $H_0 = \frac{\gamma RT_0}{g}$. These two parameters are important because the volume has a stratification, meaning that the pressure changes with height according to $\partial_z P = -\rho g$ (hydrostatic balance). In a neutrally stable and isentropic volume, the rate of temperature change with height is the adiabatic temperature gradient, which can be calculated from the ideal gas law. Similarly, the isothermal density gradient defines the density scale height H, which can be understood as the characteristic length scale for a stratified volume. This is a brief declaration of the important thermodynamics and constants. A much more detailed description and derivation can be found in the book by Kundu and Cohen, 2001 in Chapters 1.8 until 1.10.

These parameters will appear in the dimensionless equations, which is what we are investigating next. The procedure is the same as last time. In fact, it is the same procedure as every time[1]. Lengths are scaled with the height d, time with the thermal diffusion time $\frac{d^2}{\kappa_0}$, velocities with the thermal diffusion velocity $\frac{d}{\kappa_0}$, the density with the density at the top boundary ρ_0, and temperatures with the temperature of the top boundary and the temperature difference $\frac{T-T_0}{\Delta T}$. Again, the same scales are applied to the temperature split shown in Equation (2.6). The Coriolis force will be scaled with the global rate of rotation Ω. The resulting equations are

$$\partial_t \rho + \boldsymbol{\nabla} \cdot (\rho \mathbf{v}) = 0 \tag{2.22}$$

---

[1]This is a well hidden "Dinner for One" reference.

for the continuity equation,

$$\partial_t \mathbf{v} + (\mathbf{v} \cdot \boldsymbol{\nabla}) \, \mathbf{v} = -\frac{1}{\rho} \boldsymbol{\nabla} \left[(T + {}^{T_0}\!/_{\Delta T}) \, \rho \right] \frac{1}{\gamma} {}^{H_0}\!/_d \mathrm{Pr}\mathrm{Ra} - \hat{z} \mathrm{Ra}\mathrm{Pr}^{T_0}\!/_{\Delta T}$$

$$- 2 \frac{\mathrm{Pr}}{\mathrm{Ek}} \hat{y} \times \mathbf{v} + \mathrm{Pr} \frac{1}{\rho} \left(\boldsymbol{\nabla}^2 \mathbf{v} + \frac{1}{3} \boldsymbol{\nabla} \left(\boldsymbol{\nabla} \cdot \mathbf{v} \right) \right) \qquad (2.23)$$

for the Navier-Stokes equation, and

$$\partial_t T + (\mathbf{v} \cdot \boldsymbol{\nabla}) \, T = \gamma \frac{1}{\rho} \boldsymbol{\nabla}^2 T - (\gamma - 1) \left(T + {}^{T_0}\!/_{\Delta T} \right) \boldsymbol{\nabla} \cdot \mathbf{v}$$

$$+ \frac{1}{\rho} \left[e_{ij} - \frac{1}{3} \boldsymbol{\nabla} \cdot \mathbf{v} \delta_{ij} \right]^2 2\gamma \left(\gamma - 1 \right) {}^{d}\!/_{H_0} \frac{1}{\mathrm{Ra}} \qquad (2.24)$$

for the temperature equation. The equation of state can also be made dimensionless

$$P = (\gamma - 1) \, \rho \left(T + \frac{T_0}{\Delta T} \right). \qquad (2.25)$$

Primes are omitted for clarity.

Here, two parameters are the same as in the Boussinesq case. The Prandtl number $\mathrm{Pr} = \frac{\nu_0}{\kappa_0}$ and the Ekman number $\mathrm{Ek} = \frac{\nu_0}{\Omega d^2}$ are identical. Only the Rayleigh number $\mathrm{Ra} = \frac{g \frac{\Delta T}{T_0} d^3}{\kappa_0 \nu_0}$ is slightly changed because the volume expansion coefficient is the inverse temperature of the top boundary. The adiabatic index γ is used as a parameter as well. Two additional parameters are introduced, which have a similar meaning. The first one is

$$\text{the number of density scale heights } {}^{d}\!/_{H_0} = \frac{dg}{\gamma R T_0} \qquad (2.26)$$

and the second is

$$\text{the number of temperature "scales" } {}^{\Delta T}\!/_{T_0}. \qquad (2.27)$$

These two parameters are the ones that set the "compressibility" since they are related to the density stratification. The density scale height of the troposphere can be calculated assuming $g \approx 9.8\,\mathrm{m\,s^{-2}}$, $T_0 \approx 220\,\mathrm{K}$, $\gamma = 1.4$, and the gas constant of air being $R = 287\,\mathrm{J\,kg^{-1}\,K^{-1}}$ giving $H_0 \approx 9\,\mathrm{km}$ according to Salby, 1996. Assuming the height of the troposphere is $d \approx 10\,\mathrm{km}$ it can be calculated that ${}^{d}\!/_{H_0} \approx 1.1$. Using the same temperature and further assuming that the total temperature drop across the troposphere is $\Delta T \approx 65\,\mathrm{K}$, it can also be calculated that ${}^{\Delta T}\!/_{T_0} \approx 0.3$. Generally, taking the limit ${}^{d}\!/_{H_0} \ll 1$ and ${}^{\Delta T}\!/_{T_0} \ll 1$ tends towards incompressibility.

One more parameter is set by the initial conditions, which is the total mass of the system. The initial conditions will be discussed in the following Section 2.2.3.

A combination of the two numbers of scale heights can be related to the adiabatic temperature gradient

$$\frac{\Delta T_{\mathrm{ad}}}{\Delta T} = \frac{gd}{c_P \Delta T} = (\gamma - 1)\, {}^{T_0}\!/\!{}_{\Delta T}{}^{d}\!/\!{}_{H_0}, \tag{2.28}$$

which is a redundant parameter in this set. Nevertheless, it is useful in determining a criterion for instability because the temperature gradient across the domain has to be larger than the adiabatic temperature gradient

$$\frac{\Delta T_{ad}}{\Delta T} < 1$$
$$\Rightarrow (\gamma - 1)\, {}^{T_0}\!/\!{}_{\Delta T}{}^{d}\!/\!{}_{H_0} < 1$$
$$\Rightarrow {}^{d}\!/\!{}_{H_0} < \frac{1}{\gamma - 1}\, {}^{\Delta T}\!/\!{}_{T_0}. \tag{2.29}$$

Calculating the speed of sound from Equation (2.21) at the top boundary yields the smallest speed of sound in the volume since the temperature is higher at the bottom. Therefore, it is advisable to compute the speed of sound at the bottom boundary and it can also be made dimensionless

$$c = \sqrt{\mathrm{Ra}\mathrm{Pr}\,{}^{H_0}\!/\!{}_{d}\left(T + {}^{T_0}\!/\!{}_{\Delta T}\right)} \tag{2.30}$$
$$\Rightarrow c(z = 0) = \sqrt{\mathrm{Ra}\mathrm{Pr}\,{}^{H_0}\!/\!{}_{d}\left(1 + {}^{T_0}\!/\!{}_{\Delta T}\right)}.$$

This set of parameters is not unique. Other authors prefer parameters like the polytropic index

$$n = \frac{c_V}{c_P - c_V} = \frac{1}{\gamma - 1}, \tag{2.31}$$

which is the exponent of the adiabatic statification as explained by Kundu and Cohen, 2001. One more common and interesting parameter often used is the dissipation number

$$\mathcal{D} = \frac{\alpha_0 g d}{c_P} = \frac{\Delta T_{ad}}{T_0}$$
$$= (\gamma - 1)\, {}^{d}\!/\!{}_{H_0}. \tag{2.32}$$

It is a measure for the compressibility and is related to the number of scale heights in this set of parameters. This parameter is for example used by experimental set ups done by Menaut et al., 2019. They achieved a dissipation number of $\mathcal{D} = 0.06$, which relates to ${}^{d}\!/\!{}_{H_0} \approx 0.1$ in the parameter set of this work. Additionally, they also achieved a temperature at the top boundary of $T_0 \approx 300\,\mathrm{K}$ and a temperature difference across the domain of $\Delta T \approx 30\,\mathrm{K}$, which translates to ${}^{\Delta T}\!/\!{}_{T_0} \approx 0.1$ in the parameter set of this work.

2.2.3 Initial and boundary conditions

The equations of motion described in Sections 2.2.1 and 2.2.2 have the same boundary conditions but different initial conditions. The different initial conditions originate from the fact that the ideal gas equation has a density field and a physically meaningful pressure. Therefore, the hydrostatic state with a linear temperature field is the initial state, which gets reduced to just the linear temperature field for the Boussinesq simulations. Both start by stating that the initial velocity field is $\mathbf{v} = 0$. This also means that the initial density or pressure field is zero in the Boussinesq case. Under these conditions, the temperature equation reduces to a Laplace equation

$$\boldsymbol{\nabla}^2 T = 0 \tag{2.33}$$

with two fixed temperature boundaries. The solution to this equation is

$$T = {}^{T_0}\!/_{\Delta T} + T_s = {}^{T_0}\!/_{\Delta T} + 1 - z, \tag{2.34}$$

which is true for the ideal gas and the Boussinesq case. This is also the background state for the temperature split in Equation (2.6), which simplifies the left-hand side as well as the Laplace term of Equation (2.7)

$$\partial_t T + (\mathbf{v} \cdot \boldsymbol{\nabla}) T - \gamma \kappa \boldsymbol{\nabla}^2 T = \partial_t \theta + (\mathbf{v} \cdot \boldsymbol{\nabla}) \theta - v_z - \gamma \kappa \boldsymbol{\nabla}^2 \theta. \tag{2.35}$$

This applies to the Boussinesq and ideal gas version of this equation. With this, the initial conditions of the Boussinesq case are fully described.

The initial conditions for the ideal gas case still require an initial density field. This can be calculated by using the compressible Navier-Stokes Equation (2.23), setting $\mathbf{v} = 0$, and inserting the temperature initial condition (2.34)

$$\frac{1}{\rho_s} \partial_z \left[\left((1 - z) \, {}^{\Delta T}\!/_{T_0} + 1 \right) \rho_s \right] \frac{1}{\gamma} {}^{H_0}\!/_d \mathrm{PrRa} {}^{T_0}\!/_{\Delta T} = -{}^{T_0}\!/_{\Delta T} \mathrm{PrRa}$$

$$\Rightarrow \frac{1}{\rho_s} \left[\rho_s \left(-{}^{\Delta T}\!/_{T_0} \right) + \left((1 - z) \, {}^{\Delta T}\!/_{T_0} + 1 \right) \partial_z \rho_s \right] = -\gamma {}^d\!/_{H_0}$$

$$\Rightarrow \frac{1}{\rho_s} \partial_z \rho_s = \frac{-\gamma {}^d\!/_{H_0} + {}^{\Delta T}\!/_{T_0}}{(1 - z) \, {}^{\Delta T}\!/_{T_0} + 1} = \frac{-\gamma {}^d\!/_{H_0} {}^{T_0}\!/_{\Delta T} + 1}{1 + {}^{T_0}\!/_{\Delta T} - z}, \tag{2.36}$$

where ρ_s is the stationary density field. This differential equation is solved by

$$\rho_s = \rho_0 \left(\frac{1}{1 + {}^{\Delta T}\!/_{T_0} (1 - z)} \right)^{1 - \gamma {}^d\!/_{H_0} {}^{T_0}\!/_{\Delta T}} \tag{2.37}$$

with ρ_0 the density at the top boundary. Plugging in the values for the troposphere given in Section 2.2.2, it can be calculated that the density at the bottom is about $\frac{\rho_s(z=0)}{\rho_0} \approx 3$

times higher than at the top.

The boundary conditions for the ideal gas and Boussinesq case are the same. There is no physical reason for the density to have a boundary condition so only a numerical one is required to keep the mass constant. The zero flux condition

$$\nabla_\perp \rho = 0 \tag{2.38}$$

will be used meaning that the density gradient perpendicular to the wall is zero.

The temperature of the top and bottom boundary is fixed and the other walls are insulating meaning that

$$T(z = 1) = {}^{T_0}/_{\Delta T} \text{ and } T(z = 0) = {}^{T_0}/_{\Delta T} + 1 \tag{2.39}$$

$$\Rightarrow \theta(z = 1) = 0 \text{ and } \theta(z = 0) = 0 \text{ with} \tag{2.40}$$

$$\nabla_\perp T = 0 \tag{2.41}$$

$$\Rightarrow \nabla_\perp \theta = 0 \tag{2.42}$$

everywhere else. This simplification of the boundary conditions for θ can be traced back to the choice of the background state. Only in the case of periodic boundary conditions will the zero flux side walls be replaced with

$$T(x = 0) = T(x = L/d) \tag{2.43}$$

$$\Rightarrow \theta(x = 0) = \theta(x = L/d) \tag{2.44}$$

and similarly for the density.

The velocity has the more interesting choice of boundary conditions since this choice influences the results dramatically and can be set independently for all walls. Three choices are used here. First is the fixed velocity boundary called no slip condition for example at the top wall

$$\mathbf{v}(z = 1) = 0, \tag{2.45}$$

meaning that the fluid has the velocity of the wall, which is not moving in this case. These types of boundary conditions are considered valid for fluid solid interactions on a macroscopic level.

The second choice is the so called free slip boundary

$$\nabla_\perp \mathbf{v}_{||} = 0 \text{ and} \tag{2.46}$$

$$\mathbf{v}_\perp = 0 \tag{2.47}$$

16

meaning that the derivatives perpendicular to the wall of the parallel velocity components are zero and the velocity component into the wall is zero as well. These conditions allow for very high velocities parallel to the boundaries. It also removes any velocity boundary layer near the wall. These boundary conditions can usually be found in liquid to liquid boundaries.

The third and last choice is again the periodic boundaries

$$\mathbf{v}\left(x = 0\right) = \mathbf{v}\left(x = L/d\right).$$ (2.48)

Periodic boundary conditions are used to simulate infinitely extended domains, which also assumes that the patterns found are infinitely extending and periodic.

2.2.4 Flow dependent measures

Commonly, measures characterizing the flow are collected during the runtime of a simulation. These measures are also free of dimensions similarly to the control parameters introduced in Sections 2.2.1 and 2.2.2 like the Rayleigh number or the Ekman number. The flow dependent measures are calculated from the state of the flow, and there is no clear relation between the measures and the control parameters. Finding these relations will be the task of later chapters. Here, we will introduce them and demonstrate use cases of these measures.

The first measure to be introduced is called the Nusselt number

$$\mathrm{Nu} = \frac{\text{total thermal transport}}{\text{diffusive thermal transport}}.$$ (2.49)

The Nusselt number is the most common measure used in the study of thermal convection because it characterizes the main transport property. There are analog versions for transport of salinity as for example the Sherwood number. A discussion about these types of numbers and their ratios is often used in double-diffusive convection. This type of convection has two diffusive scalars like temperature and salinity, which both influence the density similarly to Equation (2.9). An introduction to these topics can be found in the book of Radko, 2013 and the Nusselt number is defined in Chapter three of said book.

All these measures start with a value of $\mathrm{Nu} = 1$ for no convection because the total transport is merely diffusive. Numbers larger than one indicate that the Rayleigh number is larger than the critical Rayleigh number and that fluid motion has set in. During the

simulation, the Nusselt number will be computed from the temperature gradient near one of the two boundaries

$$\mathrm{Nu} = \frac{1}{\mathcal{A}} \int_{\mathcal{A}} \boldsymbol{\nabla} T|_{z=0,1} \mathrm{d}\mathcal{A}. \tag{2.50}$$

The bottom boundary ($z = 0$) is chosen for both incompressible and compressible convection. Later chapters will look at the difference in the Nusselt number regarding the top and bottom boundary.

The second set of measures is calculated from the flow velocity. Above all, the kinetic energy density

$$E_{\mathrm{kin}} = \frac{1}{\mathcal{V}} \int_{\mathcal{V}} \frac{1}{2} \rho \mathbf{v}^2 \mathrm{d}\mathcal{V} \tag{2.51}$$

will be used to judge the condition of the flow whether a transient flow structure is present or if a statistically stationary state is reached. The density factor is set to one for the incompressible simulations. Generally, it is not advisable to compute the average velocity from the kinetic energy due to the factor of the density.

Therefore, a similar measure is computed, which is called the Péclet number

$$\mathrm{Pe} = \frac{vd}{\kappa_0}, \tag{2.52}$$

and which is calculated with a characteristic velocity v, a length scale d, and the thermal diffusivity κ_0. This is precisely the dimensionless velocity, which was used in Sections 2.2.1 and 2.2.2. Therefore, the Péclet number is calculated as the root mean square (RMS) value of the dimensionless velocity

$$\mathrm{Pe} = \sqrt{\frac{1}{\mathcal{V}} \int_{\mathcal{V}} \mathbf{v}^2 \mathrm{d}\mathcal{V}}. \tag{2.53}$$

From this definition it is also possible to compute a Reynolds number

$$\mathrm{Re} = \frac{vd}{\nu_0} \tag{2.54}$$

because it is similar to the Péclet number and only the diffusivity needs to be switched. Therefore, the Reynolds number will be calculated with the help of the Prandtl number from Equation (2.17)

$$\mathrm{Re} = \frac{\mathrm{Pe}}{\mathrm{Pr}}. \tag{2.55}$$

Both of these two measures show the strength of inertial forces compared to the two viscous forces (thermal and momentum viscous), which are thermal diffusion for the

Péclet number and momentum diffusion for the Reynolds number. Values large compared to one indicate that inertial forces dominate and laminar flow structures are unlikely to be found. For example, the flows in microfluidics meaning pipes, tubes and channels with diameters of micro meters usually have $1 \approx \mathrm{Re} < 100$ and are usually assumed to be laminar. The jet created during breathing or speaking for example has $\mathrm{Re} \approx 10^3$ and is showing some turbulent eddies in addition to staying coherent for a few decimeters as shown by Abkarian et al., 2020.

The last measure depending on the flow velocity is called the Rossby number

$$\mathrm{Ro} = \frac{v}{d\Omega},\tag{2.56}$$

which depends on the characteristic velocity v, length scale d and rate of rotation Ω. Similarly to the Reynolds number, the Rossby number can be calculated with the help of the Ekman number from Equation (2.18)

$$\mathrm{Ro} = \mathrm{ReEk}.\tag{2.57}$$

Others use the Rossby number instead of the Ekman number as a dimensionless parameter because they use is a characteristic velocity as a scale. For example, the free fall velocity $v_{\text{free fall}} = \sqrt{\alpha_0 g \Delta T d}$ can be used in the definition of the Rossby number. This is a very different number to the one used in this work. Rossby numbers should only be compared carefully. Furthermore, it is commonly assumed that at $\mathrm{Ro} = 1$ occurs the transition between flow structures being influenced by the Coriolis force ($\mathrm{Ro} < 1$) and the Coriolis force being neglected ($\mathrm{Ro} > 1$). For example high and low pressure zones in Earth's troposphere have $\mathrm{Ro} \approx 0.1$ and are influenced by the Coriolis force. These types of flows are also called geostrophic flows meaning that they are large scale, away from the boundaries and horizontally balanced between the Coriolis force and the pressure gradient. A flow in geostrophic balance has almost no velocity component along the axis of rotation except in the boundary layers. Compare this to a flow in a lake, which is orders of magnitude smaller than a pressure zone but is influenced by the same global rate of rotation. The Rossby number in the lake will be large compared to one $\mathrm{Ro} \gg 1$ and the flows are therefore not in a geostrophic balance. A more detailed description of the geostrophic balance can be found in Chapter 14.5 of Kundu and Cohen, 2001. The criterion for the transition using the flow dependent Rossby number is part of the initial investigations in this work and will be described in Chapter 3.

Numbers presented in figures and tables are always time averaged meaning that the time

integral

$$\mathrm{Nu} = \frac{1}{\mathcal{T}} \int_{\mathcal{T}} \frac{1}{\mathcal{A}} \int_{\mathcal{A}} \boldsymbol{\nabla} T|_{z=0,1} \mathrm{d}\mathcal{A}\mathrm{d}\mathcal{T} \tag{2.58}$$

is calculated over a time range $\mathcal{T} = t_1 - t_0$, where $t_{1,0}$ are time points between which the flow is considered to be in a statistically stationary state. However, the integral for velocity dependent measures is calculated differently because the average has to be an RMS average

$$\mathrm{Pe} = \sqrt{\frac{1}{\mathcal{T}} \int_{\mathcal{T}} \frac{1}{\mathcal{V}} \int_{\mathcal{V}} \mathbf{v}^2 \mathrm{d}\mathcal{V}\mathrm{d}\mathcal{T}}, \tag{2.59}$$

where the square root is the last operation to be performed.

A state is considered statistically stationary if measures like the kinetic energy density or the Nusselt number are fluctuating around a mean value. Choosing a suitable time range is easy for stationary states, but for oscillating and turbulent states it is important to integrate over many oscillation periods in order to get an accurate average. Generally, at least 40 periods are included in the time range, which is chosen as a trade off between a long enough simulation time and a compute time that does not exceed a few weeks of wall time.

All of these dimensionless measures can also be used to relate between experiments and numerics as well as between different scales. This is known as the similarity principle. Take the Reynolds number for example. It depends on the flow velocity, a length scale and the kinematic viscosity. Knowing this, it is possible to create similar results if the length is halved and the velocity doubled. This is especially useful in scaling experiments, for example the problem of measuring the flow around an impractically large object like an aeroplane can be solved by scaling the object down and in turn increasing the flow velocity. Many textbooks like the one from Rein, 2020 have more examples and list further measures as well. In this case, it is important to note that these measures help us relate to experimental results and allow us to calculate scaling laws, which in turn help with extrapolating results to more realistic dimensions.

2.3 Numerics

The Equations of motion (2.1), (2.3), and (2.5) regardless if they are incompressible or compressible have to be solved numerically since no general solution is known for either. A straightforward approach for solving both sets of equations is to perform time stepping of the basic variables like velocity, temperature and density. Two different as well

as mixed flavours are possible here but only an explicit time stepping method allows us to successively compute steps without needing the full field at all times. This gives us an easy way to spread the computational effort over multiple devices or processors as explained later.

Some interesting tricks can be applied to the spatial operators to make it almost perfectly accurate with spectral methods or work on inhomogeneous meshed like element methods. We are taking a simpler route in using finite differences since these methods are well established and allow for spatial separation of the computation into small kernels or domains. These only need the next few neighbouring points and can be computed in parallel speeding up the computation. This also allows us to spread the work load onto multiple devices or processors since only the next neighbours are needed locally.

Both ideas are intentionally chosen because we aim to run this computation on Graphics-Processing Units (GPUs), which are designed to perform operations in parallel. Most often they are used to render images or scenes quickly and have special hardware to compute lighting effects and image manipulations in parallel. They achieve this parallelization by utilizing multiple cores, which each can compute the same instruction on multiple data points at the same time. It is like a machine that fills bottles with some liquid (say beer) and can fill many (say 10) bottles at once before reloading the same amount of bottles in one cycle. This allows the machine to fill almost ten times as much beer in the same time as a machine filling only a single bottle would.

Here, this behaviour is used to perform the same finite difference operations on the entire volume (or plane) of data at the same time. In comparison, a CPU only running one line of code on a single data point (even though it has a higher speed) cannot achieve the same memory throughput as a GPU.

We are using GPUs from Nvidia, which is one of the leading companies if it comes to fast GPUs. This also means that we can use their programming environment called CUDA, which has a very comprehensive programming guide[2]. The following chapters will highlight the specific methods used for time stepping, the choice of grid type, the specific finite difference methods used, as well as the boundary conditions and their implementations. The specific finite difference stencils used here as well as some small introduction into the programming philosophy can be found in the appendix in Sections 7.2 and 7.3.

The program designed for this work has been validated against existing Boussinesq solutions, which showed deviations below 1%. Additionally, the same program has been

---

[2]https://docs.nvidia.com/cuda/cuda-c-programming-guide/index.html tested at 08.11.2022

used in many other works before (Tilgner, 2012, Goepfert and Tilgner, 2016 and others), emphasizing the validity of the results. Furthermore, the compressible part of the program could not be checked against existing result. Validation was performed in the same manner as Tilgner, 2011 does by checking for conservation of both kinetic and internal energy, which yields similar results to the article. The results are therefore assumed to be equally valid.

2.3.1 Time stepping

Explicit time stepping taught in schools and universities usually starts with an Euler step. Say we have an equation like this

$$\partial_t x(t) = -v(t), \tag{2.60}$$

were x is some variable (say space), which varies in time with some variable v (say velocity). This can be interpreted in an incremental way as the approximation

$$\frac{x\left(t_{i+1}\right) - x\left(t_i\right)}{\Delta t} \approx -v\left(t_i\right), \tag{2.61}$$

were Δt is the step length in time between the two time points t_i and t_{i+1}. We recover the original formula by applying the limit of $\Delta t \to 0$.

This is already the Euler method since we have the position and velocity at time point t_i or set it to some value as an initial condition, for example, $x\left(t_0\right) = 0$ and $v\left(t_0\right) = 1$. Assuming we know how $v(t)$ behaves (say constant velocity in this example), we can successively compute the next position by solving the equation

$$x\left(t_{i+1}\right) = x\left(t_i\right) + \Delta t\left(-v\left(t_i\right)\right) + \mathcal{O}\left(\Delta t^2\right). \tag{2.62}$$

This method is very simple and has some major problems in stability and energy conservation indicated by the order sign $\mathcal{O}$ to simplify this discussion. The reader is advised to look into the book of Fletcher, 2000 for more information about this type of time step in order to fully grasp the draw backs and how to arrive at this order of the error term. For this reason, we have chosen an explicit time stepping method with a higher order in the error term, namely the Runge-Kutta 3 (RK3) method, which has an error of order $\mathcal{O}\left(\Delta t^4\right)$. The RK3 method is similar to an Euler step, but includes some trial steps in between. Basically, this method performs a partial Euler step to predict the result, uses this result for some more trial steps, and ultimately averages the trial steps to arrive at a more accurate result. There are many flavours of RK methods indicated by the amount

of trial steps. For example RK2 takes one trial step and RK4 takes three, which can be linked to the order of the error term. Therefore, a higher RK version has a smaller error term compared to smaller versions. There are also some more wild combinations like the popular RK45 method, which takes three trial steps and does some additional error correction similar to an RK5 method. For more information about these types of methods the reader is again advised to look into the book of Fletcher, 2000 but we digress.

The specific RK3 method chosen here has the important property of only needing two versions of the fields (two different time points) instead of the usual three for the regular RK3 or more for higher order methods. This greatly reduces the amount of memory needed since GPUs only have a small amount of memory available (few Gigabyte) compared to the CPU (few hundred Gigabyte). Therefore, the RK3 method is a good balance between not running too many steps but still allowing for moderately small errors. This method was calculated by Williamson, 1980 and looks like this

$$
\begin{aligned}
k_1 &= \Delta t f(x_0) & &\text{with } x_1 = x_0 + \frac{1}{3}k_1, \\
k_2 &= \Delta t f(x_1) - \frac{5}{9}k_1 & &\text{with } x_2 = x_1 + \frac{15}{16}k_2, \\
k_3 &= \Delta t f(x_2) - \frac{153}{128}k_2 & &\text{with } x_3 = x_2 + \frac{8}{15}k_3
\end{aligned}
\tag{2.63}
$$

for the next complete time step for a single scalar field x and a right-hand side $f(x)$. This method was later improved by Kennedy, Carpenter, and Lewis, 2000. The improvements are not implemented here but mentioned for completeness and future updates to the method. The authors also calculated other low storage schemes with higher orders of up to RK7.

The more challenging tasks are the spatial derivatives as discussed in the next chapter and therefore the RK3 method is sufficient.

2.3.2 Collocated vs. Staggered finite differences

As mentioned before, the spatial discretization is more of a problem compared to the one in time. First of all, a decision on the type of grid has to be made. We will only show the problem in one dimension to keep it simple. Imagine a one dimensional grid like the one shown in the Figure 2.2. The top grid shows a collocated and the bottom a staggered arrangement. Scalar fields are shown as dots and vector fields as arrows. Each position has a grid spacing of Δx to the next one. Only focus on the top grid for now.
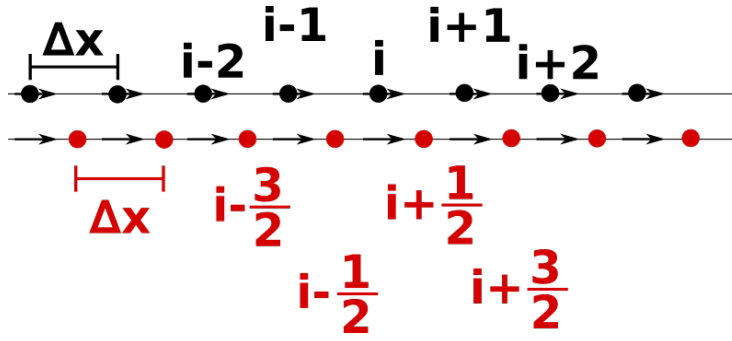
Figure 2.2: One dimensional grid representation. The dots are scalar fields and the arrows are a vector field. Only some index i and some neighbours are shown. Top is a collocated and bottom a staggered grid arrangement. The difference is the shifted scalar field shown in red. The shift width is half a grid spacing.

Computing the gradient of some scalar field on the collocated grid is simply

$$\partial_x \rho \approx \frac{\rho_{i+1} - \rho_{i-1}}{2\Delta x} \tag{2.64}$$

because we only need the neighbours for this central finite difference scheme. Divergences and other operators can be handled in the same manner. The collocated arrangement is the most basic grid that is taught in numerics courses. It has one major problem especially for compressible dynamics.

As shown above, the equation for conservation of mass (2.1) relies on the computation of

$$\boldsymbol{\nabla} \cdot (\rho \mathbf{v}) = \mathbf{v} \cdot \boldsymbol{\nabla}\rho + \rho \boldsymbol{\nabla} \cdot \mathbf{v}. \tag{2.65}$$

The right-hand side is easy to implement but does not strictly ensure conservation of mass, which the left-hand side does. Therefore, it is advisable to compute the divergence of the product. Looking at central finite differences one observes that only the two neighbouring points are needed but not the center point itself. Additionally, a scalar field like the density is only needed in the pressure gradient, which means that the density can be accurate up to an additive constant. This additive constant is usually fixed by some boundary or initial condition.

Going back to the continuity equation, we find that odd and even indices only need even and odd indices for both calculations. Herein lies the problem because odd and even indices are now allowed to be accurate up to a constant that can be different for both. This is commonly known as density or pressure oscillations. These are only a numeric artifact and have no physical meaning. It is vital to get rid of these oscillations to have

physically meaningful results.

One way to fix this is by using the right-hand side of (2.65) with an upwind scheme for $\mathbf{v} \cdot \boldsymbol{\nabla} \rho$. The upwind scheme will introduce some numerical diffusion but also uses the center point since it consists of backwards and forwards differences depending on the flow being forwards or backwards. Some more detail about this is given in the appendix 7.2. The added numerical diffusion breaks conservation of mass completely and the density has to be reset at each sampling step. This method was successfully used by Tilgner, 2011 in order to keep the collocated grid.

A much more elegant but also more difficult approach is to use a staggered grid arrangement. This arrangement is shown at the bottom of Figure 2.2 with the differences to the collocated grid highlighted in red. The difference is that the scalar field is shifted by half a grid spacing to the right. A gradient can now be calculated with a single grid spacing. For example, look at the density gradient for the vector component at position i, which is calculated like this

$$\partial_x \rho \approx \frac{\rho_{i+\frac{1}{2}} - \rho_{i-\frac{1}{2}}}{\Delta x}. \tag{2.66}$$

This scheme disallows density oscillations but means that the term

$$\boldsymbol{\nabla} \cdot (\rho \mathbf{v}) \approx \frac{\frac{1}{2}\left(\rho_{i+\frac{1}{2}} + \rho_{i+\frac{3}{2}}\right) v_{x,i+1} - \frac{1}{2}\left(\rho_{i+\frac{1}{2}} + \rho_{i-\frac{1}{2}}\right) v_{x,i}}{\Delta x} \tag{2.67}$$

at position $i + \frac{1}{2}$ includes interpolations between the two grids. The density needs to be interpolated onto the vector grid and afterwards the product can be differentiated back to the scalar grid. This complication with the interpolations is the central implementation problem. This problem as well as the implementation of the grid is very well explained in book of Griebel, Dornseifer, and Neunhoeffer, 1998 in Chapter three.

The programming effort is small compared to the benefit of physically meaningful results in the case of compressible dynamics. Details about the two-dimensional grid implementation and the corresponding finite differences schemes can be found in the appendix in Sections 7.1 and 7.2. Additional information about how to handle the half grid spacings in program and memory are also given in the appendix sections.

2.3.3 Pseudo compressible simulations

The fully compressible equations (2.22), (2.23), and (2.24) can be solved in the manner described above. All of these five equations include a time derivative for all primary

fields. Therefore, the RK3 can be applied directly and all fields can be stepped in time. This is not the case for the Boussinesq equations (2.10), (2.14), and (2.15). The continuity equation is reduced to a constraint on the divergence of the velocity fields. This equation can be used to formulate an equation for the pressure in the Navier-Stokes equation by taking the divergence of (2.14) leading to

$$\boldsymbol{\nabla}^2 p = \boldsymbol{\nabla} \cdot \left(- \left(\mathbf{v} \cdot \boldsymbol{\nabla} \right) \mathbf{v} - 2\frac{\mathrm{Pr}}{\mathrm{Ek}} \hat{y} \times \mathbf{v} + \mathrm{RaPr} T \hat{z} \right). \tag{2.68}$$

This is a Poisson equation for the pressure. Solving it involves more complicated numerics than discussed here.

There is a way to avoid solving this complicated Laplace equation by choosing the equation of state

$$p = c^2 \rho \tag{2.69}$$

with c^2 being some speed of sound squared. This equation is called the pseudo compressible equation of state and allows for a small compressibility, which is only depending on the density scaled by the speed of sound. The continuity equation becomes

$$\partial_t \rho = \boldsymbol{\nabla} \cdot \mathbf{v} \tag{2.70}$$

and can be integrated with the RK3 method shown above. This also introduces a new parameter, which has to be chosen carefully. A Mach number, the ratio between the largest velocity and the speed of sound

$$\mathrm{Ma} = \frac{\max \left(\mathbf{v} \right)}{c} < 0.1 \tag{2.71}$$

can be calculated to estimate the smallest speed of sound possible. The boundary of $\mathrm{Ma} < 0.1$ is generally considered to be close to the Boussinesq limit and the c^2 parameter in all simulations presented here was chosen to fulfill this limit. This method is originally from Chorin, 1967 and is explained in more detail in said article.

2.3.4 Bounds for the time step size

The time step size is limited by an upper bound. This bound depends either on the diffusion, advection or rotational effects. The effects due to diffusion are characterized by

$$\Delta t_{\mathrm{diff}} = C_{\mathrm{diff}} \Delta x^2, \tag{2.72}$$

where Δx is the smallest of the grid spacings, and C_{diff} is a constant close to one half and depending on the time stepping and finite difference method. This can be understood as diffusion from one grid spot to the next within one time step which limits the time step size.

Similarly, the restriction due too advection commonly known as the CFL-criterion

$$\Delta t_{\mathrm{adv}} = C_{\mathrm{adv}} \frac{\Delta x}{v_{\mathrm{max}}} \tag{2.73}$$

depends on the smallest grid spacing Δx, and the largest velocity v_{max} in the system. Again, C_{adv} is a constant close to one half. This criterion can be understood to restrict the time step by the time it takes for some fluid volume or wave to travel one grid spacing at the largest possible speed. Both cases, meaning Boussinesq and ideal gas, have a speed of sound and most simulations will run with velocities far away from this speed. The Boussinesq speed of sound is an artificially set parameter as explained in Section 2.3.3. The speed of sound of the ideal gas simulations is also set by the parameters but depends on the temperature as well. Therefore, it is not perfectly constant but an upper limit can be found by computing it at the lower boundary. This upper limit can be used for the time step. Ultimately, this limit is only valid if the largest Mach number is smaller than one. If it is, the time step size has to be reevaluated and adjusted. These two constraints can be calculated directly from the finite difference representations as shown in the book by Fletcher, 2000.

The last restriction is the global rate of rotation, which is only important for the Boussinesq simulation because the speed of sound is set artificially. In order to consider the simulation incompressible, the sound waves have to be able to travel across the domain within one rotation period, meaning

$$c^2 \gg \left(\frac{\mathrm{Pr}}{2\pi \mathrm{Ek}} \right)^2$$
$$\Rightarrow c^2 \mathrm{Ek}^2 > 0.5. \tag{2.74}$$

This is the same criterion as used by Tilgner, 2012 for similar simulations. The speed of sound needed to fulfill this restriction, as well as the Mach number limitation described in Section 2.3.3 sets a time step according to the CFL-criterion shown above.

3 When is a 2D approximation applicable

The approximation of a 2D flow is generally considered to be wrong unless it is justified by forces acting on the flow like the Coriolis force, or in very shallow but wide volumes using the shallow water approximation. We will be working with a domain that is constrained by the Coriolis force since we seek a model for convection at the equator region of gas planets like Jupiter or Earth's outer core. Usually, these regions are not shallow with Jupiter's outer non metallic layer having a depth of a few ten percents of its radius, or Earth's outer core having a depth larger than the radius of the inner core.

There is a phenomenon which describes the influence of the Coriolis force on the flow that will help us simplify to 2D simulations. This phenomenon can be demonstrated with a simple experiment for children and it can often be found at a science fair. It consists of a container filled with water, which is placed on a turntable and rotated with a few rotations per minute. Some ink with the same density as water is dropped into the container once the spin up face is complete. It can be seen that the ink only spreads horizontally and does only diffuse vertically as soon as the initial vertical momentum is dissipated. This phenomenon is described by the Taylor-Proudman theorem and is explained in some detail in the Book Kundu and Cohen, 2001 in Chapter 14.5. The Taylor-Proudman theory states that flow aligns in a plane perpendicular to the axis of rotation because the Coriolis force is only balanced by the pressure gradient if the rate of rotation is fast enough. The measure for "fast enough" is generally assumed to be a Rossby number smaller than one as explained in Section 2.2.4. This criterion is not strict, which is what we want to change here. We want to know how large the global rate of rotation has to be for the flow to perfectly align perpendicular to the axis of rotation giving us a reason for ignoring flow along this axis and allowing us to run 2D simulations without loss of generality.

A few simplifications will be used to answer this question. First, we will be running simulations with the Boussinesq approximation. Second, we will be using free slip boundaries because we want to remove all boundary layers, which would introduce a 3D behaviour. This is especially true for the bounding walls perpendicular to the axis of rotation that

will exhibit Ekman layers, which are known to introduce a flow along the axis. Third and finally, the chosen geometry shown in Section 2.1 has no curvatures, which would also change the flow structure.

This chapter will begin by highlighting some differences of 2D and 3D convection in this specific geometry. Afterwards, we will show a theory that has been investigated mathematically a few decades ago and will help us predict the transition line between perfect 2D and 3D flow. These flow structures consisting of a vortex with elliptical streamlines will be characterized with their Reynolds and Rossby numbers making the transition line independent of the convection driving the system. Most of the content in this chapter has been published in an article by Lüdemann and Tilgner, 2022. The arguments given in that article are repeated here and completed with additional information to broaden the understanding of the results.

The results for all simulations are given in the Appendix 7.5 in Tables 7.1 - 7.19. All 3D results are split into one Ekman number for each table. A horizontally dashed line in the table marks the transition between the numerical 2D and full 3D simulations. Additionally, the c^2 parameter as well as the number of grid points in horizontal $N_x = N_y$ and in vertical direction N_z are given for the 3D simulations. In contrast, the parameters N_x and N_z represent the number of elements in the 2D simulations, which all used a polynomial order of 8 in each element.

3.1 Differences in scaling laws

The comparison between the 2D and the 3D flow will be done by comparing their scaling laws of the Nusselt and Reynolds number with respect to the Rayleigh number. A set of 2D simulations spanning a wide range of Rayleigh numbers will be compared to a range of Rayleigh numbers with different Ekman numbers for the 3D simulations. Additionally, a dependence on the Prandtl number, which can be seen in the theoretical scaling law, is tested for the 2D simulations.

All 3D simulations were performed with the finite difference GPU code but most of the 2D simulations were performed with the NEK5000 software package[1]. Those simulations were run by Marie-Christine Volk. She used NEK5000 in her Bachelor thesis and agreed to run some simulations for this project after handing in her thesis. NEK5000 is a spectral element solver, that employs an adaptive time stepping method and solves the

---

[1] https://nek5000.mcs.anl.gov/ checked on the 19.01.2023 at 16:16
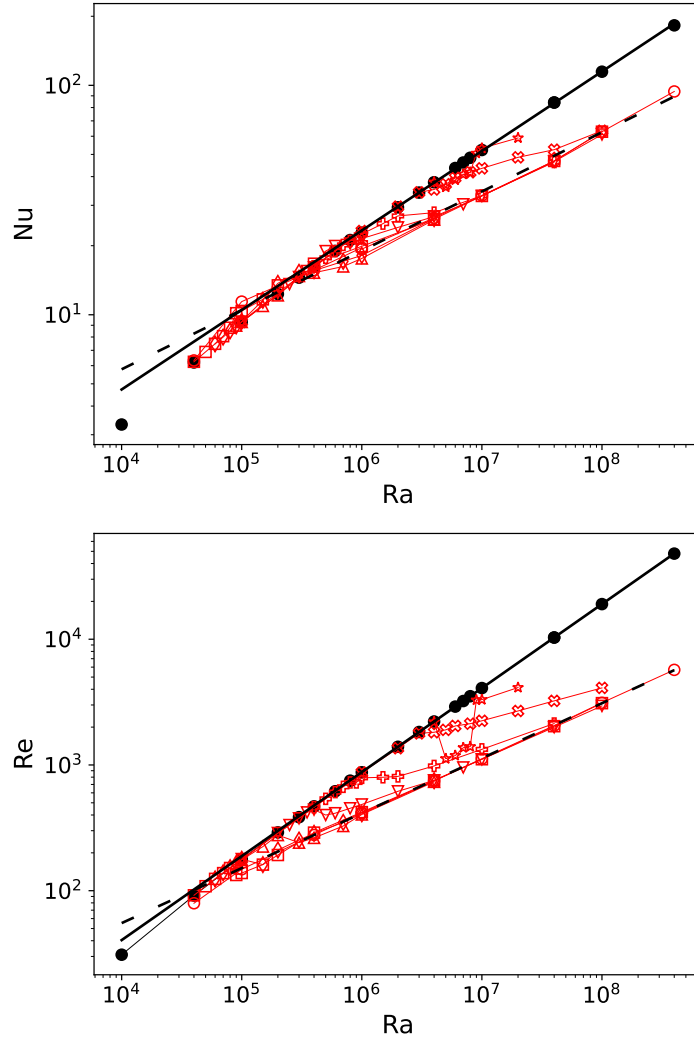
Figure 3.1: Shown are the scaling laws for the Nusselt number on the top and the Reynolds number on the bottom. Closed black symbols are the 2D simulations and open red symbols are the full 3D simulations. Circles represent $Ek = \infty$ or rotation free, squares $Ek = 10^{-2}$, diamonds $Ek = 7 \times 10^{-3}$, upward triangles $Ek = 3 \times 10^{-3}$, downward triangles $Ek = 10^{-3}$, pluses $Ek = 4 \times 10^{-4}$, crosses $Ek = 10^{-4}$, and stars $Ek = 4 \times 10^{-5}$ simulations. The solid lines are the best fit for the 2D scaling laws $Nu = 0.19 \times Ra^{0.35}$ and $Re = 0.09 \times Ra^{0.67}$, and the dashed lines are the best fit for the 3D scaling laws $Nu = 0.54 \times Ra^{0.26}$ and $Re = 0.99 \times Ra^{0.44}$. The lines connecting the points are for visual guidance only. This is part of Figures 1 and 2 from Lüdemann and Tilgner, 2022.
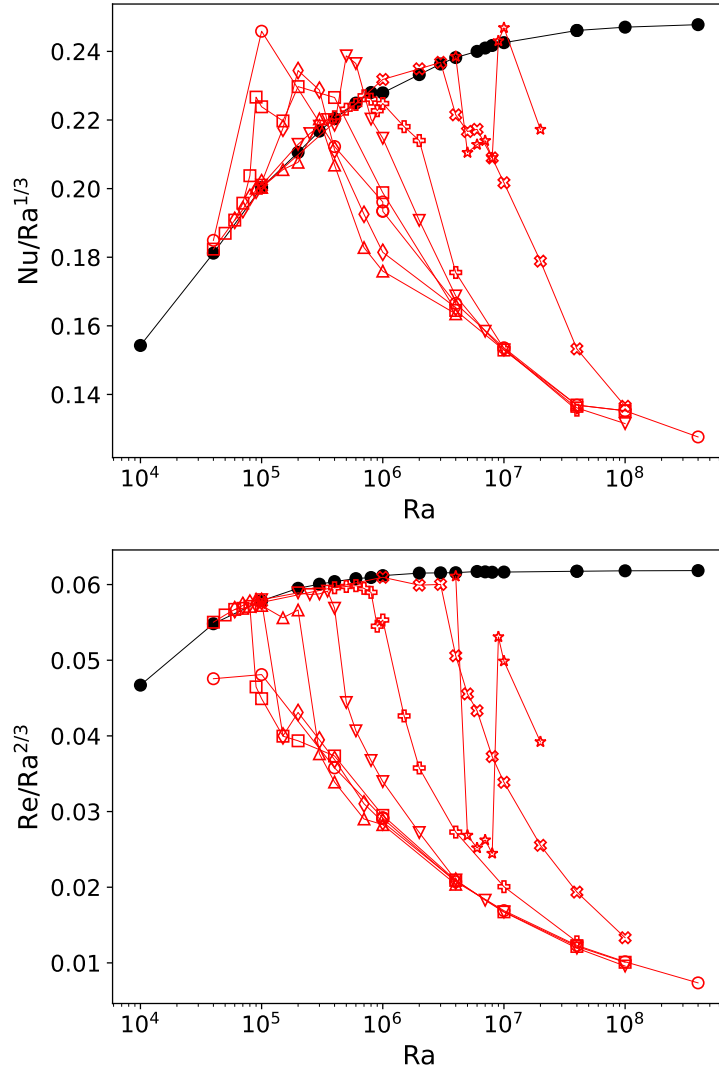
Figure 3.2: This figure shows the same symbols, colours and arrangement as in Figure 3.1 with all data points rescaled by the 2D scaling laws. Both scaling laws are rounded to the nearest fractions being $\mathrm{Nu} \propto \mathrm{Ra}^{1/3}$ and $\mathrm{Re} \propto \mathrm{Ra}^{2/3}$. The lines connection the points are for visual guidance only. This is part of Figures 1 and 2 from Lüdemann and Tilgner, 2022.

actual incompressibility condition $\boldsymbol{\nabla} \cdot \mathbf{v} = 0$ and not the pseudo incompressible condition from Section 2.3.3. The pseudo compressible condition makes the time stepping very stiff since the c^2 value has to be chosen carefully and because the flow velocity in the 2D simulations increases rapidly with the Rayleigh number. Additionally, the finite difference code needs a much higher spatial resolution compared to the spectral methods

of NEK5000. Furthermore, NEK5000 uses elements, meaning the computational volume is split into smaller volumes. The smaller volumes are then computed using spectral methods. This allows for an irregular placement of the elements. For example, the boundary can be resolved with more elements and the bulk can be slightly under resolved without increasing the overall number of elements. Therefore, it was beneficial to perform the 2D computations with NEK5000. It was verified that both codes give the same results for the same parameters.

First we will concentrate on the case with $\mathrm{Pr} = 0.7$. This Prandtl number will later be used in the calculations for the ideal gas. Both scaling laws for the Nusselt number and the Reynolds number are shown in Figure 3.1. The fill style and colour differentiates between the 2D (closed and black) and the 3D (open and red) simulations. Furthermore, the different Ekman number are shown by different symbols are described in the caption of Figure 3.1. Additionally, shown are two scaling laws for each measure. The solid lines are always for the 2D simulations and the dashed lines are for the 3D simulations. The best fit for the scaling laws are

$$\mathrm{Nu_{2D}} = 0.19 \times \mathrm{Ra}^{0.35}, \tag{3.1}$$

$$\mathrm{Nu_{3D}} = 0.54 \times \mathrm{Ra}^{0.26}, \tag{3.2}$$

$$\mathrm{Re_{2D}} = 0.09 \times \mathrm{Ra}^{0.67}, \tag{3.3}$$

$$\mathrm{Re_{3D}} = 0.99 \times \mathrm{Ra}^{0.44}. \tag{3.4}$$

Looking at the plot shows that the scaling laws for the 3D simulations could be improved by additional points as well as larger Rayleigh numbers.

More informative are the rescaled plots of both measures, which are shown in Figure 3.2. Here, the 2D scaling laws are rounded to the nearest fractions $\mathrm{Nu} \propto \mathrm{Ra}^{1/3}$ and $\mathrm{Re} \propto \mathrm{Ra}^{2/3}$. It can be seen that the 2D simulations asymptotically approach the scaling law and a fixed pre factor.

A much more striking observation is that the 3D simulations with a finite Ekman number stay very, very close too or on top of the 2D simulations with the same Rayleigh number until some critical Rayleigh number is reached. Afterwards, the measures differ more and more from the 2D counterparts until they eventually converge to the data points for the infinite Ekman number simulations.

This difference of 3D simulations is what we are interested in here. Apparently, there is no physical difference between 2D and 3D measures if the Rayleigh number is below the critical value. This critical value is going to be investigated further in the next Chapter 3.3.

For now, we will continue with the investigation of the scaling laws since the scaling of
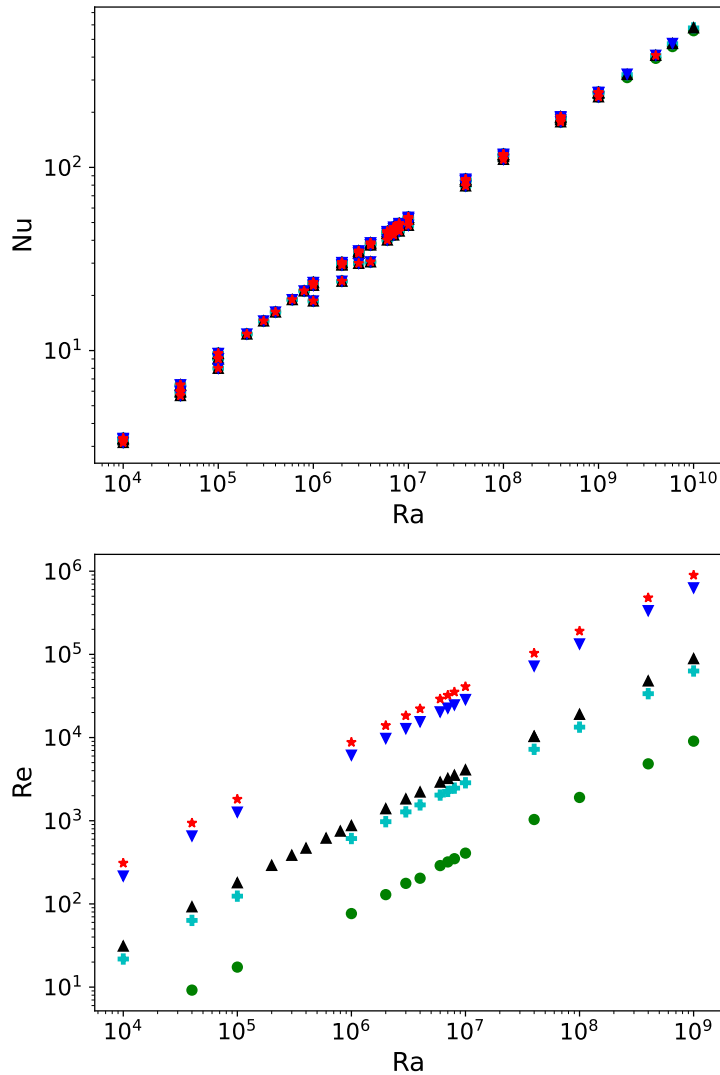
Figure 3.3: Shown are 2D simulations with different Prandtl numbers for the Nusselt number on the top and the Reynolds number in the bottom. The green circles are $Pr = 7$, cyan pluses are $Pr = 1$, black upwards triangles are $Pr = 0.7$, which is the default for all later plots, blue downward triangles are $Pr = 0.1$, and red stars are $Pr = 0.07$. The Nusselt number does not show a Prandtl number dependence and the Reynolds number does show one as indicated by the theoretical scaling laws in Equations (3.11) and (3.12).

the 2D Reynolds number differs from the usual $Re \propto Ra^{1/2}$ scaling by a lot. Rayleigh-Bénard convection is a widely studied phenomenon, that received plenty of theoretical
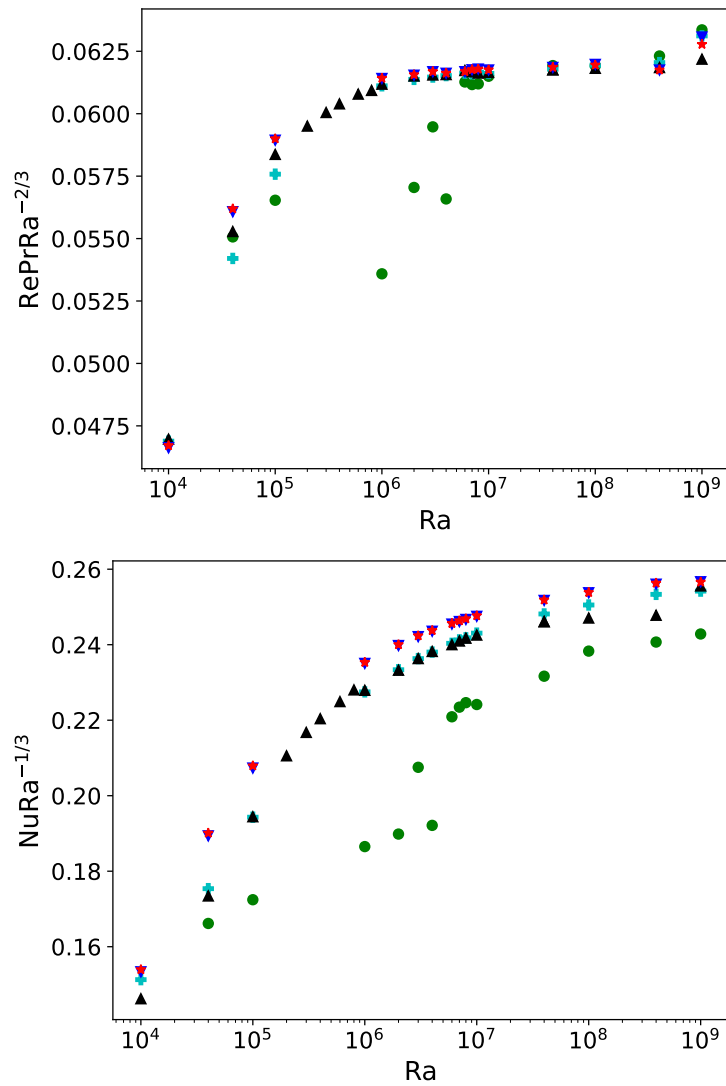
Figure 3.4: Shown are again 2D simulations with different Prandtl numbers and the symbols, colour and arrangement is the same as in Figure 3.3. The data is rescaled with the theoretical scaling laws shown in Equations (3.11) and (3.12).

treatment as well as many large scale parameter studies have been performed. These were accumulated into the so called Grossmann-Lohse theory and published in a set of articles by Grossmann and Lohse, 2000, Grossmann and Lohse, 2001, and Grossmann and Lohse, 2002. Some further improvements were made but only the original scaling laws are of interest here. For completeness it is important to note that the specific boundary conditions used here with free-slip velocity and fixed temperature boundaries

were specifically investigated by Whitehead and Doering, 2011 and Whitehead and Doering, 2012 but their emphasis was on upper bounds for the scaling laws.

The argument for the scaling laws in this work inspired by Grossmann and Lohse, 2001 is repeated below for completeness. The authors of the Grossmann-Lohse theory argue that the dissipation rate of kinetic ε_u and thermal energy ε_θ can be split into contributions of the bulk and the boundary

$$\varepsilon_u = \varepsilon_{u,\text{bulk}} + \varepsilon_{u,\text{BL}}, \tag{3.5}$$

$$\varepsilon_\theta = \varepsilon_{\theta,\text{bulk}} + \varepsilon_{\theta,\text{BL}}. \tag{3.6}$$

The global dissipation rates can be calculated and expressed in terms of the two measures as well as the parameters Ra and Pr as done by the authors

$$\varepsilon_u = \frac{\nu_0^3}{d^4}\left(\text{Nu} - 1\right)\text{RaPr}^{-2} \overset{\text{Nu}\gg 1}{\approx} \frac{\nu_0^3}{d^4}\text{NuRaPr}^{-2}, \tag{3.7}$$

$$\varepsilon_\theta = \kappa_0 \frac{(\Delta T)^2}{d^2}\text{Nu}. \tag{3.8}$$

All other contributions can only be estimated up to a constant scaling factor. Since only the exponents are of interest here, all relations are proportionalities from now on. Continuing with the argument, we will now use one of the contributions, either bulk or boundary layer depending on the flow structure. It is apparent from time series of the kinetic energy density as well as the Nusselt number that the 2D flow field is fully laminar and converges to a stationary field for all tested Rayleigh numbers. Furthermore, the 3D flow field becomes already turbulent for small Rayleigh numbers. This difference in flow structure will now be taken into account for the right-hand side of the dissipation rates. Laminar thermal boundary layers still exist and therefore the dissipation of thermal energy can be expressed by

$$\varepsilon_\theta = \varepsilon_{\theta,\text{BL}} \sim \kappa_0 \frac{(\Delta T)^2}{d^2}\left(\text{RaPr}\right)^{1/2}. \tag{3.9}$$

The flow structure is laminar, which is why we assume that the velocity boundary layer extends through the entire domain and therefore the dissipation of kinetic energy is

$$\varepsilon_u = \varepsilon_{u,\text{BL}} \sim \frac{\nu_0^3}{L^4}\text{Re}^2. \tag{3.10}$$

This is similar to the very high Prandtl number regime calculated by Grossmann and Lohse, 2001, where the dissipation is considered to be in the laminar bulk. Inserting and solving these two coupled equations leads to these scaling laws

$$\text{Nu} \propto \text{Ra}^{1/3}\text{Pr}^0, \tag{3.11}$$

$$\text{Re} \propto \text{Ra}^{2/3}\text{Pr}^{-1}. \tag{3.12}$$

36

Interestingly, the scaling laws from the dissipation rates indicate that the Reynolds number scaling should be Prandtl dependent and the Nusselt number scaling should not. This can also be investigated by running a short additional parameter study varying the Prandtl number (again with the help of Marie-Christine Volk). Results of this study are shown in Figure 3.3, and rescaled by the scaling laws (3.11) and (3.12) in Figure 3.4. The results for $\mathrm{Pr} = 7$ differ from the scaling laws. One reason for this difference in the regime $10^5 \leq \mathrm{Ra} \leq 10^7$ is that the flow reached a different state, which consists of two instead of the one roll and the state becomes time dependent. The flow stabilizes back into a single time independent roll for large Rayleigh numbers but still differs slightly in the Nusselt number. This suggests that higher Prandtl numbers behave differently in 2D compared to Prandtl number of unity and lower. Additionally, the Reynolds scaling first converges to a common pre factor but starts to depart for $\mathrm{Ra} > 10^8$. This could mean that the flow rearranges again and the scaling converges to a different one. Ultimately, none of the 2D simulations reached a time dependent state for high Rayleigh numbers. All converged into a steady state. Higher resolution simulations with higher Rayleigh numbers are needed to confirm that these simulations will indeed become time dependent at some point. For now, it looks like the idea of the velocity boundary layer "extending" through the domain is still accurate for simulations with free slip boundaries that should not have a boundary layer.

Similar calculations for the 3D scaling laws are also possible. The kinetic energy density as well as the Nusselt number show time dependent behaviour for most 3D simulations. Therefore, assuming that the dissipation of kinetic energy takes place mainly in the bulk especially since the free slip boundary conditions do not have dissipative boundary layers seems appropriate. This case is also handled in the original Grossmann-Lohse theory and the rate of energy dissipation is given as

$$\varepsilon_u = \varepsilon_{u,\mathrm{bulk}} \sim \frac{\nu_0}{d^4}\,\mathrm{Re}^3\,. \tag{3.13}$$

The dissipation of thermal energy is handled in the same manner since the thermal boundary layer is still laminar. Again, solving this set of equations leads to these scaling laws

$$\mathrm{Nu} \propto \mathrm{Ra}^{1/5}\mathrm{Pr}^{1/5} = \mathrm{Ra}^{0.2}\mathrm{Pr}^{0.2} \tag{3.14}$$

$$\mathrm{Re} \propto \mathrm{Ra}^{2/5}\mathrm{Pr}^{-3/5} = \mathrm{Ra}^{0.4}\mathrm{Pr}^{-0.6}\,. \tag{3.15}$$

Comparing these to the best fit results from Equations (3.2) and (3.4) disregarding the Prandtl number dependence shows some resemblance. As mentioned before, the best fit

exponents of the 3D simulations could be improved by running simulations with higher Rayleigh number. Also, no study in the Prandtl number space has been performed due too time constrain. Arguing with these dissipations rates is not perfectly accurate (more "wand waving" than "wingardium leviosa"[2]) but these scaling laws fit our best fit scaling laws very well for the 2D and reasonably well for the 3D simulations.

3.2 Tracing the 2D to 3D transition line
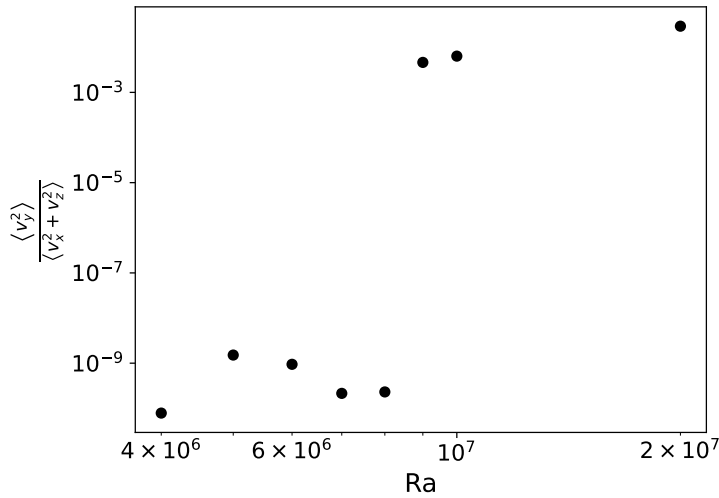
Figure 3.5: This plot shows the anisotropy (ratio of kinetic energy along the axis of rotation and perpendicular) over a range of Rayleigh numbers for a single Ekman number $Ek = 4 \times 10^{-5}$. The jump between very small and moderate ratios is the cross over point where a 3D simulations has no longer a numerically 2D flow. This is Figure 3 from Lüdemann and Tilgner, 2022.

The Section 3.1 highlighted a transition from the 3D simulations that reached numerically the same state as the actual 2D simulations. It was mentioned that the transition line can be traced and the interval of Rayleigh numbers between which the transition occurs marked. Looking at the results in Figure 3.2, it becomes evident that a more reliable measure for the transition needs to be found. The transition in the Reynolds plot is more clear to trace compared to the Nusselt number plot. Therefore, a measure using the kinetic energy looks most promising especially combined with the knowledge of

---

[2]This is a Harry Potter reference for those who missed it.
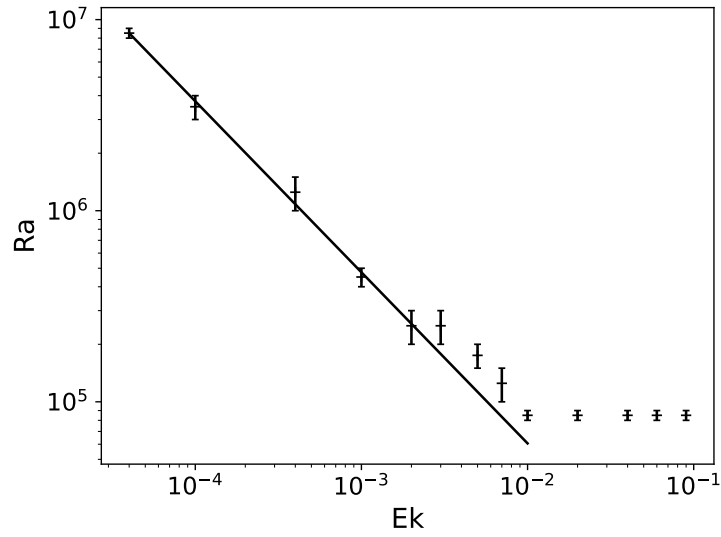
Figure 3.6: Shown is the stability boundary in the Ra-Ek plain. The interval of the Rayleigh numbers between which the boundary has been observed is plotted as an error bar. A best fit through the intervals for $\text{Ek} \leq 2 \times 10^{-3}$ is indicated as the solid line with $\text{Ra} = 982 \times \text{Ek}^{-0.9}$. This is Figure 4 from Lüdemann and Tilgner, 2022.

the Taylor-Proudman theorem. The easiest measure to think of is called the anisotropy

$$\frac{\left\langle v_y^2 \right\rangle}{\left\langle v_x^2 + v_z^2 \right\rangle} = \frac{\frac{1}{\mathcal{T}} \int_{\mathcal{T}} \frac{1}{\mathcal{V}} \int_{\mathcal{V}} v_y^2 \mathrm{d}\mathcal{V}\mathrm{d}\mathcal{T}}{\frac{1}{\mathcal{T}} \int_{\mathcal{T}} \frac{1}{\mathcal{V}} \int_{\mathcal{V}} \left(v_y^2 + v_z^2 \right) \mathrm{d}\mathcal{V}\mathrm{d}\mathcal{T}} \qquad (3.16)$$

and it represents a ratio of kinetic energy in the velocity component along the axis of rotation v_y compared to the two components perpendicular to it v_x and v_z. The angular brackets indicate volume and time averages. This measure can be calculated for all 3D simulations and plotted for a single Ekman number. One of these can be seen in Figure 3.5 as an example. This figure also stresses the meaning of a 3D simulation being numerically 2D. A perfect 2D simulation would have exactly $v_y = 0$ everywhere. However, this is not reachable for 3D simulations since all of them are started with 3D initial conditions to make sure that a 3D state can actually be reached if it exists. Therefore, the residual energy in the v_y component are round off errors of the single precision calculation. The jump between very small and moderate anisotropy is present for all Ekman numbers investigated here. However, it is not as visible for large Ekman numbers. For those large Ekman numbers the detachment point of the Reynolds number in Figure 3.2 is used in addition for finding the transition.
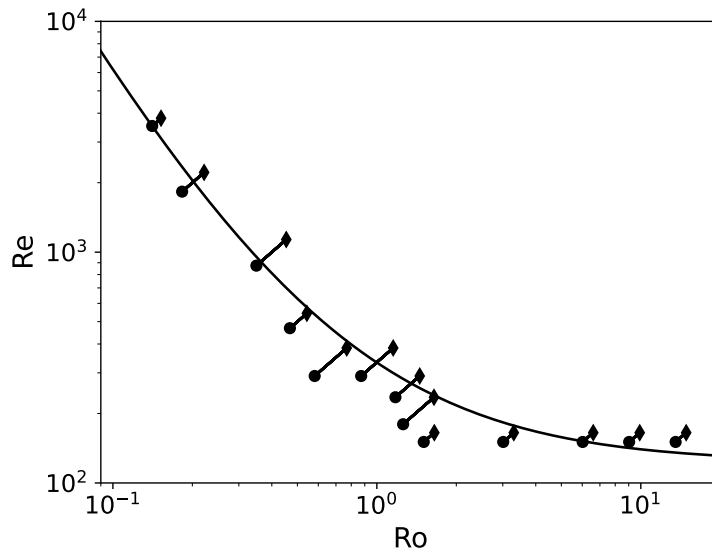
Figure 3.7: Shown is the stability boundary in the Re-Ro plain. The data is the same as in Figure 3.6 but the flow dependent measures are used instead of the control parameters. Circles represent the last simulation that was 2D and the diamonds represent the 2D results corresponding to the first 3D simulation. The black line shows the transition line calculated from the elliptical instability with strict bounds for k_0 as shown in Section 3.3.4. This is part of Figure 5 from Lüdemann and Tilgner, 2022.

Resulting from these traces are Rayleigh intervals for each Ekman number, which are shown in Figure 3.6. The error bars extend from the last 2D to the first 3D simulations, meaning that the transition takes place between these two numbers.

This transition is not unique because changing the Rayleigh number of the first 3D simulation to the last 2D one does not always stabilize the flow again. A full set of hysteresis simulations needs to be run in order to find the transition from 3D to 2D flow. This was not done here since we are interested in the transition from 2D to 3D and not the other way around.

It is visible in Figure 3.6 that no scaling exists for large Ekman numbers and deviations from the constant Rayleigh number only occur once $\mathrm{Ek} < 10^{-2}$. The scaling law is fitted to the center of the intervals for $\mathrm{Ek} \leq 2 \times 10^{-3}$ and the resulting law is $\mathrm{Ra} = 982 \times \mathrm{Ek}^{-0.9}$. Calculating a scaling law from the control parameters strongly depends on the boundary conditions, as indicated in Section 3.1. Furthermore, the scaling law indicates that buoyancy becomes less important for small Ekman numbers. This can be further investigated by comparing characteristic time scales, which are $t_{\mathrm{rot}} = 1/\Omega$ for the influence of

rotation, and the free fall time scale $t_{\text{free fall}} = \sqrt{d/g\alpha_0 \Delta T}$ for buoyancy. Computing the ratio of both results in a control parameter dependent Rossby number

$$\text{Ro}_{\text{free fall}} = \frac{t_{\text{rot}}}{t_{\text{free fall}}} = \sqrt{\frac{\text{RaEk}^2}{\text{Pr}}}. \tag{3.17}$$

The value of this Rossby number for $\text{Ek} = 10^{-3}$ is $\text{Ro}_{\text{free fall}} \approx 0.82$, and for $\text{Ek} = 10^{-5}$ is $\text{Ro}_{\text{free fall}} \approx 0.066$ highlighting that buoyancy looses its influence for small Ekman numbers.

Therefore, it is beneficial to use flow dependent measures for a more general scaling law. This law is shown in Figure 3.7, where the transition intervals are translated into the Reynolds and Rossby plane. The Reynolds number is directly calculated from the flow and the Rossby number is calculated from the Reynolds number with the help of the Ekman number as described in Section 2.2.4. Circles represent the last Rayleigh number that was numerically 2D. The diamonds show the 2D Reynolds number for the first 3D simulations. These Reynolds numbers are read from the true 2D simulations in order to have an interval in Reynolds between which the transition takes place. This is necessary because the Reynolds number of the 3D simulations is smaller than the last 2D simulation.

It can be observed that the behaviour in the Re-Ro plane is similar to the behaviour in the Ra-Ek plain with a transition at a constant Reynolds number for large Rossby and an increasing transitional Reynolds number for smaller Rossby numbers. Interestingly, Ro = 1 seems to be a transition for the influence of the Coriolis force but it is not a transition region. Even simulations with a small Rossby numbers can destabilize into a 3D flow if the Reynolds number is large enough.

The black line shown in Figure 3.7 is a theoretical transition line calculated from the elliptical instability, which is explained in the next section. This theoretical curve fits the transition intervals well for small Rossby numbers and also approaches a constant Reynolds number for large Rossby numbers.

3.3 Elliptical instability

The stability theory of infinitely extending, elliptical vortices has been developed in the late 80s of the last century. Much work has been done by Craik, Criminale, and Gaster, 1986, Bayly, 1986, Landman and Saffman, 1987, Craik, 1989, and Waleffe, 1990. A comprehensive review has been written by Kerswell, 2002. The reason for us focusing
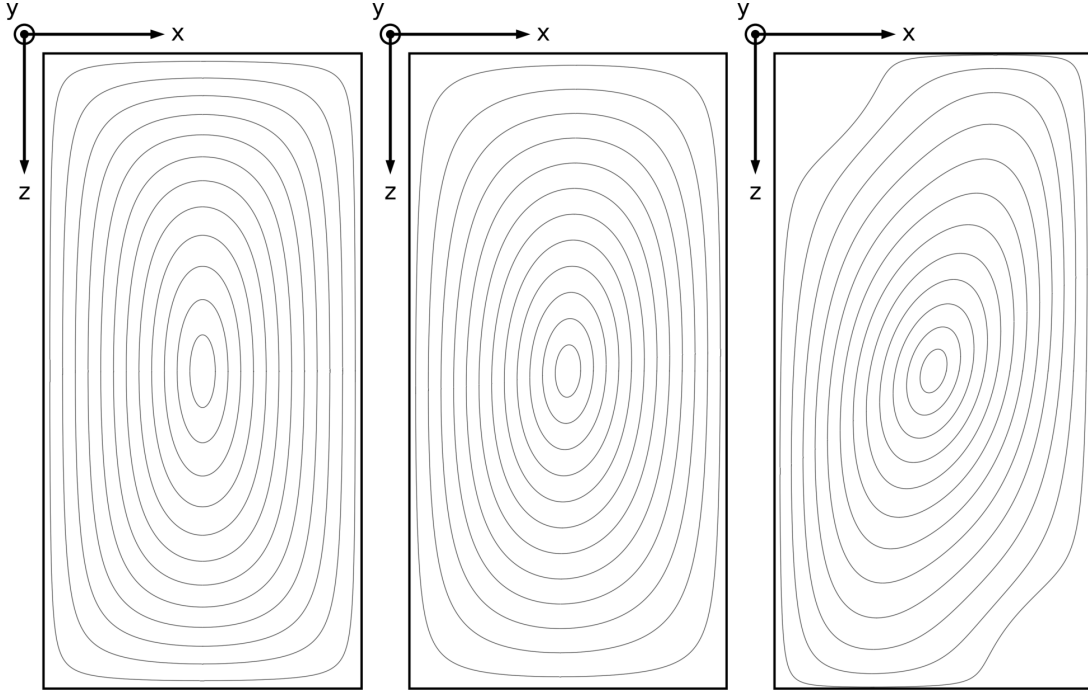
Figure 3.8: Shown are streamlines at different Rossby numbers. The right image shows a large Rossby number, the center one shows Ro ≈ 1, and the left one shows a small Rossby number. This is Figure 7 from Lüdemann and Tilgner, 2022.

on the stability theory of elliptical vortices can be found by looking at streamlines of the 2D flow, as shown in Figure 3.8. All three images are streamlines calculated from the 2D flow at different Rossby numbers, with the right most one having a large Rossby number, the middle one having a Rossby number of about one, and the left most one having a small Rossby number. The flow aligns with the boundaries due to the free slip boundary conditions and the aspect ratio of one half forces the vortex into an elliptical shape. It can be further observed that the ellipticity of the streamlines changes, becoming more elliptical for small Rossby numbers.

Calculating the boundaries of stability from a linear theory is much less computationally intensive compared to running linear simulations of the full problem. Additionally, further insight into the flow properties can be gained by working with a simplified theory. The calculations shown here, have mostly been published by the authors mentioned at the beginning of this section and a condensed version has been published by Lüdemann and Tilgner, 2022. This work will expand more on the calculations starting by introducing the basic equations in Section 3.3.1, followed by their dimensionless form as well as a parameter comparison in Section 3.3.2 because the dimensions of this simplified problem

42

are different from the full flow problem. The solution to the wave vector is given in Section 3.3.3. This section will conclude with the full stability calculations and their numerical solution in Section 3.3.4, as well as the approximation for the scaling at large Rossby numbers in Section 3.3.5.

3.3.1 Basic equation
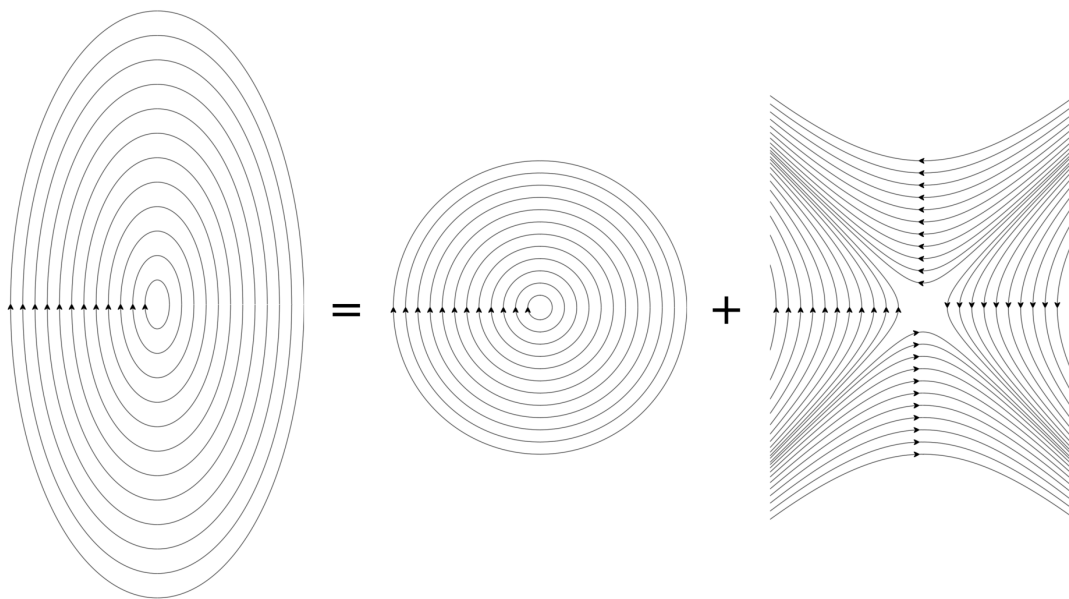
Figure 3.9: Shown are elliptical streamlines decomposed into their circular and hyperbolic parts. The Circular flow is the antisymmetric part and the hyperbolic flow is the symmetric part of Equation (3.18).

An infinitely extending vortex, with elliptical streamlines can be described by the velocity field

$$
\mathbf{U} = \begin{pmatrix} 0 & 0 & \Gamma - \epsilon \\ 0 & 0 & 0 \\ -\Gamma - \epsilon & 0 & 0 \end{pmatrix} \cdot \mathbf{x} = \underline{\underline{A}} \cdot \mathbf{x}, \tag{3.18}
$$

where Γ is half of the dimensional vorticity and ϵ is the dimensional rate of strain. Both are spatially uniform and are required to full fill this relation $|\epsilon| < |\Gamma|$ for elliptical streamlines. A scheme of this velocity field can be seen in Figure 3.9. The elliptical streamlines on the left are shown as the sum of two base flows consisting of a circular flow, which is the antisymmetric part of $\underline{A}$, and a hyperbolic flow profile which is the symmetric part of $\underline{A}$.

This is a linear stability theory and to this end, the full velocity field $\mathbf{u}$ is split into the elliptical background field and small perturbations

$$\mathbf{u} = \mathbf{U} + \mathbf{u}'. \tag{3.19}$$

The perturbations are split into Fourier modes and are of the form

$$\mathbf{u}' = \mathcal{R}\left\{ \mathbf{v}(t) e^{i\mathbf{k}(t)\cdot\mathbf{x}} \right\}. \tag{3.20}$$

This flow satisfies the dimensional Navier-Stokes and continuity equations in the Boussinesq approximation

$$\partial_t \mathbf{u} + (\mathbf{u} \cdot \boldsymbol{\nabla}) \mathbf{u} = -\frac{1}{\rho_0} \boldsymbol{\nabla} p + \nu_0 \boldsymbol{\nabla}^2 \mathbf{u} - 2\boldsymbol{\Omega} \times \mathbf{u}, \tag{3.21}$$

$$\boldsymbol{\nabla} \cdot \mathbf{u} = 0. \tag{3.22}$$

Dimensional equations are used here because this theory has different scales from the equations highlighted in Section 2.2 since no thermal diffusion is present. Their dimensionless form and a comparison to known parameters will be given in section 3.3.2.

The pressure is also split into Fourier modes

$$p(t) = \hat{p}(t) e^{i\mathbf{k}(t)\cdot\mathbf{x}}. \tag{3.23}$$

The Coriolis term has a global rate of rotation with $\boldsymbol{\Omega} = \Omega\hat{y}$ as described in Section 2.1. Plugging the separation (3.19) into the continuity equations leads to

$$\boldsymbol{\nabla} \cdot \mathbf{u}' = \mathbf{k} \cdot \mathbf{v} = 0. \tag{3.24}$$

The same separation in the Navier-Stokes equation results in

$$\partial_t \mathbf{u}' + \underbrace{\mathbf{U} \cdot \boldsymbol{\nabla} \mathbf{U}}_{\text{gradient}} + \underbrace{\mathbf{U} \cdot \boldsymbol{\nabla} \mathbf{u}'}_{III} + \underbrace{\mathbf{u}' \cdot \boldsymbol{\nabla} \mathbf{U}}_{II} + \underbrace{\mathbf{u}' \cdot \boldsymbol{\nabla} \mathbf{u}'}_{I} = -\frac{1}{\rho_0} \boldsymbol{\nabla} p + \nu_0 \boldsymbol{\nabla}^2 \mathbf{u}' - 2\boldsymbol{\Omega} \times \mathbf{u}' \tag{3.25}$$

The term containing the basic flow squared is a gradient and therefore neglected. The other three terms have to be calculated further, starting with the last one

$$\begin{aligned} I &= \mathbf{u}' \cdot \boldsymbol{\nabla} \mathbf{u}' \\ &= e^{i\mathbf{k}\cdot x} (\mathbf{v} \cdot \mathbf{k}) e^{i\mathbf{k}\cdot x} \\ &= 0. \end{aligned} \tag{3.26}$$

44

The second one leads to

$$
\begin{aligned}
II &= \mathbf{u}' \cdot \boldsymbol{\nabla} \mathbf{U} \\
&= e^{i\mathbf{k}\cdot x} \mathbf{v} \cdot \boldsymbol{\nabla} \underline{\underline{A}} \cdot \mathbf{x} \\
&= e^{i\mathbf{k}\cdot x} \underline{\underline{A}} \cdot \mathbf{v},
\end{aligned}
\tag{3.27}
$$

because of the antisymmetric part of $\underline{A}$. Finally, the third one results in

$$
\begin{aligned}
III &= \mathbf{U} \cdot \boldsymbol{\nabla} \mathbf{u}' \\
&= \left(\underline{\underline{A}} \cdot \mathbf{x} \cdot \boldsymbol{\nabla} \right) \mathbf{v} e^{i\mathbf{k}\cdot x} \\
&= i\mathbf{v} e^{i\mathbf{k}\cdot x} \left(\underline{\underline{A}}^T \cdot \mathbf{k} \right) \cdot \mathbf{x}.
\end{aligned}
\tag{3.28}
$$

Additionally, the time derivative has to be calculated since $\mathbf{v}(t)$ and $\mathbf{k}(t)$ are both time dependent

$$
\partial_t \mathbf{u}' = (\partial_t \mathbf{v}) \, e^{i\mathbf{k}\cdot x} + i\mathbf{v} e^{i\mathbf{k}\cdot x} (\partial_t \mathbf{k}) \cdot \mathbf{x}.
\tag{3.29}
$$

Ultimately, with the time derivative as well as term III, we get an evolution equation for the wave vector itself

$$
\partial_t \mathbf{k} = -\underline{\underline{A}}^T \cdot \mathbf{k}
\tag{3.30}
$$

because the spatially dependent terms are imaginary and have to cancel for the velocity field to remain real.

With these calculations, we arrive at an equation for the velocity amplitude

$$
\partial_t \mathbf{v} + \underline{\underline{A}} \cdot \mathbf{v} = -\frac{1}{\rho_0} \mathbf{k}\hat{p} - \nu_0 |\mathbf{k}|^2 \mathbf{v} - 2\boldsymbol{\Omega} \times \mathbf{v},
\tag{3.31}
$$

which is similar to the one obtained by Landman and Saffman, 1987 with an additional Coriolis term. This equation still contains dimensions, which will be removed shortly and the pressure can be projected out for the numerical calculations. This projection will be handled in detail with the dimensionless form of the equation.

3.3.2 Dimensionless form

Dimensionless variables are introduced before proceeding with investigating the behaviour of equation (3.31). The symbols remain the same but all equations are considered dimensionless from now on.

The half vorticity Γ is used as a time scale and the height d, introduced for the full flow

simulations, as a length scale. This length scale is arbitrary for the infinitely extended vortex but will become relevant once bounding surfaces are introduced to the theory. The density ρ_0 is assumed to be constant and the rate of global rotation scales with Ω, which is also constant. Introducing these scales in the elliptical flow (3.18) gives the ellipticity $\beta = \epsilon/\Gamma$ as one dimensionless parameter and changes the matrix

$$\underline{\underline{A}} = \begin{pmatrix} 0 & 0 & 1 - \beta \\ 0 & 0 & 0 \\ -1 - \beta & 0 & 0 \end{pmatrix}. \tag{3.32}$$

The value of $0 \leq \beta \leq 1$ differentiates between the circular solid body rotation $\beta = 0$ and the Couette flow $\beta = 1$. Both of those cases are stable flows, as was highlighted by Craik, Criminale, and Gaster, 1986.

A new pressure field $\tilde{p}$ with correct units is introduced but not stated because it will be projected out later. Equation (3.31) changes to

$$\partial_t \mathbf{v} + \underline{\underline{A}} \cdot \mathbf{v} = -\mathbf{k}\tilde{p} - \mathrm{Re}_\beta^{-1} |\mathbf{k}|^2 \mathbf{v} - 2\mathrm{Ro}_\beta^{-1} \underline{\underline{\Omega}} \cdot \mathbf{v}. \tag{3.33}$$

A matrix is substituting the vector product for the Coriolis term

$$\underline{\underline{\Omega}} = \begin{pmatrix} 0 & 0 & 1 \\ 0 & 0 & 0 \\ -1 & 0 & 0 \end{pmatrix}. \tag{3.34}$$

This substitution makes the Coriolis term similar to the ones containing the matrix $\underline{\underline{A}}$. Two newly introduced parameters are similar to the ones known as the Reynolds number

$$\mathrm{Re}_\beta = \frac{\Gamma d^2}{\nu_0} \tag{3.35}$$

and the Rossby number

$$\mathrm{Ro}_\beta = \frac{\Gamma}{\Omega}. \tag{3.36}$$

These two are called η and ω by Lüdemann and Tilgner, 2022. The length d is used to make the wave number k_0 dimensionless, which is an additional important parameter. It will be used because the theory implies an infinite vortex but the full flow simulations are contained by walls, which limit the largest possible wavelengths.

The parameters called Re_β and Ro_β are similar to the Reynolds and Rossby number introduced in Section 2.2.4. They differ by a geometry dependent factor, which can be

calculated by applying Equation (2.53) to the elliptical base flow from Equation (3.18) with matrix $\underline{\underline{A}}$ from (3.32)

$$\frac{1}{\mathcal{V}} \int_{-L/2}^{L/2} \mathrm{d}x \int_{-L/2}^{L/2} \mathrm{d}y \int_{-d/2}^{d/2} \mathrm{d}z \left[(1-\beta)^2 \, z^2 + (1+\beta)^2 \, x^2\right] =$$
$$4 \int_{-1/4}^{1/4} \mathrm{d}x \int_{-1/4}^{1/4} \mathrm{d}y \int_{-1/2}^{1/2} \mathrm{d}z \left[(1-\beta)^2 \, z^2 + (1+\beta)^2 \, x^2\right] =$$
$$\frac{1}{12} \left[(1-\beta)^2 + \frac{1}{4}(1+\beta)^2\right]. \tag{3.37}$$

This factor translates the two sets of parameters

$$\mathrm{Re} = \mathrm{Re}_\beta \sqrt{\frac{1}{12} \left[(1-\beta)^2 + \frac{1}{4}(1+\beta)^2\right]}, \tag{3.38}$$

$$\mathrm{Ro} = \mathrm{Ro}_\beta \sqrt{\frac{1}{12} \left[(1-\beta)^2 + \frac{1}{4}(1+\beta)^2\right]}. \tag{3.39}$$

All that remains to be done is choosing a suitable value for the ellipticity β. The ellip-
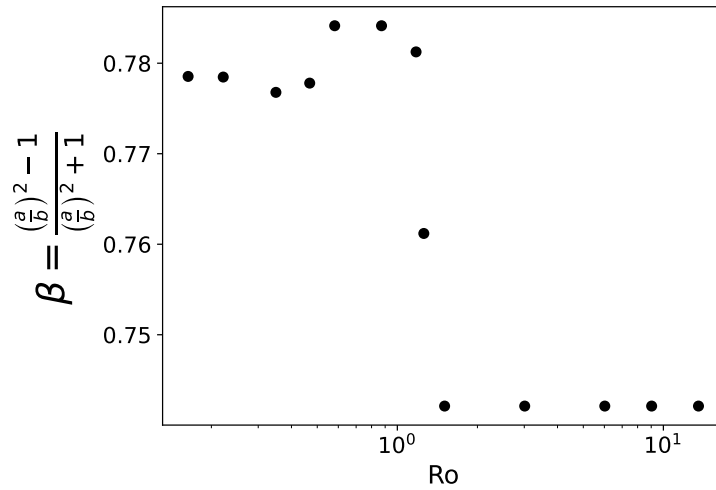
Figure 3.10: Shown is the ellipticity of the streamlines for the 2D full flow simulations for different Rossby numbers. It is calculated from the eigenvalues $1/a$ and $1/b$ of the Jacobian of the velocity field at the center of the cell. This is Figure 6 from Lüdemann and Tilgner, 2022.

ticity β can be calculated from the ratio of the two semi axis of the elliptical streamlines, which we will call a and b

$$\beta = \frac{\left(\frac{a}{b}\right)^2 - 1}{\left(\frac{a}{b}\right)^2 + 1}. \tag{3.40}$$

Looking back at the streamlines for different Rossby numbers of the flow in Figure 3.8, it can be observed that the flow aligns with the boundaries. The inverse aspect ratio of the cell gives a value for $a/b = 2$, which can be calculated into $\beta = 0.6$. It can also be seen that the center most streamline changes it's ellipticity, therefore using the geometry for the ellipticity seems ill advised.

A more accurate approach to calculating the ellipticity is to calculate the Jacobian at the center of the cell and compute the eigenvalues. One of the eigenvalues will be zero because it is a 2D flow and the other two give the inverse of the two semi axis $1/a$ and $1/b$. They can be computed into a value for the ellipticity β according to Equation (3.40). This calculation can be done for many simulations at different Rossby numbers. The results can be seen in Figure 3.10. It can be observed that the ellipticity changes at Ro ≈ 1, which is reflected in the changes of the streamlines observed in Figure 3.8. The absolute changes in the β value are small however, allowing us to use a value of $\beta = 0.78$ for all later calculations. Finally, the geometric compensation factor for the Reynolds and Rossby number can be calculated Re $\approx 0.26 \mathrm{Re}_\beta$ for this ellipticity.

3.3.3 Solution for the wave vector $\mathbf{k}(t)$

The evolution equation for the wave vector $\mathbf{k}(t)$ (3.30) can be solved in closed form. This solution is shown by Craik, Criminale, and Gaster, 1986 and the result is reproduced here for completeness. All variables are dimensionless in this calculation. A solution to Equation (3.30) is

$$\mathbf{k}(t) = e^{-\underline{\underline{A}}^T t} \cdot \mathbf{k}(0). \tag{3.41}$$

The exponential term can be calculated by an inverse Laplace transformation

$$
\begin{aligned}
e^{-\underline{\underline{A}}^T t} &= \mathcal{L}_q^{-1}\left[\left(q\underline{\underline{I}} + \underline{\underline{A}}^T\right)^{-1}\right] \\
&= \begin{pmatrix}
\cos\left(\sqrt{1-\beta^2}(t-t_0)\right) & 0 & \frac{\beta-1}{\sqrt{1-\beta^2}}\sin\left(\sqrt{1-\beta^2}(t-t_0)\right) \\
0 & 1 & 0 \\
\frac{\beta+1}{\sqrt{1-\beta^2}}\sin\left(\sqrt{1-\beta^2}(t-t_0)\right) & 0 & \cos\left(\sqrt{1-\beta^2}(t-t_0)\right)
\end{pmatrix},
\end{aligned} \tag{3.42}
$$

where $\underline{\underline{I}}$ is the identity matrix, q the transformation variable, and t_0 an integration constant. It can already be seen that the solution has a time periodicity of $2\pi/\sqrt{1-\beta^2}$.

A suitable initial wave vector $\mathbf{k}(0)$ without loss of generality needs to be chosen

$$\mathbf{k}(0) = k_0 \begin{pmatrix} 0 \\ \cos\theta \\ \sin\theta \end{pmatrix}, \tag{3.43}$$

which has an angle θ to the $\hat{y}$-axis and length k_0. The wave number is made dimensionless with the height d.

After careful calculations we are left with this time dependent elliptical wave vector

$$\mathbf{k} = k_0 \begin{pmatrix} \alpha_\beta \sin\theta \sin\left(\sqrt{1-\beta^2}(t-t_0)\right) \\ \cos\theta \\ \sin\theta \cos\left(\sqrt{1-\beta^2}(t-t_0)\right) \end{pmatrix}, \tag{3.44}$$

with $\alpha_\beta = \sqrt{1+\beta/1-\beta}$ being the aspect ratio of the elliptical streamlines. This result is similar to the one obtained by Landman and Saffman, 1987, with the axis being permutations due to the different geometry in this work.

3.3.4 Full stability calculations

We start again with equation (3.33). In order to compute the stability of this equation, we need to calculate the pressure. The pressure can be projected out by multiplying equation (3.33) with $\mathbf{k}$ and using the continuity equation (3.24), resulting in

$$\mathbf{k} \cdot \partial_t \mathbf{v} + \mathbf{k} \cdot \underline{\underline{A}} \cdot \mathbf{v} = |\mathbf{k}|^2 \hat{p} - 2\mathrm{Ro}_\beta^{-1} \mathbf{k} \cdot \underline{\underline{\Omega}} \cdot \mathbf{v}. \tag{3.45}$$

The time derivative needs to be be calculated

$$\partial_t \left(\mathbf{k} \cdot \mathbf{v}\right) = 0 = \partial_t \mathbf{k} \cdot \mathbf{v} + \mathbf{k} \cdot \partial_t \mathbf{v}$$
$$\Rightarrow -\mathbf{k} \cdot \partial_t \mathbf{v} = \left(-\mathbf{k} \cdot \underline{\underline{A}}\right) \cdot \mathbf{v}$$
$$\Rightarrow \mathbf{k} \cdot \partial_t \mathbf{v} = \mathbf{k} \cdot \underline{\underline{A}} \cdot \mathbf{v}. \tag{3.46}$$

Plugging equation (3.46) into equation (3.45) results in the pressure equation

$$2\mathbf{k} \cdot \underline{\underline{A}} \cdot \mathbf{v} = |\mathbf{k}|^2 \hat{p} - 2\mathrm{Ro}_\beta^{-1} \mathbf{k} \cdot \underline{\underline{\Omega}} \cdot \mathbf{v}$$
$$\Rightarrow \hat{p} = \frac{2\mathbf{k}}{|\mathbf{k}|^2} \left(\underline{\underline{A}} + \mathrm{Ro}_\beta^{-1} \underline{\underline{\Omega}}\right) \cdot \mathbf{v}. \tag{3.47}$$

This relation can be plugged into equation (3.33)

$$\partial_t \mathbf{v} = \frac{2\mathbf{k}\mathbf{k}^T}{|\mathbf{k}|^2} \left(\underline{\underline{A}} + \mathrm{Ro}_\beta^{-1} \underline{\underline{\Omega}}\right) \cdot \mathbf{v} - \underline{\underline{A}} \cdot \mathbf{v} - 2\mathrm{Ro}_\beta^{-1} \underline{\underline{\Omega}} \cdot \mathbf{v} - \mathrm{Re}_\beta^{-1} |\mathbf{k}|^2 \mathbf{v}, \tag{3.48}$$

where $\mathbf{k}\mathbf{k}^T$ is the outer product of the wave vector. This is a Mathieu equation with an additional viscosity term, meaning that this equation is linear in the velocity with time periodic prefactors. A good introduction into this type of equations is given by Jordan and Smith, 2007 in Chapter nine. The authors Craik, Criminale, and Gaster, 1986 show that the viscosity term can be projected out by calculating

$$\hat{\mathbf{v}} = e^{\mathrm{Re}_\beta^{-1} \int_0^t |\mathbf{k}|^2 \mathrm{d}t} \mathbf{v}. \tag{3.49}$$

Finally, we can write a growth equation with a time periodic prefactor

$$\partial_t \hat{\mathbf{v}} = \underline{\underline{Q}}(t) \cdot \hat{\mathbf{v}} \tag{3.50}$$

with the prefactor being

$$\underline{\underline{Q}}(t) = \frac{2\mathbf{k}\mathbf{k}^T}{|\mathbf{k}|^2} \left(\underline{\underline{A}} + \mathrm{Ro}_\beta^{-1} \underline{\underline{\Omega}} \right) - \underline{\underline{A}} - 2\mathrm{Ro}_\beta^{-1} \underline{\underline{\Omega}}. \tag{3.51}$$

This is a similar problem to the other authors and can be solved with the Floquet theory

$$\partial_t \underline{\underline{M}}(t) = \underline{\underline{Q}}(t) \cdot \underline{\underline{M}}(t), \tag{3.52}$$

with the initial condition $\underline{\underline{M}}(0) = \underline{\underline{I}}$ being the identity matrix.

The eigenvalues at $t = 2\pi/\sqrt{1-\beta^2}$ are the Floquet multipliers μ_i. These determine the growth of the solution, which is of the form

$$\hat{\mathbf{v}}(t) = \mu_i \mathbf{f}_i = e^{\sigma_i t} \mathbf{f}_i, \tag{3.53}$$

where $\mathbf{f}_i$ is the eigenvector for eigenvalue μ_i. We can calculate the growth rates from the eigenvalues

$$\sigma_i = \frac{\sqrt{1-\beta^2}}{2\pi} \log \mu_i. \tag{3.54}$$

It is easy to see that one multiplier, say μ_3, is $\mu_3 = 1$ because $\underline{\underline{Q}}$ has one row and column equal to zero and is therefore rank deficient. Due to conservation properties and symmetries, the other multipliers have to be $\mu_1 \mu_2 = 1$ with both of them being either real and reciprocal, or complex conjugate of each other. Only the real, reciprocal eigenvalues are of interest because the complex ones are temporally oscillating solutions. Therefore, we can calculate the growth rate as shown in equation (3.54).

The influence of viscosity on the growth rates can be calculated similarly and is shown in equation (3.49). The detailed calculation of the integral is shown by Craik, Criminale,

and Gaster, 1986 and the result is

$$\sigma_\nu = -\text{Re}_\beta^{-1} \int_0^{2\pi/\sqrt{1-\beta^2}} |\mathbf{k}|^2 \mathrm{d}t$$
$$= -\text{Re}_\beta^{-1} k_0^2 \left(1 + \frac{1}{2}\left(\alpha^2 - 1\right)\sin^2\theta\right). \tag{3.55}$$

The combined rate of growth is

$$\sigma = \frac{1}{2\pi}\left(\sqrt{1-\beta^2}\log\mu_1 - 2\pi\text{Re}_\beta^{-1}\frac{1-\beta\cos^2\theta}{1-\beta}\right). \tag{3.56}$$

Equation (3.52) can be integrated numerically and the eigenvalues computed from the result at $t = 2\pi/\sqrt{1-\beta^2}$. Finally, the growth rate depends on the initial wave number k_0, as well as the angle θ, the ellipticity β, the Rossby Ro_β, and the Reynolds number Re_β.

This is the point were we leave the path created by the other authors because the full flow simulations have boundaries which need to be applied to the stability analysis. To that end, a suitable ellipticity of $\beta = 0.76$ has been chosen in Section 3.3.2. Additionally, a maximum growth rate condition is applied to the angle θ. Since marginal stability is of interest here, only the largest growth rate is needed, leading to a maximization problem for the angles θ.

Furthermore, the wave number k_0 has a lower limit and is directly linked to the angle θ because the full flow simulations are compute in a box of specific length and height as indicated in Figure 3.11. The idea is that the wave number has to be large enough to fit at least half of a wavelength into the direction parallel and perpendicular to the axis of rotation. The angle θ as well as the two components of the wave vector are sketched into the geometry in Figure 3.11 highlighting the choice of lengths. Ultimately, the restrictions on the vector length are

$$k_0\cos\theta \geq k_{||} = 2\pi, \tag{3.57}$$
$$k_0\sin\theta \geq k_\perp = \pi. \tag{3.58}$$

This restriction ensures that the normal velocity component at the boundaries is zero as required by the free-slip boundary condition. However, this treatment of the boundaries is not equal to the free-slip boundary condition of the full flow simulations. Nonetheless, this approximation is sufficient to include the geometric constraints and useful insight can be gained by it.

Only the Rossby Ro_β and Reynold Re_β number have to be set or found after all these restrictions are applied. A maximization algorithm for the growth rates over all angles $0 \leq \theta \leq \pi$ with the restriction on the wave number is computed. One Ro_β value and a
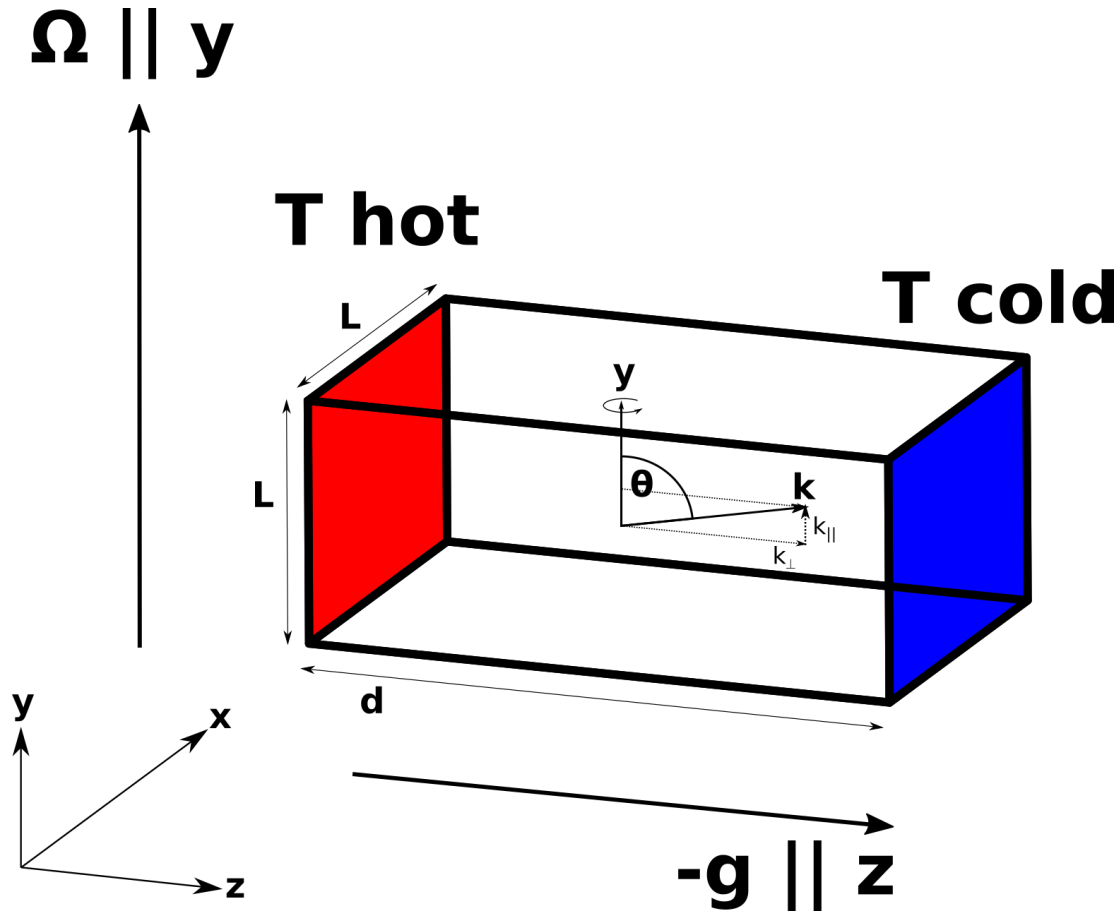
Figure 3.11: Shown is the geometry introduced in Section 2.1 with the addition of the disturbance wave vector. The wave vector rotates in time in a plain perpendicular to the axis of rotation (y-axis) and therefore has a component parallel $k_{||}$ and a component perpendicular to it $k_{\perp}$. Both are limited by a largest wavelength in order to fit one half wavelength into the geometry.

bracket in Re_{β} are chosen, which include a change in sign for the largest growth rate. A root finder is used to calculated the Re_{β} at which the largest growth rate becomes zero. These calculations are repeated for a range in Ro_{β}. The results for the inviscid case and the inviscid, rotating case without the restriction on the wave number have been compared to Craik, 1989 and Landman and Saffman, 1987 for validation.

One interesting observation can be gained by this validation. Specifically, Craik, 1989 showed that the range of angles θ, which destabilises, becomes smaller and converges towards π. The result is that the parallel component of the wave vector becomes very small compared to the overall length k_0. Therefore, the influence the Coriolis force
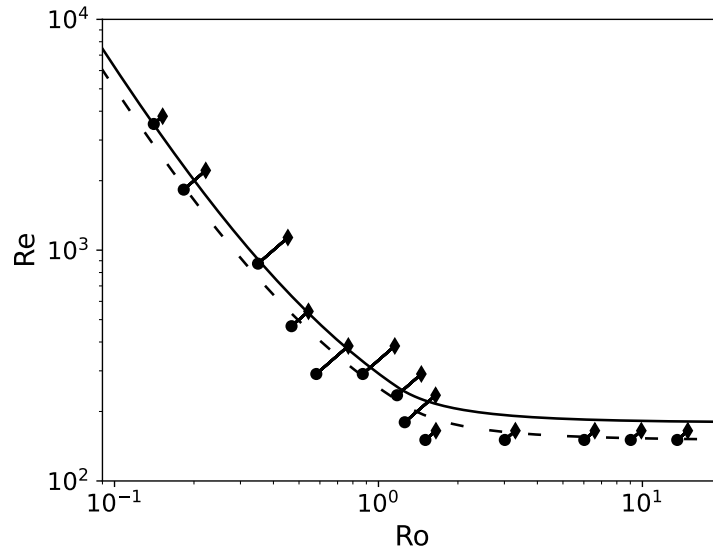
Figure 3.12: Shown is the same stability boundary from the full flow simulations as shown in Figure 3.7. The results of the stability calculations are shown for two different β values with $\beta = 0.8$ the solid and $\beta = 0.76$ for the dashed line. The restrictions for the wave number are $k_{||} = {}^{5\pi}/_3$ and $k_\perp = 2\pi$, which is considered a best fit to the results of the full flow simulations. This is Figure 8 from Lüdemann and Tilgner, 2022.

has on this stability problem is increased by the boundaries compared to the infinitely extending vortex. This will become more apparent in Section 3.3.5.

Results of the full stability analysis for the strict bounds on the wave number from Equations (3.57) and (3.58) are shown in Figure 3.7 for $\beta = 0.78$. These results fit the transition of the full flow simulations reasonably well. The asymptotic behaviour for the limit Ro $\to 0$ agrees with the full flow simulations but the behaviour for large Ro does not. It is reasonable to assume that two different β values are required to fit both extremes, considering that the ellipticity of the full flow simulations changes from large to small Ro, as indicated in Figure 3.10. Additionally, the strict constraints on the wave number are changed to a best fit result with $k_{||} = {}^{5\pi}/_3$, and $k_\perp = 2\pi$ since observations of the streamlines show that the flow prefers a full wavelength in the vertical direction. The resulting curves are shown in Figure 3.12 for two value of β with $\beta = 0.80$ as the solid line for small Ro, and $\beta = 0.76$ as the dashed line for large Ro. Additionally, a scaling law of

$$\mathrm{Re} \approx 100\mathrm{Ro}^{-2} \tag{3.59}$$

can be obtained from the results for small Ro and $\beta = 0.8$. This scaling law is true for most values of β and only the prefactor changes. Therefore, a small β approximation can be applied to calculate this scaling law analytically. This calculation is shown in the next Section 3.3.5.

3.3.5 $\mathrm{Ro} \to 0$ and the scaling law

It is instructive to investigate the limit $\mathrm{Ro} \to 0$ which can be done analytically in the case $\beta \ll 1$. We follow the calculations of Craik, 1989, Waleffe, 1990, and Kerswell, 2002 in order to find an expression for this limit. Firstly, we multiply equation (3.33) with $\mathbf{v}$, which removes the pressure term due to the continuity equation and gives an energy equation

$$\frac{\mathrm{d}}{\mathrm{d}t} \frac{1}{2} |\mathbf{v}|^2 = -\mathbf{v} \cdot \left(\underline{\underline{A}} + 2\mathrm{Ro}_\beta^{-1} \underline{\underline{\Omega}} \right) \cdot \mathbf{v} - \mathrm{Re}_\beta^{-1} |\mathbf{k}|^2 |\mathbf{v}|^2$$

$$= 2\beta v_x v_z - \mathrm{Re}_\beta^{-1} |\mathbf{k}|^2 |\mathbf{v}|^2. \tag{3.60}$$

Secondly, the field $\mathbf{v}(t) = \left(\mathbf{v}_0(t) + \beta \mathbf{v}_1(t) + \mathcal{O}(\beta^2) \right) e^{\sigma t}$ is expressed as a series in β for $\beta \ll 1$ and the leading order terms are investigated further. This approximation is applied to the wave vector as well, leading to

$$\mathbf{k}(t) = k_0 \begin{pmatrix} \sin\theta \sin t \\ \cos\theta \\ \sin\theta \cos t \end{pmatrix}, \tag{3.61}$$

which is the wave vector of Kelvin-waves for uniformly rotating flow. The underlying flow field can be computed as well, which is shown by Greenspan, 1968 in Chapter 4. The flow field counter rotates around $\mathbf{k}$ with rate

$$\Gamma = 2 \left(1 + \mathrm{Ro}_\beta^{-1} \right) \cos\theta \tag{3.62}$$

and can be written as

$$\mathbf{v_0} = \frac{1}{2} e^{-\mathrm{Re}_\beta^{-1} k_0^2 t} \begin{pmatrix} -(1-\cos\theta)\sin\left(\Gamma_+ t + \Phi\right) - (1+\cos\theta)\sin\left(\Gamma_- t + \Phi\right) \\ -2\sin\theta \sin\left(\Gamma t + \Phi\right) \\ -(1-\cos\theta)\cos\left(\Gamma_+ t + \Phi\right) + (1+\cos\theta)\cos\left(\Gamma_- t + \Phi\right) \end{pmatrix}$$

$$= \hat{\mathbf{v}}_0 e^{-\mathrm{Re}_\beta^{-1} k_0^2 t}, \tag{3.63}$$

with an arbitrary and constant phase Φ, and $\Gamma_\pm = \Gamma \pm 1$. This solution can now be inserted into the energy equation (3.60) for the leading order term with the left-hand

side being

$$\frac{1}{|\mathbf{v}|^2}\frac{\mathrm{d}}{\mathrm{d}t}\frac{1}{2}|\mathbf{v}|^2 = \frac{1}{|\hat{\mathbf{v}}_0|^2 e^{2\left(\sigma-\mathrm{Re}_\beta^{-1}k_0^2\right)t}}\frac{\mathrm{d}}{\mathrm{d}t}\frac{1}{2}|\hat{\mathbf{v}}_0|^2 e^{2\left(\sigma-\mathrm{Re}_\beta^{-1}k_0^2\right)t}$$

$$= \frac{1}{e^{2\left(\sigma-\mathrm{Re}_\beta^{-1}k_0^2\right)t}}\frac{\mathrm{d}}{\mathrm{d}t}\frac{1}{2}e^{2\left(\sigma-\mathrm{Re}_\beta^{-1}k_0^2\right)t} + \frac{1}{|\hat{\mathbf{v}}_0|^2}\frac{\mathrm{d}}{\mathrm{d}t}\frac{1}{2}\underbrace{|\hat{\mathbf{v}}_0|^2}_{=\text{ const.}}$$

$$= \sigma - \mathrm{Re}_\beta^{-1}k_0^2$$

$$= \sigma', \tag{3.64}$$

and the right-hand side as shown in equation (3.60) divided by $|\mathbf{v}|^2$. The full equation for the growth rate is

$$\frac{\beta}{4}\left[(1-\cos\theta)^2\sin\left[2\left(\Gamma_+ t+\Phi\right)\right] - (1+\cos\theta)^2\sin\left[2\left(\Gamma_- t+\Phi\right)\right] - 2(1-\cos^2\theta)\sin\left(2t\right)\right]$$

$$= \sigma' + \mathrm{Re}_\beta^{-1}k_0^2 \tag{3.65}$$

We follow the conclusion from Craik, 1989, Waleffe, 1990, and Kerswell, 2002 by finding the largest inviscid growth rate at either $\Gamma_+ = 0$ or $\Gamma_- = 0$ with $\Phi = \pm\pi/4$. An expression linking Ro_β and θ can be found by using Equation (3.62)

$$\Gamma = 2\left(1+\mathrm{Ro}_\beta^{-1}\right)\cos\theta = \pm 1,$$

$$\Rightarrow \cos\theta = \frac{1}{2\left(1+\mathrm{Ro}_\beta^{-1}\right)}. \tag{3.66}$$

This is already an interesting observation, since it highlights that $\cos\theta$ tends towards zero as Ro tends towards zero, meaning that the angle θ tends towards π and therefore closer to the plane perpendicular to the axis of rotation. Incidentally, this confirms the observation from Section 3.3.4.

Plugging the Relation (3.66) into Equation (3.65) yields

$$\sigma' = \frac{\beta}{16}\frac{\left(3+2\mathrm{Ro}_\beta^{-1}\right)^2}{\left(1+\mathrm{Ro}_\beta^{-1}\right)^2} - \mathrm{Re}_\beta^{-1}k_0^2. \tag{3.67}$$

The wave number k_0 has a lower bound because of the bounding box in the full flow simulation. Simply using a fixed $k_{0,\min}$ in Equation (3.67) results in a constant critical Reynolds number $\mathrm{Re} > {}^{(2k_{0,\min})^2}/\beta$ at small Ro. This is the result observed by the other authors mentioned above but not the one we observed in the full flow simulations. However, in Section 3.3.4 it is stated that the minimal wave number is limited by

$$k_{0,\min} = \frac{2\pi}{\cos\theta} = 4\pi\left(1+\mathrm{Ro}_\beta^{-1}\right), \tag{3.68}$$

where Equation (3.66) was used again.

Finally, we can calculate the marginal stability by setting $\sigma' = 0$ in Equation (3.67) and plugging in the minimum wave number from Equation (3.68)

$$\mathrm{Re}_\beta^{-1} 16\pi^2 \left(1 + \mathrm{Ro}_\beta^{-1}\right)^2 = \frac{\beta}{16} \frac{\left(3 + 2\mathrm{Ro}_\beta^{-1}\right)^2}{\left(1 + \mathrm{Ro}_\beta^{-1}\right)^2}$$

$$\Rightarrow \mathrm{Re}_\beta^{-1} = \frac{\beta}{256\pi^2} \frac{\left(3 + 2\mathrm{Ro}_\beta^{-1}\right)^2}{\left(1 + \mathrm{Ro}_\beta^{-1}\right)^4}$$

$$\Rightarrow \mathrm{Re}_\beta = \frac{256\pi^2}{\beta} \frac{\mathrm{Ro}_\beta^{-4} + 4\mathrm{Ro}_\beta^{-3} + 6\mathrm{Ro}_\beta^{-2} + 4\mathrm{Ro}_\beta^{-1} + 1}{4\mathrm{Ro}_\beta^{-2} + 12\mathrm{Ro}_\beta^{-1} + 9}$$

$$\Rightarrow \mathrm{Re}_\beta \underbrace{\approx}_{\mathrm{Ro}_\beta \to 0} \frac{64\pi^2}{\beta} \mathrm{Ro}_\beta^{-2}$$

$$\Rightarrow \mathrm{Re}_\beta \propto \mathrm{Ro}_\beta^{-2} \iff \mathrm{Re} \propto \mathrm{Ro}^{-2}. \tag{3.69}$$

Calculating the prefactor with the geometric factor from Equation (3.37) gives ≈ 200. This is the same order of magnitude as the one in Equation (3.59) but is off by a factor of two, which is no surprise since $\beta = 0.8$ is not small compared to one.

One more interesting observation can be made with this result. For small Ro, the wave number can be approximated with $k_0 \sim 4\pi\mathrm{Ro}_\beta^{-1}$. Checking the magnitude of the advection term with the base flow in Equation (3.25) yields $(\mathbf{U} \cdot \boldsymbol{\nabla}) \mathbf{u}' \sim |\mathbf{u}'|\mathrm{Ro}_\beta^{-1}$, which is comparable to the Coriolis force $2\mathrm{Ro}_\beta^{-1}\hat{y} \times \mathbf{u}'$. Additionally, the time derivative is also comparable to the Coriolis force. This means that the geostrophic limit breaks even for small Ro because this limit requires that the Coriolis force is only balanced by the pressure gradient and not the advection term. Therefore, the vortex can destabilize even for small Rossby numbers.

4 Is 2D compressible convection different

An interesting comparison is to run the same parameters as the 3D simulations from Tilgner, 2011 and find out how different the 2D approximation actually is. To this end, we remove the Coriolis term from the equations, change the aspect ratio to $L/d = 2$ with no-slip top and bottom surfaces, and periodic horizontal boundaries. The results of this work are given in the Tables 7.20 and 7.21. A compressed version of this chapter is published by Lüdemann and Tilgner 2023 (Manuscript submitted 22.03.2023 to Physical Review Fluids). This work will add additional simulations and some more comparisons. Tilgner, 2011 pointed out that both the Nusselt number as well as the Rayleigh number need to be calculated with the superadiabatic temperature gradient. Convection can only start if the prescribed temperature difference is larger than the adiabatic gradient, meaning $\Delta T_{\mathrm{ad}}/\Delta T < 1$ as describe in Section 2.2.2. Therefore, the Nusselt number

$$\mathrm{Nu}_* = \frac{\mathrm{Nu} - \Delta T_{\mathrm{ad}}/\Delta T}{1 - \Delta T_{\mathrm{ad}}/\Delta T} \tag{4.1}$$

is only reported as the superadiabatic Nusselt number. Similarly, the Rayleigh number is reported as

$$\begin{aligned}
\mathrm{Ra}_* &= \frac{gd^3\left(\Delta T - \Delta T_{\mathrm{ad}}\right)}{T_0 \kappa_0 \nu_0} \\
&= \mathrm{Ra}\left(1 - (\gamma - 1)\,{}^{d/H_0}\!T_0/\Delta T\right),
\end{aligned} \tag{4.2}$$

the superadiabatic Rayleigh number.

The results are split into two section. The first being about the scaling laws and relations that work similarly in 3D and 2D in Section 4.1. The second, Section 4.2, is about differences. All results presented here include dataset for the 3D simulations which is given by Prof. Dr. Andreas Tilgner in a private communication. The dataset with the 3D results from Tilgner, 2011 are shown with black symbols. They are used as a comparison. All 2D results generated in this work are shown as coloured symbols with a similar scheme as the one by Tilgner, 2011.

Blue symbols are $\Delta T_{\mathrm{ad}}/\Delta T = \frac{1}{15}$ with $\Delta T/T_0 = 0.1$ (plus), and $\Delta T/T_0 = 1.0$ (cross). Green

symbols are $\Delta T_{\mathrm{ad}}/\Delta T = \frac{2}{3}$ with $\Delta T/T_0 = 0.1$ (empty squares), $\Delta T/T_0 = 0.3$ (full squares), $\Delta T/T_0 = 1.0$ (empty upward triangles), $\Delta T/T_0 = 3.0$ (full upward triangles), $\Delta T/T_0 = 10.0$ (empty downward triangles), $\Delta T/T_0 = 30.0$ (full downward triangles), and $\Delta T/T_0 = 100.0$ (empty diamonds). Finally, the red symbols are $\Delta T_{\mathrm{ad}}/\Delta T = \frac{4}{5}$ with $\Delta T/T_0 = 0.1$ (empty circles), $\Delta T/T_0 = 1.0$ (full circles), and $\Delta T/T_0 = 10.0$ (left filled circles).

Some of the figures compare the 2D and 3D datasets directly and others show both datasets separately. It is possible that some points only show up in the separated figures since they do not occur in the original 3D dataset.

4.1 Similarities between 2D and 3D simulations
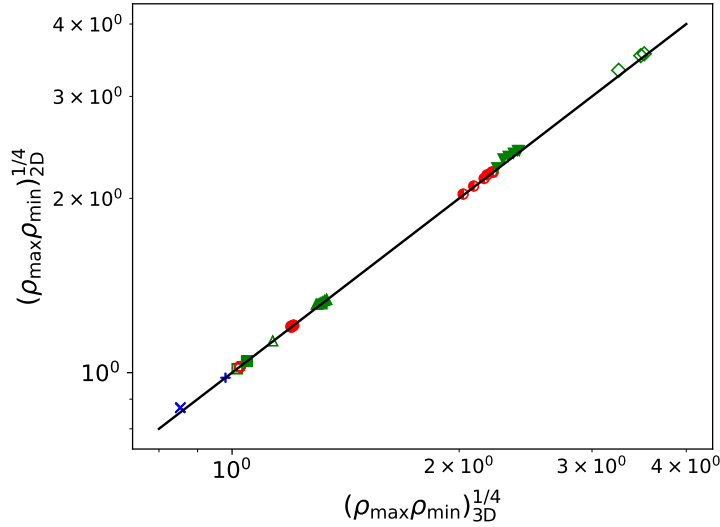
Figure 4.1: Shown is the characteristic density in comparison between the 3D (x-axis) and 2D (y-axis) simulations. The blue symbols are $\Delta T_{\mathrm{ad}}/\Delta T = \frac{1}{15}$ with $\Delta T/T_0 = 0.1$ (plus), and $\Delta T/T_0 = 1.0$ (cross). The green symbols are $\Delta T_{\mathrm{ad}}/\Delta T = \frac{2}{3}$ with $\Delta T/T_0 = 0.1$ (empty squares), $\Delta T/T_0 = 0.3$ (full squares), $\Delta T/T_0 = 1.0$ (empty upward triangles), $\Delta T/T_0 = 3.0$ (full upward triangles), $\Delta T/T_0 = 10.0$ (empty downward triangles), $\Delta T/T_0 = 30.0$ (full downward triangles), and $\Delta T/T_0 = 100.0$ (empty diamonds). The red symbols are $\Delta T_{\mathrm{ad}}/\Delta T = \frac{4}{5}$ with $\Delta T/T_0 = 0.1$ (empty circles), $\Delta T/T_0 = 1.0$ (full circles), and $\Delta T/T_0 = 10.0$ (left filled circles). The black line is the diagonal 3D = 2D.
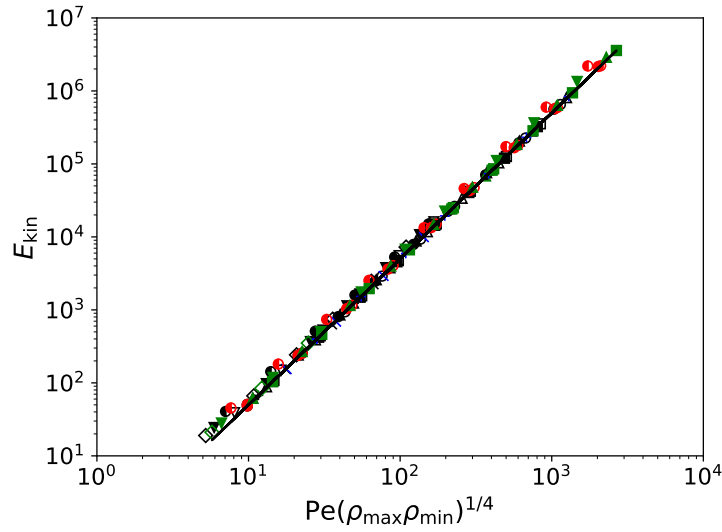
Figure 4.2: Shown is the kinetic energy density E_{kin} as a function of Péclet number Pe with the characteristic density $(\rho_{\text{max}}\rho_{\text{min}})^{1/4}$. The symbols and colours are the same as in Figure 4.1. The 3D dataset is shown with the same symbols but only in black. The drawn scaling law is the one obtained by Tilgner, 2011 with $E_{\text{kin}} = \frac{1}{2}\text{Pe}^2\sqrt{\rho_{\text{max}}\rho_{\text{min}}}$.

The article by Tilgner, 2011 identified a characteristic density

$$(\rho_{\text{max}}\rho_{\text{min}})^{1/4}\,,\tag{4.3}$$

which is used in scaling laws with the Péclet number, kinetic energy density, and the Rayleigh number. Therefore, this combination is checked against the newly generated 2D dataset. This comparison can be seen in Figure 4.1 with the x-axis representing the 3D dataset and the y-axis the 2D dataset, and the diagonal is marked with a black line. It is clear to see that this characteristic density is the same for both 2D and 3D simulations.

The first scaling law that uses the characteristic density, is the relation between the kinetic energy density E_{kin} and the Péclet number Pe. This is shown in Figure 4.2 where all data points, 3D as well as 2D, collapse onto the same scaling law, which is given by Tilgner, 2011 $E_{\text{kin}} = \frac{1}{2}\text{Pe}^2 (\rho_{\text{max}}\rho_{\text{min}})^{1/4}$. Again, both datasets agree very well, highlighting the comparability of the characteristic density.

Another scaling law agreeing between 3D and 2D simulations is the scaling law of the kinetic energy density and a free fall velocity calculated at one of the boundaries. This free fall velocity can be calculated locally at the boundary and the calculation given by
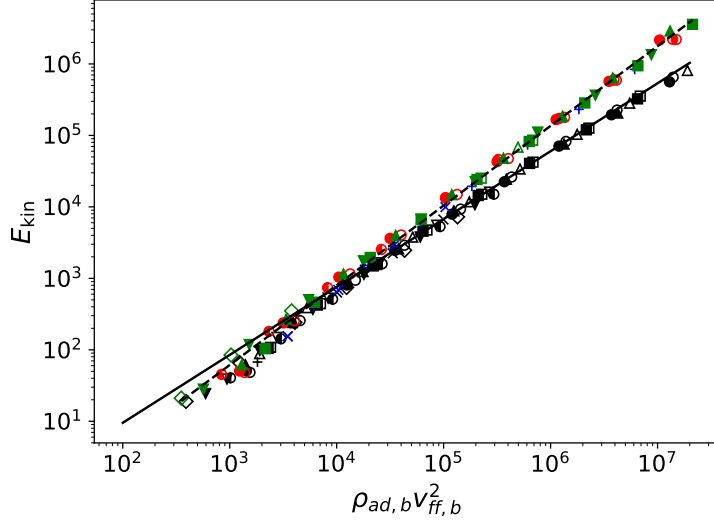
Figure 4.3: Shown is the kinetic energy density E_{kin} as a function of the adiabatic boundary density $\rho_{\text{ad},b}$ and the free fall velocity $v_{\text{ff},b}$ at the bottom boundary. The symbols are the same as in Figure 4.1 with black symbols representing the 3D dataset, the solid, black line is the scaling law obtained by Tilgner, 2011 $E_{\text{kin}} = 0.12 \left(\rho_{\text{ad,b}} v_{\text{ff},b}^2 \right)^{0.95}$, and the dashed, black line is the 2D scaling law $E_{\text{kin}} = 0.28 \left(\rho_{\text{ad,b}} v_{\text{ff},b}^2 \right)^{1.12}$.

Tilgner, 2011 is repeated here at the bottom boundary for completeness. An overbar denotes horizontal averages in the following calculations, for example, $\overline{\rho_b}$ is the horizontally averaged density at the bottom boundary. A dimensional temperature at the two boundaries can be calculated by assuming the adiabatic temperature gradient extends through the entire domain

$$T_{\text{ad},b} = T_m + \frac{1}{2} \Delta T_{\text{ad}} \qquad (4.4)$$

with $T_m = \left(\overline{\theta}_m + \frac{1}{2} \right) \Delta T + T_0$, where $\overline{\theta}_m$ is the horizontally averaged temperature fluctuation at the midplane in the simulation. This temperature can be used with the same assumption to calculate the density at the two boundaries

$$\rho_{\text{ad},b} = \overline{\rho}_m \left(\frac{T_{\text{ad},b}}{T_m} \right)^{1/(\gamma-1)}. \qquad (4.5)$$

Again, $\overline{\rho}_m$ is the horizontally averaged density at the midplane.

Similarly to before, the free fall velocity is calculated from the balance between the advection and the buoyancy term, which results in $|\rho (\mathbf{v} \cdot \boldsymbol{\nabla}) \mathbf{v}| \sim \Delta \rho g d \left(d/\kappa_0 \right)^2$, where $\Delta \rho = \rho_{\text{ad},b} - \overline{\rho}_b$ is the density difference of a fluid parcel to the adiabatic stratification.
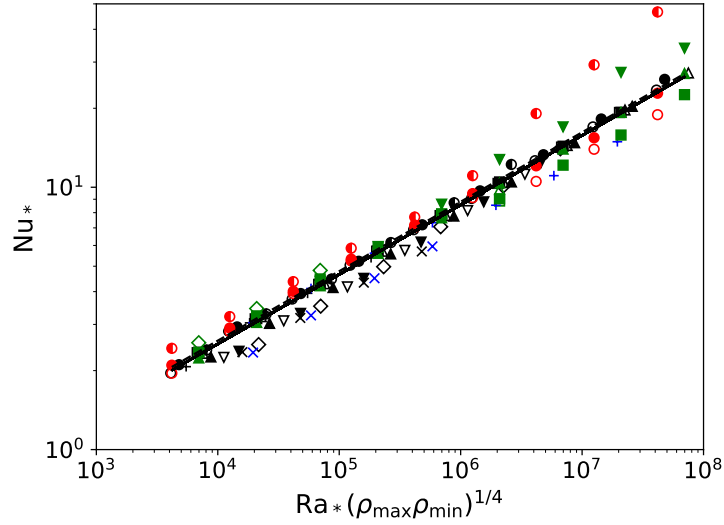
Figure 4.4: Shown is the superadiabatic Nusselt number Nu_* as a function of the supera-
diabatic Rayleigh number Ra_* and the characteristic density $(\rho_{max}\rho_{min})^{1/4}$.
The symbols are the same as in Figure 4.1 with black symbols representing
the 3D dataset, the solid line is the scaling law obtained by Tilgner, 2011
$Nu_{*,3D} = 0.22 \left[Ra_* (\rho_{max}\rho_{min})^{1/4} \right]^{0.265}$, and the dashed line is the 2D scaling
law $Nu_{*,2D} = 0.275 \left[Ra_* (\rho_{max}\rho_{min})^{1/4} \right]^{0.25}$.

This density difference $\Delta\rho$ can also be calculated at the top boundary and is responsible
for accelerating the parcel. It is assumed that the pressure variations acting on the fluid
parcel while traveling remain constant, meaning the $\Delta\rho/\rho$ remains constant, given that
the parcel does not exchange temperature with the environment. Therefore, it can be
calculated that the parcel traveling the distance d has a free fall velocity, expressed in
units κ_0/d, which can be written as

$$v_{\text{free fall},b} = v_{ff,b} = \left(\frac{\rho_{\text{ad},b} - \overline{\rho}_b}{\overline{\rho}_b} Pr Ra^{T_0}/\Delta T \right)^{1/2}. \tag{4.6}$$

The free fall velocity is called v_{ff} by Tilgner, 2011, which is adopted here for easy
comparability. A similar expression can be calculated for the top boundary.

This free fall velocity is used to compute a kinetic energy density and compared against
the kinetic energy density for the full simulation. The result is show in Figure 4.3 with
the 3D dataset shown with black symbols. The scaling law obtained by Tilgner, 2011
$E_{\text{kin}} = 0.12 \left(\rho_{\text{ad},b} v_{ff,b}^2 \right)^{0.95}$ is indicated with the solid line. A best fit scaling law for
the new 2D dataset is shown as a dashed line with $E_{\text{kin}} = 0.28 \left(\rho_{\text{ad},b} v_{ff,b}^2 \right)^{1.12}$. The
difference in the scaling laws highlighted in Figure 4.3 is interpreted as minimal since a

perfect scaling would be an exponent of 1 and the 3D dataset is slightly below and the 2D dataset slightly above this value. Choosing the top boundary for this comparison yields similar results.

The last comparison that is considered similar for the 3D as well as 2D simulations is the scaling of the superadiabatic Nusselt number Nu_* with the superadiabatic Rayleigh number Ra_* and the characteristic density $(\rho_{\max}\rho_{\min})^{1/4}$. This is shown in Figure 4.4. Again, the 3D dataset uses black symbols and the solid line is the scaling law obtained by Tilgner, 2011

$$\mathrm{Nu}_{*,\mathrm{3D}} = 0.22 \left[\mathrm{Ra}_* \left(\rho_{\max}\rho_{\min} \right)^{1/4} \right]^{0.265}. \tag{4.7}$$

The dashed line is the best fit to the new 2D dataset

$$\mathrm{Nu}_{*,\mathrm{2D}} = 0.275 \left[\mathrm{Ra}_* \left(\rho_{\max}\rho_{\min} \right)^{1/4} \right]^{0.25}. \tag{4.8}$$

These two scaling laws are very similar but some of the data points, especially the red left filled circles ($\Delta T_{\mathrm{ad}}/\Delta T = \frac{4}{5}$, $\Delta T/T_0 = 10.0$), scale differently for large Ra_*. This indicates that the agreement could be due to the still moderate Nusselt numbers which are always below $\mathrm{Nu} < 50$ and only span one decade. Simulations with larger Ra_* are needed to confirm that those simulations do indeed change their scaling.

4.2 Differences between 2D and 3D simulations

Considering that the two scaling laws for the superadiabatic Nusselt numbers Nu_* agree well, it is reasonable to directly compare these numbers for both datasets. This comparison is shown in Figure 4.5. The left filled, red circles reaching above the scaling law in Figure 4.4 are not included in Figure 4.5 because no 3D counter parts exist. It becomes clear that there is some seemingly systematical deviation, which was missed with the comparison of the scaling laws. The 2D Nusselt numbers become smaller than the 3D counter parts for $\mathrm{Nu} > 10$. This is interesting even though the deviations are small, because the comparison between 2D and 3D convection in the Boussinesq approximation highlighted in Section 3.1 shows the opposite behaviour. It is important to note that the Nusselt number compared here is smaller than $\mathrm{Nu} < 30$. Therefore, care has to be taken with drawing conclusions.

Seeing that the Nusselt number deviates slightly between 2D and 3D convection, suggests that the velocity dependent measures are similarly different. A comparison of the Péclet
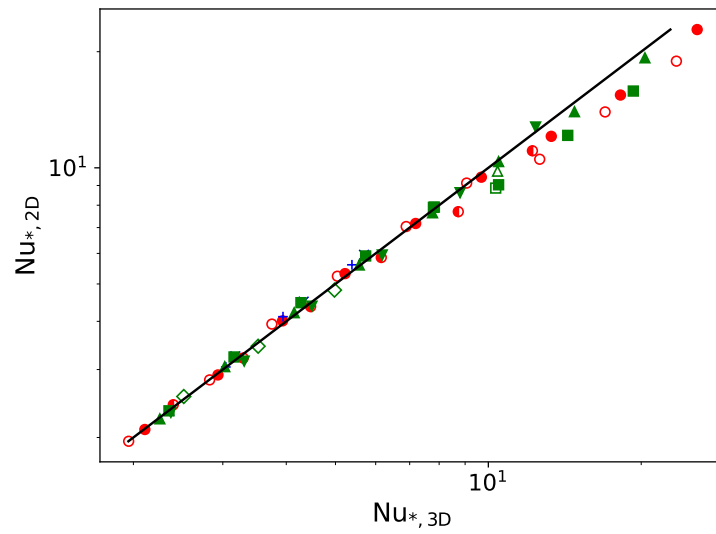
Figure 4.5: Shown is a comparison between the superadiabatic Nusselt number Nu_* for the 3D dataset on the x-axis and the 2D dataset on the y-axis. The symbols are the same as in Figure 4.1 and the line is the diagonal 3D = 2D. The left filled, red circles reaching above the scaling in Figure 4.4 are not included here, since no counterparts exist in the 3D dataset.
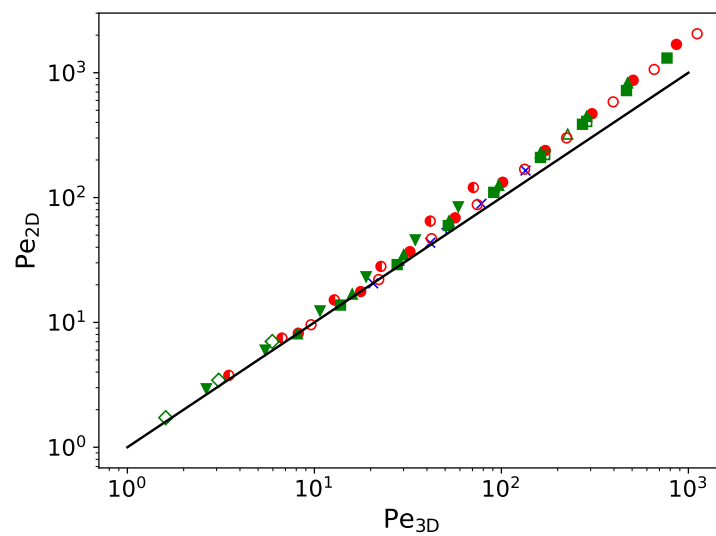
Figure 4.6: Shown is a comparison between the Péclet number Pe for the 3D dataset on the x-axis and the 2D dataset on the y-axis. The symbols are the same as in Figure 4.1 and the line is the diagonal 3D = 2D.
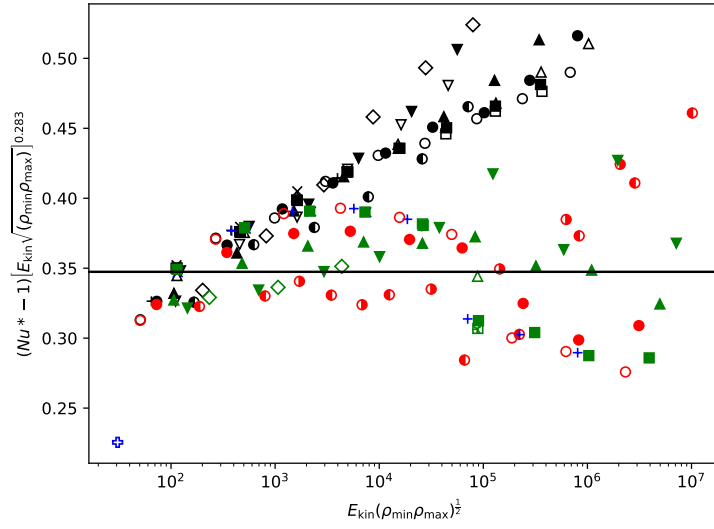
Figure 4.7: Shown is the superadiabatic Nusselt number Nu_* compensated with the best fit scaling law for the kinetic energy density E_{kin} and the characteristic density $(\rho_{max}\rho_{min})^{1/4}$, which is $Nu_{*,2D} - 1 = 0.355 \left(E_{kin} \sqrt{\rho_{max}\rho_{min}} \right)^{0.283}$. The symbols are the same as in Figure 4.1 and the 3D dataset is shown with black symbols. The solid line shows the pre factor 0.355 of the best fit result.
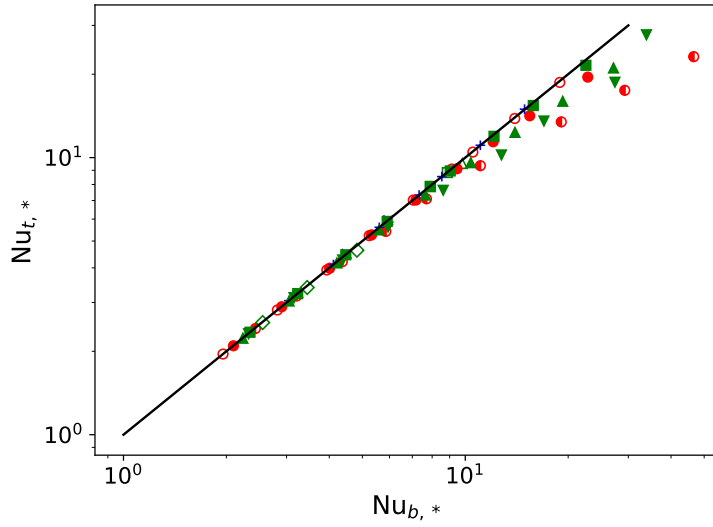
Figure 4.8: Shown is a comparison between the superadiabatic Nusselt number Nu_* from the 2D dataset calculated at the top (y-axis) and bottom (x-axis) boundary. The symbols are the same as in Figure 4.1 and the line is the diagonal $Nu_{t,*} = Nu_{b,*}$.

numbers Pe is shown in Figure 4.6 with the 3D Péclet number on the x-axis and the 2D Péclet number on the y-axis. Here, we observe that the 2D Péclet number systematically exceeds the 3D one once $\text{Pe} > 100$. In this case, the difference reaches about a factor of two for $\text{Pe} \approx 10^3$. This increased Péclet number in combination with the lower Nusselt number is an, as of now, unknown behaviour and indicates that the flow structures are very different. Additionally, the investigation of the 2D and 3D Boussinesq convection in Section 3.1 suggests that an increase of the Nusselt number also includes an increase in the Péclet number. Further investigations are needed to draw conclusions about the flow and boundary layer structure, as well the behaviour once a turbulent regime is reached. Continuing with the comparison, one last interesting scaling law highlighted by Tilgner, 2011 is the dependence between the superadiabatic Nusselt number and the kinetic energy density. Using the characteristic density, a scaling law of

$$\text{Nu}_{*,\text{3D}} - 1 = \frac{2}{7} \left(E_{\text{kin}} \sqrt{\rho_{\max} \rho_{\min}} \right)^{1/3} \tag{4.9}$$

is reported by Tilgner, 2011 for the 3D dataset. A similar best fit for the 2D dataset can be found in the compensated plot of Figure 4.7. Here, the 3D dataset is again shown with black symbols and a horizontal line is drawn to indicate the pre factor of the best fit scaling law

$$\text{Nu}_{*,\text{3D}} - 1 = 0.355 \left(E_{\text{kin}} \sqrt{\rho_{\max} \rho_{\min}} \right)^{0.283} . \tag{4.10}$$

These two scaling laws are very different and a closer look at Figure 4.7 shows that the 3D dataset has a much narrower grouping compared to the 2D scaling law even though it is compensated with the 2D scaling law instead of the 3D one. This further adds to the suggestion that the flow structures are different and more investigations are needed to fully grasp the differences, especially since no direct comparison of the time dependent flow structure with this 3D dataset is possible.

Seeing that the two datasets are very different in the end, it is beneficial to evaluate the differences in the 2D Nusselt numbers computed at the top and bottom boundary. Such a comparison is shown in Figure 4.8 with the bottom boundary Nusselt number (the default for all other plots) on the x-axis and the Nusselt number calculated at the top boundary on the y-axis. The line indicates the diagonal $\text{Nu}_{t,*} = \text{Nu}_{b,*}$. Again, it is visible that these two Nusselt numbers computed from the same simulations differ for the largest Nusselt numbers calculated. This further highlights the differences in the boundary layers near the top and bottom boundaries. No 3D data was available to compare the Nusselt number at the top boundary, which is required to further investigate

the differences between 2D and 3D compressible convection.

Finally, one more information can be gained with Figure 4.8. It can be observed that the Nusselt number of the top boundary is always larger than the one at the bottom boundary, indicating that the top boundary layer is smaller. In order to properly resolve both boundary layers numerically, it is required to have at least a few points in the boundary layer as indicated by Shishkina et al., 2010 for the Boussinesq approximation. Therefore, the top boundary layer is the one constraining the resolution, not the bottom one. Alternatively, an unstructured grid with higher resolution close to the top boundary could be used.

5 What happens if we add the Coriolis force

Now, we reintroduce the Coriolis force but keep the aspect ratio of $L/d = 2$ with the no-slip top and bottom boundaries. This way, we can build on the results of last section and check what effects the Coriolis force has on, for example, the thermal transport. The results of this parameter study can be found in Tables 7.22 until 7.51. Three different compressibilities are investigated with $\Delta T/T_0 = d/H_0 = 1$, $\Delta T/T_0 = d/H_0 = 0.1$, and $\Delta T/T_0 = d/H_0 = 0.01$. These correspond to a single value for $\Delta T_{\mathrm{ad}}/\Delta T = \frac{2}{3}$ which are the green symbols in Section 4. Only a single value is chosen here because the distinction between different values can be ignored if the superadiabatic variables and measures, Ra_* and Nu_*, are used.

Horizontal free-slip boundaries are investigated as well as the horizontally periodic ones from the last section. Both, top and bottom bounding surfaces remain no-slip, since these correspond to the experimentally achievable ones. The results of the parameter study can be seen in Figure 5.1 for the superadiabatic Nusselt number Nu_* as a function of the superadiabatic Rayleigh number Ra_*. Symbols filled in the top half correspond to $\Delta T/T_0 = d/H_0 = 1.0$, fully filled symbols to $\Delta T/T_0 = d/H_0 = 0.1$, and bottom half filled symbols correspond to $\Delta T/T_0 = d/H_0 = 0.01$. As stated in Section 2.2.2, the combination $\Delta T/T_0 = d/H_0 = 0.1$ is experimentally achievable, therefore it gets the most attention. The symbols and colours correspond to different Ekman numbers with black circles for $\mathrm{Ek} = \infty$, red squares for $\mathrm{Ek} = 10^{-3}$, blue diamonds for $\mathrm{Ek} = 10^{-4}$, green hexagons for $\mathrm{Ek} = 10^{-5}$, and cyan pluses for $\mathrm{Ek} = 10^{-6}$. The horizontal free-slip boundaries are shown in the top graph and the horizontally periodic ones are shown in the bottom graph. Only parameters above the onset with $\mathrm{Nu} > 1.01$ are included in this dataset.

Both different types of horizontal boundary conditions show a change in the critical Rayleigh number with a change in the Ekman number. Both also show that the data points for different Ek approach the values of the non rotating case $\mathrm{Ek} = \infty$ once the Rayleigh number is large enough. The scaling law for both sets of non rotating
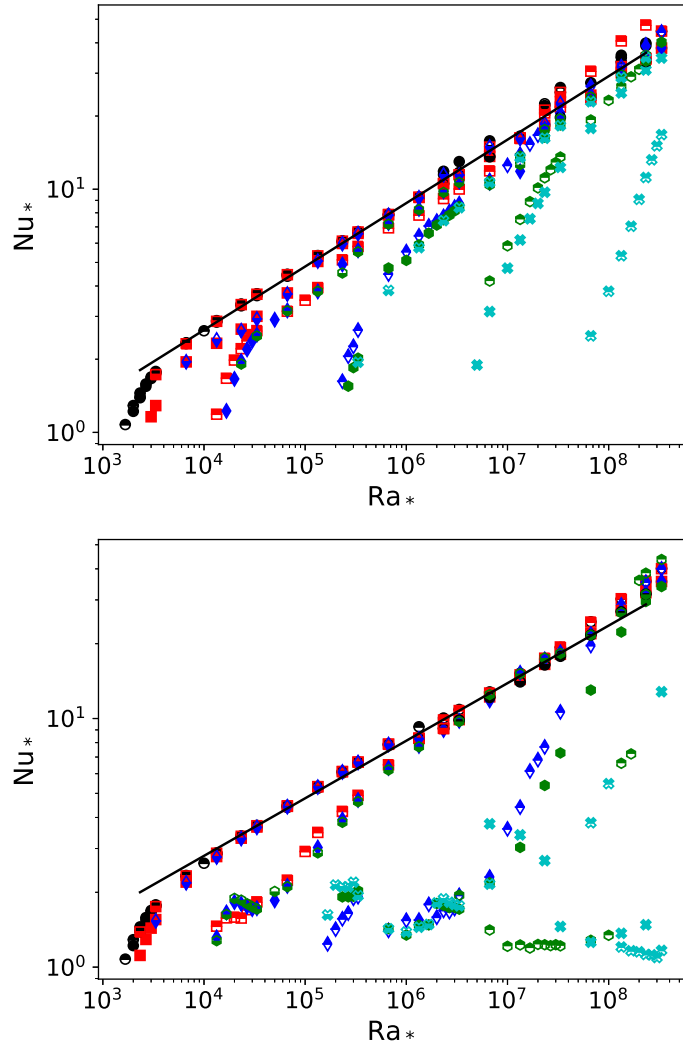
Figure 5.1: Shown is the superadiabatic Nusselt number Nu_* as a function of the supera-
diabatic Rayleigh number Ra_*. Both graphs have no-slip top and bottom
boundaries but the horizontal boundaries are free slip in the top and peri-
odic in the bottom graph. The fill style represents different compressibility's
with $\Delta T/T_0 = d/H_0 = 1.0$ (top filled), $\Delta T/T_0 = d/H_0 = 0.1$ (fully filled), and
$\Delta T/T_0 = d/H_0 = 0.01$ (bottom filled). The symbols and colours differentiate
the Ekman numbers with $Ek = \infty$ (black circles), $Ek = 10^{-3}$ (red squares),
$Ek = 10^{-4}$ (blue diamonds), $Ek = 10^{-5}$ (green hexagons), and $Ek = 10^{-6}$
(cyan pluses). The black line is a best fit scaling for the non rotating simu-
lations with $Nu_* = 0.24Ra_*^{0.26}$ in the top graph and $Nu_* = 0.33Ra_*^{0.23}$ in the
top graph.
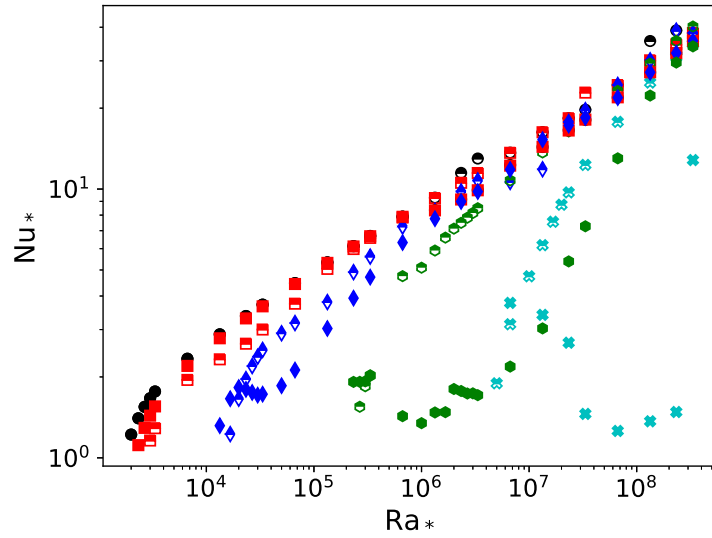
Figure 5.2: Shown is the superadiabatic Nusselt number Nu_* as function of the superadiabatic Rayleigh number Ra_* for $\Delta T/T_0 = d/H_0 = 0.1$. The symbols and colours are the same as in Figure 5.1. Both types of horizontal walls are shown with the free-slip boundaries as top filled, and the periodic boundaries with fully filled symbols.

simulations is indicated by a black line with

$$Nu_{*,\text{free-slip}} = 0.24 Ra_*^{0.26}, \tag{5.1}$$

for the case bound by horizontal, free-slip walls and

$$Nu_{*,\text{periodic}} = 0.33 Ra_*^{0.23}, \tag{5.2}$$

for the horizontally periodic case. These scaling laws are close enough to assume that this scaling law is independent of the boundary conditions.

This is where the similarities end. The horizontally periodic simulations (bottom in Figure 5.1) start with a steep rise in Nu_* but than reach a plateau or even drop back down to $Nu_* \approx 1$. The reason for this difference is the onset of zonal flow, meaning a large horizontal wind component. The horizontal velocity component u_x becomes large compared to the vertical speed u_z, which suppresses fluid parcels from reaching the other boundaries. The thermal energy is instead transported diffusively and the thermal gradient becomes linear in the entire simulation domain.

Furthermore, the parameters experiencing this wind span a larger range in Ra_* if Ek gets smaller. Also, once the wind looses its influence on the thermal convection, the
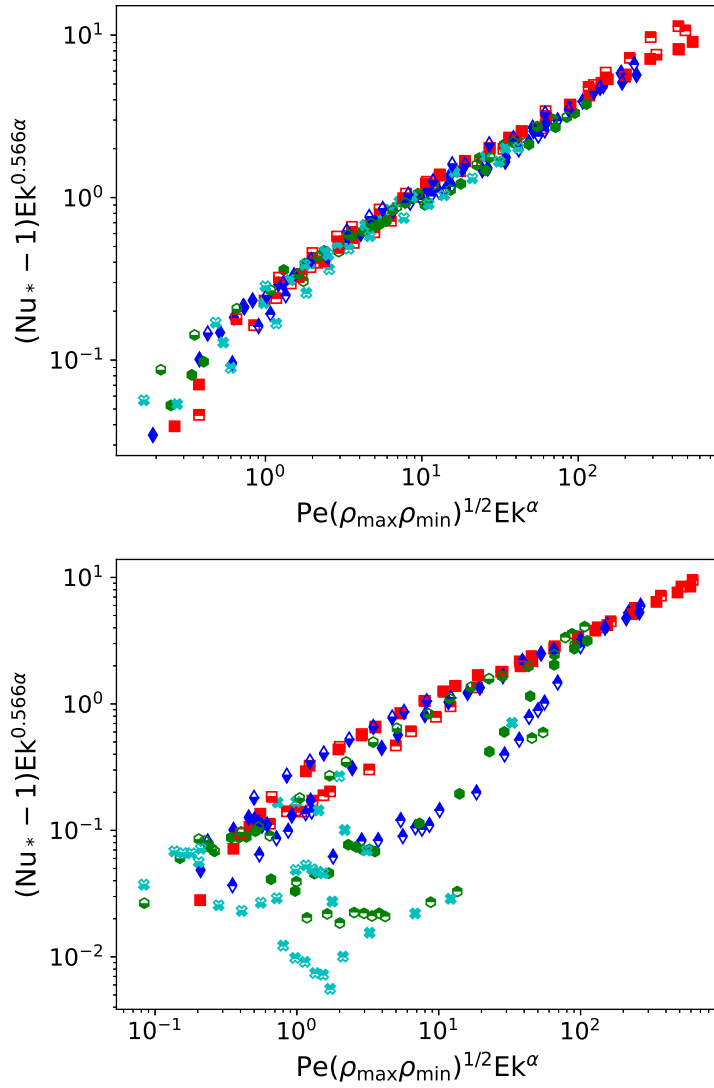
Figure 5.3: Shown is a compensated version of the results from Figure 5.1. The symbols and orientation is also the same as in Figure 5.1. The superadiabatic Nusselt number is shown as a function of the Péclet number Pe and the characteristic density squared. The different rates of rotation are compensated with the Ekman number Ek and the exponent is a best fit result for the horizontal free slip boundaries (top graph) with $\alpha = 0.36$.

transition to the non rotating case becomes steeper. This strongly suggest that even though the increasing Rayleigh number drives the thermal convection more strongly, more energy is transferred into the horizontal motion. Therefore, a process of transporting energy from many vertical modes into the zero mode (constant movement) of the

horizontal velocity has to be present. The Coriolis force is responsible for the transfer of energy from vertical to horizontal, but another process has to be at play to transfer energy from larger wave numbers into the wave number zero mode.

A direct comparison between the two boundary conditions for a single value of $\Delta T/T_0 = d/H_0 = 0.1$, the experimental parameter, can be see in Figure 5.2. The symbols filled in the top half are for the horizontal free-slip boundaries and the fully filled symbols are for the horizontally periodic simulations. Here, it becomes evident that both types of boundary conditions have a different critical Rayleigh number. This is especially obvious for the blue diamonds representing $Ek = 10^{-4}$.

One more information can be gained from the reduced complexity. Following the fully filled, green hexagons for $Ek = 10^{-5}$, the horizontally periodic simulations, reveals multiple, abrupt changes in the Nusselt number. These changes in the thermal transport highlight that the flow undergoes many state changes in the regime where the zonal wind is strongest. Around $Ra_* \approx 10^6$ the thermal transport reaches a minimum. This indicates that the zonal wind is strongest here. Afterwards, at $Ra_* \approx 2 \times 10^6$, an abrupt change in the Nusselt number is visible followed by a slight decrease, which is again followed by the steep increase until the non rotating Nusselt numbers are reached. This abrupt change shows that thermal convection breaks through the wind and increases the thermal transport for this region in Ra_*. A similar behaviour can be observed for $Ek = 10^{-6}$, the cyan pluses.

Ultimately, these changes in the Nusselt number should become more subtle once a regime of multiple direction changes is observed in the horizontal velocity component. These exist in regions of smaller Ekman number as observed by Verhoeven and Stellmach, 2014. None of the simulations investigated here have shown more than one major wind direction. This is partly due to the no-slip, vertical boundaries compared to the free-slip ones from Verhoeven and Stellmach, 2014, as well as the larger aspect ratio of $L/d = 2$ compared to their ratio of $L/d = 1$. Especially, the free-slip boundary conditions are known to generate a strong shear flow since the velocities are allowed to be largest at the top and bottom boundary. The aspect ratio is also an important factor because small aspect ratios with horizontally periodic boundaries are know to generate strong shear flow even in the Boussinesq approximation as shown by Poel et al., 2014 and later by Wang et al., 2020 with a larger range of aspect ratios.

Going back to the delayed onset, one is tempted to apply a compensation to the data sets from Figure 5.1, especially since the behaviour is similar to the one observed for rotating Rayleigh-Bénard convection, where the axis of gravity and rotation are in parallel. Such a

compensation is done by Schmitz and Tilgner, 2009. It cannot be assumed that the same compensation can be applied here since the original work was done under the Boussinesq approximation and with a different geometry. Following a similar argument as Schmitz and Tilgner, 2009 used, a scaling of $(\mathrm{Nu}_* - 1)\mathrm{Ek}^{0.566\alpha}$ with $\mathrm{Pe}\,(\rho_{\max}\rho_{\min})^{1/2}\,\mathrm{Ek}^\alpha$ can be obtained by using Relation (4.10). The kinetic energy is translated to the Péclet number by using the relation shown in Figure 4.2. The exponent α is used as a best fit parameter and it is found that $\alpha = 0.36$ is optimal. A compensated version of Figure 5.1 can be found in Figure 5.3 with the same symbols and again with horizontal free-slip boundaries in the top and horizontal periodic simulations in the bottom graph.

As expected, a reasonable agreement with the scaling law can be observed for the horizontal, free-slip boundaries. This is expected because the compensation aligns all simulations which are reaching the non rotating scaling for large values of Nu_*. The small values of Nu_* have a similar scaling in Figure 5.1, indicating that an optimal compensation can be found.

This is not true for the horizontally periodic simulations. Here, as explained above, the behaviour before increasing towards the non rotating case is very different for different Ekman numbers. Therefore, only the simulations actually reaching towards the non rotating scaling align in this compensation.

The next Section will take a deeper look into the delayed onset and investigate the similarity in the behaviour compared to the different geometry with the Boussinesq approximation. This is especially important since the investigation in Chapter 3 does not show this delayed onset for the Boussinesq simulations in the same geometry.

5.1 Delayed onset of convection

Calculating the linear equations starts with the equations of motion (2.22), (2.23), and (2.24) which are repeated here for the sake of the argument

$$\partial_t \rho + \boldsymbol{\nabla} \cdot (\rho \mathbf{v}) = 0, \tag{5.3}$$

$$\partial_t \mathbf{v} + (\mathbf{v} \cdot \boldsymbol{\nabla})\,\mathbf{v} + 2\frac{\mathrm{Pr}}{\mathrm{Ek}}\hat{y} \times \mathbf{v} = -\frac{1}{\rho}\boldsymbol{\nabla}\left[(T + {}^{T_0}\!/\!{}_{\Delta T})\,\rho\right]\frac{1}{\gamma}{}^{H_0}\!/\!{}_d\mathrm{PrRa}$$
$$- \hat{z}\mathrm{PrRa}{}^{T_0}\!/\!{}_{\Delta T} + \frac{\mathrm{Pr}}{\rho}\left[\boldsymbol{\nabla}^2\mathbf{v} + \frac{1}{3}\boldsymbol{\nabla}\left(\boldsymbol{\nabla}\cdot\mathbf{v}\right)\right], \tag{5.4}$$

$$\partial_t T + (\mathbf{v} \cdot \boldsymbol{\nabla})\,T = \frac{\gamma}{\rho}\boldsymbol{\nabla}^2 T - (\gamma - 1)\,(T + {}^{T_0}\!/\!{}_{\Delta T})\,\boldsymbol{\nabla}\cdot\mathbf{v}$$
$$\left[e_{ij} - \frac{1}{3}\left(\boldsymbol{\nabla}\cdot\mathbf{v}\right)\delta_{ij}\right]^2 \frac{2\gamma\,(\gamma - 1)}{\rho}{}^d\!/\!{}_{H_0}\frac{1}{\mathrm{Ra}}. \tag{5.5}$$

72
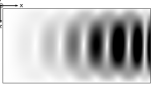
These equations are linearised about background states with $\mathbf{v} = 0$, T_s, and ρ_s, which are calculated in Section 2.2.3. The temperature background field T_s is defined by diffusive heat transport as shown in Equation (2.34) and repeated here

$$T_s = 1 - z. \tag{5.6}$$

The density background field ρ_s can be calculated with the help of the Navier-Stokes equation (2.23), which is shown in equation (2.37) and repeated here

$$\rho_s = \rho_0 \left(\frac{1}{1 + \Delta T/T_0(1 - z)} \right)^{1 - \gamma\, d/H_0 T_0/\Delta T}. \tag{5.7}$$

Furthermore, the equation of state holds for the background fields, meaning

$$P_s = (\gamma - 1)\, \rho_s \left(T_s + T_0/\Delta T \right) \tag{5.8}$$

with the hydrostatic pressure P_s. The gradient of the hydrostatic pressure can also be calculated in the dimensionless variables

$$\boldsymbol{\nabla} P_s = -\hat{z}\rho_s\gamma\,(\gamma - 1)\, d/H_0 T_0/\Delta T. \tag{5.9}$$

We will modify the Navier-Stokes equation for later convenience. To this end, we reintroduce the pressure as a full variable and multiply with the density

$$\rho \left(\partial_t\mathbf{v} + (\mathbf{v} \cdot \boldsymbol{\nabla})\,\mathbf{v} + 2\frac{\mathrm{Pr}}{\mathrm{Ek}}\hat{y} \times \mathbf{v} \right) = -\,\boldsymbol{\nabla} P\frac{1}{(\gamma - 1)\gamma}\,H_0/d\mathrm{PrRa}$$
$$-\,\rho\hat{z}\mathrm{PrRa}\,T_0/\Delta T + \mathrm{Pr}\left[\boldsymbol{\nabla}^2\mathbf{v} + \frac{1}{3}\boldsymbol{\nabla}\left(\boldsymbol{\nabla} \cdot \mathbf{v} \right) \right]. \tag{5.10}$$

These basic equations are used to calculate the standard form of the linearised equation. We continue by linearising the equations of motion around the background fields with the velocity perturbations $\mathbf{u}$, the temperature $T = T_s + \theta$, which is conveniently split in the same manner as described in Section 2.2, the density $\rho = \rho_s + \rho_1$, and the pressure $P = P_s + P_1$. Starting with the continuity equation (2.22)

$$\partial_t\rho_1 + \boldsymbol{\nabla} \cdot \left(\rho_s\mathbf{u} \right), \tag{5.11}$$

we will be ignoring terms containing more than one perturbation variable. Next, we are linearising the temperature equation (2.24)

$$\partial_t\theta - u_z = \frac{\gamma}{\rho_s}\boldsymbol{\nabla}^2\theta - (\gamma - 1)\left(T_s + T_0/\Delta T \right) \boldsymbol{\nabla} \cdot \mathbf{u}, \tag{5.12}$$

where the factor in front of the Laplace only retains the density background field.

Lastly, we turn our sights on the Navier-Stokes equations (5.10), which requires a bit

of work. We start by linearising the velocity, splitting all other terms manually, and dividing by ρ_s

$$\frac{\rho_s + \rho_1}{\rho_s}\left[\partial_t \mathbf{u} + 2\frac{\text{Pr}}{\text{Ek}}\hat{y}\times\mathbf{u}\right] = -\frac{1}{\rho_s}\frac{1}{(\gamma-1)\gamma}{}^{H_0/d}\text{PrRa}\boldsymbol{\nabla}\left(P_s + P_1\right)$$
$$-\frac{\rho_s+\rho_1}{\rho_s}\hat{z}\text{PrRa}^{T_0/\Delta T} + \frac{\text{Pr}}{\rho_s}\left[\boldsymbol{\nabla}^2\mathbf{u} + \frac{1}{3}\boldsymbol{\nabla}\left(\boldsymbol{\nabla}\cdot\mathbf{u}\right)\right].\quad(5.13)$$

We can identify the hydrostatic gradient and simplify this equation further

$$\frac{\rho_s + \rho_1}{\rho_s}\left[\partial_t \mathbf{u} + 2\frac{\text{Pr}}{\text{Ek}}\hat{y}\times\mathbf{u}\right] = -\frac{1}{\rho_s}\frac{1}{(\gamma-1)\gamma}{}^{H_0/d}\text{PrRa}\boldsymbol{\nabla}P_1$$
$$-\frac{\rho_1}{\rho_s}\hat{z}\text{PrRa}^{T_0/\Delta T} + \frac{\text{Pr}}{\rho_s}\left[\boldsymbol{\nabla}^2\mathbf{u} + \frac{1}{3}\boldsymbol{\nabla}\left(\boldsymbol{\nabla}\cdot\mathbf{u}\right)\right].\quad(5.14)$$

The term $\frac{1}{\rho_s}\boldsymbol{\nabla}P_1$ can also be expressed differently, because

$$\boldsymbol{\nabla}\left(\frac{P_1}{\rho_s}\right) = \frac{1}{\rho_s}\boldsymbol{\nabla}P_1 + P_1\boldsymbol{\nabla}\frac{1}{\rho_s}$$
$$= \frac{1}{\rho_s}\boldsymbol{\nabla}P_1 - \frac{P_1}{\rho_s}\boldsymbol{\nabla}\ln\left(\rho_s\right).\quad(5.15)$$

Introducing Expression (5.15) into the linear Navier-Stokes equation (5.14) and setting the term $\frac{\rho_s+\rho_1}{\rho_s} = 1$, transforms it into the standard form

$$\partial_t\mathbf{u} + 2\frac{\text{Pr}}{\text{Ek}}\hat{y}\times\mathbf{u} = \frac{1}{(\gamma-1)\gamma}{}^{H_0/d}\text{PrRa}\left[-\boldsymbol{\nabla}\left(\frac{P_1}{\rho_s}\right) - \frac{P_1}{\rho_s}\boldsymbol{\nabla}\ln\left(\rho_s\right)\right]$$
$$-\frac{\rho_1}{\rho_s}\hat{z}\text{PrRa}^{T_0/\Delta T} + \frac{\text{Pr}}{\rho_s}\left[\boldsymbol{\nabla}^2\mathbf{u} + \frac{1}{3}\boldsymbol{\nabla}\left(\boldsymbol{\nabla}\cdot\mathbf{u}\right)\right].\quad(5.16)$$

The reason for this game of pressures[1] is that we can calculate the pressure P_1 and interchange the density variation in the buoyancy term with temperature variations. A comprehensive overview of this standard form can be found in the article by Brown, Vasil, and Zweibel, 2012. They compute an energy equation using the entropy and continue to interchange the background gradient with either entropy, temperature, or density similarly to this calculation. This set of equations is also similar to the one obtained by Wood and Bushby, 2016. They calculated their equations using conservation of energy in a much stricter manner than in the original work by Ogura and Phillips, 1961. It is possible to transform the equations from Wood and Bushby, 2016 into the ones used here, which is left to the reader as an exercise[2]. This makes these equations appear

---

[1]A rather bad Game of Thrones reference

[2]Just kidding. Calculated the factors they use, compare them to the non dimensional ones here, and substitute one of their gradients to get the pressure p_1 back into the equations.

similar to the Boussinesq equations and aids the interpretation.

In order to perform this exchange, it is required to linearise the equation of state (2.25)

$$P_s + P_1 = (\gamma - 1)(\rho_1 + \rho_s)(\theta + T_s + {}^{T_0}/\Delta T)$$

$$= (\gamma - 1)(\rho_1 \theta + \rho_1(T_s + {}^{T_0}/\Delta T) + \rho_s \theta + \rho_s(T_s + {}^{T_0}/\Delta T))$$

$$\Rightarrow P_1 = (\gamma - 1)(\rho_1 \theta + \rho_1(T_s + {}^{T_0}/\Delta T) + \rho_s \theta), \tag{5.17}$$

where the equation of state for the background fields (5.8) is used. The term $\rho_1 \theta$ will be dropped for the linearisation. Furthermore, we take the logarithm of the equation of state for the background fields

$$\ln\left(\frac{P_s}{\gamma - 1}\right) = \ln \rho_s + \ln(T_s + {}^{T_0}/\Delta T) \tag{5.18}$$

in order to exchange the gradient of the logarithm in Equation (5.16).

This exchange results in the following calculations

$$\frac{P_1}{\rho_s}\boldsymbol{\nabla}\ln(\rho_s) = \frac{P_1}{\rho_s}\left(\boldsymbol{\nabla}\ln\left(\frac{P_s}{\gamma-1}\right) - \boldsymbol{\nabla}\ln(T_s + {}^{T_0}/\Delta T)\right)$$

$$= \frac{P_1}{\rho_s}\left(\frac{1}{\rho_s(T_s + {}^{T_0}/\Delta T)}\boldsymbol{\nabla}P_s - \boldsymbol{\nabla}\ln(T_s + {}^{T_0}/\Delta T)\right)$$

$$= -\frac{P_1}{\rho_s}\boldsymbol{\nabla}\ln(T_s + {}^{T_0}/\Delta T) - \frac{P_1}{\rho_s}\frac{1}{(T_s + {}^{T_0}/\Delta T)}\hat{z}\gamma(\gamma-1){}^{d}/H_0{}^{T_0}/\Delta T$$

$$= -\frac{P_1}{\rho_s}\boldsymbol{\nabla}\ln(T_s + {}^{T_0}/\Delta T) - \left(\frac{\rho_1}{\rho_s} + \frac{\theta}{(T_s + {}^{T_0}/\Delta T)}\right)\hat{z}\gamma(\gamma-1){}^{d}/H_0{}^{T_0}/\Delta T.$$

$$\tag{5.19}$$

Introducing Equation (5.19) into the standard form of the linear Navier-Stokes equation (5.16) yields

$$\partial_t \mathbf{u} + 2\frac{\mathrm{Pr}}{\mathrm{Ek}}\hat{y} \times \mathbf{u} = \frac{1}{(\gamma-1)\gamma}{}^{H_0}/d\mathrm{PrRa}\left[-\boldsymbol{\nabla}\left(\frac{P_1}{\rho_s}\right) + \frac{P_1}{\rho_s}\boldsymbol{\nabla}\ln(T_s + {}^{T_0}/\Delta T)\right]$$

$$+ \frac{\theta}{T_s + {}^{T_0}/\Delta T}\hat{z}\mathrm{PrRa}{}^{T_0}/\Delta T + \frac{\mathrm{Pr}}{\rho_s}\left[\boldsymbol{\nabla}^2\mathbf{u} + \frac{1}{3}\boldsymbol{\nabla}(\boldsymbol{\nabla}\cdot\mathbf{u})\right]. \tag{5.20}$$

Ultimately, the pressure P_1 can be substituted using the linear equation of state (5.17)

$$\partial_t \mathbf{u} + 2\frac{\mathrm{Pr}}{\mathrm{Ek}}\hat{y} \times \mathbf{u} = \frac{\theta}{T_s + {}^{T_0}/\Delta T}\hat{z}\mathrm{PrRa}{}^{T_0}/\Delta T + \frac{\mathrm{Pr}}{\rho_s}\left[\boldsymbol{\nabla}^2\mathbf{u} + \frac{1}{3}\boldsymbol{\nabla}(\boldsymbol{\nabla}\cdot\mathbf{u})\right]$$

$$+ \frac{1}{\gamma}{}^{H_0}/d\mathrm{PrRa}\left[-\boldsymbol{\nabla}\left(\frac{\rho_1}{\rho_s}(T_s + {}^{T_0}/\Delta T) + \theta\right) - \left(\frac{\rho_1}{\rho_s} + \frac{\theta}{T_s + {}^{T_0}/\Delta T}\right)\boldsymbol{\nabla}(T_s + {}^{T_0}/\Delta T)\right]. \tag{5.21}$$

Further investigations require the linear Equations (5.11), (5.12), and (5.21) to have constant coefficients, which can be achieved by assuming that $\rho_1 \ll \rho_s$ and $\theta \ll T_s + {}^{T_0}/\Delta T$.

Furthermore, it can be assumed that the temperature offset dominates the temperature profile since $|T_s| \leq 1$ and $T_0/\Delta T \gg 1$. Also, the approximation $d/H_0 \ll 1$ is required to substitute $\rho_s = \rho_0$.

The linear continuity equation (5.11) changes to

$$
\begin{aligned}
\partial_t \frac{\rho_1}{\rho_0} &= -v_z \boldsymbol{\nabla} \rho_s - \boldsymbol{\nabla} \cdot \mathbf{v} \\
&= -\left(\Delta T/T_0 - \gamma d/H_0\right) v_z - \boldsymbol{\nabla} \cdot \mathbf{v},
\end{aligned}
\tag{5.22}
$$

where the density background from Equation (2.37) was Taylor expanded to first order. The linear temperature equation with constant coefficients is

$$
\partial_t \theta = u_z + \frac{\gamma}{\rho_0} \boldsymbol{\nabla}^2 \theta - (\gamma - 1) \, T_0/\Delta T \boldsymbol{\nabla} \cdot \mathbf{u}.
\tag{5.23}
$$

Finally, the linear Navier-Stokes equation with constant coefficients is

$$
\begin{aligned}
\partial_t \mathbf{u} + 2\frac{\mathrm{Pr}}{\mathrm{Ek}} \hat{y} \times \mathbf{u} &= \hat{z}\theta \mathrm{PrRa} + \frac{\mathrm{Pr}}{\rho_0}\left[\boldsymbol{\nabla}^2 \mathbf{u} + \frac{1}{3}\boldsymbol{\nabla}\left(\boldsymbol{\nabla} \cdot \mathbf{u}\right)\right] \\
&- \frac{1}{\gamma} H_0/d \mathrm{PrRa}\left[\boldsymbol{\nabla}\left(\frac{\rho_1}{\rho_s} T_0/\Delta T + \theta\right) - \left(\frac{\rho_1}{\rho_0} + \theta \Delta T/T_0\right)\hat{z}\right].
\end{aligned}
\tag{5.24}
$$

The set of linear equations with constant coefficients (5.22), (5.23), and (5.24) can be solved with perturbations of the form

$$
\frac{\rho_1}{\rho_0} = \hat{\rho} e^{i(\mathbf{k}\cdot\mathbf{r}+\sigma t)},
\tag{5.25}
$$

$$
\mathbf{u} = \hat{\mathbf{u}} e^{i(\mathbf{k}\cdot\mathbf{r}+\sigma t)},
\tag{5.26}
$$

$$
\theta = \hat{\theta} e^{i(\mathbf{k}\cdot\mathbf{r}+\sigma t)},
\tag{5.27}
$$

with wave vector $\mathbf{k}$, complex frequency σ, and complex amplitudes $\hat{\rho}$, $\hat{\mathbf{u}}$, and $\hat{\theta}$, which are independent of time and space. All three boundary conditions, free-slip, no-slip, and periodic, can be approximated by a combination of sin and cos terms. In order to fit the modes to the boundaries, the wave numbers will be restricted to $k_z = \pi$ and $k_x = n\pi$ with $n = 0, 1, 2, 3, \ldots$ a positive integer. Therefore, it is reasonable to split the perturbations into Fourier modes without specifically applying any boundary conditions. Inserting the Fourier ansatz into the linear equations with constant coefficients results

in a matrix representation

$$\underline{\underline{M}} - \sigma\underline{\underline{I}} =$$

$$
\begin{bmatrix}
-\sigma & 0 \\
0 & -\sigma - \frac{\gamma}{\rho_0}k^2 \\
-ik_x\frac{1}{\gamma}\mathrm{RaPr}T_0/\Delta T H_0/d & -ik_x\frac{1}{\gamma}\mathrm{RaPr}H_0/d \\
\frac{1}{\gamma}\mathrm{RaPr}H_0/d\left(-ik_z T_0/\Delta T + 1\right) & -\frac{1}{\gamma}\mathrm{RaPr}H_0/d\left(ik_z + \Delta T/T_0\right) + \mathrm{PrRa}
\end{bmatrix}
$$

$$
\begin{bmatrix}
-ik_x & -ik_z - \left(\Delta T/T_0 - \gamma d/H_0\right) \\
-ik_x\left(\gamma - 1\right)T_0/\Delta T & 1 - ik_z\left(\gamma - 1\right)T_0/\Delta T \\
-\sigma - \frac{\mathrm{Pr}}{\rho_0}\left(k^2 + \frac{1}{3}k_x^2\right) & -2\frac{\mathrm{Pr}}{\mathrm{Ek}} - \frac{1}{3}\frac{\mathrm{Pr}}{\rho_0}k_x k_z \\
2\frac{\mathrm{Pr}}{\mathrm{Ek}} - \frac{1}{3}\frac{\mathrm{Pr}}{\rho_0}k_x k_z & -\sigma - \frac{\mathrm{Pr}}{\rho_0}\left(k^2 + \frac{1}{3}k_z^2\right)
\end{bmatrix} . \tag{5.28}
$$

The solutions of the characteristic polynomial $\det|\underline{\underline{M}} - \sigma\underline{\underline{I}}| = 0$ give the growth rates of the system. Numerically it is easier to calculate the eigenvalues of the Matrix $\underline{\underline{M}}$. The critical Rayleigh number can be calculated by finding the zero crossing of the largest eigenvalue, which is a function of the wave vector components and the Rayleigh number. Alternatively, the matrix can be further simplified. A very popular approximation used in atmospheric science is called the anelastic approximation originally proposed by Ogura and Phillips, 1961. As stated above, a good overview of different variations of this approximation can be found in the article by Brown, Vasil, and Zweibel, 2012. This approximation is mainly used to remove sound waves from the solutions, which has the great benefit of increasing the time step. Systems with a large number of density scale heights have a large speed of sound compared to the regularly observed velocities. These sound waves have to be resolved by the numerical integration leading to much smaller time steps. The program used in this work suffers from this problem, which is the reason for choosing parameters close to $\Delta T/T_0 = d/H_0 = 0.1$ where the Mach number is $\mathrm{Ma} \approx 0.3$. Generally, these sound waves do not add to the convection physics and are only a result of using a gas instead of an incompressible liquid. Therefore, it is generally possible to ignore sound waves and in turn increase the efficiency of the numerical simulations.

The anelastic approximation, similarly to the one introduced in this section, relies on small variations compared to a background field. It is the choice of the background field that is the subject of much debate. Most use an adiabatic stratification, which is applicable in many cases once the parameters are far from the onset as investigated by Verhoeven, Wiesehöfer, and Stellmach, 2015 and Verhoeven and Glatzmaier, 2018. In order to further investigate this approximation, the Equations (5.11), (5.12), and (5.20) can be easily changed to represent the anelastic approximation. Only the term $\partial_t\rho_1$
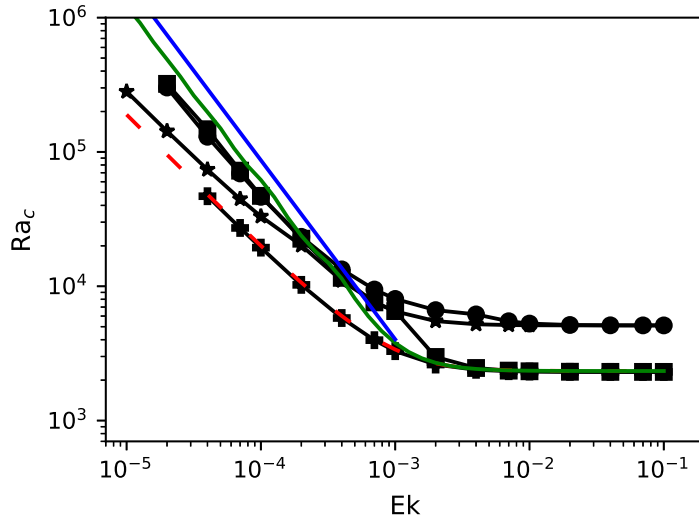
Figure 5.4: Shown is the critical Rayleigh number Ra_c as a function of the Ekman number Ek for $\Delta T/T_0 = d/H_0 = 0.1$. The dashed red line is calculated from the eigenvalues of the linear system with constant coefficients in Equation (5.28), the solid green line removes the term $\partial_t \rho_1$, making this system anelastic, and the blue line indicates a scaling law of $Ra_c \propto \text{Ek}^{-4/3}$. All black symbols are simulations using the time integrated linear equations with different boundary conditions. The pluses are horizontally periodic with free-slip top and bottom boundaries. The stars are similar but with no-slip vertical boundaries. The circles use no-slip vertical and free-slip horizontal boundaries. Finally, the squares use free-slip vertical and horizontal boundaries with an aspect ratio of $L/d = 1$.

needs to be removed in order to implement that approximation. Alternatively, the term $\sigma \hat{\rho}$ can be removed from the linear system with constant coefficients (5.28) to achieve the same effect. This reduces the number of eigenvalues to two, which can be handled in the same way as the full problem.

Additionally, the linear equations can be stepped in time with the program used in this work, allowing the investigation of boundary effects. Neither of the two linear systems with constant coefficients uses specific boundary conditions. Instead the wave numbers are restricted to approximate the presence of boundaries. Therefore, it is enlightening to investigate the effect of boundaries separately.

Calculating the critical Rayleigh number from the time dependent system is done by running simulations close to the onset with some large random noise in the tempera-
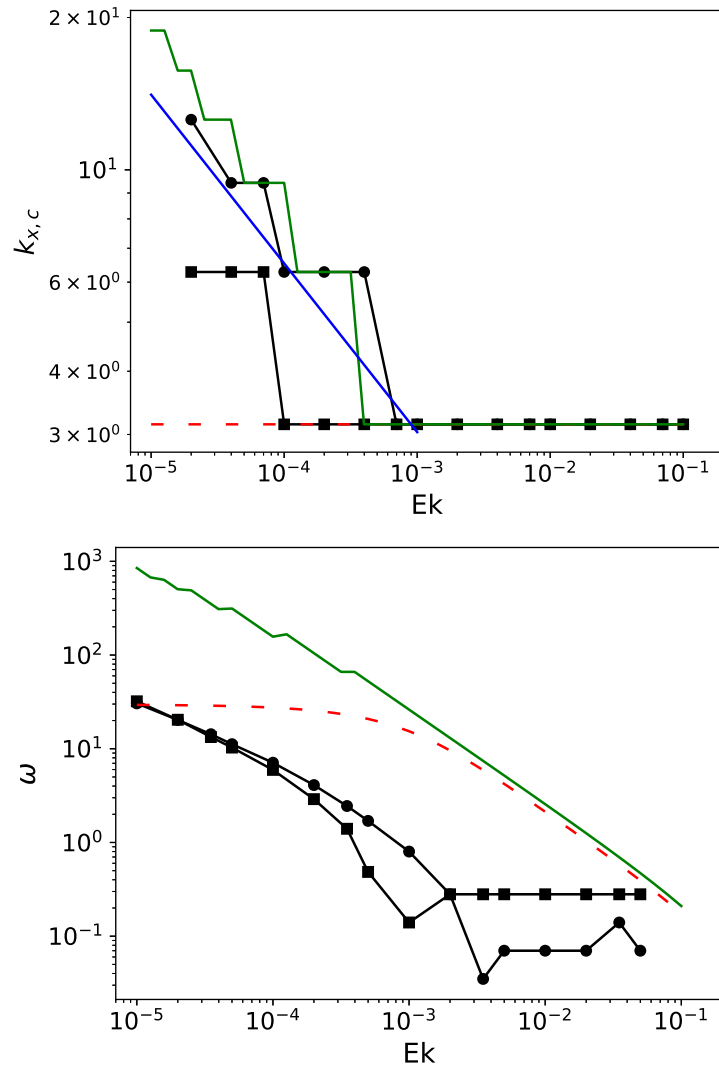
Figure 5.5: Shown are the critical, horizontal wave number $k_{x,c}$ in the top graph and the critical frequency ω_c, which is the imaginary part of the growth rate, in the bottom graph as a function of the Ekman number Ek. The symbols are the same as in Figure 5.4. The blue line for the critical wave number indicates a scaling law of $k_{x,c} \propto \text{Ek}^{-1/3}$.

ture field. The result is a flow field that either grows or decays in time, meaning that the kinetic energy either increases or decreases. The rate of in-/ decrease can be approximated by $E_{\text{kin}} \propto e^{\sigma t}$, with the growth rate σ. Running simulations with different Rayleigh numbers across the onset gives growth rates that change sign and therefore the critical Rayleigh number can be calculated for $\sigma = 0$.

The results of the critical Rayleigh number Ra_c as a function of the Ekman number Ek
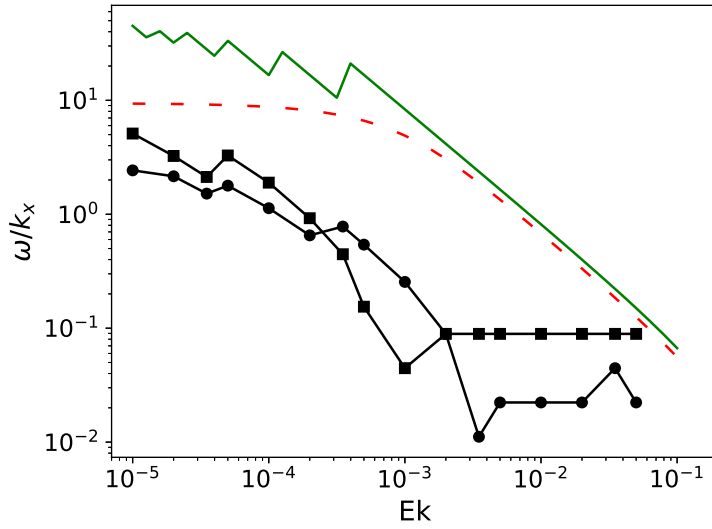
Figure 5.6: Shown is the critical phase velocity $\omega_c/k_{x,c}$ as a function of the Ekman number Ek. The symbols are the same as in Figure 5.4.

are shown for $\Delta T/T_0 = d/H_0 = 0.1$ in Figure 5.4. All results with additional values for $\Delta T/T_0$ and d/H_0 are given in Tables 7.68 until 7.72. Solutions of the eigenvalue problem are shown with lines and solutions from the time integrated equations are shown with symbols. The dashed red line is for the solutions of the full Eigenvalue problem, and the solid green line for the anelastic approximation. Additionally, the solid blue line indicates a scaling of $\mathrm{Ra}_c \propto \mathrm{Ek}^{-4/3}$. The best fit to the dashed red line is a scaling law of $\mathrm{Ra}_c \propto \mathrm{Ek}^{-1}$.

The solutions for the time integrated equations are computed for different boundary conditions. Pluses are used for simulations with free-slip vertical and periodic horizontal boundaries in a domain with an aspect ratio of $L/d = 2$. Stars are used for simulations, where vertical boundaries are replaced with no-slip ones. Circles also use no-slip vertical boundaries but replace the horizontal ones with free-slip boundaries. Finally, the squares free-slip boundaries on both vertical and horizontal walls and change the aspect ratio to $L/d = 1$.

It is clear to see that the anelastic approximation and the fully compressible eigenvalue problem show different scaling laws starting from about Ek $= 10^{-3}$. Remarkably, the free-slip vertical and horizontally periodic, time integrated solutions show the same scaling. Changing to no-slip vertical boundaries introduces an offset in the critical Rayleigh number for Ek $\gg 1$, which is similar to regular Rayleigh-Bénard convection. The scaling for Ek $\ll 1$ approaches the one of the full eigenvalue problem.

80
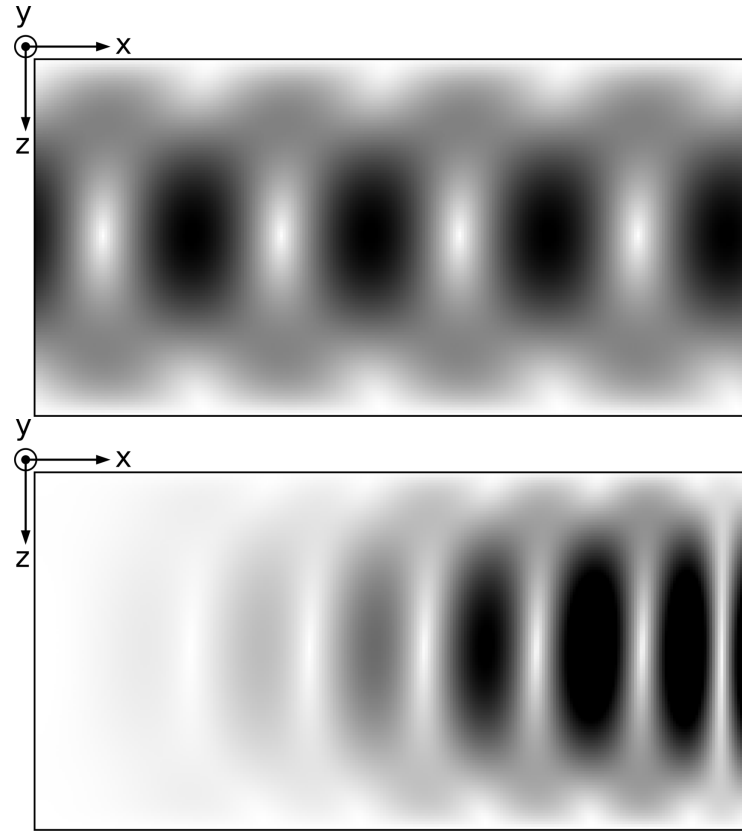
Figure 5.7: Shown are snapshots of the velocity magnitude $|\mathbf{v}|$ (dark is fast) of the results for the time integrated, linear equations. The flow field is a set of vortices which are aligned with the y-axis. The top flow field is the result of the horizontally periodic, and vertical free-slip boundaries. The bottom flow field is the result of introducing horizontal free-slip walls. Both simulations have an Ekman number of $\mathrm{Ek} = 4 \times 10^{-5}$, and $\Delta T/T_0 = d/H_0 = 0.1$, as well as a Rayleigh number of $\mathrm{Ra} = 7.4 \times 10^4$ in the top graph and $\mathrm{Ra} = 1.3 \times 10^5$ in the bottom graph.

Introducing free-slip horizontal walls does not change the behaviour for $\mathrm{Ek} \gg 1$ but does change the scaling for $\mathrm{Ek} \ll 1$. Both sets of simulations using free-slip horizontal boundaries approach the scaling of the anelastic approximation.

A similar investigation can be performed for the critical horizontal wave number $k_{x,c}$ and frequency ω_c, which is shown in Figure 5.5. The critical frequency is the imaginary part of the growth rate and is proportional to the size of the time derivatives. The symbols and colours are the same as in Figure 5.4 but the stars and pluses are omitted because both follow the scaling of the full Eigenvalue problem. The top graph shows

the wave number and the bottom one the frequency. It can be observed that the critical wave number for the full eigenvalue problem stays constant and the critical frequency approaches a threshold. The anelastic approximation in contrast changes the critical wave number drastically and therefore a scaling of $k_{x,c} \propto \mathrm{Ek}^{-1/3}$ is indicated as the blue line. Both sets of simulations with the free-slip horizontal walls also increase the critical wave number and frequency.

Calculating the critical phase velocity $\omega_c/k_{x,c}$ shown in Figure 5.6 reveals that the velocity field travels horizontally through the domain. The free-slip horizontal walls hinder this movement but do not fully stop it. Both, the full as well as the anelastic eigenvalue problem have a higher phase velocity, but the time dependent solutions approach their speed for $\mathrm{Ek} \ll 1$.

A view of the flow field can enlighten this observation. Two snapshots[3] of the velocity magnitude $|\mathbf{v}|$ (dark means fast) is shown in Figure 5.7. Both are solutions to the linear equations with $\mathrm{Ek} = 4 \times 10^{-5}$, $\Delta T/T_0 d/H_0 = 0.1$, and no-slip vertical walls. The top graph shows the flow field for $\mathrm{Ra} = 7.4 \times 10^4$ with periodic horizontal walls and the bottom graph shown $\mathrm{Ra} = 1.3 \times 10^5$ with free-slip horizontal walls. The flow field is a set of vortices which centers are shown in a light tone and are aligned with the y-axis.

The flow field for the periodic boundaries is a standing wave traveling in prograde (positive x) direction. In contrast to that, the flow field for the free-slip horizontal walls also travels in prograde direction but vortices are generated on the left-hand side and annihilated on the right-hand side. Apparently, this reduced freedom of movement allows the time dependence of the density fluctuations to be dropped, making the solution anelastic. This results highlights that the critical frequency of the fully compressible Eigenvalue problem has a strong influence on the time derivative of the density perturbations. Remember that the ω_c in the anelastic approximation is the frequency for the temperature and velocity fields, not for the density field.

5.2 Hysteresis comparable to experiment

The specific geometry of the experiment done by Menaut et al., 2019 is investigated in this section. No-slip boundaries on all walls in addition to the aspect ratio of $L/d = 0.5$, as used earlier, are chosen here to stay as close to the experiment as possible. Furthermore, the parameters $\Delta T/T_0$ and d/H_0 are increased by a factor of two compared to the

---

[3]A flipbook is read backwards, from the last page to the first.
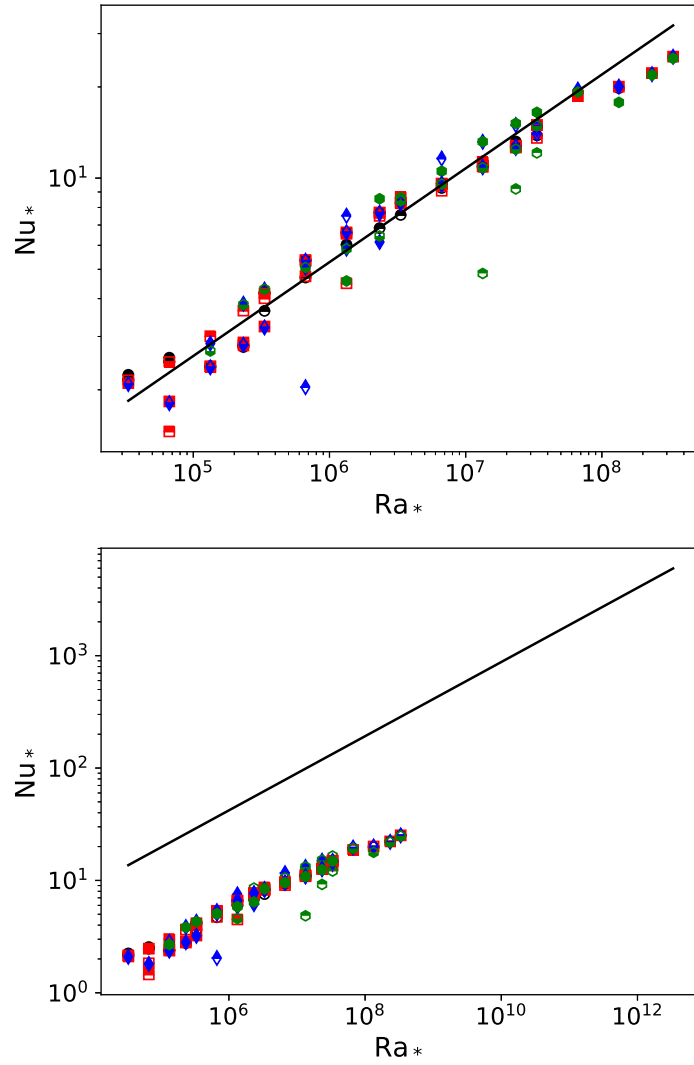
Figure 5.8: Shown is the superadiabatic Nusselt number Nu_* as a function of the superadiabatic Rayleigh number Ra_* for three different values of $\Delta T/T_0 = d/H_0 = 2$ (top half filled), $\Delta T/T_0 = d/H_0 = 0.2$ (fully filled), and $\Delta T/T_0 = d/H_0 = 0.02$ (bottom half filled). The aspect ratio is $L/d = 0.5$ with no-slip boundaries at all walls. The symbols and colours are for different Ekman numbers with $\mathrm{Ek} = \infty$ (black circles), $\mathrm{Ek} = 10^{-3}$ (red squares), $\mathrm{Ek} = 10^{-4}$ (blue diamonds), and $\mathrm{Ek} = 10^{-5}$ (green hexagons). Both graphs show the same data but the scaling law (black line) in the top one is the best fit to the non rotating dataset $\mathrm{Nu}_* = 0.07\mathrm{Ra}_*^{0.31}$ and the in the bottom is the one obtained by Menaut et al., 2019 with $\mathrm{Nu}_* = 0.44\mathrm{Ra}_*^{0.3}$.
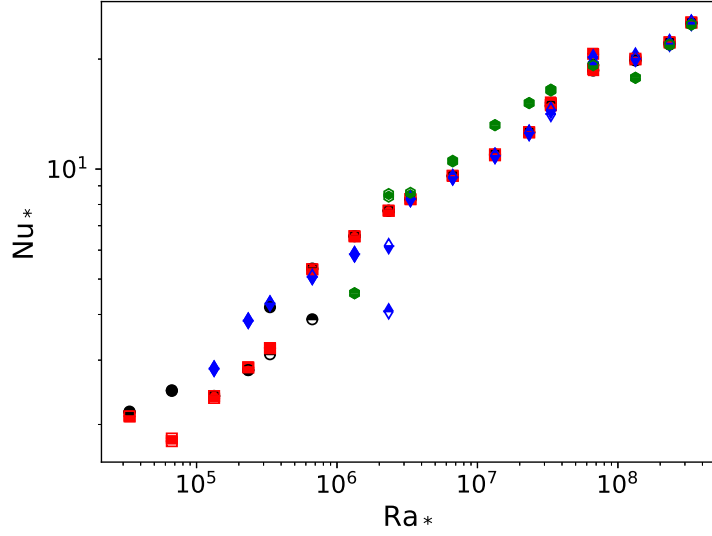
Figure 5.9: Shown is the superadiabatic Nusselt number Nu_* as a function of superadiabatic Rayleigh number Ra_* for $\Delta T/T_0 = d/H_0 = 0.2$ and the same geometry, colours, and symbols as in Figure 5.8. The bottom filled symbols are started with the initial conditions shown in Section 2.2.3 and the top filled symbols are started from the largest Ra_* of the same Ek and continued to run with a smaller Ra_*.

estimate given in Section 2.2.2. This means that $\Delta T/T_0 = d/H_0 = 0.2$, $\Delta T/T_0 = d/H_0 = 2.0$, and $\Delta T/T_0 = d/H_0 = 0.02$ are investigated here. The reason for this change is to increase the density contrast in order to get closer to the targeted 20%. Tables 7.52 until 7.67 contain the full datasets.

Results are shown in Figure 5.8 with top filled symbols for $\Delta T/T_0 = d/H_0 = 2.0$, fully filled symbols for $\Delta T/T_0 = d/H_0 = 0.2$, and bottom filled symbols for $\Delta T/T_0 = d/H_0 = 0.02$. Colours and symbols differentiate the Ekman number with Ek $= \infty$ (black circles), Ek $= 10^{-3}$ (red squares), Ek $= 10^{-4}$ (blue diamonds), and Ek $= 10^{-5}$ (green hexagons). The top and bottom graph show the same dataset but the scaling laws (black lines) are different. The top graph shows the best fit to the non rotating dataset with $Nu_* = 0.07Ra_*^{0.31}$, and the bottom graph shows the scaling law obtained by Menaut et al., 2019, which is $Nu_* = 0.44Ra_*^{0.3}$. Both scaling laws have a very similar exponent but differ in the pre factor.

This difference could be attributed either to the 2D approximation or to the differences in the compressibility. Interestingly, the best fit scaling law has a pre factor that is even small compared to the scaling laws in Equations (5.1) and (5.2). This suggest that

the change in the horizontal boundary condition has a strong impact on the thermal transport. It can also be observed that the thermal transport has a small jump at about $Ra_* \approx 10^8$ for all Ek considered. This further highlights that the flow structures observed in this set of simulations is still undergoing changes. Considering the range in superadiabatic Rayleigh number measured by Menaut et al., 2019 between $10^{11} \leq Ra_* 10^{13}$, it is very likely that the flow structures observed here are very different and may not be turbulent enough to reach a thermal transport that large.

The reason for investigating this specific geometry was the hysteresis Menaut et al., 2019 reported. They performed experiments at a fixed rate of rotation and either increased or decreased the prescribed temperature difference across the volume. Their results show that the superadiabatic Nusselt number scales differently depending on the direction of the temperature change. This behaviour is interpreted by them as a hysteresis since it was reproducible. Similarly, it is possible to start the simulations from the initial conditions shown in Section 2.2.3, run them until a statistically stationary state is reached, change the Rayleigh number and let them continue to run until they are again statistically stationary. This type of hysteresis test has been done for $\Delta T/T_0 = d/H_0 = 0.2$ in order to be close to the experimental values. Results are shown in Figure 5.9 with bottom filled symbols for the simulations started with the initial conditions. Top filled symbols are used for the simulations that used the largest Rayleigh number of simulations with the same Ekman number to perform the hysteresis runs. Colours and symbols are the same as in Figure 5.8.

It can be observed that a small loop of hysteresis exists for $Ek = 10^{-4}$ (blue diamonds) at $Ra_* \approx 3 \times 10^6$, as well as $Ek = \infty$ (black circles) at $Ra_* \approx 3 \times 10^5$. In our case, the hysteresis is very weak and not similar to the one observed by Menaut et al., 2019. A different set of hysteresis test was performed by only using the next higher Rayleigh number simulation in order to slowly change the parameter instead of abruptly changing it. This resulted in simulations which showed no hysteresis.

Similarly, simulations using the non rotating, statistically stationary flow field are used to continue simulations with increased rated of rotation. This would be similar to starting convection in the centrifuge and than turning on the rotation. Again, no hysteresis is found.

It is important to note that the behaviour observed by Menaut et al., 2019 looks very similar to the delayed onset, meaning that the thermal transport increases towards the scaling of the non rotating values. This behaviour can also be observed for the set of simulations presented here, indicating that it is not influenced by the change in aspect ratio

as well as the boundary conditions. Considering the larger Rayleigh and smaller Ekman numbers of the experiment, it is possible that this hysteresis behaviour is connected to the delayed onset and can also be observed numerically if the parameters match the experimental ones.

6 How does it all fit together

The results presented in the earlier chapters have been designed to aid the investigation of convection experiments using centrifugal acceleration. Two specific experiments, one using water done by Jiang et al., 2020, and one using a gas and stratification effects by Menaut et al., 2019, can be compared directly. The experiment in water can be investigated using the Boussinesq approximation. The experiment with a gas is the one that is of most interest here. Both will be compared to the elliptical stability problem, but only the later one can be compared with the compressible onset. Therefore, we start with the 2D approximation of the flow in Section 6.1, followed by the discussion about compressible convection in Sections 6.2 and 6.3. Ultimately, this chapter and this thesis will end with some final remarks, as well as some so called "glory runs", and an outlook for future work in Section 6.4.

6.1 Simplification of a 2D flow

Experiments using centrifugal acceleration as a much stronger gravitational acceleration carry an additional feature. The geometry shown in Figure 2.1 is affected by the Coriolis force which is directly linked to the centrifugal acceleration. An experimental study cannot be performed without it, a numerical one can. Therefore, studying the effects of the Coriolis force in a geometry where global rate of rotation and gravitational acceleration are independent can lead to interesting simplifications.

The most interesting one is to compute the flow in 2D, saving large amounts of memory, compute time, and electrical energy. Earlier works, for example by Schmalzl, Breuer, and Hansen, 2004 and Pandey et al., 2016, have shown that calculating measures, like thermal transport in form of the Nusselt number or velocity dependent measures like the Reynolds number, strongly differ if convection in 2D or 3D is investigated. In fact, the results of this work presented in Section 3.1 emphasise these strong differences with two, very different scaling laws for the 2D and 3D measures.

Therefore, it is of vital importance to know under what conditions a 2D simplification is applicable. The investigation presented in Section 3.3 showed that the transition between a constrained 2D and a full 3D flow can be described by an inertial instability. A transition, depending on the ellipticity of the flow, can be found and a transition line traced, in the mechanical, Reynolds-Rossby space. Earlier work by Clausen and Tilgner, 2014 concluded that this elliptical instability does not depend on compressibility, making this description applicable to both experiments.

The water experiment by Jiang et al., 2020 used the free fall velocity to calculate their Rossby number. As described before, a Rossby number computed from flow velocities is needed for the instability. Therefore, it is difficult to compare this experiment with our results. Nonetheless, they did their own investigation and found a specific transition between 2D and 3D flow which can be linked to our results if flow velocities are measured in the future. A comparison of the control parameter relations with the Rayleigh and Ekman numbers is not sufficient, because the relation between Reynolds and Rayleigh numbers strongly depends on the boundaries, which are different.

The experiment by Menaut et al., 2019, does give measure for the velocities. They use relations between either the pressure gradient and the Coriolis force or between the pressure gradient and the advection term to calculate a velocity. Their resulting Rossby number is between 0.01 and 0.1. This can be calculated into a Reynolds number using their Ekman number. They report an Ekman number between 10^{-7} and 10^{-6} resulting in $10^4 \leq \mathrm{Re} \leq 10^5$. These Reynolds and Rossby numbers fulfill the relation $\mathrm{Re} < 100\mathrm{Ro}^{-2}$, found as an approximate scaling law in Section 3.3.5. The conclusion is that the flow in the experiment by Menaut et al., 2019 can be approximated as 2D if the boundaries are far away, say, in the center between the surfaces perpendicular to the axis of rotation. Being far away from the boundaries is necessary because the experiment has Ekman layers at these boundaries, which always break the 2D simplification.

6.2 Compressible convection

Once it was established that a 2D simplification is indeed applicable, a study of compressible convection followed. Initial investigations ignored the effects of the Coriolis force in order to estimate how different 2D compressible convection scales compared with full 3D simulations. Scaling laws with the Boussinesq approximation are very different between 2D and 3D flows but compressible convection is already different for full 3D flow. Therefore, investigating the difference between 2D and 3D before reintroducing

the Coriolis force can aid later studies.

Earlier work by Tilgner, 2011 provided a set of parameters to compare with. Following the motto "Gotta catch'em all"[1], a study reproducing all of the parameters was performed. This allowed us to directly compare the same levels of compression as well as the same thermal driving strengths. It was found that the density changes across the domain, called the characteristic density, is the same. Furthermore, it was shown that the scaling of the kinetic energy with the Péclet number using the characteristic density is the same. Additionally, the scaling law for the superadiabatic thermal transport Nu_* with the superadiabatic Rayleigh number Ra_* is almost identical. There are some differences, for example, the 2D Nusselt number seems to be getting smaller in contrast to the 3D one. Studies with larger Rayleigh numbers for both are required to conclusively state this difference.

Much more striking and easier to see is the difference in the Péclet number between 2D and 3D flow. There, it is clear to see that the 2D Péclet number is getting larger than the 3D one. Putting both information together results in an observation which is very different to the one obtained for the Boussinesq approximation. There, both the Nusselt number and the Péclet number are larger for the 2D flows. The compressible convection should also follow this trend if the parameters d/H_0 and $\Delta T/T_0$ are becoming small, which is not directly observed. It is important to note that the difference is only visible in the Nusselt number of the Boussinesq approximation if it is large, for example close to $\mathrm{Nu} \approx 100$. The measured Nusselt numbers for the compressible convection are all below $\mathrm{Nu} < 25$. More simulations with larger Rayleigh numbers are required to bring this difference to the light.

Interestingly, the result of this investigation is that 2D and 3D compressible convection are much more similar than the Boussinesq study was. This aids our conclusion that it is sufficient to investigate only 2D compressible convection given that the global rotation is fast enough.

Comparing the results presented here and the ones given by Tilgner, 2011 with work done within the anelastic approximation, for example, by Jones, Mizerski, and Kessar, 2022 proves difficult. The anelastic approximation relies on a specific background field, which is set arbitrarily and often assumed to be adiabatic for simplicity. Therefore, the density ratio is set by the background field and is not part of the resulting flow field. This density ratio, which can be calculated using the dissipation number, is used as a control parameter, for example by Verhoeven and Stellmach, 2014, Verhoeven, Wiese-

---

[1]Sadly the only Pokémon reference.

höfer, and Stellmach, 2015, or Verhoeven and Glatzmaier, 2018. Simulations performed in this work can be linked to a specific dissipation number but this does not represent a fixed density ratio.

One possibility is to compare measured relations, like the boundary layer thicknesses calculated by Jones, Mizerski, and Kessar, 2022. This requires a large parameter study with different amounts of density scale heights to find comparable density ratios. Once those have been identified, a comparison between the thermal and velocity boundary layer thickness can be done. Some quick comparisons with smaller density ratios revealed that the velocities reported by Jones, Mizerski, and Kessar, 2022 are already different compared with this work, as well as the one from Tilgner, 2011, by at least 50%.

Therefore, a different approach is required, where the equations of motion are split in the same manner as in this work but the deviations from the background field are kept small by the careful choice of the parameters. This approach is similar to the one done by Verhoeven and Glatzmaier, 2018.

6.3 Rotating compressible convection

Introducing the Coriolis force again and running a parameter study with different rates of rotation, revealed a delayed onset. This geometry only shows this behaviour if compressible convection is considered. Convection under the Boussinesq approximation does not show a similar behaviour. In fact, the observed delay and consequent approach of the Nusselt number to the non rotating scaling is observed in the Boussinesq approximation for a geometry where the axis of rotation is aligned with the axis of gravity. A study investigating this behaviour in the Boussinesq approximation was done by Schmitz and Tilgner, 2009. These authors introduced a compensation for the scaling law that collapsed the data for the Nusselt number into two regimes, one which is influenced by the rotation, and one that is not. A similar compensation can be applied for the data of this work revealing a similar collapse.

This leads to the conclusion that, again, two regimes can be identified, one where the combination of Péclet number, characteristic density, and Ekman number is smaller than one and rotation does affect the thermal transport, and one where the product is larger than one and rotation is irrelevant. This transition can be traced for different Ekman numbers.

The delayed onset can also be reproduced with a linear theory. Remarkably, the scaling
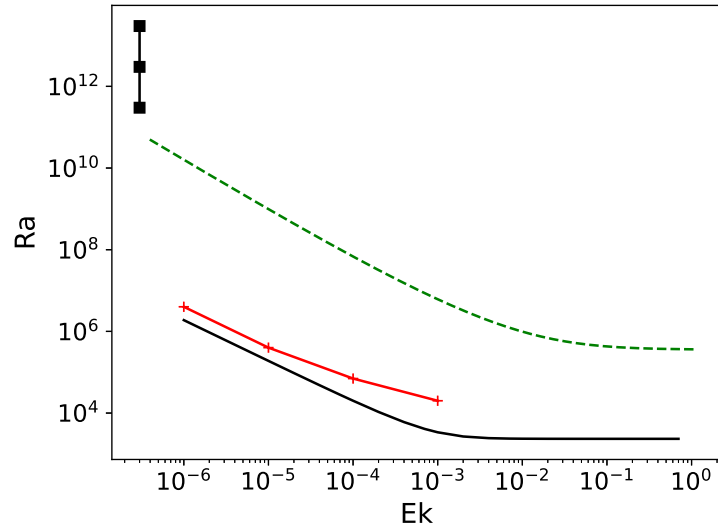
Figure 6.1: Shown are the three transition lines in the parameter space of the Rayleigh and Ekman number calculated for $\Delta T/T_0 = d/H_0 = 0.1$. The solid black line is the critical Rayleigh number. The red pluses are the transition between rotation dependent and independent scaling for the Nusselt number from Section 5. The dashed green line is the transition calculated from the elliptical instability for $\beta = 0.73$. The black squares mark the experimental parameters for the highest rotational speed from Menaut et al., 2019. The other parameters are all further to the right at a similar Ra range.

of the critical Rayleigh number with the Ekman number is very different for the fully compressible equations compared to the anelastic ones. The indicated scaling for the anelastic approximation $Ra_c \propto Ek^{-4/3}$ matches the one obtained by Busse and Simitev, 2014. They also predict that the critical wave number scales with $k_{x,c} \propto Ek^{-1/3}$, which matches our data as well.

The fully compressible scaling is $Ra_c \propto Ek^{-1}$ and the critical wave number stays constant. This difference in scaling can be attributed to the removal of the time dependence of the density perturbations, which is easy to see with the chosen linear equations. A set of time dependent simulations using the linear equations confirmed the scaling for the fully compressible convection and revealed a drift of the critical mode in prograde direction. This drift was also observed by Busse and Simitev, 2014 and Currie and Tobias, 2016. In our case, it can be attributed to the compressible beta effect, which is similar to the topographic beta effect. The topographic beta effect describes the generation of vorticity due to vortex stretching in an unevenly bound domain with sloping top and

bottom surfaces like in a sphere. A vortex travels in and out of a domain with increasing or decreasing height, increasing or decreasing the width of the vortex, leading to generation of vorticity. The compressible beta effect works in the same way, since vortices move in and out of more or less dense regions, leading to a compression or expansion of the vortex and in turn, to the generation of vorticity.

This drift can be inhibited by side walls but not fully stopped. Therefore, the time dependence of the density perturbation becomes less relevant for the bound domain, and the anelastic approximation can be used. Most studies use a cylindrical or spherical geometry which can be considered unbounded in the horizontal direction. Using the anelastic approximation in such geometries close to the onset can lead to very different results. More work needs to be done to understand the relevance of this drift on the time dependence of the density perturbations in order to fully grasp when the anelastic approximation can be used. Ultimately, it is possible that the anelastic approximation becomes relevant again far away form the onset as Verhoeven and Glatzmaier, 2018 discussed in great detail.

One more interesting observation can be made with the results from the onset regardless of the boundary conditions. The critical mode consists of many slender convection rolls similar to the ones observed in the elliptical geometry, especially if the Ekman number is small. This allows the conclusion that the results from Chapter 3.3 can be used without much modification. Therefore, a simple parameter space in Rayleigh and Ekman numbers can be found showing the results of this investigation. This parameter space calculated for $\Delta T/T_0 = d/H_0 = 0.1$ is shown in Figure 6.1, where the solid black line indicates the critical Rayleigh number. The red pluses indicate the transition between rotation dependent and independent scaling of the thermal transport and the green dashed line shows the transition from 2D to 3D flow due to the elliptical instability. The translation from the Reynolds-Rossby dependent scaling to the Rayleigh-Ekman space was performed using the scaling law of the Péclet number with the Rayleigh number. The parameters of the experiment by Menaut et al., 2019 with their highest rate of rotation, are shown with black squares.

It can be observed that a large portion of the parameter space between the critical Rayleigh number and the elliptical instability line can be considered independent of the Coriolis force. The thermal transport behaves differently from the non rotating case only between the red pluses and the solid black line. This is true at least for the enclosed volumes, which the experiment is. Periodic domains do not fit into this parameter space in the same manner but still obey the solid black and dashed green lines.

Furthermore, the experimental parameters are all above the line for the elliptical instability, meaning that these parameters cannot be estimated to be 2D. This observation contrasts the results from earlier stating that the estimated Reynolds and Rossby numbers are bellow the transition line. An explanation is that the estimations used for calculating the velocities assumes a 2D flow. Another explanation is that even those estimates are marginal to the transition line. Also, it is not fully clear what value for the ellipticity β should be chosen. The one used in the parameter space is close to the lower limit ensuring that this is the lowest transition line possible. If the flow is much more circular, than the transition line moves to higher values for Rayleigh. More information about the flow profile is required to make a better guess for the ellipticity.

One last parameter study was performed close to the experimental geometry and boundary. Its purpose was to identify a hysteresis observed in the experiment. A large scale parameter study with different initial conditions close to the experimentally used ideas revealed small hysteresis loops which are different from the ones observed by Menaut et al., 2019. It is possible that such hysteresis can only be observed at the parameters of the experiment. Additionally, it is also possible that the hysteresis is an effect of the 3D nature of the flow, especially since the flow cannot be considered close to the 2D approximation. However, the scaling measured in the experiment does look qualitatively similar to the one obtained here. Therefore, the hysteresis loops could also be due to being close to the onset of convection.

Even more disturbing is the difference in the actual numbers of the thermal transport. The experimentally observed Nusselt number is an order of magnitude larger than the numerically observed one. This can only be the case if it is either a strong 3D effect or, more likely, overestimated. Interestingly, the exponent of the scaling law fits well with the one obtained numerically. Only the pre factor is very different.

6.4 Final remarks and outlook

This work set out to investigate the effects of recently performed experiments in the regime of centrifugal acceleration generating large Rayleigh numbers and most interestingly, effects of compressible convection. One possible simplification was investigated allowing the use of a 2D flow instead of computing the full 3D flow field. A transition line was found and explained by an inertial instability due to the elliptical nature of the resulting vortex. This transition line was used as an argument to run all compressible simulations with a 2D flow.
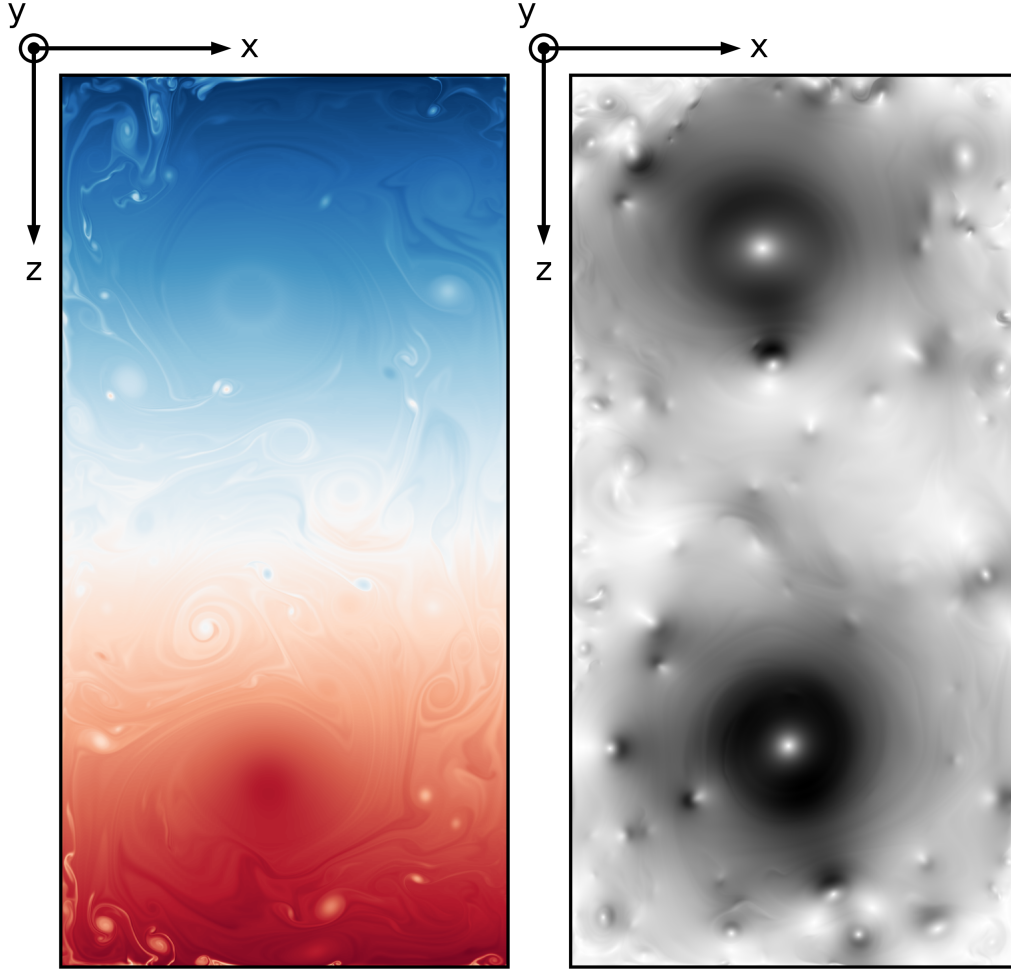
Figure 6.2: Shown is a snapshot of a simulation close to the experiment of Menaut et al., 2019, with Ra $= 10^{12}$, Ek $= 5 \times 10^{-7}$, no-slip wall on all sides, and spatial resolutions of $N_z = 4096$ and $N_x = 2048$ points. The left graph shows temperature perturbations θ with blue bellow and red above the background field T_s. The right graph shows velocity magnitude $|\mathbf{u}|$ with darker tones meaning faster. The Nusselt number is Nu $= 98$, which still lies on the best fit scaling law of this work found in the top of Figure 5.8.

A further study compared the results for compressible convection without the effects of the Coriolis force between the 2D approximation in this work and the full 3D flow of an earlier work. The results indicate that both are close but diverge for large Rayleigh numbers in a manner unknown before, because the thermal transport is smaller but the flow velocities are larger.

An additional study reintroduced the Coriolis force and found a delayed onset of the
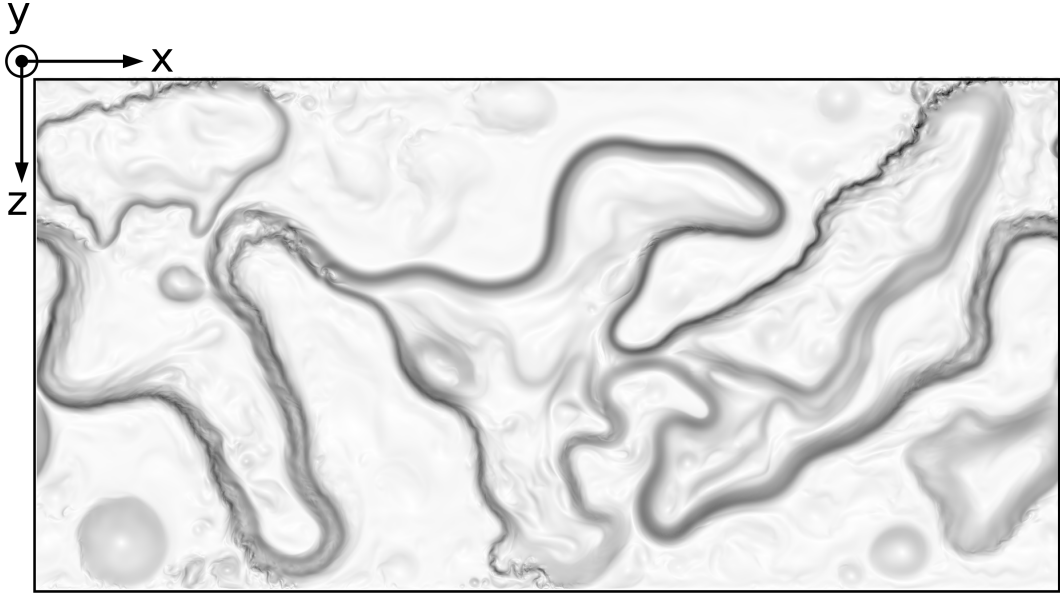
Figure 6.3: Shown is the velocity magnitude $|\mathbf{u}|$ with darker meaning faster, for a parameter close to the zonal wind simulations from Verhoeven and Stellmach, 2014. The parameters are Ra $= 10^{12}$, Ek $= 10^{-9}$, vertical boundaries are no-slip, horizontal boundaries are periodic, and spatial resolutions are $N_z = 2048$ and $N_x = 4096$ points. The entire volume is drifting in prograde (positive x) direction while the bands of high velocity are flowing in retrograde direction, similar to the jet stream (Rossby wave).

convection. The new critical Rayleigh numbers were investigated and compared for fully compressible convection and the popular anelastic approximation, revealing striking differences. These differences are in line with earlier work and lead to the conclusion that this approximation is only applicable for larger Rayleigh numbers far from the onset. One final study intended to find a hysteresis in the thermal transport of the experiment but could not be reproduced by this work.

One final task is looking into what is possible in the future, meaning the so called "glory runs". To this end, two simulations are performed at the edge of possibility of the simulation. One uses the geometry and boundary conditions of the experiment as well as their largest rotational speed resulting in an Ekman number of Ek $= 5 \times 10^{-7}$ and an Rayleigh number of Ra $= 10^{12}$. A spatial resolution of $N_z = 4096$ and $N_x = 2048$ points is used. These parameters exceed the range of the 2D approximation shown in Figure 6.1 but allow some insight into the flow field structure. The results are shown in Figure 6.2, with the temperature perturbations θ on the left, with blue smaller and red greater

than the temperature background T_s, and the velocity magnitude $|\mathbf{u}|$ on the right, with darker meaning faster. The two vortices are clearly visible in the velocity field, as well as the additional smaller vortices. Furthermore, the temperature field indicates that the resolution was sufficient to resolve the smaller structure. Interestingly, the structures are close to circular, indicating that they could actually be considered 2D. Therefore, the transition line of the elliptical instability moves to larger Rayleigh numbers and could cover the experimental parameters.

The second simulation uses a parameter discussed by Verhoeven and Stellmach, 2014, which is $\mathrm{Ra} = 10^{12}$ and $\mathrm{Ek} = 10^{-9}$ with an aspect ratio of $L/d = 2$, $\Delta T/T_0 = d/H_0 = 0.1$, periodic horizontal boundaries and vertical no-slip boundary conditions. They investigate the strength of zonal flow, meaning the prograde and retrograde winds found in deep atmospheres like the one on Jupiter. Their results show many changes in sign of the horizontal velocity component while moving radially inward. Compared to the results shown here, they use an aspect ratio of $L/d = 1$ and free-slip vertical walls. The flow observed here and shown in Figure 6.3 with the velocity magnitude $|\mathbf{v}|$ (darker = faster), is very different. For one, the clear bands of prograde and retrograde movement are not visible here. The entire volume is moving in prograde direction in our simulations. Only the thin, high velocity bands are flowing in retrograde direction while being advected in the opposite direction. Furthermore, these bands are neither stationary nor stable. As mentioned before, they flow to the left but buckle and bend until disconnecting from the main flow and reconnecting elsewhere. They look vaguely similar to the jet stream (Rossby wave) found in Earths atmosphere.

This results clearly show that boundary conditions have a strong influence on the zonal flow and change the entire organization of said flow. Future work can now isolate a domain where the 2D approximation is applicable. The experiment might not be fully 2D, but the second, high parameter simulation, is. Afterwards the effects of velocity boundary conditions as well as aspect ratios should be investigated. Finally, a structure and speed analysis of the drift as well as the thin high velocity bands can follow.

7 Appendix

7.1 2D grid

The Chapter 2.3.2 only showed the one dimensional grid. Here, we will expand to a two-dimensional grid. The step to the three-dimensional grid is left to the reader.

Both types of grids are shown in the Figure 7.1 with the collocated arrangement on top and the staggered arrangement shown on the bottom. They differ by the placement of the scalar and velocity components similarly to the one dimensional case. Scalar fields meaning density, pressure, temperature and similar fields are shown in red. The two velocity components are shown as vectors in their respective directions. Both grids can be easily expanded into three-dimensional space by adding the direction out of the plane and applying the principles shown below.

Greyed points are outside of the computational domain and are called halo points since they form a layer or halo around the points inside and on the boundary of the computational domain. The size of the halo domain is marked with HS, which stands for halo size. These halo points are used to compute finite differences on and beyond the boundaries in order to use the same schemes for all points. An alternative without halo would be to use one sided finite differences close to and on the boundaries. This makes the programming a bit more cumbersome and slower especially in GPU accelerated applications.

The collocated arrangement (on the top in Figure 7.1) is the easiest and most understandable arrangement. All vector components and scalar fields reside on the edges and all have values on the boundaries. This means that a grid with the index interval $[0 : N_x - 1 \times 0 : N_y - 1]$ has N_x by N_y points including both boundaries. Boundary conditions are needed for all variables even if they do not have physical ones like the density or pressure for example.

The staggered grid shown on the bottom of Figure 7.1 is more complicated but has some immediate benefits as explained in Chapter 2.3.2. The scalar fields are shifted by half a
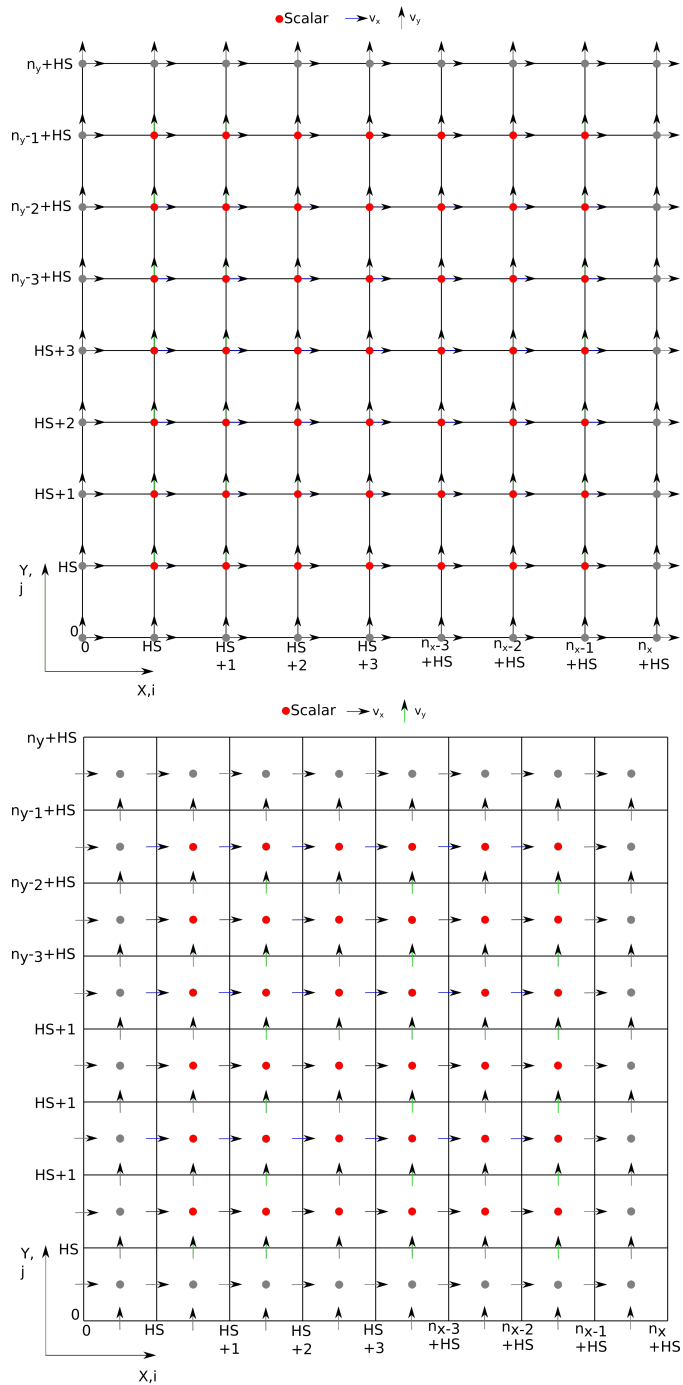
Figure 7.1: On the top is the collocated and on the bottom the staggered grid arrangement for two-dimensional variables. Observe the different positions of the scalar fields as well as the two vector components. Internal and boundary points are coloured while points outside the domain are greyed.

grid spacing into the center of the grid cell. Therefore, it is immediately visible that there are no direct boundary points. The vector components are moved by half a grid spacing in the one (two in 3D) direction, they are not facing into (off axis direction). This means that the x-velocity is moved up by half a grid spacing in y-direction. Also, the y-velocity is moved to the right by half a grid spacing. Similarly to the scalar components, this shift in the vector components removes boundary points in the off axis direction meaning v_x has no boundary points in y-direction and vice versa for v_y. Summarizing, this can be seen more easily in the index notation

$$T_{ij}|_{\text{collocated}} = T_{i+\frac{1}{2}j+\frac{1}{2}}|_{\text{staggered}}, \tag{7.1}$$

$$v_{x,ij}|_{\text{collocated}} = v_{x,ij+\frac{1}{2}}|_{\text{staggered}}, \tag{7.2}$$

$$v_{y,ij}|_{\text{collocated}} = v_{y,i+\frac{1}{2}j}|_{\text{staggered}}, \tag{7.3}$$

where the indices i and j are integers counting from 0 to $N_x - 1$ and $N_y - 1$. This means that some interpolations are needed for multiplications of variables on different grids as shown before. The finite difference stencils used on both grids are explained in great detail in the next Chapter 7.2.

Additionally, the number of points for the scalar fields are reduced by one, which is due to the reduction of the direct boundary points. Therefore, it is beneficial to also reduce the number of points for the velocity components by one, which is easily done for the off axis direction but is a problem in the other one. The problem is that v_x, for example, has a value on the x boundaries but only enough points for one of them. This can be solved by allowing the velocity to have an additional point in one direction or by using the halo point for setting the boundary condition. The latter has been chosen here for better homogeneity in memory. As a matter of fact, the halo points in the staggered grid are also needed to enforce the boundary conditions for the fields, which are set directly in the collocated grid. For example, the temperature field has fixed value boundaries top and bottom, which can be set directly in the collocated grid but has to be set as an average of the last inner and halo point for the staggered grid. The exact handling of the boundary conditions for both grids is shown in Chapter 7.2.3.

7.2 Finite difference stencils

These are all the finite difference operators that are used on the collocated and staggered grid. The notational convention is to drop the order symbol $\mathcal{O}$ in favor of the $\approx$ sign to

make it more readable. All differences except for the upwind differences are of fourth order for the collocated and of second order for the staggered grid. The staggered grid differences are only of second order since the interpolations are only hardware accelerated to second order. Therefore, it is not necessary and much more difficult to calculated the differences to higher orders. Higher order interpolations and differences do exist and are highlighted by for example these authors Albin, D'Angelo, and Vervisch, 2012.

The indices for all three directions x, y and z are i, j and k. These are all the 3D operators and the 2D ones are analog with one dimension removed. It is highly advisable to look at the grid in Figure 7.1 for reference. This is especially true if you want to understand the staggered grid differences and interpolations without stretching one's imagination to the limit.

7.2.1 Collocated grid

The Laplace operator of some scalar field in 3D is $\boldsymbol{\nabla}^2 T = \left(\partial_x^2 + \partial_y^2 + \partial_z^2\right) T$ so all we need is an operator for the double derivative and apply it to all directions. The scheme for this double derivative operator in the direction x with step size Δx is

$$\partial_x^2 T \approx \frac{-T_{i+2jk} + 16T_{i+1jk} - 30T_{ijk} + 16T_{i-1jk} - T_{i-2jk}}{12\Delta x^2}. \tag{7.4}$$

The other two directions are only index permutations and have the same scheme.

A divergence operator of some vector field in 3D is $\boldsymbol{\nabla} \cdot \mathbf{v} = \partial_x v_x + \partial_y v_y + \partial_z v_z$. Here we only need an operator for the first derivative, which in the direction x with step size Δx is

$$\begin{aligned} \partial_x v_x &\approx \frac{-v_{x,i+2jk} + 8v_{x,i+1jk} - 8v_{x,i-1jk} + v_{x,i-2jk}}{12\Delta x} \\ &\approx \frac{(8v_{x,i+1jk} - 8v_{x,i-1jk}) + (v_{x,i-2jk} - v_{x,i+2jk})}{12\Delta x}. \end{aligned} \tag{7.5}$$

The other directions are again only index permutations. Important to note is that the second line of that formula has reduced round off errors since the multiply and add operator is implemented with reduced round off errors. Therefore, it is beneficial to subtract similarly multiplied variables from each other. The gradient operator of some scalar field in 3D is $\boldsymbol{\nabla} T = \partial_x T \hat{x} + \partial_y T \hat{y} + \partial_z T \hat{z}$ and also contains only first derivatives and uses the same scheme as shown above.

The most complicated operator is the advection term as usual. It involves a multiplication and a first order derivative operator. The advection term is unstable if central

differences are applied, which is often shown in basic numerics courses. Therefore, we handle this term with upwind differences, which are forward or backward differences depending on the flow direction. They are calculated backwards for forwards flow and forward for backward flow. This stabilizes the finite differences but also introduces some numerical diffusion because those differences are only of third order. The lower order and the added diffusion is small compared to the physical diffusion and can mostly be neglected in turbulent flow. Some care has to be taken if the flow becomes stationary because the rate of convergence will be slower and the final state will not be reached accurately.

The advection operator in 3D of some scalar field is $(v \cdot \boldsymbol{\nabla}) T = (v_x \partial_x + v_y \partial_y + v_z \partial_z) T$. This means that first derivatives with backwards and forwards differencing are needed. These can be written like this

$$
\begin{aligned}
v_x \partial_x T_{ijk} &\approx v_{x,ijk}
\begin{cases}
\frac{2T_{i+1jk} + 3T_{ijk} + T_{j-2kl} - 6T_{i-1jk}}{6\Delta x} & \text{if } v_i >= 0 \\[2mm]
\frac{-T_{j+2kl} + 6T_{i+1jk} - 3T_{ijk} - 2T_{i-1jk}}{6\Delta x} & \text{otherwise}
\end{cases} \\[4mm]
&\approx v_{x,ijk}
\begin{cases}
\frac{T_{j-2kl} + 2T_{i+1jk} + 3T_{ijk} - 6T_{i-1jk}}{6\Delta x} & \text{if } v_i >= 0 \\[2mm]
\frac{-T_{j+2kl} - 2T_{i-1jk} - 3T_{ijk} + 6T_{i+1jk}}{6\Delta x} & \text{otherwise}
\end{cases}
\end{aligned}
\tag{7.6}
$$

in the direction x and the step size Δx. The index symmetry is more obvious in the second version and is similarly for the other two directions as they are only index permutations.

7.2.2 Staggered grid

The Laplace operator for some scalar field on the staggered grid is the same as on the collocated grid. Only the order is different meaning that it uses fewer points and looks like this

$$
\partial_x^2 T \approx \frac{T_{i+1jk} - 2T_{ijk} + T_{i-1jk}}{\Delta x^2}
\tag{7.7}
$$

for the direction x and the step size Δx.

This is all in terms of similarities to the collocated grid. Most important to note is that all differentiation operators used have a different form depending on the grids involved. This means that a vector component differentiated onto the scalar grid has a different form from a scalar differentiated onto a vector grid. Also, it is important to note that single grid spacing operators should be used whenever possible.

Divergences are already computed differently since the divergence is a scalar field that is computed in the center of the grid cell at the same position as for example the temperature. Due to the choice of coordinates, we only need to compute this difference

$$\partial_x v_x \approx \frac{v_{x,i+1jk} - v_{x,ijk}}{\Delta x} \tag{7.8}$$

for the x direction and with step size Δx. The other two directions work similarly and are only index permutations of this one.

A gradient can be calculated in a similar manner from the scalar grid to the vector grid meaning the differences look like this

$$\partial_x T \approx \frac{T_{ijk} - T_{i-1jk}}{\Delta x} \tag{7.9}$$

for the direction x with step size Δx. Again, the other two directions are similar due to the choice of grid arrangement.

Any other first order derivative that is performed on the same grid needs to be calculated with central differences. This is especially true for the advection term. For example the derivative of v_x on the grid for v_x looks like this

$$\partial_x v_x \approx \frac{v_{x,i+1jk} - v_{x,i-1jk}}{2\Delta x} \tag{7.10}$$

in the direction x with step size Δx and

$$\partial_z v_x \approx \frac{v_{x,ijk+1} - v_{x,ijk-1}}{2\Delta z} \tag{7.11}$$

for the derivative in direction z with step size Δz. It is also possible and important to interpolate these derivatives to only be computed over one grid spacing for example in direction x

$$
\begin{aligned}
\partial_x v_x &\approx \frac{v_{x,i+1jk} + v_{x,ijk} - v_{x,ijk} - v_{x,i-1jk}}{2\Delta x} \\
&= \frac{\frac{1}{2}\left(v_{x,i+1jk} + v_{x,ijk}\right) - \frac{1}{2}\left(v_{x,ijk} + v_{x,i-1jk}\right)}{\Delta x} \\
&= \frac{v_{x,i+\frac{1}{2}jk} - v_{x,i-\frac{1}{2}jk}}{\Delta x}.
\end{aligned} \tag{7.12}
$$

This interpolation is needed for stopping the decoupling of odd and even indices. The educated reader might have noticed that this interpolation is pointless in this case. This is true for $\partial_x v_x$ but this interpolation becomes important if the half grid spacing derivatives are multiplied with some other variable.

The complication with the multiplication arises especially with the multiplication between grids. The first example here is the divergence in the continuity equation. It is

vital to compute the divergence of the product $\boldsymbol{\nabla}\cdot(\rho\mathbf{v}) = \partial_x\left(\rho v_x\right) + \partial_y\left(\rho v_y\right) + \partial_z\left(\rho v_z\right)$ in order to ensure conservation of mass. Therefore, it is important to compute the derivatives $\partial_x\left(\rho v_x\right)$, which required an interpolation of ρ onto the v_x grid and then a finite difference operation from the v_x grid back to the ρ grid. This operation looks like this

$$\partial_x\left(\rho v_x\right) \approx \frac{\frac{1}{2}\left(\rho_{ijk} + \rho_{i+1jk}\right)v_{x,i+1jk} - \frac{1}{2}\left(\rho_{ijk} + \rho_{i-1jk}\right)v_{x,ijk}}{\Delta x} \tag{7.13}$$

with grid spacing Δx and the other directions are again index permutations.

The most prominent and most problematic computation is again the advection term. It involves a differentiation between two vector grids and an interpolated multiplication. The simplest is the term on the same grid meaning $v_x\partial_x v_x$, which has been shown earlier. Note that we do not use upwind differences here since it will introduce a lot more numerical diffusion due to the lower order. This would completely invalidate the results. Also, central differences of this term on the staggered grid do not exhibit the same instabilities as on the collocated grid.

Much more involved is for example the term $v_z\partial_z v_x$. All other terms follow the same scheme as this one so it will be shown in detail and the reader is advised to trace it on the grid and write down the others by hand. This derivative looks like this

$$
\begin{aligned}
v_z\partial_z v_x &\approx \frac{\frac{1}{2}\left(v_{z,ijk} + v_{z,i-1jk}\right) + \frac{1}{2}\left(v_{z,ijk+1} + v_{z,i-1jk+1}\right)}{2}\frac{v_{x,ijk+1} - v_{x,ijk-1}}{2\Delta z} \\
&= v_{z,i-\frac{1}{2}jk+\frac{1}{2}}\frac{\frac{1}{2}\left(v_{x,ijk} + v_{x,ijk+1}\right) - \frac{1}{2}\left(v_{x,ijk} + v_{x,ijk-1}\right)}{\Delta z} \\
&= v_{z,i-\frac{1}{2}jk+\frac{1}{2}}\frac{v_{x,ijk+\frac{1}{2}} - v_{x,ijk-\frac{1}{2}}}{\Delta z}
\end{aligned}
\tag{7.14}
$$

with grid spacing Δz. Yes, you have counted correctly. There are 5 interpolations and 4 v_z points needed for this monstrosity. Fortunately, this is as complicated as it can get with the staggered grid.

An educated reader might have noticed the use of half grid spacings in the indices for example $v_{z,i-\frac{1}{2}jk+\frac{1}{2}}$. This notational convention has been chosen because CUDA as the chosen acceleration language has the possibility to perform the interpolations during a single memory fetch operation, which speeds up the calculations. This will be explained in a later chapter about CUDA namely the Section 7.3.

There is one more term, which is a bit complicated. It is the heating term in the temperature equation, which has derivatives of the velocity onto the scalar grid. This term can be simplified before finite differences are applied. That term and some more simplification will be discussed in the Section 7.4.

7.2.3 Boundary conditions

Usually it is enough to state the boundary conditions as done in Section 2.2.3. Here, the two different types of grids especially the staggered grid proves difficult to implement all of the conditions. Therefore, they will be reiterated here with much more detail about the numerical implementation.

The easiest ones are the periodic conditions because the numeric implementation is identical for both grids. The first point is connected to the last point hence it has a neighbour to the side outside of the domain. Any difference at the boundary requires the point on the other side.

Fixed boundary conditions are also more easily implemented. The collocated grid has values on the boundary, which need to be set. Derivatives on the boundary need a point outside, which was called the halo point on Section 7.1. This point has to reflect the boundary condition meaning that some set value like zero temperature has to be averaged

$$
\begin{aligned}
& T\left(z=1\right) = 0 \\
\Rightarrow & \frac{1}{2}\left(T\left(z=1+\Delta z\right) + T\left(z=1-\Delta z\right)\right) = T\left(z=1\right)) \\
\Rightarrow & T\left(z=1+\Delta z\right) = -T\left(z=1-\Delta z\right).
\end{aligned}
\tag{7.15}
$$

This is the same for the other directions and is also the implementation for the no slip velocity boundary conditions. Larger stencils like the ones for the collocated grid set the other points in the same way. The average of the points around the boundary has to be the boundary value.

This is even true for the staggered grid were no direct boundary value exists for most fields. The average of the value close to the boundary and the one beyond has to be the boundary value. All velocities have at least one grid point on the boundary and one or two close to it.

The last boundary condition is the free slip or no flux boundary condition. This one sets the gradient to a specific value hence the halo points can be set by applying the finite differences. The implementation on the collocated grid is shown with a boundary in the

x direction

$$\partial_x T|_{x=0} = 0$$
$$\Rightarrow \frac{T_{i+1j} - T_{i-1j}}{2\Delta x}|_{i=0} = 0$$
$$\Rightarrow \frac{T_{1j} - T_{-1j}}{2\Delta x} = 0$$
$$\Rightarrow T_{-1j} = T_{1j}. \tag{7.16}$$

An implementation on the staggered grid is similar and left to the reader as an exercise. Larger stencils are handled similarly with points further into the domain.

The density has no direct boundary conditions as stated in Section 2.2.3. No flux boundaries can be set but there is an alternative. It is possible to simply extrapolate the density into the top and bottom wall simulating a portion of a larger domain and setting the side wall to no flux boundaries. This would ensure that the derivatives close to the boundary would not produce strange behaviours.

7.3 CUDA enhancements and programming philosophy

The reasons for using GPU acceleration has been explained in Section 2.3 with some detail. This chapter is about tips and tricks that the author used while working on this simulation as well as some general introduction into the concepts of GPU programming. Specifically, how to extract the most performance out of the acceleration since the main goal of using a GPU instead of CPU is to increase the number of time steps per second of compute time (as well as increasing the efficiency of electrical power per time step since GPUs are very energy efficient). Continuing with the bottle filling machine analogy, we will start by looking at memory management and thread distribution. This will also include some basic ideas of how threading and single instruction multiple data (SIMD) works on an GPU. Afterwards, we will look into how to set the boundary conditions as well as some limitations of GPU computing with problems like volume integrals. Finally, some remarks on the general programming philosophy, future potential and handling multiple GPUs will close this guide. The actual programming is covered in the programming guides and will differ between for example CUDA and OpenCL.

There exist tools that compute performance counters and aid in improving the efficiency of the code. For CUDA it is called "nsight", which is an invaluable tool in tracing memory leaks and finding under performing kernel calls. It is recommended to test

kernels with different sizes of thread blocks and memory alignment with this tool to optimize the thread arrangement and therefore the GPU utilization.

7.3.1 Memory and threads of a GPU

The analogy of the bottle filling machine is a simple example for an accelerated 1D problem. This is exactly the type of problem to be solved during the update step of the RK3 algorithm. A memory location has to be read, multiplied with some constants and written back into a different memory location. A CPU would simply do all this very fast. A GPU needs a bit more work.

GPUs contain many processor cores (about 10 for most) called streaming multiprocessors (SM). One SM has many arithmetic units, mostly 32 or 64 and some local cache. This means that one SM can perform the same computations on 32 memory locations at the same time, which are called threads. These 32 threads are called a warp and a block of threads consists of multiple warps. Under filling a warp is not recommended and will cost performance, which is why powers of two are recommended as a good memory size. Each warp steps through the code simultaneously until a synchronization barrier or the end of the routine is reached. At that point the next warp is loaded and steps through the program. This abstraction allows for the high compute utilization (usage of all cores and units) but strains the memory bandwidth. Especially the new gaming oriented GPUs have very high core counts but the memory cannot keep up.

This is exactly the reason why strong emphasis lies on memory fetching, caching and linear usage. Looking at the finite differences shown in Section 7.2 it becomes evident that a single memory location is needed a few times. For example the velocity $v_{x,ijk}$ is needed for itself in the Laplace term and others as well as for the other velocity components in the advection term. Therefore, it is beneficial to cache this value locally in the L2 cache. This allows the SM to reach this value much quicker because the global memory is accessed by all SM and the local cache by only one. Additionally, the L2 cache is a faster but smaller memory type compared to the global one. In CUDA terms, it is called the shared memory because it is shared between threads of a warp and also among many warps of a thread block executed on a single SM. This cache can be allocated and loaded manually, which most programs do during the initialization of a GPU kernel.

An alternative approach to manually loading the L2 cache is to use the texture pipeline. This pipeline is especially fast in gaming GPUs. The texture pipeline is a specific memory fetcher that can fetch and cache memory locations to L2 and has a simple in-

terface for addressing the memory. A very useful feature of the texture fetching is the interpolation between memory location. Using a staggered grid arrangement requires interpolations between memory locations, which the texture pipeline can perform within a single memory fetch operation especially if both values to be interpolated are already cached. Additionally, it can handle out of bounds points and either mirror back into the volume for free- and no-slip boundary conditions as well as periodically close the boundary. Care must be taken during the update step because the memory bound to the texture reference can only be written using a surface object in CUDA.

Another method of caching is the constant memory. It works similarly to the texture pipeline but uses only single values. This is especially useful for constant factors like Ra or Pr but also the $1/\Delta x$ values, which are needed for almost all calculations. Declaring these values as constants allows each SM to load them into the L2 cache and access them faster, which reduces fetching time compared to hard coding these values.

Fetching and caching are only half of the important considerations about memory handling. Much more important is memory alignment. A warp can execute most efficiently if the memory locations to be accessed are linearly aligned one after the other. Striding across the memory as well as loading unordered will slow down the memory fetcher and therefore the entire execution of the program on all SM. It is always good practice to have a linearly aligned memory and address it using pointer or address arithmetic. For example a 3D volume with dimensions N_x, N_y and N_z can be aligned linearly and addressed by this formula for a position

$$r\left(i_x, i_y, i_z\right) = i_z + i_y \times N_z + i_x \times N_z \times N_y. \tag{7.17}$$

Looking closely at this equation reveals that the z-direction (index i_z) is addressed linearly in memory. The y-directions (index i_y) consists of jumps over N_z data points and strides in lines. Finally, the x-directions (index i_x) consists of jumps over $N_z \times N_y$ data points and strides in planes.

The addressing of the threads has to mirror this memory alignment meaning that the fast changing index that addresses inside a warp (most often the first) has to address the z-direction and the second the y-direction. The third dimension is handled differently since it is more efficient to keep planes in memory and only load the next plane once the current one is done computing. This saves memory and allows the SM to better schedule the warps of a block that computes the same plane. An example would be to load a single x-plane as well as the neighbouring planes (called halo planes) in order to compute the finite differences. After this plane is computed (which might involve multiple warps) a memory roll on these planes is performed rolling the next plane into computation,

rolling out the halo plane that is no longer needed and fetching the next plane to be used for the halo. This trick keeps the warp count small and reuses as much memory in cache as possible. The shape of this plane is not yet assigned and it is advisable to stretch is as far as possible in z-direction to optimize memory access.

A simple representation of the memory alignment can be found in Figure 7.2. The
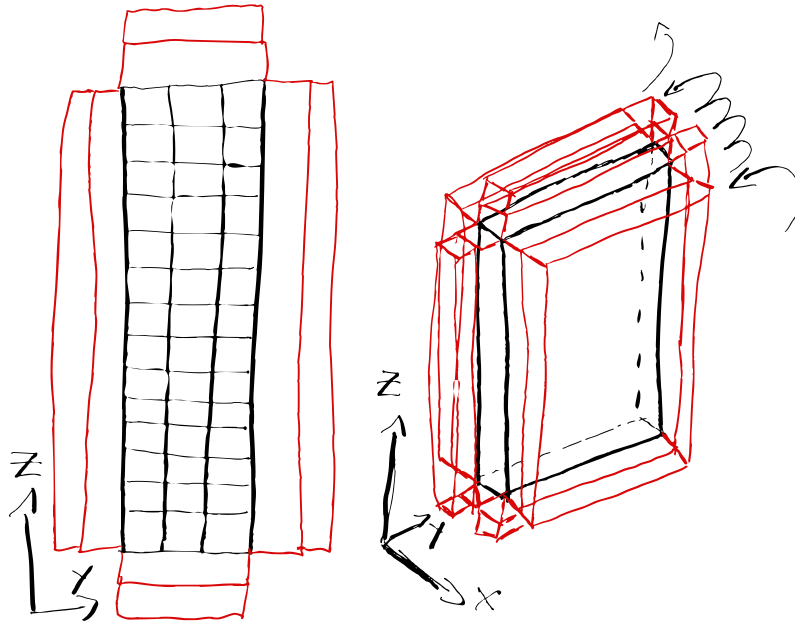
Figure 7.2: Shown are two sketches of the memory layout for the computation kernel. The computation domain is marked black and the halo domain is marked red. On the left, you can see a single 2D plane of the x-direction. On the right, you can see the 3D memory layout with the memory rolling indicated by arrows.

halo is marked in red and the current computation plane is black. On the left, you can see the 2D memory alignment of a single plane in the x-direction with a HS of two on each side. On the right, you can see the 3D memory alignment with the planes in the x-direction highlighted, as well as the memory roll indicated by arrows.

To illustrate this in an example we choose $N_x = N_y = 256$ and $N_z = 512$ with finite differences of second order meaning that we need one halo point in each direction. We are neglecting boundary effects here since those will be reviewed in the next Section 7.3.2. An efficient choice is to fill one warp with only linear memory. Therefore the first thread count is 32 in this example and the second thread count can be 2, 4 or 8

in order to reuse as much cached memory as possible without overflowing. The block size is chosen to have one thread for each point in the $N_y \times N_z$ plane meaning that we have 16 blocks of threads in z-direction and between 128 and 32 blocks of threads in y-direction. Each thread loads the memory location assigned to it and all threads that are on the boundary of the domain must load one or two additional halo points. All warps are synchronized after the loading phase to ensure that all data is loaded in time. Afterwards, the warps perform the same operation for the two halo planes required. Once the memory is loaded the computations can run and all warps are again synchronized after completion. The cached planes are then swapped or rolled in memory, the next one loaded and the local i_x index increased for the next computation. This loop continues until all planes are computed. The memory rolling is not required in 2D but could also be applied depending on the size of the domain. These are the basics of thread and memory alignment as well as thread scheduling. How to actually implement these ideas depends on the chosen language.

7.3.2 Boundary conditions

This section portrays two different approaches to handling the boundary conditions. The first is straight forward but costs performance and the second one is more difficult to implement but is executed in the main kernel. Both implement the algorithm explained in Section 7.2.3.

The easiest algorithm to implement extends the global memory in all directions with enough points for the halo (called HS for halo size). This means that the number of points are $N_x + 2HS$, $N_y + 2HS$ and $N_z + 2HS$ in the equation (7.17). Three kernel routines are required to set all these halo points once the volume is ready for the next computation. Each of them sets a $2HS$ plane of values on all faces of the volume. Especially the kernel setting the boundary conditions in x-direction will stride heavily. Additionally, there is an overhead for calling three rather short kernels (compared to the main kernel) to run at each RK step. The main kernel only needs to read from memory without much divergence between threads and no computation of boundaries is needed. The divergence of threads means that some threads within a warp need to execute different instructions compared to the rest leading to threads waiting within a warp. This version worked best on old hardware were the branch prediction as well as thread management was not fully optimized.

Modern GPUs have a much better possibility by setting the boundary conditions in

local shared memory. The idea is the same and the main kernel checks if a thread has out of bounds neighbours and sets their halo according to the boundary condition algorithm. The main idea is that all points outside of the domain are already existing points either mirrored with or without sign change or they are from the other wall in case of periodic boundaries. Especially the z-boundaries are handled more efficiently because the thread at the boundary has already loaded the points needed from global memory and only needs to copy or copy and change sign. The same applies to the y-direction with some additional memory fetching in case of periodic boundary conditions. Only the x-direction might need special handling in case it is spread over multiple devices, which is not handled here. Otherwise, it works in the same way as the y-direction.

This version has the additional benefit of a power of two in the number of memory locations occupied. Unfortunately, care must be taken if any variable is accessed using the texture pipeline. As explained earlier, the texture pipeline can handle boundary conditions especially periodic ones very easily. Also free-slip boundary conditions are easy to compute because no sign change is required. The mirror condition in CUDA works on the last point so the mirror point of the boundary point is the boundary point itself. Some short index manipulation can be applied to get the point further out. No-slip boundary conditions as well as the fixed temperature conditions do require a sign change. This has to be handled separately with an additional bit that is set for all points and is multiplied as a sign to all computations with only the signs for the boundary conditions flipped. Some programming and memory overhead as well as thread divergence is created this way but the benefits of removing the three additional kernels as well as using the texture pipeline outweigh the overhead. Some more optimization could be found here by implementing a sign reversion during the memory fetch as a feature of the texture pipeline.

7.3.3 Volume integrals

Examples for volume integrals are the calculation of the kinetic energy density and for area integrals the computation of the Nusselt number or performing horizontal averaging. All of these computations are reduction algorithms, which take a set of memory locations and add them to a scalar. This is very challenging for a GPU to compute because it is not truly parallel since all threads write to a single memory location.

There are recursive algorithms that maintain some performance on the GPU but are still not the best solution since they could exhibit data hazards if implemented incorrectly.

It is more efficient to shift all the volumes back down from the GPU and perform these operations on the CPU. This has the benefit of including the CPU in the calculation, decoupling the memory locations and computing all integrals independently without blocking the GPU. The GPU can go on computing more time steps while the CPU is utilized with an additional thread (additional to the one managing the kernel calls) that computes all averages and also handles the writing to file. Some future direct storage algorithms might allow the GPU to write to disk directly but this is not tested as of the time of writing.

Therefore it is beneficial to perform these calculations on the CPU, especially if a very efficient file handling algorithm like HDF5[1] is used. HDF5 is designed to store data tables in a relatable and annotate able data format. Additionally, it allows for compression and sliced reading and writing meaning that not the entire dataset has be read or written. This comes in handy if the entire volume or some slice is saved to disk for an animation or some later computation.

7.3.4 General programming philosophy

Running computations on a GPU always requires a code executing on the CPU, transferring data and calling the kernel in the correct order. The author has the policy of writing a program that is compiled once and stands alone with a single file as output that contains all information needed to run the simulations. This is achieved by passing the parameters for the simulation like number of points, time step size or the physical parameters Ra, Pr and others as command line parameters. The HDF5 output file includes the initial fields, which contain all important parameters as attributes. The initial fields are overwritten at the end of the time loop as restart conditions. This ensures that the simulation can be restarted without further information. Also future improvements of the finite differences or the kernel can be compiled into the program and older simulation data can be continued without data loss.

The HDf5 file format also allows for the file being kept open for writing by a single process but other processes can open the file read only and extract data during the run time. This is helpful for plotting time dependent data like the kinetic energy or the Nusselt number in order to judge the progress of the simulation.

---

[1] https://www.hdfgroup.org/solutions/hdf5/ checked on 31.01.2023

7.3.5 Future changes and multi GPU

The code in its most efficient version is only able to calculate the 2D flow fields. Future improvement have to include the ability to compute volume data, which needs a new kernel. Also, advancements in AI research introduced so called tensor cores, which are highly efficient matrix computing devices. An implementation of these as well as the so called ray tracing cores could also benefit the performance of this code, because these modules are currently unused.

Running 3D simulations has one major problem because a lot more global memory is needed for the volume. Usually GPUs do not have much in terms of global memory, early models have $3\,\mathrm{GB}$ and newer models a maximum of $80\,\mathrm{GB}$. Therefore, it is required to use multiple devices if the sum of all volumes extends beyond this size. Additionally, it is beneficial to split the work load across multiple devices even if one card can hold all of the volumes for additional speed up.

Fortunately, current GPU can communicate with each other and access each other memory, which is especially useful with the unified memory model. This model allows for one pointer to extend and address multiple GPUs. The memory fetcher can be told what portion of memory is on what device and can therefore fetch the required memory from other cards if it is needed. This is especially important because no extra memory transfer has to be initiated by the CPU.

A good candidate for splitting is one of the horizontal directions, say the x-direction for simplicity. For example, a two GPU system splits the volume in two in the middle of the x-direction and all threads that need memory from beyond the cut simply fetch it over the fastest link between the GPU. This is handled automatically by the GPU driver and the memory fetcher. All the programmer has to do is to allow the access and assign each portion of the pointer to the devices.

These are some of the general ideas, which were implemented in the simulation used for this work. Implementing these takes a lot more knowledge about the programming environment and compilers. Hopefully, these few concepts are a good starting point for further studies of the actual programming guides, which are much more detailed and can be a bit confusing without some basic understanding.

112

7.4 Computing the heating term and other simplifications

Solving equations (2.14) and (2.15) is as simple as using the finite difference operators shown in Section 7.2. Solving equations (2.23) and (2.24) is less straight forward because of additional terms that need to be handled. One additional term is the gradient of the velocity divergence $\boldsymbol{\nabla}\left(\boldsymbol{\nabla}\cdot\mathbf{v}\right)$. There are two ways to handle this term. The first is to compute the divergence separately and use this value to compute the gradient, which would mean that some kind of boundary condition is required. Continuing with what was discussed in Section 7.3, this could be achieved in an additional kernel and an additional volume variable that saves this divergence. This kernel would need to be called before each RK step. An appropriate boundary condition would be the no flux boundaries meaning that the gradient of the divergence at all walls is zero. This version costs performance because an additional kernel has to be started, which runs through an entire cycle of fetching memory, computing and saving back, more global memory is required and boundary conditions need to be applied.

The second way to compute this term would be to split the gradient into components and compute them in the main loop. One of the terms can be added to the Laplace of the velocity and the others are mixed second derivatives for example

$$
\begin{aligned}
\boldsymbol{\nabla}\left(\boldsymbol{\nabla}\cdot\mathbf{v}\right)|_x &= \partial_x\left(\partial_x v_x + \partial_y v_y + \partial_z v_z\right) \\
&= \partial_x^2 v_x + \partial_x\partial_y v_y + \partial_x\partial_z v_z.
\end{aligned}
\tag{7.18}
$$

This way does not need additional global memory and most of these components are cached because they are needed elsewhere. The mixed derivatives can also be expressed in finite differences, which is repetition on a collocated grid and would look like this for a staggered grid

$$
\partial_x\partial_z v_z = \frac{\left(v_{z,ijk+1} - v_{z,ijk}\right)\frac{1}{\Delta z} - \left(v_{z,i-1jk+1} - v_{z,i-1jk}\right)\frac{1}{\Delta z}}{\Delta x}.
\tag{7.19}
$$

Other components are handled similarly. Only one additional value needs to be cached for this operation.

The other additional term is the viscous heating in equation (2.24), which also involves the divergence of the velocity and some mixed derivatives. With some algebra it can be

simplified

$$\left[\frac{1}{2}\left(\partial_j v_i + \partial_i v_j\right) - \frac{1}{3}\boldsymbol{\nabla}\cdot\mathbf{v}\delta_{ij}\right]^2 = \left(\partial_x v_x - \frac{1}{3}\boldsymbol{\nabla}\cdot\mathbf{v}\right)^2 + \frac{1}{2}\left(\partial_x v_y + \partial_y v_x\right)^2$$
$$+ \left(\partial_y v_y - \frac{1}{3}\boldsymbol{\nabla}\cdot\mathbf{v}\right)^2 + \frac{1}{2}\left(\partial_x v_z + \partial_z v_x\right)^2$$
$$+ \left(\partial_z v_z - \frac{1}{3}\boldsymbol{\nabla}\cdot\mathbf{v}\right)^2 + \frac{1}{2}\left(\partial_y v_z + \partial_z v_y\right)^2. \tag{7.20}$$

All of these derivatives have been demonstrated before.

7.5 Tables

Ra	c^2	N_x	N_z	Nu	E_{kin}	Pe	Re	Ro
4.00×10^4	1.00×10^7	256	256	6.32	1.55×10^3	5.56×10^1	7.95×10^1	0.00
1.00×10^5	1.00×10^7	256	256	1.14×10^1	5.37×10^3	1.04×10^2	1.48×10^2	0.00
4.00×10^5	2.00×10^8	256	256	1.56×10^1	1.89×10^4	1.94×10^2	2.77×10^2	0.00
1.00×10^6	1.00×10^9	128	256	1.93×10^1	4.23×10^4	2.90×10^2	4.16×10^2	0.00
1.00×10^6	2.50×10^8	256	256	1.93×10^1	4.24×10^4	2.91×10^2	4.16×10^2	0.00
1.00×10^6	1.00×10^9	256	512	1.96×10^1	4.26×10^4	2.92×10^2	4.17×10^2	0.00
4.00×10^6	5.00×10^9	256	512	2.64×10^1	1.36×10^5	5.20×10^2	7.46×10^2	0.00
1.00×10^7	1.00×10^9	256	512	3.31×10^1	3.08×10^5	7.82×10^2	1.12×10^3	0.00
4.00×10^7	1.00×10^{10}	256	512	4.68×10^1	1.04×10^6	1.44×10^3	2.06×10^3	0.00
1.00×10^8	1.00×10^{10}	256	1024	6.28×10^1	2.39×10^6	2.18×10^3	3.12×10^3	0.00
4.00×10^8	1.00×10^{11}	512	2048	9.40×10^1	7.98×10^6	3.99×10^3	5.71×10^3	0.00

Table 7.1: 3D simulation results from Chapter 3 for $\mathrm{Ek} = \infty$.

Ra	c^2	N_x	N_z	Nu	E_{kin}	Pe	Re	Ro
1.00×10^4	1.00×10^7	128	128	3.34	2.37×10^2	2.18×10^1	3.11×10^1	2.80
2.00×10^4	1.00×10^7	128	128	4.60	7.24×10^2	3.80×10^1	5.44×10^1	4.89
3.00×10^4	1.00×10^7	128	128	5.49	1.34×10^3	5.18×10^1	7.40×10^1	6.66
4.00×10^4	1.00×10^7	128	128	6.24	2.07×10^3	6.44×10^1	9.20×10^1	8.28
5.00×10^4	1.00×10^7	128	128	6.90	2.89×10^3	7.60×10^1	1.09×10^2	9.77
6.00×10^4	1.00×10^7	128	128	7.81	3.70×10^3	8.60×10^1	1.23×10^2	1.11×10^1
7.00×10^4	1.00×10^9	128	256	8.40	4.61×10^3	9.60×10^1	1.37×10^2	1.23×10^1
8.00×10^4	1.00×10^9	128	256	9.58	5.32×10^3	1.03×10^2	1.47×10^2	1.33×10^1
9.00×10^4	1.00×10^9	128	256	1.09×10^1	4.62×10^3	9.62×10^1	1.37×10^2	1.24×10^1
9.00×10^4	1.00×10^{10}	128	256	1.05×10^1	5.92×10^3	1.09×10^2	1.55×10^2	1.40×10^1
1.00×10^5	1.00×10^9	128	256	1.13×10^1	5.21×10^3	1.02×10^2	1.46×10^2	1.31×10^1

Table 7.2: 3D simulation results from Chapter 3 for $\mathrm{Ek} = 9\times10^{-2}$.

Ra	c^2	N_x	N_z	Nu	E_{kin}	Pe	Re	Ro
2.00×10^4	1.00×10^7	128	256	4.61	7.24×10^2	3.81×10^1	5.44×10^1	3.26
3.00×10^4	1.00×10^7	128	256	5.51	1.34×10^3	5.18×10^1	7.41×10^1	4.44
4.00×10^4	1.00×10^7	128	256	6.26	2.07×10^3	6.44×10^1	9.20×10^1	5.52
5.00×10^4	1.00×10^7	128	256	6.92	2.89×10^3	7.60×10^1	1.09×10^2	6.51
6.00×10^4	1.00×10^7	128	128	7.74	3.72×10^3	8.63×10^1	1.23×10^2	7.39
7.00×10^4	1.00×10^9	128	256	8.35	4.58×10^3	9.57×10^1	1.37×10^2	8.21
8.00×10^4	1.00×10^9	128	256	9.40	5.45×10^3	1.04×10^2	1.49×10^2	8.95
9.00×10^4	1.00×10^9	128	256	1.08×10^1	4.56×10^3	9.55×10^1	1.36×10^2	8.18
9.00×10^4	1.00×10^{10}	128	256	9.77	6.42×10^3	1.13×10^2	1.62×10^2	9.71
1.00×10^5	1.00×10^9	128	256	1.12×10^1	5.11×10^3	1.01×10^2	1.44×10^2	8.67

Table 7.3: 3D simulation results from Chapter 3 for Ek $= 6 \times 10^{-2}$.

Ra	c^2	N_x	N_z	Nu	E_{kin}	Pe	Re	Ro
1.50×10^4	1.00×10^7	128	128	4.06	4.62×10^2	3.04×10^1	4.34×10^1	1.74
2.00×10^4	1.00×10^7	128	128	4.61	7.24×10^2	3.81×10^1	5.44×10^1	2.17
3.00×10^4	1.00×10^7	128	128	5.49	1.34×10^3	5.18×10^1	7.40×10^1	2.96
4.00×10^4	1.00×10^7	128	128	6.24	2.07×10^3	6.44×10^1	9.19×10^1	3.68
5.00×10^4	1.00×10^7	128	128	6.89	2.89×10^3	7.60×10^1	1.09×10^2	4.34
6.00×10^4	1.00×10^7	128	128	7.61	3.75×10^3	8.66×10^1	1.24×10^2	4.95
7.00×10^4	1.00×10^9	128	256	8.34	4.50×10^3	9.49×10^1	1.36×10^2	5.42
8.00×10^4	1.00×10^9	128	256	9.33	5.34×10^3	1.03×10^2	1.48×10^2	5.91
9.00×10^4	1.00×10^9	128	256	1.07×10^1	4.45×10^3	9.43×10^1	1.35×10^2	5.39
1.00×10^5	1.00×10^9	128	256	1.10×10^1	4.98×10^3	9.98×10^1	1.43×10^2	5.70

Table 7.4: 3D simulation results from Chapter 3 for Ek $= 4 \times 10^{-2}$.

Ra	c^2	N_x	N_z	Nu	E_{kin}	Pe	Re	Ro
2.00×10^4	1.00×10^7	128	128	4.61	7.25×10^2	3.81×10^1	5.44×10^1	1.09
3.00×10^4	1.00×10^7	128	128	5.50	1.34×10^3	5.19×10^1	7.41×10^1	1.48
4.00×10^4	1.00×10^7	128	128	6.24	2.07×10^3	6.44×10^1	9.20×10^1	1.84
5.00×10^4	1.00×10^7	128	128	6.89	2.89×10^3	7.60×10^1	1.09×10^2	2.17
6.00×10^4	1.00×10^7	128	128	7.47	3.78×10^3	8.69×10^1	1.24×10^2	2.48
7.00×10^4	1.00×10^9	128	256	8.32	4.57×10^3	9.56×10^1	1.37×10^2	2.73
8.00×10^4	1.00×10^9	128	256	8.99	5.54×10^3	1.05×10^2	1.50×10^2	3.01
9.00×10^4	1.00×10^9	128	256	1.04×10^1	4.29×10^3	9.26×10^1	1.32×10^2	2.65
1.00×10^5	1.00×10^9	128	256	1.07×10^1	4.69×10^3	9.69×10^1	1.38×10^2	2.77

Table 7.5: 3D simulation results from Chapter 3 for Ek $= 2 \times 10^{-2}$.

Ra	c^2	N_x	N_z	Nu	E_{kin}	Pe	Re	Ro
4.00×10^4	1.00×10^7	128	128	6.24	2.07×10^3	6.44×10^1	9.19×10^1	9.19×10^{-1}
5.00×10^4	1.00×10^7	128	128	6.89	2.89×10^3	7.60×10^1	1.09×10^2	1.09
6.00×10^4	1.00×10^7	128	128	7.47	3.78×10^3	8.69×10^1	1.24×10^2	1.24
7.00×10^4	1.00×10^9	128	256	8.07	4.66×10^3	9.66×10^1	1.38×10^2	1.38
8.00×10^4	1.00×10^9	128	256	8.78	5.62×10^3	1.06×10^2	1.51×10^2	1.51
9.00×10^4	1.00×10^9	128	256	1.02×10^1	4.36×10^3	9.33×10^1	1.33×10^2	1.33
1.00×10^5	1.00×10^9	128	256	1.04×10^1	4.68×10^3	9.68×10^1	1.38×10^2	1.38
1.50×10^5	1.00×10^9	128	256	1.17×10^1	6.36×10^3	1.13×10^2	1.61×10^2	1.61
2.00×10^5	1.00×10^9	128	256	1.34×10^1	9.06×10^3	1.35×10^2	1.92×10^2	1.92
4.00×10^5	5.00×10^7	256	256	1.67×10^1	2.06×10^4	2.03×10^2	2.90×10^2	2.90
1.00×10^6	1.00×10^8	256	256	1.99×10^1	4.35×10^4	2.94×10^2	4.21×10^2	4.21
4.00×10^6	2.50×10^8	256	256	2.61×10^1	1.39×10^5	5.25×10^2	7.52×10^2	7.52
1.00×10^7	1.00×10^9	256	512	3.29×10^1	3.02×10^5	7.75×10^2	1.11×10^3	1.11×10^1
4.00×10^7	5.00×10^9	256	512	4.68×10^1	1.01×10^6	1.42×10^3	2.03×10^3	2.03×10^1
1.00×10^8	1.00×10^{10}	256	1024	6.28×10^1	2.36×10^6	2.17×10^3	3.10×10^3	3.10×10^1

Table 7.6: 3D simulation results from Chapter 3 for Ek $= 10^{-2}$.

Ra	c^2	N_x	N_z	Nu	E_{kin}	Pe	Re	Ro
6.00×10^4	1.00×10^7	128	128	7.47	3.77×10^3	8.69×10^1	1.24×10^2	8.69×10^{-1}
7.00×10^4	1.00×10^7	128	128	7.99	4.73×10^3	9.72×10^1	1.39×10^2	9.72×10^{-1}
8.00×10^4	5.00×10^7	128	256	8.51	5.71×10^3	1.07×10^2	1.53×10^2	1.07
9.00×10^4	1.00×10^9	128	256	8.94	6.65×10^3	1.15×10^2	1.65×10^2	1.15
1.00×10^5	1.00×10^9	128	256	9.36	7.75×10^3	1.24×10^2	1.78×10^2	1.24
1.50×10^5	1.00×10^9	128	256	1.16×10^1	6.38×10^3	1.13×10^2	1.61×10^2	1.13
2.00×10^5	1.00×10^9	128	256	1.37×10^1	1.09×10^4	1.47×10^2	2.11×10^2	1.47
3.00×10^5	5.00×10^7	128	256	1.53×10^1	1.56×10^4	1.77×10^2	2.53×10^2	1.77
4.00×10^5	5.00×10^7	128	128	1.56×10^1	2.00×10^4	2.00×10^2	2.86×10^2	2.00
7.00×10^5	1.00×10^8	128	128	1.71×10^1	2.99×10^4	2.44×10^2	3.49×10^2	2.45
1.00×10^6	2.50×10^8	128	128	1.81×10^1	4.10×10^4	2.86×10^2	4.09×10^2	2.86
4.00×10^6	5.00×10^8	256	256	2.62×10^1	1.38×10^5	5.23×10^2	7.49×10^2	5.24

Table 7.7: 3D simulation results from Chapter 3 for Ek $= 7 \times 10^{-3}$.

Ra	c^2	N_x	N_z	Nu	E_{kin}	Pe	Re	Ro
6.00×10^4	1.00×10^7	128	128	7.47	3.77×10^3	8.69×10^1	1.24×10^2	6.20×10^{-1}
7.00×10^4	1.00×10^7	128	128	7.99	4.73×10^3	9.72×10^1	1.39×10^2	6.94×10^{-1}
8.00×10^4	5.00×10^7	128	256	8.51	5.71×10^3	1.07×10^2	1.53×10^2	7.63×10^{-1}
9.00×10^4	5.00×10^7	128	256	8.95	6.76×10^3	1.16×10^2	1.66×10^2	8.30×10^{-1}
1.00×10^5	1.00×10^{10}	256	512	9.07	7.33×10^3	1.21×10^2	1.73×10^2	8.65×10^{-1}
1.50×10^5	1.00×10^{10}	256	512	1.10×10^1	1.26×10^4	1.59×10^2	2.27×10^2	1.13
2.00×10^5	1.00×10^9	128	256	1.28×10^1	9.03×10^3	1.34×10^2	1.92×10^2	9.60×10^{-1}
2.00×10^5	1.00×10^{10}	256	512	1.26×10^1	8.56×10^3	1.31×10^2	1.87×10^2	9.35×10^{-1}
3.00×10^5	1.00×10^9	128	256	1.42×10^1	1.20×10^4	1.55×10^2	2.22×10^2	1.11
3.00×10^5	1.00×10^{10}	256	512	1.42×10^1	1.19×10^4	1.55×10^2	2.21×10^2	1.10

Table 7.8: 3D simulation results from Chapter 3 for Ek $= 5 \times 10^{-3}$.

Ra	c^2	N_x	N_z	Nu	E_{kin}	Pe	Re	Ro
9.00×10^4	1.00×10^7	128	256	8.97	6.80×10^3	1.17×10^2	1.67×10^2	5.00×10^{-1}
1.00×10^5	1.00×10^9	256	512	9.30	7.60×10^3	1.23×10^2	1.76×10^2	5.28×10^{-1}
1.50×10^5	1.00×10^{10}	256	512	1.09×10^1	1.23×10^4	1.57×10^2	2.24×10^2	6.73×10^{-1}
2.00×10^5	1.00×10^{10}	256	512	1.21×10^1	1.88×10^4	1.94×10^2	2.77×10^2	8.30×10^{-1}
3.00×10^5	1.00×10^{10}	256	512	1.48×10^1	1.42×10^4	1.69×10^2	2.41×10^2	7.23×10^{-1}
4.00×10^5	1.00×10^{10}	256	512	1.52×10^1	1.69×10^4	1.84×10^2	2.63×10^2	7.89×10^{-1}
7.00×10^5	1.00×10^8	128	128	1.62×10^1	2.62×10^4	2.29×10^2	3.27×10^2	9.80×10^{-1}
1.00×10^6	2.50×10^8	128	128	1.76×10^1	4.00×10^4	2.82×10^2	4.04×10^2	1.21
4.00×10^6	5.00×10^8	256	256	2.60×10^1	1.32×10^5	5.13×10^2	7.34×10^2	2.20

Table 7.9: 3D simulation results from Chapter 3 for Ek $= 3 \times 10^{-3}$.

Ra	c^2	N_x	N_z	Nu	E_{kin}	Pe	Re	Ro
1.00×10^5	5.00×10^7	128	256	9.37	7.84×10^3	1.25×10^2	1.79×10^2	3.58×10^{-1}
1.50×10^5	1.00×10^9	128	256	1.11×10^1	1.36×10^4	1.65×10^2	2.35×10^2	4.71×10^{-1}
2.00×10^5	1.00×10^9	128	256	1.24×10^1	2.03×10^4	2.01×10^2	2.88×10^2	5.75×10^{-1}
3.00×10^5	1.00×10^9	128	256	1.55×10^1	1.91×10^4	1.96×10^2	2.79×10^2	5.59×10^{-1}
3.00×10^5	5.00×10^7	128	256	1.55×10^1	1.92×10^4	1.96×10^2	2.80×10^2	5.59×10^{-1}
4.00×10^5	1.00×10^9	128	256	1.62×10^1	2.86×10^4	2.39×10^2	3.42×10^2	6.83×10^{-1}

Table 7.10: 3D simulation results from Chapter 3 for Ek $= 2 \times 10^{-3}$.

Ra	c^2	N_x	N_z	Nu	E_{kin}	Pe	Re	Ro
1.00×10^5	1.00×10^7	256	256	9.33	7.81×10^3	1.25×10^2	1.78×10^2	1.78×10^{-1}
2.00×10^5	1.00×10^8	256	512	1.25×10^1	2.03×10^4	2.01×10^2	2.88×10^2	2.88×10^{-1}
2.50×10^5	1.00×10^9	128	256	1.36×10^1	2.71×10^4	2.33×10^2	3.33×10^2	3.33×10^{-1}
3.00×10^5	1.00×10^9	128	256	1.46×10^1	3.47×10^4	2.63×10^2	3.76×10^2	3.76×10^{-1}
3.50×10^5	1.00×10^9	128	256	1.55×10^1	4.31×10^4	2.94×10^2	4.20×10^2	4.20×10^{-1}
4.00×10^5	1.00×10^{10}	256	512	1.61×10^1	4.77×10^4	3.09×10^2	4.41×10^2	4.41×10^{-1}
5.00×10^5	1.00×10^9	256	512	1.89×10^1	3.91×10^4	2.80×10^2	4.00×10^2	4.00×10^{-1}
6.00×10^5	1.00×10^8	256	512	1.99×10^1	4.18×10^4	2.89×10^2	4.13×10^2	4.13×10^{-1}
8.00×10^5	1.00×10^8	256	256	2.04×10^1	5.01×10^4	3.17×10^2	4.52×10^2	4.52×10^{-1}
1.00×10^6	2.50×10^8	256	256	2.15×10^1	5.77×10^4	3.40×10^2	4.85×10^2	4.85×10^{-1}
2.00×10^6	2.50×10^8	256	256	2.40×10^1	9.34×10^4	4.32×10^2	6.17×10^2	6.17×10^{-1}
4.00×10^6	2.50×10^8	256	256	2.68×10^1	1.39×10^5	5.27×10^2	7.54×10^2	7.54×10^{-1}
7.00×10^6	1.00×10^9	256	512	3.03×10^1	2.24×10^5	6.68×10^2	9.56×10^2	9.56×10^{-1}
1.00×10^7	1.00×10^9	256	512	3.30×10^1	3.01×10^5	7.75×10^2	1.11×10^3	1.11
4.00×10^7	5.00×10^9	256	512	4.65×10^1	9.77×10^5	1.40×10^3	2.00×10^3	2.00
1.00×10^8	5.00×10^{10}	512	1024	6.10×10^1	2.13×10^6	2.06×10^3	2.95×10^3	2.95

Table 7.11: 3D simulation results from Chapter 3 for Ek $= 10^{-3}$.

Ra	c^2	N_x	N_z	Nu	E_{kin}	Pe	Re	Ro
4.00×10^5	2.00×10^8	256	256	1.63×10^1	5.23×10^4	3.23×10^2	4.62×10^2	1.85×10^{-1}
5.00×10^5	2.00×10^8	256	256	1.77×10^1	7.08×10^4	3.76×10^2	5.38×10^2	2.15×10^{-1}
6.00×10^5	1.00×10^9	256	256	1.89×10^1	9.07×10^4	4.26×10^2	6.08×10^2	2.43×10^{-1}
7.00×10^5	5.00×10^8	256	512	2.02×10^1	1.10×10^5	4.69×10^2	6.70×10^2	2.68×10^{-1}
8.00×10^5	1.00×10^{10}	128	256	2.10×10^1	1.29×10^5	5.08×10^2	7.26×10^2	2.90×10^{-1}
9.00×10^5	1.00×10^{10}	256	512	2.15×10^1	1.29×10^5	5.08×10^2	7.26×10^2	2.90×10^{-1}
1.00×10^6	1.00×10^{10}	256	512	2.25×10^1	1.53×10^5	5.53×10^2	7.90×10^2	3.16×10^{-1}
1.50×10^6	1.00×10^{10}	128	256	2.50×10^1	1.56×10^5	5.58×10^2	7.98×10^2	3.19×10^{-1}
2.00×10^6	1.00×10^{10}	128	256	2.70×10^1	1.61×10^5	5.68×10^2	8.11×10^2	3.24×10^{-1}
4.00×10^6	1.00×10^9	256	256	2.79×10^1	2.36×10^5	6.87×10^2	9.82×10^2	3.93×10^{-1}
1.00×10^7	5.00×10^9	256	256	3.30×10^1	4.34×10^5	9.31×10^2	1.33×10^3	5.32×10^{-1}
4.00×10^7	1.00×10^{10}	256	512	4.63×10^1	1.12×10^6	1.49×10^3	2.14×10^3	8.54×10^{-1}

Table 7.12: 3D simulation results from Chapter 3 for Ek $= 4 \times 10^{-4}$.

Ra	c^2	N_x	N_z	Nu	E_{kin}	Pe	Re	Ro
1.00×10^5	1.00×10^8	256	256	9.30	7.71×10^3	1.24×10^2	1.77×10^2	1.77×10^{-2}
1.00×10^6	2.50×10^8	256	512	2.32×10^1	1.86×10^5	6.09×10^2	8.71×10^2	8.71×10^{-2}
2.00×10^6	5.00×10^8	256	512	2.96×10^1	4.52×10^5	9.51×10^2	1.36×10^3	1.36×10^{-1}
3.00×10^6	1.00×10^9	256	512	3.42×10^1	7.79×10^5	1.25×10^3	1.78×10^3	1.78×10^{-1}
4.00×10^6	1.00×10^9	256	512	3.52×10^1	8.12×10^5	1.27×10^3	1.82×10^3	1.82×10^{-1}
5.00×10^6	1.00×10^{10}	256	512	3.70×10^1	8.87×10^5	1.33×10^3	1.90×10^3	1.90×10^{-1}
6.00×10^6	2.00×10^9	256	512	3.95×10^1	1.02×10^6	1.43×10^3	2.04×10^3	2.04×10^{-1}
8.00×10^6	2.50×10^9	256	512	4.18×10^1	1.11×10^6	1.49×10^3	2.13×10^3	2.13×10^{-1}
1.00×10^7	2.50×10^9	256	512	4.35×10^1	1.24×10^6	1.57×10^3	2.25×10^3	2.25×10^{-1}
2.00×10^7	5.00×10^9	256	512	4.85×10^1	1.77×10^6	1.88×10^3	2.69×10^3	2.69×10^{-1}
4.00×10^7	5.00×10^9	256	512	5.24×10^1	2.56×10^6	2.26×10^3	3.23×10^3	3.23×10^{-1}
1.00×10^8	1.00×10^{10}	256	1024	6.34×10^1	4.12×10^6	2.87×10^3	4.10×10^3	4.10×10^{-1}

Table 7.13: 3D simulation results from Chapter 3 for Ek $= 10^{-4}$.

Ra	c^2	N_x	N_z	Nu	E_{kin}	Pe	Re	Ro
4.00×10^6	5.00×10^9	256	512	3.79×10^1	1.19×10^6	1.54×10^3	2.20×10^3	8.80×10^{-2}
5.00×10^6	5.00×10^9	128	256	3.60×10^1	3.08×10^5	7.85×10^2	1.12×10^3	4.49×10^{-2}
6.00×10^6	5.00×10^9	128	256	3.87×10^1	3.46×10^5	8.32×10^2	1.19×10^3	4.75×10^{-2}
7.00×10^6	5.00×10^9	128	256	4.09×10^1	4.61×10^5	9.60×10^2	1.37×10^3	5.48×10^{-2}
8.00×10^6	5.00×10^9	128	256	4.18×10^1	4.79×10^5	9.78×10^2	1.40×10^3	5.59×10^{-2}
9.00×10^6	5.00×10^9	256	512	5.06×10^1	2.64×10^6	2.30×10^3	3.28×10^3	1.31×10^{-1}
1.00×10^7	5.00×10^9	256	1024	5.32×10^1	2.68×10^6	2.31×10^3	3.31×10^3	1.32×10^{-1}
2.00×10^7	5.00×10^9	256	1024	5.90×10^1	4.17×10^6	2.89×10^3	4.13×10^3	1.65×10^{-1}

Table 7.14: 3D simulation results from Chapter 3 for Ek $= 4 \times 10^{-5}$.

Ra	N_x	N_z	Nu	E_{kin}	Pe	Re
4.00×10^4	12	24	5.68	2.07×10^3	6.44×10^1	9.20
1.00×10^5	12	24	8.00	7.42×10^3	1.22×10^2	1.74×10^1
1.00×10^6	64	128	1.87×10^1	1.44×10^5	5.36×10^2	7.66×10^1
2.00×10^6	12	24	2.39×10^1	4.11×10^5	9.06×10^2	1.29×10^2
3.00×10^6	12	24	2.99×10^1	7.65×10^5	1.24×10^3	1.77×10^2
4.00×10^6	12	24	3.05×10^1	1.02×10^6	1.43×10^3	2.04×10^2
6.00×10^6	12	24	4.01×10^1	2.05×10^6	2.02×10^3	2.89×10^2
7.00×10^6	12	24	4.27×10^1	2.50×10^6	2.24×10^3	3.20×10^2
8.00×10^6	12	24	4.49×10^1	3.00×10^6	2.45×10^3	3.50×10^2
1.00×10^7	12	24	4.83×10^1	4.07×10^6	2.85×10^3	4.08×10^2
4.00×10^7	12	24	7.92×10^1	2.62×10^7	7.24×10^3	1.03×10^3
1.00×10^8	16	32	1.11×10^2	8.90×10^7	1.33×10^4	1.91×10^3
4.00×10^8	12	24	1.77×10^2	5.72×10^8	3.38×10^4	4.83×10^3
1.00×10^9	16	32	2.43×10^2	2.01×10^9	6.34×10^4	9.05×10^3

Table 7.15: 2D simulation results from Chapter 3 for Pr = 7. These results were collected by Marie-Christine Volk.

Ra	N_x	N_z	Nu	E_{kin}	Pe	Re
1.00×10^4	12	24	3.26	2.37×10^2	2.18×10^1	2.18×10^1
4.00×10^4	12	24	6.00	2.01×10^3	6.34×10^1	6.34×10^1
1.00×10^5	12	24	9.02	7.69×10^3	1.24×10^2	1.24×10^2
1.00×10^6	12	24	2.28×10^1	1.87×10^5	6.11×10^2	6.11×10^2
2.00×10^6	12	24	2.94×10^1	4.75×10^5	9.74×10^2	9.74×10^2
3.00×10^6	12	24	3.41×10^1	8.17×10^5	1.28×10^3	1.28×10^3
4.00×10^6	12	24	3.78×10^1	1.20×10^6	1.55×10^3	1.55×10^3
6.00×10^6	12	24	4.37×10^1	2.07×10^6	2.03×10^3	2.03×10^3
7.00×10^6	12	24	4.62×10^1	2.54×10^6	2.25×10^3	2.25×10^3
8.00×10^6	12	24	4.84×10^1	3.04×10^6	2.47×10^3	2.47×10^3
1.00×10^7	12	24	5.24×10^1	4.09×10^6	2.86×10^3	2.86×10^3
4.00×10^7	12	24	8.49×10^1	2.61×10^7	7.23×10^3	7.23×10^3
1.00×10^8	12	24	1.16×10^2	8.90×10^7	1.33×10^4	1.33×10^4
4.00×10^8	12	24	1.87×10^2	5.67×10^8	3.37×10^4	3.37×10^4
1.00×10^9	16	32	2.54×10^2	1.99×10^9	6.31×10^4	6.31×10^4

Table 7.16: 2D Simulation results from Chapter 3 for Pr = 1. These results were collected by Marie-Christine Volk.

Ra	N_x	N_z	Nu	E_{kin}	Pe	Re
1.00×10^4	4	8	3.15	2.38×10^2	2.18×10^1	3.11×10^1
4.00×10^4	4	8	5.93	2.09×10^3	6.47×10^1	9.24×10^1
1.00×10^5	4	8	9.02	7.91×10^3	1.26×10^2	1.80×10^2
2.00×10^5	13	26	1.23×10^1	2.07×10^4	2.04×10^2	2.91×10^2
3.00×10^5	13	26	1.45×10^1	3.62×10^4	2.69×10^2	3.84×10^2
4.00×10^5	13	26	1.62×10^1	5.37×10^4	3.28×10^2	4.68×10^2
6.00×10^5	13	26	1.90×10^1	9.35×10^4	4.32×10^2	6.18×10^2
8.00×10^5	13	26	2.12×10^1	1.38×10^5	5.25×10^2	7.50×10^2
1.00×10^6	4	8	2.28×10^1	1.87×10^5	6.12×10^2	8.74×10^2
2.00×10^6	4	8	2.94×10^1	4.77×10^5	9.76×10^2	1.39×10^3
3.00×10^6	4	8	3.41×10^1	8.20×10^5	1.28×10^3	1.83×10^3
4.00×10^6	4	8	3.78×10^1	1.20×10^6	1.55×10^3	2.22×10^3
6.00×10^6	4	8	4.36×10^1	2.08×10^6	2.04×10^3	2.91×10^3
7.00×10^6	4	8	4.61×10^1	2.55×10^6	2.26×10^3	3.22×10^3
8.00×10^6	4	8	4.83×10^1	3.04×10^6	2.47×10^3	3.52×10^3
1.00×10^7	4	8	5.23×10^1	4.09×10^6	2.86×10^3	4.09×10^3
4.00×10^7	4	8	8.42×10^1	2.61×10^7	7.22×10^3	1.03×10^4
4.00×10^7	4	8	8.42×10^1	2.61×10^7	7.22×10^3	1.03×10^4
1.00×10^8	4	8	1.15×10^2	8.87×10^7	1.33×10^4	1.90×10^4
4.00×10^8	4	8	1.83×10^2	5.64×10^8	3.36×10^4	4.80×10^4
1.00×10^9	16	32	2.56×10^2	1.93×10^9	6.22×10^4	8.88×10^4

Table 7.17: 2D simulation results from Chapter 3 for Pr = 0.7. These results were collected by Marie-Christine Volk.

Ra	N_x	N_z	Nu	E_{kin}	Pe	Re
1.00×10^4	12	24	3.30	2.34×10^2	2.16×10^1	2.16×10^2
4.00×10^4	12	24	6.48	2.15×10^3	6.56×10^1	6.56×10^2
1.00×10^5	12	24	9.62	8.06×10^3	1.27×10^2	1.27×10^3
1.00×10^6	12	24	2.35×10^1	1.89×10^5	6.14×10^2	6.14×10^3
2.00×10^6	12	24	3.02×10^1	4.77×10^5	9.77×10^2	9.77×10^3
3.00×10^6	12	24	3.49×10^1	8.23×10^5	1.28×10^3	1.28×10^4
4.00×10^6	12	24	3.87×10^1	1.21×10^6	1.55×10^3	1.55×10^4
6.00×10^6	12	24	4.46×10^1	2.07×10^6	2.04×10^3	2.04×10^4
7.00×10^6	12	24	4.71×10^1	2.55×10^6	2.26×10^3	2.26×10^4
8.00×10^6	12	24	4.93×10^1	3.05×10^6	2.47×10^3	2.47×10^4
1.00×10^7	12	24	5.33×10^1	4.11×10^6	2.87×10^3	2.87×10^4
4.00×10^7	12	24	8.61×10^1	2.62×10^7	7.23×10^3	7.23×10^4
1.00×10^8	12	24	1.18×10^2	8.91×10^7	1.34×10^4	1.34×10^5
4.00×10^8	12	24	1.89×10^2	5.62×10^8	3.35×10^4	3.35×10^5
1.00×10^9	16	32	2.57×10^2	1.99×10^9	6.31×10^4	6.31×10^5

Table 7.18: 2D simulation results from Chapter 3 for Pr = 0.1. These results were collected by Marie-Christine Volk.

Ra	N_x	N_z	Nu	E_{kin}	Pe	Re
1.00×10^4	12	24	3.32	2.35×10^2	2.17×10^1	3.10×10^2
4.00×10^4	12	24	6.50	2.16×10^3	6.57×10^1	9.39×10^2
1.00×10^5	12	24	9.65	8.08×10^3	1.27×10^2	1.82×10^3
1.00×10^6	12	24	2.35×10^1	1.89×10^5	6.14×10^2	8.77×10^3
2.00×10^6	12	24	3.02×10^1	4.78×10^5	9.77×10^2	1.40×10^4
3.00×10^6	12	24	3.50×10^1	8.23×10^5	1.28×10^3	1.83×10^4
4.00×10^6	12	24	3.87×10^1	1.21×10^6	1.55×10^3	2.22×10^4
6.00×10^6	12	24	4.46×10^1	2.07×10^6	2.04×10^3	2.91×10^4
7.00×10^6	12	24	4.71×10^1	2.55×10^6	2.26×10^3	3.23×10^4
8.00×10^6	12	24	4.94×10^1	3.05×10^6	2.47×10^3	3.53×10^4
1.00×10^7	12	24	5.34×10^1	4.11×10^6	2.87×10^3	4.10×10^4
4.00×10^7	12	24	8.61×10^1	2.62×10^7	7.24×10^3	1.03×10^5
1.00×10^8	12	24	1.18×10^2	8.91×10^7	1.33×10^4	1.91×10^5
4.00×10^8	12	24	1.89×10^2	5.62×10^8	3.35×10^4	4.79×10^5
1.00×10^9	16	32	2.57×10^2	1.97×10^9	6.28×10^4	8.97×10^5

Table 7.19: 2D simulation results from Chapter 3 for Pr = 0.07. These results were collected by Marie-Christine Volk.

$\Delta T/T_0$	d/H_0	Ra	Nu	E_{kin}	Pe	Re	$100\overline{\theta}_m$	ρ_m	$\rho_{\max}$	$\rho_{\min}$
1.00	1.00	6.00×10^6	3.93	6.84×10^4	3.22×10^2	4.60×10^2	1.32	1.28	1.68	9.88×10^{-1}
1.00	1.00×10^{-1}	2.00×10^3	1.00	2.44×10^{-21}	8.51×10^{-11}	1.22×10^{-10}	4.33×10^{-14}	7.14×10^{-1}	9.98×10^{-1}	5.62×10^{-1}
1.00	1.00×10^{-1}	2.00×10^4	2.25	1.54×10^2	2.05×10^1	2.94×10^1	-1.48	7.28×10^{-1}	1.00	5.67×10^{-1}
1.00	1.00×10^{-1}	2.00×10^5	4.27	2.92×10^3	8.93×10^1	1.28×10^2	-2.60	7.30×10^{-1}	1.01	5.71×10^{-1}
1.00	1.00×10^{-1}	6.00×10^3	1.21	8.15	4.74	6.77	-8.56×10^{-1}	7.22×10^{-1}	9.97×10^{-1}	5.61×10^{-1}
1.00	1.00×10^{-1}	6.00×10^4	3.10	6.90×10^2	4.34×10^1	6.21×10^1	-2.12	7.29×10^{-1}	1.01	5.69×10^{-1}
1.00	1.00×10^{-1}	6.00×10^5	5.62	9.92×10^3	1.65×10^2	2.35×10^2	-2.96	7.31×10^{-1}	1.01	5.72×10^{-1}
1.00	1.20	2.00×10^4	1.22	5.06×10^1	8.19	1.17×10^1	1.81	1.48	2.01	1.02
1.00	1.20	2.00×10^5	1.60	1.04×10^3	3.69×10^1	5.27×10^1	1.88	1.47	2.02	1.04
1.00	1.20	2.00×10^6	2.23	1.34×10^4	1.33×10^2	1.89×10^2	1.58	1.48	2.03	1.05
1.00	1.20	2.00×10^7	3.21	1.66×10^5	4.70×10^2	6.71×10^2	6.48×10^{-1}	1.48	2.05	1.02
1.00	1.20	2.00×10^8	5.36	2.16×10^6	1.69×10^3	2.41×10^3	5.34×10^{-1}	1.47	2.07	1.01
1.00	1.20	6.00×10^4	1.38	2.38×10^2	1.77×10^1	2.52×10^1	2.12	1.47	2.02	1.04
1.00	1.20	6.00×10^5	1.86	3.62×10^3	6.89×10^1	9.84×10^1	1.68	1.48	2.02	1.05
1.00	1.20	6.00×10^6	2.69	4.30×10^4	2.38×10^2	3.40×10^2	1.38	1.48	2.04	1.04
1.00	1.20	6.00×10^7	3.89	5.71×10^5	8.70×10^2	1.24×10^3	9.47×10^{-2}	1.48	2.06	1.02
1.00×10^1	1.00	2.00×10^3	1.00	7.63×10^{-22}	7.03×10^{-11}	1.00×10^{-10}	7.47×10^{-11}	2.25×10^{-1}	9.84×10^{-1}	1.36×10^{-1}
1.00×10^1	1.00	2.00×10^5	1.56	8.24×10^1	2.50×10^1	3.57×10^1	-3.66	2.64×10^{-1}	1.00	1.38×10^{-1}
1.00×10^1	1.00	6.00×10^3	1.00	1.97×10^{-22}	3.43×10^{-11}	4.91×10^{-11}	4.63×10^{-11}	2.25×10^{-1}	9.84×10^{-1}	1.36×10^{-1}
1.00×10^1	1.20×10^1	2.00×10^4	1.29	4.53×10^1	3.76	5.38	4.39	5.63	1.10×10^1	1.55
1.00×10^1	1.20×10^1	2.00×10^5	1.67	7.40×10^2	1.51×10^1	2.16×10^1	4.14	5.63	1.11×10^1	1.98
1.00×10^1	1.20×10^1	2.00×10^6	2.34	1.34×10^4	6.48×10^1	9.25×10^1	2.28	5.61	1.12×10^1	2.17
1.00×10^1	1.20×10^1	2.00×10^7	4.62	1.73×10^5	2.27×10^2	3.24×10^2	1.89	5.66	1.15×10^1	2.03
1.00×10^1	1.20×10^1	2.00×10^8	1.01×10^1	2.20×10^6	8.03×10^2	1.15×10^3	8.97×10^{-1}	5.68	1.17×10^1	1.83
1.00×10^1	1.20×10^1	6.00×10^4	1.44	1.81×10^2	7.49	1.07×10^1	4.41	5.62	1.11×10^1	1.76
1.00×10^1	1.20×10^1	6.00×10^5	1.97	2.54×10^3	2.81×10^1	4.01×10^1	3.91	5.64	1.11×10^1	2.17
1.00×10^1	1.20×10^1	6.00×10^6	3.01	4.60×10^4	1.20×10^2	1.72×10^2	1.79	5.60	1.13×10^1	2.05
1.00×10^1	1.20×10^1	6.00×10^7	6.66	5.99×10^5	4.21×10^2	6.02×10^2	1.46	5.67	1.16×10^1	1.95
1.00×10^2	1.00×10^1	2.00×10^3	1.00	1.44×10^{-16}	8.70×10^{-8}	1.24×10^{-7}	-3.37×10^{-8}	3.79×10^{-2}	8.61×10^{-1}	2.14×10^{-2}
1.00×10^2	1.00×10^1	6.00×10^3	1.00	3.02×10^{-16}	9.88×10^{-8}	1.41×10^{-7}	-3.45×10^{-8}	3.79×10^{-2}	8.61×10^{-1}	2.14×10^{-2}
1.00×10^2	1.00×10^2	2.00×10^4	1.52	2.11×10^1	1.72	2.46	6.58	1.21×10^1	2.17×10^1	5.65
1.00×10^2	1.00×10^2	2.00×10^5	2.27	3.51×10^2	7.03	1.00×10^1	5.50	1.21×10^1	2.25×10^1	6.90
1.00×10^2	1.00×10^2	6.00×10^4	1.82	8.44×10^1	3.44	4.92	6.31	1.21×10^1	2.21×10^1	7.23
1.00×10^2	1.20×10^2	2.00×10^4	1.57	6.05×10^1	1.48	2.11	4.75	4.72×10^1	1.01×10^2	7.92
1.00×10^2	1.20×10^2	2.00×10^5	2.28	7.96×10^2	5.34	7.64	4.41	4.74×10^1	1.02×10^2	1.54×10^1
1.00×10^2	1.20×10^2	2.00×10^6	4.44	1.65×10^4	2.42×10^1	3.45×10^1	2.10	4.73×10^1	1.04×10^2	1.36×10^1
1.00×10^2	1.20×10^2	6.00×10^4	1.80	2.05×10^2	2.70	3.86	4.68	4.73×10^1	1.01×10^2	1.10×10^1
1.00×10^2	1.20×10^2	6.00×10^5	3.05	3.68×10^3	1.12×10^1	1.59×10^1	3.23	4.74×10^1	1.03×10^2	1.48×10^1
1.00×10^2	1.20×10^2	6.00×10^6	6.33	5.66×10^4	4.47×10^1	6.38×10^1	1.54	4.75×10^1	1.06×10^2	1.26×10^1
1.00×10^{-1}	1.00×10^{-1}	2.00×10^6	3.30	2.52×10^4	2.21×10^2	3.16×10^2	9.27×10^{-2}	1.03	1.07	9.94×10^{-1}
1.00×10^{-1}	1.00×10^{-1}	6.00×10^3	1.07	5.39	3.23	4.61	5.62×10^{-2}	1.03	1.07	1.00
1.00×10^{-1}	1.00×10^{-1}	6.00×10^6	3.62	8.57×10^4	4.07×10^2	5.82×10^2	-1.31×10^{-1}	1.03	1.07	9.94×10^{-1}
1.00×10^{-1}	1.00×10^{-2}	2.00×10^3	1.00	1.59×10^{-10}	1.82×10^{-5}	2.60×10^{-5}	-6.14×10^{-12}	9.60×10^{-1}	1.00	9.24×10^{-1}
1.00×10^{-1}	1.00×10^{-2}	2.00×10^4	2.91	3.98×10^2	2.88×10^1	4.11×10^1	-3.47×10^{-1}	9.61×10^{-1}	1.00	9.24×10^{-1}
1.00×10^{-1}	1.00×10^{-2}	2.00×10^5	5.30	5.93×10^3	1.11×10^2	1.59×10^2	-6.86×10^{-1}	9.61×10^{-1}	9.99×10^{-1}	9.24×10^{-1}
1.00×10^{-1}	1.00×10^{-2}	2.00×10^6	8.04	7.36×10^4	3.91×10^2	5.59×10^2	-7.80×10^{-1}	9.61×10^{-1}	9.98×10^{-1}	9.25×10^{-1}
1.00×10^{-1}	1.00×10^{-2}	2.00×10^7	1.40×10^1	8.39×10^5	1.32×10^3	1.89×10^3	-8.65×10^{-1}	9.60×10^{-1}	9.97×10^{-1}	9.26×10^{-1}
1.00×10^{-1}	1.00×10^{-2}	6.00×10^3	2.01	6.97×10^1	1.20×10^1	1.72×10^1	-1.76×10^{-1}	9.61×10^{-1}	1.00	9.24×10^{-1}
1.00×10^{-1}	1.00×10^{-2}	6.00×10^4	3.91	1.53×10^3	5.64×10^1	8.05×10^1	-5.10×10^{-1}	9.61×10^{-1}	9.99×10^{-1}	9.24×10^{-1}
1.00×10^{-1}	1.00×10^{-2}	6.00×10^5	6.91	1.94×10^4	2.01×10^2	2.87×10^2	-9.20×10^{-1}	9.61×10^{-1}	9.98×10^{-1}	9.25×10^{-1}

Table 7.20: Part one of the results from Chapter 4 which are compared with the results from Tilgner, 2011.

$\Delta T/T_0$	d/H_0	Ra	Nu	E_{kin}	Pe	Re	$100\overline{\theta}_m$	ρ_m	$\rho_{\max}$	$\rho_{\min}$
1.00×10^{-1}	1.00×10^{-2}	6.00×10^6	1.04×10^1	2.31×10^5	6.94×10^2	9.91×10^2	-1.02	9.61×10^{-1}	9.98×10^{-1}	9.25×10^{-1}
1.00×10^{-1}	1.00×10^{-3}	2.00×10^4	3.08	4.33×10^2	3.01×10^1	4.30×10^1	-5.16×10^{-1}	9.54×10^{-1}	9.99×10^{-1}	9.11×10^{-1}
1.00×10^{-1}	1.00×10^{-3}	2.00×10^5	5.64	6.31×10^3	1.15×10^2	1.64×10^2	-8.96×10^{-1}	9.54×10^{-1}	9.99×10^{-1}	9.11×10^{-1}
1.00×10^{-1}	1.00×10^{-3}	2.00×10^6	8.58	7.79×10^4	4.04×10^2	5.77×10^2	-8.93×10^{-1}	9.54×10^{-1}	9.98×10^{-1}	9.12×10^{-1}
1.00×10^{-1}	1.00×10^{-3}	2.00×10^7	1.49×10^1	8.92×10^5	1.37×10^3	1.95×10^3	-9.98×10^{-1}	9.54×10^{-1}	9.97×10^{-1}	9.12×10^{-1}
1.00×10^{-1}	1.00×10^{-3}	6.00×10^3	2.14	8.02×10^1	1.30×10^1	1.85×10^1	-2.65×10^{-1}	9.54×10^{-1}	1.00	9.11×10^{-1}
1.00×10^{-1}	1.00×10^{-3}	6.00×10^4	4.15	1.63×10^3	5.84×10^1	8.35×10^1	-6.74×10^{-1}	9.54×10^{-1}	9.99×10^{-1}	9.11×10^{-1}
1.00×10^{-1}	1.00×10^{-3}	6.00×10^5	7.37	2.06×10^4	2.08×10^2	2.97×10^2	-1.12	9.54×10^{-1}	9.98×10^{-1}	9.11×10^{-1}
1.00×10^{-1}	1.00×10^{-3}	6.00×10^6	1.12×10^1	2.45×10^5	7.16×10^2	1.02×10^3	-1.17	9.54×10^{-1}	9.97×10^{-1}	9.12×10^{-1}
1.00×10^{-1}	1.20×10^{-1}	2.00×10^4	1.19	4.82×10^1	9.58	1.37×10^1	2.39×10^{-1}	1.05	1.10	1.00
1.00×10^{-1}	1.20×10^{-1}	2.00×10^5	1.59	1.15×10^3	4.69×10^1	6.69×10^1	2.46×10^{-1}	1.05	1.10	1.00
1.00×10^{-1}	1.20×10^{-1}	2.00×10^6	2.21	1.49×10^4	1.69×10^2	2.41×10^2	1.32×10^{-1}	1.05	1.10	1.00
1.00×10^{-1}	1.20×10^{-1}	2.00×10^7	2.91	1.79×10^5	5.84×10^2	8.34×10^2	-4.59×10^{-2}	1.05	1.10	9.98×10^{-1}
1.00×10^{-1}	1.20×10^{-1}	2.00×10^8	4.58	2.21×10^6	2.05×10^3	2.93×10^3	-3.71×10^{-1}	1.05	1.10	9.97×10^{-1}
1.00×10^{-1}	1.20×10^{-1}	6.00×10^4	1.36	2.55×10^2	2.20×10^1	3.15×10^1	3.08×10^{-1}	1.05	1.10	1.00
1.00×10^{-1}	1.20×10^{-1}	6.00×10^5	1.85	4.04×10^3	8.77×10^1	1.25×10^2	1.87×10^{-1}	1.05	1.10	1.00
1.00×10^{-1}	1.20×10^{-1}	6.00×10^6	2.63	4.74×10^4	3.00×10^2	4.29×10^2	8.24×10^{-2}	1.05	1.10	9.99×10^{-1}
1.00×10^{-1}	1.20×10^{-1}	6.00×10^7	3.59	5.93×10^5	1.06×10^3	1.52×10^3	-2.30×10^{-1}	1.05	1.10	9.97×10^{-1}
1.00×10^{-2}	1.00×10^{-2}	2.00×10^6	3.28	2.55×10^4	2.25×10^2	3.22×10^2	-1.84×10^{-1}	1.00	1.01	9.99×10^{-1}
1.00×10^{-2}	1.00×10^{-2}	6.00×10^6	3.61	8.71×10^4	4.17×10^2	5.95×10^2	-2.21×10^{-1}	1.00	1.01	9.99×10^{-1}
3.00	3.00	2.00×10^4	1.41	6.15×10^1	8.11	1.16×10^1	4.32	1.74	2.56	1.17
3.00	3.00	2.00×10^5	2.07	1.15×10^3	3.48×10^1	4.98×10^1	4.01	1.74	2.64	1.21
3.00	3.00	2.00×10^6	3.22	1.48×10^4	1.26×10^2	1.79×10^2	3.28	1.75	2.72	1.14
3.00	3.00	2.00×10^7	5.33	1.85×10^5	4.47×10^2	6.39×10^2	1.74	1.75	2.78	1.08
3.00	3.00	2.00×10^8	9.71	2.89×10^6	1.75×10^3	2.50×10^3	1.36×10^{-1}	1.74	2.83	1.04
3.00	3.00	6.00×10^4	1.68	2.69×10^2	1.69×10^1	2.41×10^1	4.59	1.73	2.59	1.24
3.00	3.00	6.00×10^5	2.53	3.99×10^3	6.50×10^1	9.29×10^1	3.56	1.74	2.68	1.17
3.00	3.00	6.00×10^6	4.13	4.79×10^4	2.27×10^2	3.25×10^2	2.78	1.75	2.75	1.10
3.00	3.00	6.00×10^7	7.09	6.37×10^5	8.28×10^2	1.18×10^3	1.42	1.74	2.80	1.06
3.00×10^1	3.00×10^1	2.00×10^4	1.44	2.82×10^1	2.94	4.20	6.25	5.65	9.92	2.62
3.00×10^1	3.00×10^1	2.00×10^5	2.13	5.04×10^2	1.24×10^1	1.77×10^1	5.61	5.64	1.02×10^1	3.34
3.00×10^1	3.00×10^1	2.00×10^6	3.54	6.76×10^3	4.58×10^1	6.54×10^1	4.34	5.67	1.06×10^1	2.95
3.00×10^1	3.00×10^1	2.00×10^7	6.33	1.11×10^5	1.88×10^2	2.68×10^2	1.02	5.62	1.10×10^1	2.59
3.00×10^1	3.00×10^1	2.00×10^8	1.20×10^1	1.35×10^6	6.39×10^2	9.12×10^2	8.24×10^{-1}	5.75	1.13×10^1	2.49
3.00×10^1	3.00×10^1	6.00×10^4	1.72	1.19×10^2	6.00	8.57	6.31	5.62	1.00×10^1	3.41
3.00×10^1	3.00×10^1	6.00×10^5	2.65	1.76×10^3	2.32×10^1	3.31×10^1	4.97	5.66	1.04×10^1	3.15
3.00×10^1	3.00×10^1	6.00×10^6	4.92	2.26×10^4	8.43×10^1	1.20×10^2	3.54	5.68	1.08×10^1	2.77
3.00×10^1	3.00×10^1	6.00×10^7	9.80	3.66×10^5	3.30×10^2	4.72×10^2	7.74×10^{-1}	5.72	1.12×10^1	2.56
3.00×10^{-1}	3.00×10^{-1}	2.00×10^4	1.45	1.04×10^2	1.38×10^1	1.97×10^1	1.07	1.09	1.19	1.00
3.00×10^{-1}	3.00×10^{-1}	2.00×10^5	2.16	1.96×10^3	5.97×10^1	8.53×10^1	8.55×10^{-1}	1.09	1.20	9.98×10^{-1}
3.00×10^{-1}	3.00×10^{-1}	2.00×10^6	3.30	2.41×10^4	2.10×10^2	2.99×10^2	6.32×10^{-1}	1.09	1.21	9.87×10^{-1}
3.00×10^{-1}	3.00×10^{-1}	2.00×10^7	4.71	2.85×10^5	7.20×10^2	1.03×10^3	1.21×10^{-1}	1.09	1.22	9.83×10^{-1}
3.00×10^{-1}	3.00×10^{-1}	2.00×10^8	8.18	3.58×10^6	2.55×10^3	3.65×10^3	-5.31×10^{-1}	1.09	1.22	9.78×10^{-1}
3.00×10^{-1}	3.00×10^{-1}	6.00×10^4	1.74	4.64×10^2	2.90×10^1	4.15×10^1	1.08	1.09	1.20	1.00
3.00×10^{-1}	3.00×10^{-1}	6.00×10^5	2.64	6.66×10^3	1.10×10^2	1.57×10^2	7.28×10^{-1}	1.09	1.21	9.92×10^{-1}
3.00×10^{-1}	3.00×10^{-1}	6.00×10^6	3.68	8.21×10^4	3.87×10^2	5.52×10^2	1.08×10^{-1}	1.09	1.22	9.86×10^{-1}
3.00×10^{-1}	3.00×10^{-1}	6.00×10^7	5.94	9.43×10^5	1.31×10^3	1.87×10^3	-6.45×10^{-1}	1.09	1.22	9.80×10^{-1}
3.00×10^{-2}	3.00×10^{-2}	2.00×10^6	3.29	2.55×10^4	2.25×10^2	3.21×10^2	-1.23×10^{-1}	1.01	1.02	9.98×10^{-1}
3.00×10^{-2}	3.00×10^{-2}	6.00×10^6	3.61	8.68×10^4	4.15×10^2	5.92×10^2	-2.01×10^{-1}	1.01	1.02	9.98×10^{-1}

Table 7.21: Part two of the results from Chapter 4 which are compared with the results from Tilgner, 2011.

Ra	Ra$_*$	Nu	Nu$_*$	E_{kin}	Pe	Re	$\rho_{\max}$	$\rho_{\min}$
5.00×10^3	1.67×10^3	1.03	1.08	1.39	1.46	2.09	1.59	1.00
6.00×10^3	2.00×10^3	1.10	1.29	6.22	3.09	4.41	1.59	1.01
7.00×10^3	2.33×10^3	1.15	1.45	1.12×10^1	4.14	5.92	1.59	1.01
8.00×10^3	2.67×10^3	1.19	1.58	1.64×10^1	5.01	7.16	1.59	1.02
9.00×10^3	3.00×10^3	1.23	1.69	2.18×10^1	5.77	8.24	1.60	1.02
1.00×10^4	3.33×10^3	1.26	1.78	2.73×10^1	6.45	9.21	1.60	1.02
2.00×10^4	6.67×10^3	1.44	2.32	8.81×10^1	1.16×10^1	1.65×10^1	1.60	1.04
3.00×10^4	1.00×10^4	1.54	2.62	1.57×10^2	1.54×10^1	2.20×10^1	1.61	1.04
4.00×10^4	1.33×10^4	1.61	2.84	2.30×10^2	1.86×10^1	2.66×10^1	1.61	1.04
7.00×10^4	2.33×10^4	1.77	3.32	4.70×10^2	2.66×10^1	3.80×10^1	1.61	1.05
1.00×10^5	3.33×10^4	1.88	3.65	7.26×10^2	3.31×10^1	4.73×10^1	1.61	1.05
2.00×10^5	6.67×10^4	2.13	4.39	1.64×10^3	4.97×10^1	7.10×10^1	1.62	1.06
4.00×10^5	1.33×10^5	2.41	5.24	3.58×10^3	7.36×10^1	1.05×10^2	1.62	1.06
7.00×10^5	2.33×10^5	2.68	6.04	6.63×10^3	1.00×10^2	1.43×10^2	1.62	1.06
1.00×10^6	3.33×10^5	2.86	6.59	9.76×10^3	1.22×10^2	1.74×10^2	1.62	1.06
2.00×10^6	6.67×10^5	3.27	7.81	2.05×10^4	1.76×10^2	2.51×10^2	1.62	1.07
4.00×10^6	1.33×10^6	3.75	9.26	4.24×10^4	2.54×10^2	3.62×10^2	1.63	1.07
7.00×10^6	2.33×10^6	4.62	1.19×10^1	8.35×10^4	3.54×10^2	5.05×10^2	1.63	1.08
1.00×10^7	3.33×10^6	4.57	1.17×10^1	1.10×10^5	4.10×10^2	5.86×10^2	1.63	1.07
2.00×10^7	6.67×10^6	5.94	1.58×10^1	2.50×10^5	6.13×10^2	8.75×10^2	1.64	1.08
4.00×10^7	1.33×10^7	6.18	1.65×10^1	4.35×10^5	8.16×10^2	1.17×10^3	1.63	1.07
7.00×10^7	2.33×10^7	8.02	2.21×10^1	8.62×10^5	1.14×10^3	1.63×10^3	1.64	1.08
1.00×10^8	3.33×10^7	9.40	2.62×10^1	1.18×10^6	1.33×10^3	1.90×10^3	1.65	1.08
2.00×10^8	6.67×10^7	9.80	2.74×10^1	2.19×10^6	1.82×10^3	2.60×10^3	1.64	1.08
4.00×10^8	1.33×10^8	1.18×10^1	3.34×10^1	4.74×10^6	2.68×10^3	3.82×10^3	1.64	1.07
7.00×10^8	2.33×10^8	1.40×10^1	3.99×10^1	8.64×10^6	3.62×10^3	5.16×10^3	1.64	1.06
1.00×10^9	3.33×10^8	1.55×10^1	4.46×10^1	1.30×10^7	4.44×10^3	6.34×10^3	1.64	1.05

Table 7.22: Results from Section 5.1 for $\Delta T/T_0 = d/H_0 = 1$ with free-slip horizontal walls for Ek $= \infty$ with $N_x = 512$, $N_z = 256$.

Ra	Ra$_*$	Nu	Nu$_*$	E_{kin}	Pe	Re	$\rho_{\max}$	$\rho_{\min}$
4.00×10^4	1.33×10^4	1.06	1.19	8.38	3.58	5.12	1.59	1.00
5.00×10^4	1.67×10^4	1.22	1.67	4.23×10^1	8.04	1.15×10^1	1.59	1.01
6.00×10^4	2.00×10^4	1.33	1.98	8.10×10^1	1.11×10^1	1.59×10^1	1.59	1.01
7.00×10^4	2.33×10^4	1.40	2.21	1.23×10^2	1.37×10^1	1.96×10^1	1.59	1.01
8.00×10^4	2.67×10^4	1.46	2.39	1.70×10^2	1.61×10^1	2.30×10^1	1.60	1.02
9.00×10^4	3.00×10^4	1.51	2.52	2.18×10^2	1.83×10^1	2.61×10^1	1.60	1.02
1.00×10^5	3.33×10^4	1.54	2.62	2.67×10^2	2.02×10^1	2.89×10^1	1.60	1.02
2.00×10^5	6.67×10^4	1.72	3.15	7.85×10^2	3.47×10^1	4.96×10^1	1.59	1.01
3.00×10^5	1.00×10^5	1.83	3.50	1.43×10^3	4.73×10^1	6.75×10^1	1.59	1.01
4.00×10^5	1.33×10^5	1.98	3.94	2.31×10^3	5.99×10^1	8.56×10^1	1.60	1.02
7.00×10^5	2.33×10^5	2.38	5.13	5.23×10^3	9.01×10^1	1.29×10^2	1.60	1.03
1.00×10^6	3.33×10^5	2.61	5.82	8.19×10^3	1.13×10^2	1.61×10^2	1.61	1.03
2.00×10^6	6.67×10^5	2.98	6.94	1.74×10^4	1.65×10^2	2.36×10^2	1.60	1.02
4.00×10^6	1.33×10^6	3.28	7.83	3.32×10^4	2.32×10^2	3.31×10^2	1.59	9.99×10^{-1}
7.00×10^6	2.33×10^6	3.72	9.15	6.18×10^4	3.14×10^2	4.49×10^2	1.60	1.01
1.00×10^7	3.33×10^6	4.01	1.00×10^1	9.06×10^4	3.80×10^2	5.42×10^2	1.60	1.02
2.00×10^7	6.67×10^6	4.63	1.19×10^1	1.89×10^5	5.46×10^2	7.81×10^2	1.61	1.02
4.00×10^7	1.33×10^7	6.06	1.62×10^1	4.36×10^5	8.19×10^2	1.17×10^3	1.63	1.06
7.00×10^7	2.33×10^7	7.53	2.06×10^1	7.44×10^5	1.07×10^3	1.52×10^3	1.63	1.06
1.00×10^8	3.33×10^7	7.92	2.18×10^1	1.08×10^6	1.28×10^3	1.83×10^3	1.63	1.06
2.00×10^8	6.67×10^7	1.09×10^1	3.06×10^1	2.49×10^6	1.94×10^3	2.77×10^3	1.64	1.07
4.00×10^8	1.33×10^8	1.42×10^1	4.07×10^1	4.63×10^6	2.63×10^3	3.75×10^3	1.65	1.07
7.00×10^8	2.33×10^8	1.65×10^1	4.74×10^1	1.05×10^7	3.96×10^3	5.66×10^3	1.65	1.07
1.00×10^9	3.33×10^8	1.56×10^1	4.47×10^1	1.30×10^7	4.43×10^3	6.33×10^3	1.64	1.05

Table 7.23: Results from Section 5.1 for $\Delta T/T_0 = d/H_0 = 1$ with free-slip horizontal walls for Ek $= 10^{-3}$ with $N_x = 512$, $N_z = 256$.
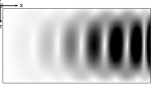
Ra	Ra$_*$	Nu	Nu$_*$	E_{kin}	Pe	Re	$\rho_{\max}$	$\rho_{\min}$
7.00×10^5	2.33×10^5	1.21	1.62	1.16×10^2	1.34×10^1	1.92×10^1	1.59	1.00
8.00×10^5	2.67×10^5	1.35	2.06	2.50×10^2	1.97×10^1	2.82×10^1	1.59	1.00
9.00×10^5	3.00×10^5	1.42	2.26	3.58×10^2	2.35×10^1	3.36×10^1	1.59	1.00
1.00×10^6	3.33×10^5	1.54	2.63	5.58×10^2	2.94×10^1	4.21×10^1	1.59	1.00
2.00×10^6	6.67×10^5	2.16	4.48	3.18×10^3	7.00×10^1	9.99×10^1	1.59	1.01
3.00×10^6	1.00×10^6	2.51	5.54	7.13×10^3	1.05×10^2	1.50×10^2	1.59	1.01
4.00×10^6	1.33×10^6	2.81	6.44	1.30×10^4	1.42×10^2	2.03×10^2	1.59	1.01
5.00×10^6	1.67×10^6	3.02	7.06	2.12×10^4	1.82×10^2	2.60×10^2	1.60	1.02
6.00×10^6	2.00×10^6	3.13	7.39	2.96×10^4	2.15×10^2	3.07×10^2	1.60	1.02
7.00×10^6	2.33×10^6	3.24	7.73	3.93×10^4	2.48×10^2	3.54×10^2	1.60	1.02
8.00×10^6	2.67×10^6	3.37	8.10	4.95×10^4	2.78×10^2	3.97×10^2	1.60	1.02
9.00×10^6	3.00×10^6	3.48	8.44	6.05×10^4	3.08×10^2	4.40×10^2	1.60	1.02
1.00×10^7	3.33×10^6	3.57	8.72	7.15×10^4	3.35×10^2	4.79×10^2	1.60	1.02
2.00×10^7	6.67×10^6	4.29	1.09×10^1	2.02×10^5	5.66×10^2	8.09×10^2	1.61	1.03
3.00×10^7	1.00×10^7	4.85	1.25×10^1	3.45×10^5	7.40×10^2	1.06×10^3	1.61	1.02
4.00×10^7	1.33×10^7	5.31	1.39×10^1	5.04×10^5	8.94×10^2	1.28×10^3	1.61	1.02
5.00×10^7	1.67×10^7	5.78	1.53×10^1	6.77×10^5	1.03×10^3	1.48×10^3	1.61	1.03
6.00×10^7	2.00×10^7	6.23	1.67×10^1	8.99×10^5	1.18×10^3	1.68×10^3	1.62	1.05
7.00×10^7	2.33×10^7	6.64	1.79×10^1	1.09×10^6	1.28×10^3	1.83×10^3	1.63	1.06
1.00×10^8	3.33×10^7	7.51	2.05×10^1	1.59×10^6	1.55×10^3	2.21×10^3	1.63	1.06
2.00×10^8	6.67×10^7	9.50	2.65×10^1	3.32×10^6	2.23×10^3	3.19×10^3	1.64	1.06
4.00×10^8	1.33×10^8	1.16×10^1	3.28×10^1	6.06×10^6	3.03×10^3	4.33×10^3	1.64	1.06
7.00×10^8	2.33×10^8	1.37×10^1	3.92×10^1	1.03×10^7	3.95×10^3	5.64×10^3	1.64	1.05
1.00×10^9	3.33×10^8	1.54×10^1	4.43×10^1	1.52×10^7	4.79×10^3	6.84×10^3	1.64	1.05

Table 7.24: Results from Section 5.1 for $\Delta T/T_0 = d/H_0 = 1$ with free-slip horizontal walls for Ek $= 10^{-4}$ with $N_x = 512$, $N_z = 256$.

Ra	Ra$_*$	Nu	Nu$_*$	E_{kin}	Pe	Re	$\rho_{\max}$	$\rho_{\min}$
2.00×10^7	6.67×10^6	2.06	4.19	4.94×10^3	8.72×10^1	1.25×10^2	1.59	1.01
3.00×10^7	1.00×10^7	2.62	5.85	1.39×10^4	1.47×10^2	2.09×10^2	1.59	1.01
4.00×10^7	1.33×10^7	3.17	7.51	2.90×10^4	2.12×10^2	3.02×10^2	1.59	1.01
5.00×10^7	1.67×10^7	3.63	8.89	4.98×10^4	2.78×10^2	3.98×10^2	1.59	1.00
6.00×10^7	2.00×10^7	4.04	1.01×10^1	7.61×10^4	3.44×10^2	4.92×10^2	1.60	1.00
7.00×10^7	2.33×10^7	4.38	1.11×10^1	1.07×10^5	4.09×10^2	5.85×10^2	1.59	1.00
8.00×10^7	2.67×10^7	4.67	1.20×10^1	1.42×10^5	4.73×10^2	6.75×10^2	1.59	9.98×10^{-1}
9.00×10^7	3.00×10^7	4.96	1.29×10^1	1.83×10^5	5.35×10^2	7.65×10^2	1.60	1.00
1.00×10^8	3.33×10^7	5.19	1.36×10^1	2.27×10^5	5.97×10^2	8.53×10^2	1.59	9.98×10^{-1}
2.00×10^8	6.67×10^7	7.09	1.93×10^1	8.49×10^5	1.16×10^3	1.65×10^3	1.60	1.00
3.00×10^8	1.00×10^8	8.40	2.32×10^1	1.75×10^6	1.67×10^3	2.39×10^3	1.61	1.01
4.00×10^8	1.33×10^8	9.48	2.64×10^1	2.89×10^6	2.14×10^3	3.06×10^3	1.61	1.01
5.00×10^8	1.67×10^8	1.03×10^1	2.90×10^1	4.23×10^6	2.59×10^3	3.70×10^3	1.61	1.01
6.00×10^8	2.00×10^8	1.10×10^1	3.11×10^1	5.76×10^6	3.02×10^3	4.31×10^3	1.61	1.01
7.00×10^8	2.33×10^8	1.15×10^1	3.26×10^1	7.31×10^6	3.40×10^3	4.85×10^3	1.62	1.01
1.00×10^9	3.33×10^8	1.31×10^1	3.72×10^1	1.20×10^7	4.37×10^3	6.24×10^3	1.62	1.01

Table 7.25: Results from Section 5.1 for $\Delta T/T_0 = d/H_0 = 1$ with free-slip horizontal walls for Ek $= 10^{-5}$ with $N_x = 512$, $N_z = 256$.

Ra	Ra_*	Nu	Nu_*	E_{kin}	Pe	Re	$\rho_{\max}$	$\rho_{\min}$
2.00×10^8	6.67×10^7	1.50	2.49	3.09×10^3	6.88×10^1	9.84×10^1	1.59	1.00
3.00×10^8	1.00×10^8	1.93	3.80	1.17×10^4	1.35×10^2	1.92×10^2	1.59	9.99×10^{-1}
4.00×10^8	1.33×10^8	2.44	5.33	2.83×10^4	2.09×10^2	2.98×10^2	1.59	1.00
5.00×10^8	1.67×10^8	3.01	7.04	5.51×10^4	2.91×10^2	4.16×10^2	1.59	1.01
6.00×10^8	2.00×10^8	3.70	9.09	9.77×10^4	3.88×10^2	5.54×10^2	1.59	1.01
7.00×10^8	2.33×10^8	4.39	1.12×10^1	1.57×10^5	4.93×10^2	7.04×10^2	1.60	1.01
8.00×10^8	2.67×10^8	5.07	1.32×10^1	2.35×10^5	6.02×10^2	8.60×10^2	1.60	1.00
9.00×10^8	3.00×10^8	5.69	1.51×10^1	3.27×10^5	7.12×10^2	1.02×10^3	1.60	1.00
1.00×10^9	3.33×10^8	6.26	1.68×10^1	4.35×10^5	8.21×10^2	1.17×10^3	1.60	1.00

Table 7.26: Results from Section 5.1 for $\Delta T/T_0 = d/H_0 = 1$ with free-slip horizontal walls for $\mathrm{Ek} = 10^{-6}$ with $N_x = 512$, $N_z = 256$.

Ra	Ra_*	Nu	Nu_*	E_{kin}	Pe	Re	$\rho_{\max}$	$\rho_{\min}$
6.00×10^3	2.00×10^3	1.07	1.22	5.60	3.29	4.70	1.07	1.00
7.00×10^3	2.33×10^3	1.13	1.40	1.19×10^1	4.80	6.85	1.07	1.00
8.00×10^3	2.67×10^3	1.18	1.55	1.84×10^1	5.96	8.52	1.07	1.00
9.00×10^3	3.00×10^3	1.22	1.67	2.50×10^1	6.96	9.95	1.07	1.00
1.00×10^4	3.33×10^3	1.26	1.77	3.19×10^1	7.86	1.12×10^1	1.07	1.00
2.00×10^4	6.67×10^3	1.45	2.34	1.08×10^2	1.45×10^1	2.06×10^1	1.07	1.00
4.00×10^4	1.33×10^4	1.63	2.88	2.86×10^2	2.35×10^1	3.36×10^1	1.07	1.00
7.00×10^4	2.33×10^4	1.79	3.37	5.87×10^2	3.37×10^1	4.81×10^1	1.07	1.00
1.00×10^5	3.33×10^4	1.91	3.72	9.08×10^2	4.19×10^1	5.99×10^1	1.07	1.00
2.00×10^5	6.67×10^4	2.16	4.47	2.05×10^3	6.29×10^1	8.99×10^1	1.07	1.00
4.00×10^5	1.33×10^5	2.45	5.34	4.46×10^3	9.29×10^1	1.33×10^2	1.07	1.00
7.00×10^5	2.33×10^5	2.71	6.13	8.22×10^3	1.26×10^2	1.80×10^2	1.07	1.00
1.00×10^6	3.33×10^5	2.90	6.69	1.21×10^4	1.53×10^2	2.18×10^2	1.07	1.00
2.00×10^6	6.67×10^5	3.30	7.90	2.52×10^4	2.21×10^2	3.16×10^2	1.07	1.00
4.00×10^6	1.33×10^6	3.76	9.29	5.20×10^4	3.17×10^2	4.53×10^2	1.07	1.00
7.00×10^6	2.33×10^6	4.49	1.15×10^1	9.13×10^4	4.20×10^2	6.01×10^2	1.07	1.00
1.00×10^7	3.33×10^6	5.00	1.30×10^1	1.53×10^5	5.44×10^2	7.76×10^2	1.07	1.00
2.00×10^7	6.67×10^6	5.22	1.37×10^1	2.73×10^5	7.27×10^2	1.04×10^3	1.07	1.00
4.00×10^7	1.33×10^7	6.09	1.63×10^1	5.54×10^5	1.04×10^3	1.48×10^3	1.07	1.00
7.00×10^7	2.33×10^7	6.78	1.83×10^1	9.79×10^5	1.38×10^3	1.97×10^3	1.07	9.99×10^{-1}
1.00×10^8	3.33×10^7	7.24	1.97×10^1	1.44×10^6	1.67×10^3	2.38×10^3	1.07	9.99×10^{-1}
2.00×10^8	6.67×10^7	8.79	2.44×10^1	2.84×10^6	2.34×10^3	3.35×10^3	1.07	1.00
4.00×10^8	1.33×10^8	1.25×10^1	3.55×10^1	7.20×10^6	3.73×10^3	5.33×10^3	1.07	9.98×10^{-1}
7.00×10^8	2.33×10^8	1.36×10^1	3.89×10^1	1.30×10^7	5.01×10^3	7.16×10^3	1.07	9.98×10^{-1}
1.00×10^9	3.33×10^8	1.34×10^1	3.81×10^1	2.05×10^7	6.29×10^3	8.99×10^3	1.07	9.99×10^{-1}

Table 7.27: Results from Section 5.1 for $\Delta T/T_0 = d/H_0 = 0.1$ with free-slip horizontal walls for $\mathrm{Ek} = \infty$ with $N_x = 512$, $N_z = 256$.

Ra	Ra$_*$	Nu	Nu$_*$	E_{kin}	Pe	Re	$\rho_{\max}$	$\rho_{\min}$
9.00×10^3	3.00×10^3	1.05	1.16	4.88	3.06	4.37	1.07	1.00
1.00×10^4	3.33×10^3	1.10	1.29	1.00×10^1	4.37	6.25	1.07	1.00
2.00×10^4	6.67×10^3	1.32	1.95	6.96×10^1	1.15×10^1	1.64×10^1	1.07	1.00
4.00×10^4	1.33×10^4	1.44	2.33	1.88×10^2	1.90×10^1	2.71×10^1	1.06	9.99×10^{-1}
7.00×10^4	2.33×10^4	1.55	2.66	3.97×10^2	2.78×10^1	3.97×10^1	1.06	9.97×10^{-1}
1.00×10^5	3.33×10^4	1.67	3.00	6.02×10^2	3.42×10^1	4.89×10^1	1.06	9.98×10^{-1}
2.00×10^5	6.67×10^4	1.92	3.75	1.46×10^3	5.32×10^1	7.60×10^1	1.06	9.99×10^{-1}
4.00×10^5	1.33×10^5	2.35	5.05	4.05×10^3	8.85×10^1	1.26×10^2	1.07	1.00
7.00×10^5	2.33×10^5	2.66	5.98	7.90×10^3	1.24×10^2	1.77×10^2	1.07	1.00
1.00×10^6	3.33×10^5	2.86	6.58	1.18×10^4	1.51×10^2	2.16×10^2	1.07	1.00
2.00×10^6	6.67×10^5	3.28	7.84	2.49×10^4	2.20×10^2	3.14×10^2	1.07	1.00
4.00×10^6	1.33×10^6	3.75	9.26	5.17×10^4	3.16×10^2	4.52×10^2	1.07	1.00
7.00×10^6	2.33×10^6	4.18	1.06×10^1	9.24×10^4	4.23×10^2	6.04×10^2	1.07	1.00
1.00×10^7	3.33×10^6	4.49	1.15×10^1	1.33×10^5	5.08×10^2	7.26×10^2	1.07	1.00
2.00×10^7	6.67×10^6	5.21	1.36×10^1	2.73×10^5	7.26×10^2	1.04×10^3	1.07	1.00
4.00×10^7	1.33×10^7	6.09	1.63×10^1	5.54×10^5	1.04×10^3	1.48×10^3	1.07	1.00
7.00×10^7	2.33×10^7	6.78	1.83×10^1	9.74×10^5	1.37×10^3	1.96×10^3	1.07	1.00
1.00×10^8	3.33×10^7	8.28	2.28×10^1	1.67×10^6	1.80×10^3	2.57×10^3	1.07	9.99×10^{-1}
2.00×10^8	6.67×10^7	8.79	2.44×10^1	2.85×10^6	2.35×10^3	3.35×10^3	1.07	1.00
4.00×10^8	1.33×10^8	1.07×10^1	3.01×10^1	5.83×10^6	3.36×10^3	4.80×10^3	1.07	1.00
7.00×10^8	2.33×10^8	1.22×10^1	3.45×10^1	1.34×10^7	5.09×10^3	7.27×10^3	1.07	1.00
1.00×10^9	3.33×10^8	1.34×10^1	3.81×10^1	2.04×10^7	6.28×10^3	8.97×10^3	1.07	9.99×10^{-1}

Table 7.28: Results from Section 5.1 for $\Delta T / T_0 = d / H_0 = 0.1$ with free-slip horizontal walls for Ek $= 10^{-3}$ with $N_x = 512$, $N_z = 256$.

Ra	Ra$_*$	Nu	Nu$_*$	E_{kin}	Pe	Re	$\rho_{\max}$	$\rho_{\min}$
5.00×10^4	1.67×10^4	1.08	1.23	1.34×10^1	5.09	7.27	1.07	1.00
6.00×10^4	2.00×10^4	1.22	1.66	5.27×10^1	1.01×10^1	1.44×10^1	1.07	1.00
7.00×10^4	2.33×10^4	1.32	1.96	9.67×10^1	1.37×10^1	1.95×10^1	1.07	1.00
8.00×10^4	2.67×10^4	1.40	2.19	1.45×10^2	1.68×10^1	2.39×10^1	1.07	1.00
9.00×10^4	3.00×10^4	1.46	2.38	1.97×10^2	1.95×10^1	2.79×10^1	1.07	1.00
1.00×10^5	3.33×10^4	1.51	2.52	2.52×10^2	2.21×10^1	3.15×10^1	1.07	1.00
1.50×10^5	5.00×10^4	1.64	2.91	5.37×10^2	3.22×10^1	4.61×10^1	1.07	1.00
2.00×10^5	6.67×10^4	1.72	3.17	8.55×10^2	4.07×10^1	5.81×10^1	1.07	1.00
4.00×10^5	1.33×10^5	1.93	3.80	2.32×10^3	6.68×10^1	9.55×10^1	1.07	1.00
7.00×10^5	2.33×10^5	2.30	4.91	6.09×10^3	1.09×10^2	1.55×10^2	1.07	1.00
1.00×10^6	3.33×10^5	2.54	5.61	9.35×10^3	1.35×10^2	1.92×10^2	1.07	1.00
2.00×10^6	6.67×10^5	3.09	7.26	2.25×10^4	2.08×10^2	2.98×10^2	1.07	1.00
4.00×10^6	1.33×10^6	3.43	8.30	4.38×10^4	2.91×10^2	4.16×10^2	1.07	1.00
7.00×10^6	2.33×10^6	3.93	9.80	8.25×10^4	3.99×10^2	5.71×10^2	1.07	1.00
1.00×10^7	3.33×10^6	4.25	1.08×10^1	1.21×10^5	4.83×10^2	6.91×10^2	1.07	1.00
2.00×10^7	6.67×10^6	4.21	1.06×10^1	2.20×10^5	6.52×10^2	9.32×10^2	1.06	9.97×10^{-1}
4.00×10^7	1.33×10^7	4.62	1.18×10^1	4.30×10^5	9.13×10^2	1.30×10^3	1.06	9.98×10^{-1}
7.00×10^7	2.33×10^7	6.59	1.78×10^1	9.85×10^5	1.38×10^3	1.97×10^3	1.07	9.99×10^{-1}
1.00×10^8	3.33×10^7	7.22	1.97×10^1	1.42×10^6	1.66×10^3	2.37×10^3	1.07	9.99×10^{-1}
2.00×10^8	6.67×10^7	8.80	2.44×10^1	2.84×10^6	2.34×10^3	3.35×10^3	1.07	9.99×10^{-1}
4.00×10^8	1.33×10^8	1.07×10^1	3.01×10^1	5.81×10^6	3.35×10^3	4.79×10^3	1.07	1.00
7.00×10^8	2.33×10^8	1.36×10^1	3.88×10^1	1.29×10^7	5.00×10^3	7.15×10^3	1.07	9.97×10^{-1}
1.00×10^9	3.33×10^8	1.34×10^1	3.81×10^1	2.05×10^7	6.29×10^3	8.99×10^3	1.07	9.99×10^{-1}

Table 7.29: Results from Section 5.1 for $\Delta T/T_0 = d/H_0 = 0.1$ with free-slip horizontal walls for Ek $= 10^{-4}$ with $N_x = 512$, $N_z = 256$.

Ra	Ra_*	Nu	Nu_*	E_{kin}	Pe	Re	ρ_{max}	ρ_{min}
8.00×10^5	2.67×10^5	1.18	1.55	1.19×10^2	1.52×10^1	2.17×10^1	1.07	1.00
9.00×10^5	3.00×10^5	1.28	1.85	2.21×10^2	2.07×10^1	2.95×10^1	1.07	1.00
1.00×10^6	3.33×10^5	1.34	2.02	3.13×10^2	2.46×10^1	3.52×10^1	1.07	1.00
2.00×10^6	6.67×10^5	2.25	4.74	3.30×10^3	8.00×10^1	1.14×10^2	1.07	1.00
3.00×10^6	1.00×10^6	2.37	5.10	6.20×10^3	1.09×10^2	1.56×10^2	1.07	1.00
4.00×10^6	1.33×10^6	2.64	5.91	1.09×10^4	1.45×10^2	2.07×10^2	1.07	1.00
5.00×10^6	1.67×10^6	2.87	6.60	1.71×10^4	1.82×10^2	2.59×10^2	1.07	1.00
6.00×10^6	2.00×10^6	3.04	7.12	2.49×10^4	2.19×10^2	3.13×10^2	1.07	1.00
7.00×10^6	2.33×10^6	3.16	7.49	3.42×10^4	2.57×10^2	3.67×10^2	1.07	1.00
8.00×10^6	2.67×10^6	3.27	7.82	4.43×10^4	2.93×10^2	4.18×10^2	1.07	1.00
9.00×10^6	3.00×10^6	3.38	8.15	5.55×10^4	3.28×10^2	4.68×10^2	1.07	1.00
1.00×10^7	3.33×10^6	3.50	8.49	6.79×10^4	3.62×10^2	5.18×10^2	1.07	1.00
2.00×10^7	6.67×10^6	4.26	1.08×10^1	2.26×10^5	6.61×10^2	9.44×10^2	1.07	1.00
4.00×10^7	1.33×10^7	5.23	1.37×10^1	6.09×10^5	1.09×10^3	1.55×10^3	1.07	9.99×10^{-1}
7.00×10^7	2.33×10^7	6.13	1.64×10^1	1.26×10^6	1.56×10^3	2.23×10^3	1.07	9.99×10^{-1}
1.00×10^8	3.33×10^7	6.79	1.84×10^1	1.98×10^6	1.96×10^3	2.80×10^3	1.07	9.99×10^{-1}
2.00×10^8	6.67×10^7	8.39	2.32×10^1	4.53×10^6	2.96×10^3	4.23×10^3	1.07	9.99×10^{-1}
4.00×10^8	1.33×10^8	1.04×10^1	2.93×10^1	9.87×10^6	4.37×10^3	6.24×10^3	1.07	9.99×10^{-1}
7.00×10^8	2.33×10^8	1.25×10^1	3.56×10^1	1.74×10^7	5.81×10^3	8.30×10^3	1.07	9.98×10^{-1}
1.00×10^9	3.33×10^8	1.41×10^1	4.03×10^1	2.46×10^7	6.90×10^3	9.86×10^3	1.07	9.98×10^{-1}

Table 7.30: Results from Section 5.1 for $\Delta T / T_0 = d / H_0 = 0.1$ with free-slip horizontal walls for $\mathrm{Ek} = 10^{-5}$ with $N_x = 512$, $N_z = 256$.

Ra	Ra_*	Nu	Nu_*	E_{kin}	Pe	Re	ρ_{max}	ρ_{min}
1.50×10^7	5.00×10^6	1.30	1.89	7.58×10^2	3.82×10^1	5.45×10^1	1.07	1.00
2.00×10^7	6.67×10^6	1.71	3.14	2.94×10^3	7.53×10^1	1.08×10^2	1.07	1.00
3.00×10^7	1.00×10^7	2.25	4.74	9.73×10^3	1.37×10^2	1.96×10^2	1.07	1.00
4.00×10^7	1.33×10^7	2.73	6.18	2.10×10^4	2.01×10^2	2.87×10^2	1.07	1.00
5.00×10^7	1.67×10^7	3.19	7.56	3.75×10^4	2.69×10^2	3.84×10^2	1.07	1.00
6.00×10^7	2.00×10^7	3.58	8.75	5.89×10^4	3.37×10^2	4.82×10^2	1.07	1.00
7.00×10^7	2.33×10^7	3.91	9.72	8.45×10^4	4.04×10^2	5.77×10^2	1.07	9.99×10^{-1}
1.00×10^8	3.33×10^7	4.77	1.23×10^1	1.90×10^5	6.07×10^2	8.67×10^2	1.07	9.99×10^{-1}
2.00×10^8	6.67×10^7	6.60	1.78×10^1	7.61×10^5	1.21×10^3	1.73×10^3	1.07	9.99×10^{-1}
4.00×10^8	1.33×10^8	8.97	2.49×10^1	2.66×10^6	2.27×10^3	3.24×10^3	1.07	9.98×10^{-1}
7.00×10^8	2.33×10^8	1.10×10^1	3.09×10^1	6.70×10^6	3.60×10^3	5.14×10^3	1.07	9.98×10^{-1}
1.00×10^9	3.33×10^8	1.22×10^1	3.46×10^1	1.19×10^7	4.80×10^3	6.86×10^3	1.07	9.98×10^{-1}

Table 7.31: Results from Section 5.1 for $\Delta T / T_0 = d / H_0 = 0.1$ with free-slip horizontal walls for $\mathrm{Ek} = 10^{-6}$ with $N_x = 512$, $N_z = 256$.

Ra	Ra$_*$	Nu	Nu$_*$	E_{kin}	Pe	Re	ρ_{max}	ρ_{min}
7.00×10^3	2.33×10^3	1.13	1.39	1.16×10^1	4.81	6.88	1.01	1.00
1.00×10^4	3.33×10^3	1.25	1.75	3.19×10^1	7.98	1.14×10^1	1.01	1.00
2.00×10^4	6.67×10^3	1.44	2.33	1.09×10^2	1.47×10^1	2.11×10^1	1.01	1.00
4.00×10^4	1.33×10^4	1.62	2.87	2.90×10^2	2.40×10^1	3.43×10^1	1.01	1.00
7.00×10^4	2.33×10^4	1.79	3.36	5.95×10^2	3.44×10^1	4.92×10^1	1.01	1.00
1.00×10^5	3.33×10^4	1.90	3.70	9.21×10^2	4.29×10^1	6.12×10^1	1.01	1.00
2.00×10^5	6.67×10^4	2.15	4.46	2.08×10^3	6.44×10^1	9.19×10^1	1.01	1.00
4.00×10^5	1.33×10^5	2.44	5.32	4.53×10^3	9.50×10^1	1.36×10^2	1.01	1.00
7.00×10^5	2.33×10^5	2.71	6.12	8.35×10^3	1.29×10^2	1.84×10^2	1.01	1.00
1.00×10^6	3.33×10^5	2.89	6.67	1.23×10^4	1.56×10^2	2.23×10^2	1.01	1.00
2.00×10^6	6.67×10^5	3.29	7.88	2.56×10^4	2.26×10^2	3.23×10^2	1.01	1.00
4.00×10^6	1.33×10^6	3.75	9.26	5.28×10^4	3.24×10^2	4.64×10^2	1.01	1.00
7.00×10^6	2.33×10^6	4.18	1.05×10^1	9.42×10^4	4.33×10^2	6.19×10^2	1.01	1.00
1.00×10^7	3.33×10^6	4.48	1.14×10^1	1.36×10^5	5.20×10^2	7.43×10^2	1.01	1.00
2.00×10^7	6.67×10^6	5.20	1.36×10^1	2.77×10^5	7.43×10^2	1.06×10^3	1.01	1.00
4.00×10^7	1.33×10^7	6.06	1.62×10^1	5.63×10^5	1.06×10^3	1.51×10^3	1.01	1.00
7.00×10^7	2.33×10^7	8.15	2.25×10^1	9.96×10^5	1.41×10^3	2.01×10^3	1.01	1.00
1.00×10^8	3.33×10^7	9.01	2.50×10^1	1.62×10^6	1.80×10^3	2.57×10^3	1.01	1.00
2.00×10^8	6.67×10^7	8.55	2.36×10^1	2.86×10^6	2.39×10^3	3.41×10^3	1.01	1.00
4.00×10^8	1.33×10^8	1.23×10^1	3.48×10^1	7.31×10^6	3.82×10^3	5.45×10^3	1.01	1.00
7.00×10^8	2.33×10^8	1.18×10^1	3.35×10^1	1.43×10^7	5.33×10^3	7.62×10^3	1.01	1.00

Table 7.32: Results from Section 5.1 for $\Delta T/T_0 = d/H_0 = 0.01$ with free-slip horizontal walls for Ek $= \infty$ with $N_x = 512$, $N_z = 256$.

Ra	Ra$_*$	Nu	Nu$_*$	E_{kin}	Pe	Re	$\rho_{\max}$	$\rho_{\min}$
6.00×10^3	2.00×10^3	1.05	1.16	4.16	2.88	4.12	1.01	1.00
7.00×10^3	2.33×10^3	1.12	1.35	1.05×10^1	4.58	6.54	1.01	1.00
8.00×10^3	2.67×10^3	1.17	1.50	1.70×10^1	5.83	8.33	1.01	1.00
9.00×10^3	3.00×10^3	1.21	1.63	2.38×10^1	6.88	9.83	1.01	1.00
1.00×10^4	3.33×10^3	1.24	1.73	3.06×10^1	7.81	1.12×10^1	1.01	1.00
2.00×10^4	6.67×10^3	1.44	2.31	1.07×10^2	1.46×10^1	2.09×10^1	1.01	1.00
4.00×10^4	1.33×10^4	1.62	2.86	2.88×10^2	2.39×10^1	3.42×10^1	1.01	1.00
7.00×10^4	2.33×10^4	1.78	3.35	5.93×10^2	3.44×10^1	4.91×10^1	1.01	1.00
1.00×10^5	3.33×10^4	1.90	3.70	9.19×10^2	4.28×10^1	6.11×10^1	1.01	1.00
2.00×10^5	6.67×10^4	2.15	4.45	2.07×10^3	6.43×10^1	9.19×10^1	1.01	1.00
4.00×10^5	1.33×10^5	2.44	5.32	4.53×10^3	9.50×10^1	1.36×10^2	1.01	1.00
7.00×10^5	2.33×10^5	2.71	6.12	8.35×10^3	1.29×10^2	1.84×10^2	1.01	1.00
1.00×10^6	3.33×10^5	2.89	6.67	1.23×10^4	1.56×10^2	2.23×10^2	1.01	1.00
2.00×10^6	6.67×10^5	3.29	7.87	2.56×10^4	2.26×10^2	3.23×10^2	1.01	1.00
4.00×10^6	1.33×10^6	3.75	9.26	5.28×10^4	3.24×10^2	4.64×10^2	1.01	1.00
7.00×10^6	2.33×10^6	4.18	1.05×10^1	9.42×10^4	4.33×10^2	6.19×10^2	1.01	1.00
1.00×10^7	3.33×10^6	4.48	1.14×10^1	1.36×10^5	5.20×10^2	7.43×10^2	1.01	1.00
2.00×10^7	6.67×10^6	5.64	1.49×10^1	2.76×10^5	7.41×10^2	1.06×10^3	1.01	1.00
4.00×10^7	1.33×10^7	6.06	1.62×10^1	5.63×10^5	1.06×10^3	1.51×10^3	1.01	1.00
7.00×10^7	2.33×10^7	7.72	2.11×10^1	1.15×10^6	1.51×10^3	2.16×10^3	1.01	1.00
1.00×10^8	3.33×10^7	9.01	2.50×10^1	1.62×10^6	1.80×10^3	2.57×10^3	1.01	1.00
2.00×10^8	6.67×10^7	8.54	2.36×10^1	2.86×10^6	2.39×10^3	3.41×10^3	1.01	1.00
4.00×10^8	1.33×10^8	1.13×10^1	3.19×10^1	7.21×10^6	3.79×10^3	5.41×10^3	1.01	1.00
7.00×10^8	2.33×10^8	1.21×10^1	3.43×10^1	1.40×10^7	5.28×10^3	7.54×10^3	1.01	1.00

Table 7.33: Results from Section 5.1 for $\Delta T/T_0 = d/H_0 = 0.01$ with free-slip horizontal walls for Ek $= 10^{-3}$ with $N_x = 512$, $N_z = 256$.

Ra	Ra$_*$	Nu	Nu$_*$	E_{kin}	Pe	Re	$\rho_{\max}$	$\rho_{\min}$
9.00×10^3	3.00×10^3	1.04	1.13	4.14	2.86	4.08	1.01	1.00
1.00×10^4	3.33×10^3	1.09	1.27	9.33	4.29	6.13	1.01	1.00
1.50×10^4	5.00×10^3	1.23	1.68	3.74×10^1	8.56	1.22×10^1	1.01	1.00
2.00×10^4	6.67×10^3	1.31	1.94	6.93×10^1	1.16×10^1	1.66×10^1	1.01	1.00
3.00×10^4	1.00×10^4	1.41	2.24	1.35×10^2	1.63×10^1	2.33×10^1	1.01	1.00
4.00×10^4	1.33×10^4	1.46	2.38	1.98×10^2	1.98×10^1	2.82×10^1	1.01	1.00
7.00×10^4	2.33×10^4	1.54	2.62	3.92×10^2	2.79×10^1	3.99×10^1	1.01	1.00
1.00×10^5	3.33×10^4	1.64	2.93	6.37×10^2	3.57×10^1	5.09×10^1	1.01	1.00
2.00×10^5	6.67×10^4	1.90	3.71	1.45×10^3	5.38×10^1	7.69×10^1	1.01	1.00
4.00×10^5	1.33×10^5	2.35	5.06	4.15×10^3	9.10×10^1	1.30×10^2	1.01	1.00
7.00×10^5	2.33×10^5	2.66	5.97	8.03×10^3	1.26×10^2	1.81×10^2	1.01	1.00
1.00×10^6	3.33×10^5	2.86	6.57	1.20×10^4	1.54×10^2	2.21×10^2	1.01	1.00
2.00×10^6	6.67×10^5	3.27	7.81	2.53×10^4	2.25×10^2	3.21×10^2	1.01	1.00
4.00×10^6	1.33×10^6	3.74	9.22	5.25×10^4	3.24×10^2	4.62×10^2	1.01	1.00
7.00×10^6	2.33×10^6	4.49	1.15×10^1	9.24×10^4	4.29×10^2	6.13×10^2	1.01	1.00
1.00×10^7	3.33×10^6	4.47	1.14×10^1	1.36×10^5	5.20×10^2	7.43×10^2	1.01	1.00
2.00×10^7	6.67×10^6	5.64	1.49×10^1	2.75×10^5	7.41×10^2	1.06×10^3	1.01	1.00
4.00×10^7	1.33×10^7	6.05	1.62×10^1	5.62×10^5	1.06×10^3	1.51×10^3	1.01	1.00
7.00×10^7	2.33×10^7	6.87	1.86×10^1	9.91×10^5	1.41×10^3	2.01×10^3	1.01	1.00
1.00×10^8	3.33×10^7	8.17	2.25×10^1	1.43×10^6	1.69×10^3	2.41×10^3	1.01	1.00
2.00×10^8	6.67×10^7	8.55	2.37×10^1	2.86×10^6	2.39×10^3	3.41×10^3	1.01	1.00
4.00×10^8	1.33×10^8	1.13×10^1	3.19×10^1	7.20×10^6	3.79×10^3	5.41×10^3	1.01	1.00
7.00×10^8	2.33×10^8	1.21×10^1	3.44×10^1	1.38×10^7	5.24×10^3	7.49×10^3	1.01	1.00

Table 7.34: Results from Section 5.1 for $\Delta T/T_0 = d/H_0 = 0.01$ with free-slip horizontal walls for Ek $= 10^{-4}$ with $N_x = 512$, $N_z = 256$.

Ra	Ra$_*$	Nu	Nu$_*$	E_{kin}	Pe	Re	ρ_{max}	ρ_{min}
6.00×10^4	2.00×10^4	1.20	1.60	4.74×10^1	9.72	1.39×10^1	1.01	1.00
7.00×10^4	2.33×10^4	1.30	1.91	9.12×10^1	1.35×10^1	1.93×10^1	1.01	1.00
8.00×10^4	2.67×10^4	1.38	2.15	1.39×10^2	1.67×10^1	2.38×10^1	1.01	1.00
9.00×10^4	3.00×10^4	1.45	2.34	1.91×10^2	1.95×10^1	2.79×10^1	1.01	1.00
1.00×10^5	3.33×10^4	1.50	2.49	2.46×10^2	2.21×10^1	3.16×10^1	1.01	1.00
2.00×10^5	6.67×10^4	1.72	3.16	8.54×10^2	4.13×10^1	5.89×10^1	1.01	1.00
4.00×10^5	1.33×10^5	1.93	3.79	2.30×10^3	6.76×10^1	9.65×10^1	1.01	1.00
7.00×10^5	2.33×10^5	2.17	4.52	5.26×10^3	1.02×10^2	1.46×10^2	1.01	1.00
1.00×10^6	3.33×10^5	2.51	5.53	9.34×10^3	1.36×10^2	1.95×10^2	1.01	1.00
2.00×10^6	6.67×10^5	3.06	7.19	2.27×10^4	2.13×10^2	3.04×10^2	1.01	1.00
4.00×10^6	1.33×10^6	3.42	8.25	4.43×10^4	2.97×10^2	4.24×10^2	1.01	1.00
7.00×10^6	2.33×10^6	3.89	9.68	8.37×10^4	4.08×10^2	5.83×10^2	1.01	1.00
1.00×10^7	3.33×10^6	4.23	1.07×10^1	1.23×10^5	4.94×10^2	7.06×10^2	1.01	1.00
2.00×10^7	6.67×10^6	4.14	1.04×10^1	2.18×10^5	6.58×10^2	9.40×10^2	1.01	1.00
4.00×10^7	1.33×10^7	4.88	1.26×10^1	4.65×10^5	9.61×10^2	1.37×10^3	1.01	1.00
7.00×10^7	2.33×10^7	6.53	1.76×10^1	9.97×10^5	1.41×10^3	2.01×10^3	1.01	1.00
1.00×10^8	3.33×10^7	7.17	1.95×10^1	1.49×10^6	1.72×10^3	2.46×10^3	1.01	1.00
2.00×10^8	6.67×10^7	8.65	2.40×10^1	2.93×10^6	2.42×10^3	3.45×10^3	1.01	1.00
4.00×10^8	1.33×10^8	1.05×10^1	2.96×10^1	5.94×10^6	3.44×10^3	4.91×10^3	1.01	1.00
7.00×10^8	2.33×10^8	1.19×10^1	3.37×10^1	1.42×10^7	5.31×10^3	7.59×10^3	1.01	1.00

Table 7.35: Results from Section 5.1 for $\Delta T/T_0 = {}^d/H_0 = 0.01$ with free-slip horizontal walls for Ek $= 10^{-5}$ with $N_x = 512$, $N_z = 256$.

Ra	Ra$_*$	Nu	Nu$_*$	E_{kin}	Pe	Re	ρ_{max}	ρ_{min}
8.00×10^5	2.67×10^5	1.15	1.46	9.84×10^1	1.40×10^1	2.00×10^1	1.01	1.00
9.00×10^5	3.00×10^5	1.26	1.78	2.04×10^2	2.02×10^1	2.88×10^1	1.01	1.00
1.00×10^6	3.33×10^5	1.32	1.95	2.91×10^2	2.41×10^1	3.44×10^1	1.01	1.00
1.50×10^6	5.00×10^5	1.72	3.15	1.21×10^3	4.90×10^1	7.00×10^1	1.01	1.00
2.00×10^6	6.67×10^5	2.21	4.63	3.16×10^3	7.93×10^1	1.13×10^2	1.01	1.00
4.00×10^6	1.33×10^6	2.59	5.78	1.06×10^4	1.45×10^2	2.07×10^2	1.01	1.00
7.00×10^6	2.33×10^6	3.15	7.44	3.30×10^4	2.56×10^2	3.66×10^2	1.01	1.00
1.00×10^7	3.33×10^6	3.47	8.40	6.70×10^4	3.65×10^2	5.21×10^2	1.01	1.00
2.00×10^7	6.67×10^6	4.22	1.06×10^1	2.26×10^5	6.70×10^2	9.58×10^2	1.01	1.00
4.00×10^7	1.33×10^7	5.16	1.35×10^1	6.14×10^5	1.11×10^3	1.58×10^3	1.01	1.00
7.00×10^7	2.33×10^7	6.07	1.62×10^1	1.28×10^6	1.59×10^3	2.28×10^3	1.01	1.00
1.00×10^8	3.33×10^7	6.75	1.82×10^1	2.01×10^6	2.00×10^3	2.86×10^3	1.01	1.00
2.00×10^8	6.67×10^7	8.30	2.29×10^1	4.60×10^6	3.03×10^3	4.33×10^3	1.01	1.00
4.00×10^8	1.33×10^8	1.03×10^1	2.88×10^1	1.01×10^7	4.49×10^3	6.41×10^3	1.01	1.00
7.00×10^8	2.33×10^8	1.23×10^1	3.48×10^1	1.78×10^7	5.96×10^3	8.52×10^3	1.01	1.00

Table 7.36: Results from Section 5.1 for $\Delta T/T_0 = {}^d/H_0 = 0.01$ with free-slip horizontal walls for Ek $= 10^{-6}$ with $N_x = 512$, $N_z = 256$.

Ra	Ra_*	Nu	Nu_*	E_{kin}	Pe	Re	ρ_{max}	ρ_{min}
5.00×10^3	1.67×10^3	1.03	1.08	1.39	1.46	2.09	1.59	1.00
6.00×10^3	2.00×10^3	1.10	1.29	6.22	3.09	4.41	1.59	1.01
7.00×10^3	2.33×10^3	1.15	1.45	1.12×10^1	4.14	5.92	1.59	1.01
8.00×10^3	2.67×10^3	1.19	1.58	1.64×10^1	5.01	7.16	1.59	1.02
9.00×10^3	3.00×10^3	1.23	1.69	2.18×10^1	5.77	8.24	1.60	1.02
1.00×10^4	3.33×10^3	1.26	1.78	2.73×10^1	6.45	9.21	1.60	1.02
2.00×10^4	6.67×10^3	1.44	2.32	8.81×10^1	1.16×10^1	1.65×10^1	1.60	1.04
3.00×10^4	1.00×10^4	1.54	2.62	1.57×10^2	1.54×10^1	2.20×10^1	1.61	1.04
4.00×10^4	1.33×10^4	1.61	2.84	2.30×10^2	1.86×10^1	2.66×10^1	1.61	1.04
7.00×10^4	2.33×10^4	1.77	3.32	4.70×10^2	2.66×10^1	3.80×10^1	1.61	1.05
1.00×10^5	3.33×10^4	1.88	3.65	7.26×10^2	3.31×10^1	4.73×10^1	1.61	1.05
2.00×10^5	6.67×10^4	2.13	4.39	1.64×10^3	4.97×10^1	7.10×10^1	1.62	1.06
4.00×10^5	1.33×10^5	2.41	5.24	3.58×10^3	7.36×10^1	1.05×10^2	1.62	1.06
7.00×10^5	2.33×10^5	2.68	6.04	6.63×10^3	1.00×10^2	1.43×10^2	1.62	1.06
1.00×10^6	3.33×10^5	2.86	6.59	9.76×10^3	1.22×10^2	1.74×10^2	1.62	1.06
2.00×10^6	6.67×10^5	3.27	7.81	2.05×10^4	1.76×10^2	2.51×10^2	1.62	1.07
4.00×10^6	1.33×10^6	3.75	9.26	4.24×10^4	2.54×10^2	3.62×10^2	1.63	1.07
7.00×10^6	2.33×10^6	4.02	1.00×10^1	8.15×10^4	3.52×10^2	5.03×10^2	1.63	1.06
1.00×10^7	3.33×10^6	4.29	1.09×10^1	1.20×10^5	4.27×10^2	6.09×10^2	1.63	1.06
2.00×10^7	6.67×10^6	4.93	1.28×10^1	2.49×10^5	6.16×10^2	8.80×10^2	1.63	1.06
4.00×10^7	1.33×10^7	5.73	1.52×10^1	5.31×10^5	9.00×10^2	1.29×10^3	1.63	1.06
7.00×10^7	2.33×10^7	6.44	1.73×10^1	1.02×10^6	1.25×10^3	1.78×10^3	1.63	1.06
1.00×10^8	3.33×10^7	7.10	1.93×10^1	1.52×10^6	1.52×10^3	2.18×10^3	1.63	1.06
2.00×10^8	6.67×10^7	8.83	2.45×10^1	3.23×10^6	2.21×10^3	3.16×10^3	1.63	1.06
4.00×10^8	1.33×10^8	1.07×10^1	3.02×10^1	7.48×10^6	3.37×10^3	4.81×10^3	1.64	1.06
7.00×10^8	2.33×10^8	1.25×10^1	3.56×10^1	1.47×10^7	4.71×10^3	6.73×10^3	1.64	1.05
1.00×10^9	3.33×10^8	1.41×10^1	4.02×10^1	2.12×10^7	5.65×10^3	8.07×10^3	1.64	1.05

Table 7.37: Results from Section 5.1 for $\Delta T/T_0 = d/H_0 = 1$ horizontally periodic for $\text{Ek} = \infty$ with $N_x = 512$, $N_z = 256$.

Ra	Ra$_*$	Nu	Nu$_*$	E_{kin}	Pe	Re	$\rho_{\max}$	$\rho_{\min}$
4.00×10^4	1.33×10^4	1.15	1.46	2.36×10^1	6.08	8.68	1.61	1.02
5.00×10^4	1.67×10^4	1.19	1.58	3.99×10^1	7.96	1.14×10^1	1.62	1.02
6.00×10^4	2.00×10^4	1.20	1.59	5.20×10^1	9.12	1.30×10^1	1.62	1.02
7.00×10^4	2.33×10^4	1.19	1.58	6.25×10^1	1.00×10^1	1.43×10^1	1.63	1.01
8.00×10^4	2.67×10^4	1.23	1.70	9.03×10^1	1.20×10^1	1.71×10^1	1.64	1.02
9.00×10^4	3.00×10^4	1.26	1.77	1.35×10^2	1.45×10^1	2.07×10^1	1.63	1.01
1.00×10^5	3.33×10^4	1.28	1.83	1.68×10^2	1.61×10^1	2.30×10^1	1.63	1.00
2.00×10^5	6.67×10^4	1.41	2.24	5.96×10^2	3.04×10^1	4.34×10^1	1.65	9.92×10^{-1}
3.00×10^5	1.00×10^5	1.64	2.92	1.41×10^3	4.61×10^1	6.58×10^1	1.64	1.03
4.00×10^5	1.33×10^5	1.83	3.48	2.29×10^3	5.87×10^1	8.39×10^1	1.64	1.04
7.00×10^5	2.33×10^5	2.08	4.23	5.15×10^3	8.79×10^1	1.26×10^2	1.63	1.05
1.00×10^6	3.33×10^5	2.30	4.91	8.26×10^3	1.11×10^2	1.59×10^2	1.63	1.05
2.00×10^6	6.67×10^5	2.84	6.52	1.93×10^4	1.71×10^2	2.44×10^2	1.62	1.06
4.00×10^6	1.33×10^6	3.44	8.33	4.19×10^4	2.52×10^2	3.60×10^2	1.63	1.06
7.00×10^6	2.33×10^6	3.96	9.87	7.66×10^4	3.41×10^2	4.87×10^2	1.63	1.06
1.00×10^7	3.33×10^6	4.25	1.08×10^1	1.13×10^5	4.14×10^2	5.91×10^2	1.63	1.06
2.00×10^7	6.67×10^6	4.89	1.27×10^1	2.40×10^5	6.04×10^2	8.63×10^2	1.63	1.06
4.00×10^7	1.33×10^7	5.66	1.50×10^1	5.10×10^5	8.82×10^2	1.26×10^3	1.63	1.05
7.00×10^7	2.33×10^7	6.49	1.75×10^1	9.61×10^5	1.21×10^3	1.73×10^3	1.63	1.05
1.00×10^8	3.33×10^7	7.13	1.94×10^1	1.47×10^6	1.50×10^3	2.14×10^3	1.63	1.06
2.00×10^8	6.67×10^7	8.81	2.44×10^1	3.20×10^6	2.21×10^3	3.15×10^3	1.64	1.06
4.00×10^8	1.33×10^8	1.08×10^1	3.03×10^1	7.50×10^6	3.37×10^3	4.81×10^3	1.64	1.06
7.00×10^8	2.33×10^8	1.26×10^1	3.57×10^1	1.47×10^7	4.71×10^3	6.72×10^3	1.64	1.05
1.00×10^9	3.33×10^8	1.40×10^1	4.01×10^1	2.12×10^7	5.65×10^3	8.08×10^3	1.64	1.05

Table 7.38: Results from Section 5.1 for $\Delta T/T_0 = d/H_0 = 1$ horizontally periodic for Ek $= 10^{-3}$ with $N_x = 512$, $N_z = 256$.

Ra	Ra_*	Nu	Nu_*	E_{kin}	Pe	Re	$\rho_{\max}$	$\rho_{\min}$
5.00×10^5	1.67×10^5	1.08	1.24	3.52×10^1	7.66	1.09×10^1	1.64	9.76×10^{-1}
6.00×10^5	2.00×10^5	1.14	1.42	8.35×10^1	1.17×10^1	1.68×10^1	1.66	9.80×10^{-1}
7.00×10^5	2.33×10^5	1.19	1.56	1.45×10^2	1.54×10^1	2.20×10^1	1.69	9.77×10^{-1}
8.00×10^5	2.67×10^5	1.22	1.65	2.11×10^2	1.86×10^1	2.65×10^1	1.70	9.77×10^{-1}
9.00×10^5	3.00×10^5	1.30	1.89	3.67×10^2	2.44×10^1	3.49×10^1	1.70	9.93×10^{-1}
1.00×10^6	3.33×10^5	1.31	1.92	4.41×10^2	2.68×10^1	3.83×10^1	1.70	9.99×10^{-1}
2.00×10^6	6.67×10^5	1.13	1.40	1.03×10^3	4.00×10^1	5.71×10^1	1.80	8.57×10^{-1}
3.00×10^6	1.00×10^6	1.18	1.54	2.58×10^3	6.33×10^1	9.04×10^1	1.78	8.73×10^{-1}
4.00×10^6	1.33×10^6	1.18	1.55	4.43×10^3	8.24×10^1	1.18×10^2	1.81	8.66×10^{-1}
5.00×10^6	1.67×10^6	1.26	1.79	8.92×10^3	1.16×10^2	1.66×10^2	1.84	8.91×10^{-1}
6.00×10^6	2.00×10^6	1.20	1.59	1.01×10^4	1.23×10^2	1.76×10^2	1.83	8.50×10^{-1}
7.00×10^6	2.33×10^6	1.23	1.69	1.50×10^4	1.50×10^2	2.14×10^2	1.84	8.60×10^{-1}
8.00×10^6	2.67×10^6	1.22	1.67	1.88×10^4	1.68×10^2	2.40×10^2	1.84	8.51×10^{-1}
9.00×10^6	3.00×10^6	1.24	1.72	2.39×10^4	1.89×10^2	2.70×10^2	1.84	8.54×10^{-1}
1.00×10^7	3.33×10^6	1.31	1.94	3.30×10^4	2.20×10^2	3.14×10^2	1.84	8.75×10^{-1}
2.00×10^7	6.67×10^6	1.43	2.30	1.13×10^5	4.06×10^2	5.80×10^2	1.82	8.64×10^{-1}
3.00×10^7	1.00×10^7	1.87	3.60	2.73×10^5	6.35×10^2	9.08×10^2	1.79	8.92×10^{-1}
4.00×10^7	1.33×10^7	2.13	4.40	4.37×10^5	8.04×10^2	1.15×10^3	1.78	9.01×10^{-1}
5.00×10^7	1.67×10^7	2.72	6.15	5.91×10^5	9.37×10^2	1.34×10^3	1.75	9.27×10^{-1}
6.00×10^7	2.00×10^7	2.94	6.83	7.82×10^5	1.08×10^3	1.55×10^3	1.74	9.31×10^{-1}
7.00×10^7	2.33×10^7	3.23	7.68	9.62×10^5	1.20×10^3	1.72×10^3	1.74	9.38×10^{-1}
1.00×10^8	3.33×10^7	4.21	1.06×10^1	1.46×10^6	1.48×10^3	2.11×10^3	1.71	9.66×10^{-1}
2.00×10^8	6.67×10^7	7.22	1.97×10^1	3.01×10^6	2.11×10^3	3.01×10^3	1.67	1.02
4.00×10^8	1.33×10^8	1.02×10^1	2.86×10^1	7.06×10^6	3.24×10^3	4.63×10^3	1.65	1.05
7.00×10^8	2.33×10^8	1.25×10^1	3.54×10^1	1.39×10^7	4.56×10^3	6.52×10^3	1.64	1.05
1.00×10^9	3.33×10^8	1.40×10^1	4.00×10^1	2.07×10^7	5.56×10^3	7.95×10^3	1.64	1.05

Table 7.39: Results from Section 5.1 for $\Delta T/T_0 = d/H_0 = 1$ horizontally periodic for $\mathrm{Ek} = 10^{-4}$ with $N_x = 512$, $N_z = 256$.

Ra	Ra$_*$	Nu	Nu$_*$	E_{kin}	Pe	Re	$\rho_{\max}$	$\rho_{\min}$
1.00×10^7	3.33×10^6	1.32	1.95	5.94×10^2	3.10×10^1	4.42×10^1	1.67	1.03
2.00×10^7	6.67×10^6	1.14	1.41	1.58×10^3	4.99×10^1	7.13×10^1	1.82	8.66×10^{-1}
3.00×10^7	1.00×10^7	1.07	1.21	2.33×10^3	6.00×10^1	8.58×10^1	1.83	8.37×10^{-1}
4.00×10^7	1.33×10^7	1.08	1.23	4.58×10^3	8.37×10^1	1.20×10^2	1.85	8.22×10^{-1}
5.00×10^7	1.67×10^7	1.06	1.19	6.99×10^3	1.03×10^2	1.47×10^2	1.86	8.08×10^{-1}
6.00×10^7	2.00×10^7	1.08	1.23	1.12×10^4	1.31×10^2	1.87×10^2	1.87	8.01×10^{-1}
7.00×10^7	2.33×10^7	1.08	1.23	1.54×10^4	1.53×10^2	2.19×10^2	1.88	7.96×10^{-1}
8.00×10^7	2.67×10^7	1.07	1.22	2.01×10^4	1.75×10^2	2.50×10^2	1.88	7.91×10^{-1}
9.00×10^7	3.00×10^7	1.08	1.23	2.55×10^4	1.97×10^2	2.81×10^2	1.88	7.89×10^{-1}
1.00×10^8	3.33×10^7	1.07	1.22	3.11×10^4	2.18×10^2	3.11×10^2	1.88	7.85×10^{-1}
2.00×10^8	6.67×10^7	1.09	1.28	1.37×10^5	4.55×10^2	6.51×10^2	1.90	7.80×10^{-1}
3.00×10^8	1.00×10^8	1.11	1.34	3.24×10^5	7.03×10^2	1.00×10^3	1.90	7.74×10^{-1}
4.00×10^8	1.33×10^8	2.87	6.61	2.88×10^6	1.98×10^3	2.83×10^3	1.96	1.06
5.00×10^8	1.67×10^8	3.07	7.20	4.20×10^6	2.39×10^3	3.42×10^3	1.95	1.06
6.00×10^8	2.00×10^8	1.26×10^1	3.59×10^1	7.74×10^6	3.32×10^3	4.74×10^3	1.61	1.36
7.00×10^8	2.33×10^8	1.35×10^1	3.84×10^1	9.59×10^6	3.71×10^3	5.29×10^3	1.62	1.36
1.00×10^9	3.33×10^8	1.52×10^1	4.36×10^1	1.49×10^7	4.62×10^3	6.60×10^3	1.64	1.30

Table 7.40: Results from Section 5.1 for $\Delta T/T_0 = d/H_0 = 1$ horizontally periodic for Ek $= 10^{-5}$ with $N_x = 512$, $N_z = 256$.

Ra	Ra$_*$	Nu	Nu$_*$	E_{kin}	Pe	Re	$\rho_{\max}$	$\rho_{\min}$
2.00×10^8	6.67×10^7	1.94	3.81	7.45×10^3	1.06×10^2	1.52×10^2	1.66	1.09
3.00×10^8	1.00×10^8	2.49	5.47	2.98×10^4	2.11×10^2	3.01×10^2	1.70	1.10
4.00×10^8	1.33×10^8	1.07	1.20	5.79×10^3	9.41×10^1	1.34×10^2	1.87	8.07×10^{-1}
5.00×10^8	1.67×10^8	1.05	1.16	8.69×10^3	1.15×10^2	1.65×10^2	1.89	7.89×10^{-1}
6.00×10^8	2.00×10^8	1.05	1.15	1.19×10^4	1.35×10^2	1.93×10^2	1.89	7.88×10^{-1}
7.00×10^8	2.33×10^8	1.04	1.12	1.69×10^4	1.60×10^2	2.29×10^2	1.91	7.72×10^{-1}
8.00×10^8	2.67×10^8	1.04	1.12	2.19×10^4	1.83×10^2	2.61×10^2	1.91	7.66×10^{-1}
9.00×10^8	3.00×10^8	1.03	1.09	2.78×10^4	2.06×10^2	2.94×10^2	1.92	7.58×10^{-1}
1.00×10^9	3.33×10^8	1.06	1.17	4.21×10^4	2.51×10^2	3.58×10^2	1.95	7.61×10^{-1}

Table 7.41: Results from Section 5.1 for $\Delta T/T_0 = d/H_0 = 1$ horizontally periodic for Ek $= 10^{-6}$ with $N_x = 512$, $N_z = 256$.

Ra	Ra$_*$	Nu	Nu$_*$	E_{kin}	Pe	Re	$\rho_{\max}$	$\rho_{\min}$
6.00×10^3	2.00×10^3	1.07	1.22	5.60	3.29	4.70	1.07	1.00
7.00×10^3	2.33×10^3	1.13	1.40	1.19×10^1	4.80	6.85	1.07	1.00
8.00×10^3	2.67×10^3	1.18	1.55	1.84×10^1	5.96	8.52	1.07	1.00
9.00×10^3	3.00×10^3	1.22	1.67	2.50×10^1	6.96	9.95	1.07	1.00
1.00×10^4	3.33×10^3	1.26	1.77	3.19×10^1	7.86	1.12×10^1	1.07	1.00
2.00×10^4	6.67×10^3	1.45	2.34	1.08×10^2	1.45×10^1	2.06×10^1	1.07	1.00
4.00×10^4	1.33×10^4	1.63	2.88	2.86×10^2	2.35×10^1	3.36×10^1	1.07	1.00
7.00×10^4	2.33×10^4	1.79	3.37	5.87×10^2	3.37×10^1	4.81×10^1	1.07	1.00
1.00×10^5	3.33×10^4	1.91	3.72	9.08×10^2	4.19×10^1	5.99×10^1	1.07	1.00
2.00×10^5	6.67×10^4	2.16	4.47	2.05×10^3	6.29×10^1	8.99×10^1	1.07	1.00
4.00×10^5	1.33×10^5	2.45	5.34	4.46×10^3	9.29×10^1	1.33×10^2	1.07	1.00
7.00×10^5	2.33×10^5	2.71	6.13	8.22×10^3	1.26×10^2	1.80×10^2	1.07	1.00
1.00×10^6	3.33×10^5	2.90	6.69	1.21×10^4	1.53×10^2	2.18×10^2	1.07	1.00
2.00×10^6	6.67×10^5	3.30	7.90	2.52×10^4	2.21×10^2	3.16×10^2	1.07	1.00
4.00×10^6	1.33×10^6	3.45	8.35	5.55×10^4	3.28×10^2	4.68×10^2	1.07	1.00
7.00×10^6	2.33×10^6	3.72	9.15	1.01×10^5	4.42×10^2	6.31×10^2	1.07	1.00
1.00×10^7	3.33×10^6	3.97	9.91	1.46×10^5	5.32×10^2	7.60×10^2	1.07	1.00
2.00×10^7	6.67×10^6	4.76	1.23×10^1	2.97×10^5	7.59×10^2	1.08×10^3	1.07	1.00
4.00×10^7	1.33×10^7	5.45	1.43×10^1	6.40×10^5	1.11×10^3	1.59×10^3	1.07	1.00
7.00×10^7	2.33×10^7	6.18	1.66×10^1	1.13×10^6	1.48×10^3	2.11×10^3	1.07	9.99×10^{-1}
1.00×10^8	3.33×10^7	6.70	1.81×10^1	1.68×10^6	1.80×10^3	2.57×10^3	1.07	9.99×10^{-1}
2.00×10^8	6.67×10^7	7.97	2.19×10^1	3.81×10^6	2.71×10^3	3.88×10^3	1.07	9.99×10^{-1}
4.00×10^8	1.33×10^8	9.72	2.72×10^1	8.26×10^6	4.00×10^3	5.71×10^3	1.07	9.99×10^{-1}
7.00×10^8	2.33×10^8	1.14×10^1	3.21×10^1	1.63×10^7	5.62×10^3	8.03×10^3	1.07	9.98×10^{-1}
1.00×10^9	3.33×10^8	1.25×10^1	3.55×10^1	2.46×10^7	6.90×10^3	9.85×10^3	1.07	9.98×10^{-1}

Table 7.42: Results from Section 5.1 for $\Delta T/T_0 = d/H_0 = 0.1$ horizontally periodic for Ek $= \infty$ with $N_x = 512$, $N_z = 256$.

Ra	Ra$_*$	Nu	Nu$_*$	E_{kin}	Pe	Re	$\rho_{\max}$	$\rho_{\min}$
7.00×10^3	2.33×10^3	1.04	1.11	3.03	2.42	3.46	1.07	1.00
8.00×10^3	2.67×10^3	1.10	1.29	8.91	4.15	5.93	1.07	1.00
9.00×10^3	3.00×10^3	1.15	1.44	1.50×10^1	5.40	7.71	1.07	1.00
1.00×10^4	3.33×10^3	1.18	1.55	2.14×10^1	6.43	9.19	1.07	1.00
2.00×10^4	6.67×10^3	1.40	2.20	9.38×10^1	1.35×10^1	1.92×10^1	1.07	1.00
4.00×10^4	1.33×10^4	1.59	2.78	2.70×10^2	2.28×10^1	3.26×10^1	1.07	1.00
7.00×10^4	2.33×10^4	1.77	3.30	5.71×10^2	3.32×10^1	4.75×10^1	1.07	1.00
1.00×10^5	3.33×10^4	1.89	3.66	8.93×10^2	4.16×10^1	5.94×10^1	1.07	1.00
2.00×10^5	6.67×10^4	2.14	4.43	2.03×10^3	6.28×10^1	8.97×10^1	1.07	1.00
4.00×10^5	1.33×10^5	2.44	5.31	4.45×10^3	9.28×10^1	1.33×10^2	1.07	1.00
7.00×10^5	2.33×10^5	2.71	6.12	8.22×10^3	1.26×10^2	1.80×10^2	1.07	1.00
1.00×10^6	3.33×10^5	2.89	6.68	1.21×10^4	1.53×10^2	2.18×10^2	1.07	1.00
2.00×10^6	6.67×10^5	3.30	7.89	2.52×10^4	2.21×10^2	3.15×10^2	1.07	1.00
4.00×10^6	1.33×10^6	3.44	8.33	5.55×10^4	3.28×10^2	4.68×10^2	1.07	1.00
7.00×10^6	2.33×10^6	3.71	9.14	1.01×10^5	4.42×10^2	6.31×10^2	1.07	1.00
1.00×10^7	3.33×10^6	3.97	9.90	1.46×10^5	5.32×10^2	7.60×10^2	1.07	1.00
2.00×10^7	6.67×10^6	4.74	1.22×10^1	2.97×10^5	7.58×10^2	1.08×10^3	1.07	1.00
4.00×10^7	1.33×10^7	5.45	1.44×10^1	6.37×10^5	1.11×10^3	1.59×10^3	1.07	1.00
7.00×10^7	2.33×10^7	6.17	1.65×10^1	1.13×10^6	1.48×10^3	2.11×10^3	1.07	9.99×10^{-1}
1.00×10^8	3.33×10^7	6.71	1.81×10^1	1.67×10^6	1.80×10^3	2.57×10^3	1.07	9.99×10^{-1}
2.00×10^8	6.67×10^7	7.98	2.19×10^1	3.77×10^6	2.70×10^3	3.86×10^3	1.07	9.99×10^{-1}
4.00×10^8	1.33×10^8	9.73	2.72×10^1	8.24×10^6	3.99×10^3	5.70×10^3	1.07	9.99×10^{-1}
7.00×10^8	2.33×10^8	1.14×10^1	3.21×10^1	1.63×10^7	5.62×10^3	8.03×10^3	1.07	9.98×10^{-1}
1.00×10^9	3.33×10^8	1.25×10^1	3.56×10^1	2.48×10^7	6.92×10^3	9.89×10^3	1.07	9.98×10^{-1}

Table 7.43: Results from Section 5.1 for $\Delta T/T_0 = d/H_0 = 0.1$ horizontally periodic for Ek $= 10^{-3}$ with $N_x = 512$, $N_z = 256$.

Ra	Ra$_*$	Nu	Nu$_*$	E_{kin}	Pe	Re	$\rho_{\max}$	$\rho_{\min}$
4.00×10^4	1.33×10^4	1.11	1.32	1.61×10^1	5.59	7.99	1.07	1.00
5.00×10^4	1.67×10^4	1.22	1.66	4.68×10^1	9.53	1.36×10^1	1.07	1.00
6.00×10^4	2.00×10^4	1.28	1.83	7.64×10^1	1.22×10^1	1.74×10^1	1.07	1.00
7.00×10^4	2.33×10^4	1.27	1.80	9.22×10^1	1.34×10^1	1.91×10^1	1.07	1.00
8.00×10^4	2.67×10^4	1.25	1.75	1.05×10^2	1.43×10^1	2.04×10^1	1.07	1.00
9.00×10^4	3.00×10^4	1.24	1.71	1.17×10^2	1.51×10^1	2.16×10^1	1.07	9.99×10^{-1}
1.00×10^5	3.33×10^4	1.24	1.73	1.38×10^2	1.64×10^1	2.34×10^1	1.07	9.99×10^{-1}
1.50×10^5	5.00×10^4	1.28	1.85	3.12×10^2	2.46×10^1	3.51×10^1	1.07	9.97×10^{-1}
2.00×10^5	6.67×10^4	1.37	2.12	5.75×10^2	3.34×10^1	4.77×10^1	1.07	9.96×10^{-1}
4.00×10^5	1.33×10^5	1.68	3.03	2.22×10^3	6.55×10^1	9.36×10^1	1.07	9.96×10^{-1}
7.00×10^5	2.33×10^5	1.98	3.93	5.78×10^3	1.06×10^2	1.51×10^2	1.07	9.97×10^{-1}
1.00×10^6	3.33×10^5	2.23	4.70	9.77×10^3	1.38×10^2	1.96×10^2	1.07	9.99×10^{-1}
2.00×10^6	6.67×10^5	2.77	6.32	2.34×10^4	2.13×10^2	3.04×10^2	1.07	1.00
4.00×10^6	1.33×10^6	3.25	7.76	5.04×10^4	3.12×10^2	4.46×10^2	1.07	1.00
7.00×10^6	2.33×10^6	3.66	8.99	9.38×10^4	4.26×10^2	6.09×10^2	1.07	9.99×10^{-1}
1.00×10^7	3.33×10^6	3.93	9.79	1.40×10^5	5.20×10^2	7.43×10^2	1.07	9.99×10^{-1}
2.00×10^7	6.67×10^6	4.61	1.18×10^1	2.95×10^5	7.56×10^2	1.08×10^3	1.07	9.99×10^{-1}
4.00×10^7	1.33×10^7	5.76	1.53×10^1	5.56×10^5	1.04×10^3	1.48×10^3	1.07	9.99×10^{-1}
7.00×10^7	2.33×10^7	6.43	1.73×10^1	1.02×10^6	1.41×10^3	2.01×10^3	1.07	9.99×10^{-1}
1.00×10^8	3.33×10^7	6.82	1.85×10^1	1.54×10^6	1.73×10^3	2.47×10^3	1.07	9.99×10^{-1}
2.00×10^8	6.67×10^7	7.96	2.19×10^1	3.68×10^6	2.67×10^3	3.81×10^3	1.07	9.99×10^{-1}
4.00×10^8	1.33×10^8	9.73	2.72×10^1	8.13×10^6	3.96×10^3	5.66×10^3	1.07	9.98×10^{-1}
7.00×10^8	2.33×10^8	1.14×10^1	3.21×10^1	1.62×10^7	5.60×10^3	8.00×10^3	1.07	9.98×10^{-1}
1.00×10^9	3.33×10^8	1.25×10^1	3.56×10^1	2.49×10^7	6.94×10^3	9.91×10^3	1.07	9.98×10^{-1}

Table 7.44: Results from Section 5.1 for $\Delta T/T_0 = d/H_0 = 0.1$ horizontally periodic for Ek $= 10^{-4}$ with $N_x = 512$, $N_z = 256$.

Ra	Ra$_*$	Nu	Nu$_*$	E_{kin}	Pe	Re	$\rho_{\max}$	$\rho_{\min}$
7.00×10^5	2.33×10^5	1.31	1.92	2.27×10^2	2.10×10^1	3.00×10^1	1.07	9.99×10^{-1}
8.00×10^5	2.67×10^5	1.31	1.92	2.95×10^2	2.40×10^1	3.42×10^1	1.07	9.98×10^{-1}
9.00×10^5	3.00×10^5	1.31	1.93	3.72×10^2	2.69×10^1	3.84×10^1	1.07	9.97×10^{-1}
1.00×10^6	3.33×10^5	1.34	2.03	4.98×10^2	3.11×10^1	4.45×10^1	1.07	9.97×10^{-1}
2.00×10^6	6.67×10^5	1.14	1.43	8.36×10^2	4.02×10^1	5.74×10^1	1.08	9.82×10^{-1}
3.00×10^6	1.00×10^6	1.12	1.35	1.83×10^3	5.95×10^1	8.50×10^1	1.09	9.77×10^{-1}
4.00×10^6	1.33×10^6	1.16	1.47	3.41×10^3	8.12×10^1	1.16×10^2	1.09	9.80×10^{-1}
5.00×10^6	1.67×10^6	1.16	1.48	5.46×10^3	1.03×10^2	1.47×10^2	1.09	9.79×10^{-1}
6.00×10^6	2.00×10^6	1.27	1.80	1.02×10^4	1.41×10^2	2.01×10^2	1.09	9.81×10^{-1}
7.00×10^6	2.33×10^6	1.26	1.77	1.32×10^4	1.60×10^2	2.28×10^2	1.09	9.80×10^{-1}
8.00×10^6	2.67×10^6	1.25	1.74	1.64×10^4	1.78×10^2	2.54×10^2	1.09	9.80×10^{-1}
9.00×10^6	3.00×10^6	1.25	1.74	2.04×10^4	1.99×10^2	2.84×10^2	1.09	9.79×10^{-1}
1.00×10^7	3.33×10^6	1.24	1.71	2.43×10^4	2.17×10^2	3.10×10^2	1.09	9.79×10^{-1}
2.00×10^7	6.67×10^6	1.40	2.19	1.03×10^5	4.45×10^2	6.36×10^2	1.09	9.81×10^{-1}
4.00×10^7	1.33×10^7	1.68	3.03	3.79×10^5	8.56×10^2	1.22×10^3	1.09	9.80×10^{-1}
7.00×10^7	2.33×10^7	2.46	5.38	1.00×10^6	1.39×10^3	1.99×10^3	1.08	9.83×10^{-1}
1.00×10^8	3.33×10^7	3.09	7.27	1.62×10^6	1.77×10^3	2.53×10^3	1.08	9.86×10^{-1}
2.00×10^8	6.67×10^7	5.00	1.30×10^1	3.76×10^6	2.70×10^3	3.85×10^3	1.08	9.91×10^{-1}
4.00×10^8	1.33×10^8	8.09	2.23×10^1	8.21×10^6	3.98×10^3	5.69×10^3	1.07	9.95×10^{-1}
7.00×10^8	2.33×10^8	1.05×10^1	2.96×10^1	1.58×10^7	5.53×10^3	7.90×10^3	1.07	9.96×10^{-1}
1.00×10^9	3.33×10^8	1.20×10^1	3.39×10^1	2.40×10^7	6.82×10^3	9.74×10^3	1.07	9.97×10^{-1}

Table 7.45: Results from Section 5.1 for $\Delta T/T_0 = d/H_0 = 0.1$ horizontally periodic for Ek $= 10^{-5}$ with $N_x = 512$, $N_z = 256$.

Ra	Ra$_*$	Nu	Nu$_*$	E_{kin}	Pe	Re	$\rho_{\max}$	$\rho_{\min}$
2.00×10^7	6.67×10^6	1.26	1.78	2.12×10^3	6.41×10^1	9.15×10^1	1.08	9.87×10^{-1}
3.00×10^7	1.00×10^7	1.17	1.51	3.61×10^3	8.35×10^1	1.19×10^2	1.09	9.78×10^{-1}
4.00×10^7	1.33×10^7	1.13	1.39	5.38×10^3	1.02×10^2	1.46×10^2	1.09	9.75×10^{-1}
5.00×10^7	1.67×10^7	1.12	1.37	8.08×10^3	1.25×10^2	1.79×10^2	1.09	9.75×10^{-1}
6.00×10^7	2.00×10^7	1.13	1.39	1.20×10^4	1.52×10^2	2.18×10^2	1.09	9.74×10^{-1}
7.00×10^7	2.33×10^7	1.10	1.29	1.40×10^4	1.65×10^2	2.35×10^2	1.10	9.72×10^{-1}
8.00×10^7	2.67×10^7	1.10	1.29	1.83×10^4	1.88×10^2	2.69×10^2	1.10	9.72×10^{-1}
9.00×10^7	3.00×10^7	1.09	1.28	2.26×10^4	2.09×10^2	2.99×10^2	1.10	9.72×10^{-1}
1.00×10^8	3.33×10^7	1.09	1.26	2.70×10^4	2.29×10^2	3.27×10^2	1.10	9.71×10^{-1}
2.00×10^8	6.67×10^7	1.09	1.27	1.08×10^5	4.57×10^2	6.53×10^2	1.10	9.69×10^{-1}
3.00×10^8	1.00×10^8	1.11	1.32	2.54×10^5	7.00×10^2	1.00×10^3	1.10	9.69×10^{-1}
4.00×10^8	1.33×10^8	1.12	1.37	4.71×10^5	9.54×10^2	1.36×10^3	1.10	9.70×10^{-1}
5.00×10^8	1.67×10^8	1.14	1.41	7.59×10^5	1.21×10^3	1.73×10^3	1.10	9.70×10^{-1}
6.00×10^8	2.00×10^8	1.16	1.47	1.11×10^6	1.46×10^3	2.09×10^3	1.10	9.69×10^{-1}
7.00×10^8	2.33×10^8	1.16	1.48	1.50×10^6	1.70×10^3	2.43×10^3	1.10	9.69×10^{-1}
8.00×10^8	2.67×10^8	1.18	1.53	1.93×10^6	1.93×10^3	2.76×10^3	1.10	9.69×10^{-1}
9.00×10^8	3.00×10^8	1.19	1.58	2.47×10^6	2.19×10^3	3.12×10^3	1.10	9.69×10^{-1}
1.00×10^9	3.33×10^8	1.21	1.63	3.26×10^6	2.51×10^3	3.58×10^3	1.10	9.70×10^{-1}

Table 7.46: Results from Section 5.1 for $\Delta T/T_0 = d/H_0 = 0.1$ horizontally periodic for Ek $= 10^{-6}$ with $N_x = 512$, $N_z = 256$.

Ra	Ra$_*$	Nu	Nu$_*$	E_{kin}	Pe	Re	$\rho_{\max}$	$\rho_{\min}$
7.00×10^3	2.33×10^3	1.13	1.39	1.16×10^1	4.81	6.88	1.01	1.00
1.00×10^4	3.33×10^3	1.25	1.75	3.19×10^1	7.98	1.14×10^1	1.01	1.00
2.00×10^4	6.67×10^3	1.44	2.33	1.09×10^2	1.47×10^1	2.11×10^1	1.01	1.00
4.00×10^4	1.33×10^4	1.62	2.87	2.90×10^2	2.40×10^1	3.43×10^1	1.01	1.00
7.00×10^4	2.33×10^4	1.79	3.36	5.95×10^2	3.44×10^1	4.92×10^1	1.01	1.00
1.00×10^5	3.33×10^4	1.90	3.70	9.21×10^2	4.29×10^1	6.12×10^1	1.01	1.00
2.00×10^5	6.67×10^4	2.15	4.46	2.08×10^3	6.44×10^1	9.19×10^1	1.01	1.00
4.00×10^5	1.33×10^5	2.44	5.32	4.53×10^3	9.50×10^1	1.36×10^2	1.01	1.00
7.00×10^5	2.33×10^5	2.71	6.12	8.35×10^3	1.29×10^2	1.84×10^2	1.01	1.00
1.00×10^6	3.33×10^5	2.89	6.67	1.23×10^4	1.56×10^2	2.23×10^2	1.01	1.00
2.00×10^6	6.67×10^5	3.29	7.88	2.56×10^4	2.26×10^2	3.23×10^2	1.01	1.00
4.00×10^6	1.33×10^6	3.44	8.31	5.64×10^4	3.35×10^2	4.79×10^2	1.01	1.00
7.00×10^6	2.33×10^6	3.70	9.10	1.03×10^5	4.52×10^2	6.46×10^2	1.01	1.00
1.00×10^7	3.33×10^6	3.95	9.84	1.49×10^5	5.44×10^2	7.77×10^2	1.01	1.00
2.00×10^7	6.67×10^6	4.72	1.22×10^1	3.01×10^5	7.75×10^2	1.11×10^3	1.01	1.00
4.00×10^7	1.33×10^7	5.35	1.40×10^1	6.66×10^5	1.15×10^3	1.65×10^3	1.01	1.00
7.00×10^7	2.33×10^7	6.14	1.64×10^1	1.14×10^6	1.51×10^3	2.15×10^3	1.01	1.00
1.00×10^8	3.33×10^7	6.60	1.78×10^1	1.73×10^6	1.86×10^3	2.65×10^3	1.01	1.00
2.00×10^8	6.67×10^7	7.89	2.17×10^1	3.87×10^6	2.77×10^3	3.96×10^3	1.01	1.00
4.00×10^8	1.33×10^8	9.62	2.69×10^1	8.25×10^6	4.05×10^3	5.79×10^3	1.01	1.00
7.00×10^8	2.33×10^8	1.12×10^1	3.16×10^1	1.65×10^7	5.74×10^3	8.20×10^3	1.01	1.00

Table 7.47: Results from Section 5.1 for $\Delta T/T_0 = d/H_0 = 0.01$ horizontally periodic for Ek $= \infty$ with $N_x = 512$, $N_z = 256$.

Ra	Ra$_*$	Nu	Nu$_*$	E_{kin}	Pe	Re	$\rho_{\max}$	$\rho_{\min}$
7.00×10^3	2.33×10^3	1.13	1.38	1.15×10^1	4.79	6.84	1.01	1.00
1.00×10^4	3.33×10^3	1.25	1.75	3.18×10^1	7.96	1.14×10^1	1.01	1.00
2.00×10^4	6.67×10^3	1.44	2.33	1.09×10^2	1.47×10^1	2.10×10^1	1.01	1.00
4.00×10^4	1.33×10^4	1.62	2.87	2.90×10^2	2.40×10^1	3.43×10^1	1.01	1.00
7.00×10^4	2.33×10^4	1.79	3.36	5.95×10^2	3.44×10^1	4.92×10^1	1.01	1.00
1.00×10^5	3.33×10^4	1.90	3.70	9.21×10^2	4.29×10^1	6.12×10^1	1.01	1.00
2.00×10^5	6.67×10^4	2.15	4.46	2.08×10^3	6.44×10^1	9.19×10^1	1.01	1.00
4.00×10^5	1.33×10^5	2.44	5.32	4.53×10^3	9.50×10^1	1.36×10^2	1.01	1.00
7.00×10^5	2.33×10^5	2.71	6.12	8.35×10^3	1.29×10^2	1.84×10^2	1.01	1.00
1.00×10^6	3.33×10^5	2.89	6.67	1.23×10^4	1.56×10^2	2.23×10^2	1.01	1.00
2.00×10^6	6.67×10^5	3.29	7.87	2.56×10^4	2.26×10^2	3.23×10^2	1.01	1.00
4.00×10^6	1.33×10^6	3.44	8.31	5.64×10^4	3.35×10^2	4.79×10^2	1.01	1.00
7.00×10^6	2.33×10^6	3.70	9.10	1.03×10^5	4.52×10^2	6.46×10^2	1.01	1.00

Table 7.48: Results from Section 5.1 for $\Delta T/T_0 = d/H_0 = 0.01$ horizontally periodic for Ek $= 10^{-3}$ with $N_x = 512$, $N_z = 256$.

Ra	Ra$_*$	Nu	Nu$_*$	E_{kin}	Pe	Re	$\rho_{\max}$	$\rho_{\min}$
1.00×10^4	3.33×10^3	1.18	1.53	2.09×10^1	6.45	9.21	1.01	1.00
2.00×10^4	6.67×10^3	1.39	2.18	9.41×10^1	1.37×10^1	1.96×10^1	1.01	1.00
4.00×10^4	1.33×10^4	1.59	2.77	2.72×10^2	2.33×10^1	3.33×10^1	1.01	1.00
7.00×10^4	2.33×10^4	1.76	3.29	5.78×10^2	3.39×10^1	4.85×10^1	1.01	1.00
1.00×10^5	3.33×10^4	1.88	3.65	9.05×10^2	4.25×10^1	6.07×10^1	1.01	1.00
2.00×10^5	6.67×10^4	2.14	4.42	2.07×10^3	6.42×10^1	9.17×10^1	1.01	1.00
4.00×10^5	1.33×10^5	2.43	5.30	4.52×10^3	9.49×10^1	1.36×10^2	1.01	1.00
7.00×10^5	2.33×10^5	2.70	6.10	8.35×10^3	1.29×10^2	1.84×10^2	1.01	1.00
1.00×10^6	3.33×10^5	2.89	6.66	1.23×10^4	1.56×10^2	2.23×10^2	1.01	1.00
2.00×10^6	6.67×10^5	3.29	7.86	2.56×10^4	2.26×10^2	3.23×10^2	1.01	1.00
4.00×10^6	1.33×10^6	3.43	8.29	5.64×10^4	3.35×10^2	4.79×10^2	1.01	1.00

Table 7.49: Results from Section 5.1 for $\Delta T/T_0 = d/H_0 = 0.01$ horizontally periodic for Ek $= 10^{-4}$ with $N_x = 512$, $N_z = 256$.

Ra	Ra$_*$	Nu	Nu$_*$	E_{kin}	Pe	Re	$\rho_{\max}$	$\rho_{\min}$
4.00×10^4	1.33×10^4	1.09	1.28	1.40×10^1	5.28	7.54	1.01	1.00
5.00×10^4	1.67×10^4	1.21	1.63	4.44×10^1	9.41	1.34×10^1	1.01	1.00
6.00×10^4	2.00×10^4	1.30	1.89	8.22×10^1	1.28×10^1	1.83×10^1	1.01	1.00
7.00×10^4	2.33×10^4	1.29	1.86	9.97×10^1	1.41×10^1	2.01×10^1	1.01	1.00
8.00×10^4	2.67×10^4	1.27	1.80	1.12×10^2	1.50×10^1	2.14×10^1	1.01	1.00
9.00×10^4	3.00×10^4	1.25	1.75	1.25×10^2	1.58×10^1	2.25×10^1	1.01	1.00
1.00×10^5	3.33×10^4	1.24	1.71	1.37×10^2	1.65×10^1	2.36×10^1	1.01	1.00
1.50×10^5	5.00×10^4	1.34	2.02	3.25×10^2	2.54×10^1	3.63×10^1	1.01	1.00
2.00×10^5	6.67×10^4	1.37	2.11	5.71×10^2	3.37×10^1	4.82×10^1	1.01	1.00
4.00×10^5	1.33×10^5	1.63	2.88	2.17×10^3	6.58×10^1	9.40×10^1	1.01	9.99×10^{-1}
7.00×10^5	2.33×10^5	1.94	3.82	5.72×10^3	1.07×10^2	1.53×10^2	1.01	1.00
1.00×10^6	3.33×10^5	2.21	4.63	9.80×10^3	1.40×10^2	2.00×10^2	1.01	1.00
2.00×10^6	6.67×10^5	2.74	6.21	2.37×10^4	2.17×10^2	3.10×10^2	1.01	1.00
4.00×10^6	1.33×10^6	3.23	7.70	5.10×10^4	3.19×10^2	4.56×10^2	1.01	1.00
1.00×10^7	3.33×10^6	3.91	9.73	1.42×10^5	5.32×10^2	7.60×10^2	1.01	1.00
2.00×10^7	6.67×10^6	4.83	1.25×10^1	2.83×10^5	7.52×10^2	1.07×10^3	1.01	1.00
4.00×10^7	1.33×10^7	5.72	1.52×10^1	5.64×10^5	1.06×10^3	1.52×10^3	1.01	1.00
7.00×10^7	2.33×10^7	6.51	1.75×10^1	1.02×10^6	1.42×10^3	2.03×10^3	1.01	1.00
1.00×10^8	3.33×10^7	6.75	1.83×10^1	1.56×10^6	1.76×10^3	2.52×10^3	1.01	1.00
2.00×10^8	6.67×10^7	7.89	2.17×10^1	3.66×10^6	2.70×10^3	3.86×10^3	1.01	1.00
4.00×10^8	1.33×10^8	9.54	2.66×10^1	8.52×10^6	4.12×10^3	5.88×10^3	1.01	1.00
7.00×10^8	2.33×10^8	1.12×10^1	3.16×10^1	1.65×10^7	5.73×10^3	8.18×10^3	1.01	1.00

Table 7.50: Results from Section 5.1 for $\Delta T/T_0 = d/H_0 = 0.01$ horizontally periodic for Ek $= 10^{-5}$ with $N_x = 512$, $N_z = 256$.

Ra	Ra$_*$	Nu	Nu$_*$	E_{kin}	Pe	Re	$\rho_{\max}$	$\rho_{\min}$
5.00×10^5	1.67×10^5	1.20	1.60	7.33×10^1	1.21×10^1	1.73×10^1	1.01	1.00
6.00×10^5	2.00×10^5	1.34	2.01	1.80×10^2	1.89×10^1	2.71×10^1	1.01	1.00
7.00×10^5	2.33×10^5	1.36	2.07	2.58×10^2	2.27×10^1	3.24×10^1	1.01	1.00
8.00×10^5	2.67×10^5	1.37	2.10	3.42×10^2	2.61×10^1	3.73×10^1	1.01	1.00
9.00×10^5	3.00×10^5	1.39	2.18	4.13×10^2	2.87×10^1	4.10×10^1	1.01	1.00
1.00×10^6	3.33×10^5	1.31	1.94	4.30×10^2	2.93×10^1	4.18×10^1	1.01	1.00
2.00×10^6	6.67×10^5	1.14	1.43	8.22×10^2	4.05×10^1	5.78×10^1	1.01	9.98×10^{-1}
3.00×10^6	1.00×10^6	1.13	1.39	1.73×10^3	5.88×10^1	8.40×10^1	1.01	9.98×10^{-1}
4.00×10^6	1.33×10^6	1.15	1.45	3.23×10^3	8.02×10^1	1.15×10^2	1.01	9.98×10^{-1}
5.00×10^6	1.67×10^6	1.16	1.48	5.42×10^3	1.04×10^2	1.48×10^2	1.01	9.98×10^{-1}
6.00×10^6	2.00×10^6	1.27	1.81	1.00×10^4	1.41×10^2	2.02×10^2	1.01	9.98×10^{-1}
7.00×10^6	2.33×10^6	1.29	1.88	1.40×10^4	1.67×10^2	2.38×10^2	1.01	9.98×10^{-1}
8.00×10^6	2.67×10^6	1.27	1.82	1.72×10^4	1.85×10^2	2.64×10^2	1.01	9.98×10^{-1}
9.00×10^6	3.00×10^6	1.26	1.78	2.07×10^4	2.03×10^2	2.90×10^2	1.01	9.98×10^{-1}
1.00×10^7	3.33×10^6	1.25	1.76	2.48×10^4	2.22×10^2	3.17×10^2	1.01	9.98×10^{-1}
2.00×10^7	6.67×10^6	1.39	2.16	1.01×10^5	4.48×10^2	6.40×10^2	1.01	9.98×10^{-1}
4.00×10^7	1.33×10^7	1.64	2.93	3.67×10^5	8.55×10^2	1.22×10^3	1.01	9.98×10^{-1}
7.00×10^7	2.33×10^7	2.40	5.21	1.00×10^6	1.41×10^3	2.02×10^3	1.01	9.98×10^{-1}
1.00×10^8	3.33×10^7	3.01	7.02	1.62×10^6	1.80×10^3	2.57×10^3	1.01	9.99×10^{-1}
2.00×10^8	6.67×10^7	4.87	1.26×10^1	3.81×10^6	2.76×10^3	3.94×10^3	1.01	9.99×10^{-1}
4.00×10^8	1.33×10^8	7.94	2.18×10^1	8.36×10^6	4.08×10^3	5.83×10^3	1.01	9.99×10^{-1}
7.00×10^8	2.33×10^8	1.04×10^1	2.91×10^1	1.60×10^7	5.65×10^3	8.07×10^3	1.01	1.00

Table 7.51: Results from Section 5.1 for $\Delta T/T_0 = d/H_0 = 0.01$ horizontally periodic for Ek $= 10^{-6}$ with $N_x = 512$, $N_z = 256$.

Ra	Ra$_*$	Nu	Nu$_*$	E_{kin}	Pe	Re	$\rho_{\max}$	$\rho_{\min}$
1.00×10^5	3.33×10^4	1.41	2.24	8.74×10^1	1.05×10^1	1.50×10^1	2.10	1.09
2.00×10^5	6.67×10^4	1.52	2.55	1.99×10^2	1.57×10^1	2.25×10^1	2.11	1.11
4.00×10^5	1.33×10^5	1.46	2.39	3.56×10^2	2.16×10^1	3.08×10^1	2.09	1.05
7.00×10^5	2.33×10^5	1.59	2.77	7.31×10^2	3.08×10^1	4.40×10^1	2.10	1.07
1.00×10^6	3.33×10^5	1.88	3.64	1.25×10^3	3.79×10^1	5.41×10^1	2.10	1.08
2.00×10^6	6.67×10^5	2.23	4.70	3.10×10^3	6.04×10^1	8.64×10^1	2.11	1.08
4.00×10^6	1.33×10^6	2.68	6.03	7.65×10^3	9.79×10^1	1.40×10^2	2.12	1.10
7.00×10^6	2.33×10^6	2.95	6.84	1.46×10^4	1.37×10^2	1.95×10^2	2.11	1.09
1.00×10^7	3.33×10^6	3.19	7.56	2.31×10^4	1.68×10^2	2.40×10^2	2.11	1.08
2.00×10^7	6.67×10^6	3.76	9.28	5.35×10^4	2.56×10^2	3.65×10^2	2.11	1.08
4.00×10^7	1.33×10^7	4.45	1.14×10^1	1.17×10^5	3.79×10^2	5.42×10^2	2.12	1.08
7.00×10^7	2.33×10^7	5.07	1.32×10^1	2.21×10^5	5.20×10^2	7.43×10^2	2.12	1.08
1.00×10^8	3.33×10^7	5.28	1.38×10^1	3.13×10^5	6.20×10^2	8.86×10^2	2.12	1.08

Table 7.52: Results from section 5.2 with $\Delta T/T_0 = d/H_0 = 2$, Ek $= \infty$ with $N_x = 128$, $N_z = 256$.

Ra	Ra$_*$	Nu	Nu$_*$	E_{kin}	Pe	Re	$\rho_{\max}$	$\rho_{\min}$
2.00×10^5	6.67×10^4	1.15	1.46	3.54×10^1	6.67	9.53	2.08	1.01
4.00×10^5	1.33×10^5	1.67	3.01	3.87×10^2	2.26×10^1	3.23×10^1	2.09	1.02
7.00×10^5	2.33×10^5	1.88	3.65	9.36×10^2	3.53×10^1	5.04×10^1	2.09	1.03
1.00×10^6	3.33×10^5	2.00	4.01	1.52×10^3	4.49×10^1	6.41×10^1	2.10	1.04
2.00×10^6	6.67×10^5	2.25	4.74	3.60×10^3	6.89×10^1	9.84×10^1	2.10	1.06
4.00×10^6	1.33×10^6	2.17	4.50	5.05×10^3	8.04×10^1	1.15×10^2	2.10	1.06
7.00×10^6	2.33×10^6	3.17	7.50	1.48×10^4	1.35×10^2	1.92×10^2	2.11	1.09
1.00×10^7	3.33×10^6	3.56	8.67	2.43×10^4	1.72×10^2	2.45×10^2	2.11	1.09
2.00×10^7	6.67×10^6	3.69	9.08	5.11×10^4	2.50×10^2	3.57×10^2	2.11	1.08
4.00×10^7	1.33×10^7	4.43	1.13×10^1	1.17×10^5	3.79×10^2	5.41×10^2	2.12	1.08
7.00×10^7	2.33×10^7	4.93	1.28×10^1	2.13×10^5	5.11×10^2	7.30×10^2	2.12	1.08
1.00×10^8	3.33×10^7	5.19	1.36×10^1	3.11×10^5	6.18×10^2	8.83×10^2	2.12	1.08

Table 7.53: Results from section 5.2 with $\Delta T/T_0 = d/H_0 = 2$, Ek $= 10^{-3}$ with $N_x = 128$, $N_z = 256$.

Ra	Ra$_*$	Nu	Nu$_*$	E_{kin}	Pe	Re	$\rho_{\max}$	$\rho_{\min}$
2.00×10^6	6.67×10^5	1.35	2.04	2.66×10^2	1.81×10^1	2.59×10^1	2.08	1.00
4.00×10^6	1.33×10^6	3.17	7.51	4.37×10^3	7.62×10^1	1.09×10^2	2.10	1.03
7.00×10^6	2.33×10^6	3.21	7.62	9.12×10^3	1.09×10^2	1.55×10^2	2.10	1.03
1.00×10^7	3.33×10^6	3.46	8.38	1.56×10^4	1.42×10^2	2.03×10^2	2.10	1.05
2.00×10^7	6.67×10^6	4.54	1.16×10^1	5.61×10^4	2.72×10^2	3.89×10^2	2.11	1.07
4.00×10^7	1.33×10^7	5.06	1.32×10^1	1.32×10^5	4.11×10^2	5.87×10^2	2.13	1.10
7.00×10^7	2.33×10^7	5.66	1.50×10^1	2.36×10^5	5.47×10^2	7.81×10^2	2.13	1.11
1.00×10^8	3.33×10^7	5.34	1.40×10^1	2.90×10^5	5.94×10^2	8.49×10^2	2.13	1.11

Table 7.54: Results from section 5.2 with $\Delta T/T_0 = d/H_0 = 2$, Ek $= 10^{-4}$ with $N_x = 128$, $N_z = 256$.

Ra	Ra$_*$	Nu	Nu$_*$	E_{kin}	Pe	Re	$\rho_{\max}$	$\rho_{\min}$
4.00×10^7	1.33×10^7	2.28	4.84	5.04×10^3	8.01×10^1	1.14×10^2	2.08	1.00
7.00×10^7	2.33×10^7	3.74	9.21	2.42×10^4	1.77×10^2	2.53×10^2	2.09	1.02
1.00×10^8	3.33×10^7	4.70	1.21×10^1	5.48×10^4	2.67×10^2	3.82×10^2	2.09	1.01

Table 7.55: Results from section 5.2 with $\Delta T/T_0 = d/H_0 = 2$, Ek $= 10^{-5}$ with $N_x = 128$, $N_z = 256$.

Ra	Ra$_*$	Nu	Nu$_*$	E_{kin}	Pe	Re	$\rho_{\max}$	$\rho_{\min}$
1.00×10^5	3.33×10^4	1.39	2.17	1.08×10^2	1.42×10^1	2.03×10^1	1.13	1.00
2.00×10^5	6.67×10^4	1.49	2.48	2.50×10^2	2.17×10^1	3.10×10^1	1.13	1.00
4.00×10^5	1.33×10^5	1.46	2.39	4.62×10^2	2.95×10^1	4.21×10^1	1.13	1.00
7.00×10^5	2.33×10^5	1.61	2.82	9.91×10^2	4.32×10^1	6.16×10^1	1.13	1.00
1.00×10^6	3.33×10^5	2.06	4.19	2.00×10^3	5.78×10^1	8.26×10^1	1.13	1.00
2.00×10^6	6.67×10^5	2.45	5.34	4.92×10^3	9.20×10^1	1.31×10^2	1.13	1.00
4.00×10^6	1.33×10^6	2.85	6.55	1.12×10^4	1.41×10^2	2.01×10^2	1.13	1.00
7.00×10^6	2.33×10^6	3.23	7.69	2.11×10^4	1.95×10^2	2.79×10^2	1.13	1.00
1.00×10^7	3.33×10^6	3.42	8.27	3.13×10^4	2.38×10^2	3.40×10^2	1.13	1.00
2.00×10^7	6.67×10^6	3.86	9.58	6.81×10^4	3.53×10^2	5.05×10^2	1.13	1.00
4.00×10^7	1.33×10^7	4.32	1.10×10^1	1.47×10^5	5.20×10^2	7.43×10^2	1.13	1.00
7.00×10^7	2.33×10^7	4.87	1.26×10^1	2.84×10^5	7.26×10^2	1.04×10^3	1.13	1.00
1.00×10^8	3.33×10^7	5.62	1.49×10^1	4.52×10^5	9.16×10^2	1.31×10^3	1.13	9.99×10^{-1}
2.00×10^8	6.67×10^7	7.08	1.93×10^1	1.04×10^6	1.39×10^3	1.98×10^3	1.13	1.00
4.00×10^8	1.33×10^8	7.28	1.98×10^1	1.96×10^6	1.90×10^3	2.72×10^3	1.13	1.00
7.00×10^8	2.33×10^8	8.06	2.22×10^1	3.31×10^6	2.49×10^3	3.55×10^3	1.13	1.00
1.00×10^9	3.33×10^8	9.04	2.51×10^1	4.85×10^6	3.02×10^3	4.31×10^3	1.13	1.00

Table 7.56: Results from section 5.2 with $\Delta T/T_0 = d/H_0 = 0.2$, Ek $= \infty$ with $N_x = 128$, $N_z = 256$.

Ra	Ra$_*$	Nu	Nu$_*$	E_{kin}	Pe	Re	$\rho_{\max}$	$\rho_{\min}$
1.00×10^5	3.33×10^4	1.37	2.11	9.92×10^1	1.36×10^1	1.94×10^1	1.13	1.00
2.00×10^5	6.67×10^4	1.28	1.83	1.43×10^2	1.64×10^1	2.34×10^1	1.13	1.00
4.00×10^5	1.33×10^5	1.46	2.39	4.53×10^2	2.92×10^1	4.17×10^1	1.13	1.00
7.00×10^5	2.33×10^5	1.62	2.87	9.99×10^2	4.33×10^1	6.19×10^1	1.13	1.00
1.00×10^6	3.33×10^5	1.75	3.24	1.63×10^3	5.53×10^1	7.91×10^1	1.13	1.00
2.00×10^6	6.67×10^5	2.44	5.32	4.89×10^3	9.17×10^1	1.31×10^2	1.13	1.00
4.00×10^6	1.33×10^6	2.85	6.55	1.12×10^4	1.40×10^2	2.00×10^2	1.13	1.00
7.00×10^6	2.33×10^6	3.23	7.69	2.11×10^4	1.95×10^2	2.79×10^2	1.13	1.00
1.00×10^7	3.33×10^6	3.43	8.28	3.13×10^4	2.38×10^2	3.40×10^2	1.13	1.00
2.00×10^7	6.67×10^6	3.86	9.58	6.81×10^4	3.53×10^2	5.05×10^2	1.13	1.00
4.00×10^7	1.33×10^7	4.33	1.10×10^1	1.47×10^5	5.20×10^2	7.43×10^2	1.13	1.00
7.00×10^7	2.33×10^7	4.87	1.26×10^1	2.85×10^5	7.26×10^2	1.04×10^3	1.13	1.00
1.00×10^8	3.33×10^7	5.65	1.50×10^1	4.54×10^5	9.19×10^2	1.31×10^3	1.13	9.99×10^{-1}
2.00×10^8	6.67×10^7	6.89	1.87×10^1	1.01×10^6	1.36×10^3	1.94×10^3	1.13	1.00
4.00×10^8	1.33×10^8	7.35	2.00×10^1	1.98×10^6	1.91×10^3	2.73×10^3	1.13	1.00
7.00×10^8	2.33×10^8	8.08	2.22×10^1	3.33×10^6	2.49×10^3	3.56×10^3	1.13	1.00
1.00×10^9	3.33×10^8	9.06	2.52×10^1	4.87×10^6	3.02×10^3	4.32×10^3	1.13	1.00

Table 7.57: Results from section 5.2 with $\Delta T/T_0 = d/H_0 = 0.2$, Ek $= 10^{-3}$ with $N_x = 128$, $N_z = 256$.

Ra	Ra$_*$	Nu	Nu$_*$	E_{kin}	Pe	Re	$\rho_{\max}$	$\rho_{\min}$
4.00×10^5	1.33×10^5	1.61	2.84	3.77×10^2	2.66×10^1	3.80×10^1	1.13	1.00
7.00×10^5	2.33×10^5	1.95	3.85	1.14×10^3	4.62×10^1	6.60×10^1	1.13	1.00
1.00×10^6	3.33×10^5	2.10	4.29	1.93×10^3	6.02×10^1	8.60×10^1	1.13	1.00
2.00×10^6	6.67×10^5	2.36	5.07	4.81×10^3	9.51×10^1	1.36×10^2	1.13	1.00
4.00×10^6	1.33×10^6	2.62	5.85	1.08×10^4	1.43×10^2	2.04×10^2	1.13	1.00
7.00×10^6	2.33×10^6	2.72	6.15	1.66×10^4	1.69×10^2	2.42×10^2	1.13	1.00
1.00×10^7	3.33×10^6	3.43	8.28	3.06×10^4	2.34×10^2	3.34×10^2	1.13	1.00
2.00×10^7	6.67×10^6	3.83	9.49	6.58×10^4	3.46×10^2	4.94×10^2	1.13	1.00
4.00×10^7	1.33×10^7	4.29	1.09×10^1	1.47×10^5	5.20×10^2	7.42×10^2	1.13	1.00
7.00×10^7	2.33×10^7	4.86	1.26×10^1	2.82×10^5	7.23×10^2	1.03×10^3	1.13	1.00
1.00×10^8	3.33×10^7	5.50	1.45×10^1	4.43×10^5	9.07×10^2	1.30×10^3	1.13	9.99×10^{-1}
2.00×10^8	6.67×10^7	7.20	1.96×10^1	1.07×10^6	1.41×10^3	2.01×10^3	1.13	1.00
4.00×10^8	1.33×10^8	7.35	2.00×10^1	1.99×10^6	1.92×10^3	2.74×10^3	1.13	1.00
7.00×10^8	2.33×10^8	8.01	2.20×10^1	3.26×10^6	2.47×10^3	3.53×10^3	1.13	1.00
1.00×10^9	3.33×10^8	9.05	2.51×10^1	4.84×10^6	3.02×10^3	4.31×10^3	1.13	1.00

Table 7.58: Results from section 5.2 with $\Delta T/T_0 = d/H_0 = 0.2$, Ek $= 10^{-4}$ with $N_x = 128$, $N_z = 256$.

Ra	Ra$_*$	Nu	Nu$_*$	E_{kin}	Pe	Re	ρ_{max}	ρ_{min}
4.00×10^6	1.33×10^6	2.19	4.57	2.23×10^3	6.40×10^1	9.14×10^1	1.13	1.00
7.00×10^6	2.33×10^6	3.52	8.55	1.02×10^4	1.38×10^2	1.97×10^2	1.13	9.99×10^{-1}
1.00×10^7	3.33×10^6	3.54	8.61	1.65×10^4	1.73×10^2	2.48×10^2	1.13	9.99×10^{-1}
2.00×10^7	6.67×10^6	4.18	1.05×10^1	5.05×10^4	3.04×10^2	4.34×10^2	1.13	1.00
4.00×10^7	1.33×10^7	5.06	1.32×10^1	1.56×10^5	5.41×10^2	7.72×10^2	1.13	1.00
7.00×10^7	2.33×10^7	5.72	1.52×10^1	3.17×10^5	7.70×10^2	1.10×10^3	1.13	1.00
1.00×10^8	3.33×10^7	6.16	1.65×10^1	4.51×10^5	9.18×10^2	1.31×10^3	1.13	1.00
2.00×10^8	6.67×10^7	7.08	1.92×10^1	1.00×10^6	1.37×10^3	1.96×10^3	1.13	1.00
4.00×10^8	1.33×10^8	6.60	1.78×10^1	1.66×10^6	1.77×10^3	2.52×10^3	1.13	9.97×10^{-1}
7.00×10^8	2.33×10^8	7.97	2.19×10^1	3.20×10^6	2.45×10^3	3.50×10^3	1.13	1.00
1.00×10^9	3.33×10^8	8.95	2.48×10^1	4.80×10^6	3.00×10^3	4.29×10^3	1.13	9.98×10^{-1}

Table 7.59: Results from section 5.2 with $\Delta T/T_0 = d/H_0 = 0.2$, Ek $= 10^{-5}$ with $N_x = 128$, $N_z = 256$.

Ra	Ra$_*$	Nu	Nu$_*$	E_{kin}	Pe	Re	ρ_{max}	ρ_{min}
1.00×10^5	3.33×10^4	1.39	2.16	1.08×10^2	1.42×10^1	2.03×10^1	1.13	1.00
2.00×10^5	6.67×10^4	1.49	2.47	2.50×10^2	2.17×10^1	3.10×10^1	1.13	1.00
4.00×10^5	1.33×10^5	1.46	2.39	4.62×10^2	2.95×10^1	4.21×10^1	1.13	1.00
7.00×10^5	2.33×10^5	1.61	2.82	9.90×10^2	4.31×10^1	6.16×10^1	1.13	1.00
1.00×10^6	3.33×10^5	1.70	3.11	1.57×10^3	5.42×10^1	7.75×10^1	1.13	1.00
2.00×10^6	6.67×10^5	1.96	3.88	3.79×10^3	8.44×10^1	1.21×10^2	1.13	1.00
4.00×10^6	1.33×10^6	2.85	6.56	1.12×10^4	1.40×10^2	2.01×10^2	1.13	1.00
7.00×10^6	2.33×10^6	3.23	7.69	2.11×10^4	1.95×10^2	2.79×10^2	1.13	1.00
1.00×10^7	3.33×10^6	3.42	8.27	3.13×10^4	2.38×10^2	3.40×10^2	1.13	1.00
2.00×10^7	6.67×10^6	3.86	9.58	6.81×10^4	3.53×10^2	5.05×10^2	1.13	1.00
4.00×10^7	1.33×10^7	4.31	1.09×10^1	1.47×10^5	5.19×10^2	7.41×10^2	1.13	1.00
7.00×10^7	2.33×10^7	4.87	1.26×10^1	2.84×10^5	7.26×10^2	1.04×10^3	1.13	1.00
1.00×10^8	3.33×10^7	5.72	1.52×10^1	4.71×10^5	9.36×10^2	1.34×10^3	1.13	1.00
1.00×10^8	3.33×10^7	5.63	1.49×10^1	4.52×10^5	9.16×10^2	1.31×10^3	1.13	9.99×10^{-1}
2.00×10^8	6.67×10^7	6.87	1.86×10^1	1.01×10^6	1.36×10^3	1.95×10^3	1.13	1.00
4.00×10^8	1.33×10^8	7.40	2.02×10^1	1.99×10^6	1.92×10^3	2.74×10^3	1.13	1.00
7.00×10^8	2.33×10^8	7.97	2.19×10^1	3.24×10^6	2.46×10^3	3.52×10^3	1.13	1.00
1.00×10^9	3.33×10^8	9.04	2.51×10^1	4.85×10^6	3.02×10^3	4.31×10^3	1.13	1.00

Table 7.60: Results from section 5.2 with $\Delta T/T_0 = d/H_0 = 0.2$, Ek $= \infty$ with $N_x = 128$, $N_z = 256$ restarted from the largest Ra with the same Ek.

Ra	Ra$_*$	Nu	Nu$_*$	E_{kin}	Pe	Re	$\rho_{\max}$	$\rho_{\min}$
1.00×10^5	3.33×10^4	1.37	2.11	9.91×10^1	1.36×10^1	1.94×10^1	1.13	1.00
2.00×10^5	6.67×10^4	1.27	1.80	1.40×10^2	1.62×10^1	2.32×10^1	1.13	1.00
4.00×10^5	1.33×10^5	1.45	2.36	4.54×10^2	2.92×10^1	4.17×10^1	1.13	1.00
7.00×10^5	2.33×10^5	1.62	2.87	9.99×10^2	4.33×10^1	6.19×10^1	1.13	1.00
1.00×10^6	3.33×10^5	1.75	3.24	1.63×10^3	5.53×10^1	7.91×10^1	1.13	1.00
2.00×10^6	6.67×10^5	2.44	5.32	4.89×10^3	9.16×10^1	1.31×10^2	1.13	1.00
4.00×10^6	1.33×10^6	2.85	6.55	1.12×10^4	1.40×10^2	2.01×10^2	1.13	1.00
7.00×10^6	2.33×10^6	3.23	7.69	2.11×10^4	1.95×10^2	2.79×10^2	1.13	1.00
1.00×10^7	3.33×10^6	3.43	8.28	3.13×10^4	2.38×10^2	3.40×10^2	1.13	1.00
2.00×10^7	6.67×10^6	3.86	9.58	6.81×10^4	3.53×10^2	5.05×10^2	1.13	1.00
4.00×10^7	1.33×10^7	4.30	1.09×10^1	1.46×10^5	5.17×10^2	7.39×10^2	1.13	1.00
7.00×10^7	2.33×10^7	4.87	1.26×10^1	2.84×10^5	7.26×10^2	1.04×10^3	1.13	1.00
1.00×10^8	3.33×10^7	5.74	1.52×10^1	4.72×10^5	9.37×10^2	1.34×10^3	1.13	1.00
1.00×10^8	3.33×10^7	5.65	1.50×10^1	4.54×10^5	9.19×10^2	1.31×10^3	1.13	9.99×10^{-1}
2.00×10^8	6.67×10^7	7.56	2.07×10^1	1.12×10^6	1.45×10^3	2.07×10^3	1.13	1.00
4.00×10^8	1.33×10^8	7.32	2.00×10^1	1.97×10^6	1.91×10^3	2.72×10^3	1.13	1.00
7.00×10^8	2.33×10^8	8.07	2.22×10^1	3.34×10^6	2.50×10^3	3.57×10^3	1.13	1.00
1.00×10^9	3.33×10^8	9.06	2.52×10^1	4.87×10^6	3.02×10^3	4.32×10^3	1.13	1.00

Table 7.61: Results from section 5.2 with $\Delta T/T_0 = d/H_0 = 0.2$, Ek $= 10^{-3}$ with $N_x = 128$, $N_z = 256$ restarted from the largest Ra with the same Ek.

Ra	Ra$_*$	Nu	Nu$_*$	E_{kin}	Pe	Re	$\rho_{\max}$	$\rho_{\min}$
4.00×10^5	1.33×10^5	1.61	2.84	3.77×10^2	2.66×10^1	3.80×10^1	1.13	1.00
7.00×10^5	2.33×10^5	1.95	3.85	1.14×10^3	4.62×10^1	6.60×10^1	1.13	1.00
1.00×10^6	3.33×10^5	2.09	4.28	1.93×10^3	6.02×10^1	8.60×10^1	1.13	1.00
2.00×10^6	6.67×10^5	2.36	5.07	4.81×10^3	9.51×10^1	1.36×10^2	1.13	1.00
4.00×10^6	1.33×10^6	2.62	5.85	1.08×10^4	1.43×10^2	2.04×10^2	1.13	1.00
7.00×10^6	2.33×10^6	2.03	4.08	1.08×10^4	1.43×10^2	2.04×10^2	1.13	9.99×10^{-1}
1.00×10^7	3.33×10^6	3.43	8.28	3.06×10^4	2.34×10^2	3.34×10^2	1.13	1.00
2.00×10^7	6.67×10^6	3.83	9.50	6.58×10^4	3.46×10^2	4.94×10^2	1.13	1.00
4.00×10^7	1.33×10^7	4.29	1.09×10^1	1.47×10^5	5.20×10^2	7.42×10^2	1.13	1.00
7.00×10^7	2.33×10^7	4.85	1.26×10^1	2.82×10^5	7.22×10^2	1.03×10^3	1.13	1.00
1.00×10^8	3.33×10^7	5.50	1.45×10^1	4.43×10^5	9.07×10^2	1.30×10^3	1.13	9.99×10^{-1}
1.00×10^8	3.33×10^7	5.38	1.42×10^1	4.33×10^5	8.93×10^2	1.28×10^3	1.13	1.00
2.00×10^8	6.67×10^7	7.41	2.02×10^1	1.11×10^6	1.44×10^3	2.05×10^3	1.13	1.00
4.00×10^8	1.33×10^8	7.48	2.04×10^1	2.03×10^6	1.93×10^3	2.76×10^3	1.13	1.00
7.00×10^8	2.33×10^8	8.09	2.23×10^1	3.32×10^6	2.49×10^3	3.56×10^3	1.13	1.00
1.00×10^9	3.33×10^8	9.05	2.51×10^1	4.84×10^6	3.02×10^3	4.31×10^3	1.13	1.00

Table 7.62: Results from section 5.2 with $\Delta T/T_0 = d/H_0 = 0.2$, Ek $= 10^{-4}$ with $N_x = 128$, $N_z = 256$ restarted from the largest Ra with the same Ek.

Ra	Ra$_*$	Nu	Nu$_*$	E_{kin}	Pe	Re	$\rho_{\max}$	$\rho_{\min}$
4.00×10^6	1.33×10^6	2.19	4.57	2.22×10^3	6.37×10^1	9.11×10^1	1.13	1.00
7.00×10^6	2.33×10^6	3.47	8.40	1.00×10^4	1.36×10^2	1.95×10^2	1.13	1.00
1.00×10^7	3.33×10^6	3.49	8.48	1.63×10^4	1.72×10^2	2.46×10^2	1.13	9.99×10^{-1}
2.00×10^7	6.67×10^6	4.16	1.05×10^1	5.03×10^4	3.03×10^2	4.32×10^2	1.13	1.00
4.00×10^7	1.33×10^7	5.06	1.32×10^1	1.56×10^5	5.41×10^2	7.72×10^2	1.13	1.00
7.00×10^7	2.33×10^7	5.72	1.52×10^1	3.17×10^5	7.70×10^2	1.10×10^3	1.13	1.00
1.00×10^8	3.33×10^7	6.16	1.65×10^1	4.51×10^5	9.18×10^2	1.31×10^3	1.13	1.00
1.00×10^8	3.33×10^7	6.13	1.64×10^1	4.56×10^5	9.24×10^2	1.32×10^3	1.13	1.00
2.00×10^8	6.67×10^7	7.11	1.93×10^1	1.01×10^6	1.37×10^3	1.96×10^3	1.13	1.00
4.00×10^8	1.33×10^8	6.59	1.78×10^1	1.66×10^6	1.77×10^3	2.52×10^3	1.13	9.97×10^{-1}
7.00×10^8	2.33×10^8	7.96	2.19×10^1	3.17×10^6	2.44×10^3	3.49×10^3	1.13	9.98×10^{-1}
1.00×10^9	3.33×10^8	8.95	2.48×10^1	4.80×10^6	3.00×10^3	4.29×10^3	1.13	9.98×10^{-1}

Table 7.63: Results from section 5.2 with $\Delta T/T_0 = d/H_0 = 0.2$, Ek $= 10^{-5}$ with $N_x = 128$, $N_z = 256$ restarted from the largest Ra with the same Ek.

Ra	Ra$_*$	Nu	Nu$_*$	E_{kin}	Pe	Re	$\rho_{\max}$	$\rho_{\min}$
1.00×10^5	3.33×10^4	1.38	2.15	1.10×10^2	1.48×10^1	2.11×10^1	1.01	1.00
2.00×10^5	6.67×10^4	1.49	2.47	2.58×10^2	2.26×10^1	3.23×10^1	1.01	1.00
4.00×10^5	1.33×10^5	1.46	2.38	4.71×10^2	3.06×10^1	4.37×10^1	1.01	1.00
7.00×10^5	2.33×10^5	1.60	2.80	1.01×10^3	4.49×10^1	6.41×10^1	1.01	1.00
1.00×10^6	3.33×10^5	2.06	4.18	2.06×10^3	6.04×10^1	8.63×10^1	1.01	1.00
2.00×10^6	6.67×10^5	2.45	5.36	5.11×10^3	9.64×10^1	1.38×10^2	1.01	1.00
4.00×10^6	1.33×10^6	2.87	6.62	1.17×10^4	1.48×10^2	2.11×10^2	1.01	1.00
7.00×10^6	2.33×10^6	3.23	7.69	2.19×10^4	2.04×10^2	2.91×10^2	1.01	1.00
1.00×10^7	3.33×10^6	3.42	8.26	3.23×10^4	2.48×10^2	3.55×10^2	1.01	1.00
2.00×10^7	6.67×10^6	3.86	9.59	7.05×10^4	3.69×10^2	5.27×10^2	1.01	1.00
4.00×10^7	1.33×10^7	4.30	1.09×10^1	1.55×10^5	5.50×10^2	7.85×10^2	1.01	1.00
7.00×10^7	2.33×10^7	4.92	1.27×10^1	2.98×10^5	7.63×10^2	1.09×10^3	1.01	1.00
1.00×10^8	3.33×10^7	5.61	1.48×10^1	4.66×10^5	9.57×10^2	1.37×10^3	1.01	1.00

Table 7.64: Results from section 5.2 with $\Delta T/T_0 = d/H_0 = 0.02$, Ek $= \infty$ with $N_x = 128$, $N_z = 256$.

Ra	Ra$_*$	Nu	Nu$_*$	E_{kin}	Pe	Re	$\rho_{\max}$	$\rho_{\min}$
1.00×10^5	3.33×10^4	1.38	2.15	1.10×10^2	1.48×10^1	2.11×10^1	1.01	1.00
2.00×10^5	6.67×10^4	1.49	2.47	2.57×10^2	2.26×10^1	3.23×10^1	1.01	1.00
4.00×10^5	1.33×10^5	1.46	2.38	4.71×10^2	3.06×10^1	4.37×10^1	1.01	1.00
7.00×10^5	2.33×10^5	1.60	2.80	1.01×10^3	4.49×10^1	6.41×10^1	1.01	1.00
1.00×10^6	3.33×10^5	2.05	4.16	2.05×10^3	6.02×10^1	8.60×10^1	1.01	1.00
2.00×10^6	6.67×10^5	2.46	5.37	5.13×10^3	9.65×10^1	1.38×10^2	1.01	1.00
4.00×10^6	1.33×10^6	2.87	6.62	1.17×10^4	1.48×10^2	2.11×10^2	1.01	1.00
7.00×10^6	2.33×10^6	3.23	7.69	2.19×10^4	2.04×10^2	2.91×10^2	1.01	1.00
1.00×10^7	3.33×10^6	3.42	8.26	3.23×10^4	2.48×10^2	3.55×10^2	1.01	1.00
2.00×10^7	6.67×10^6	3.86	9.59	7.05×10^4	3.69×10^2	5.27×10^2	1.01	1.00
4.00×10^7	1.33×10^7	4.30	1.09×10^1	1.55×10^5	5.50×10^2	7.85×10^2	1.01	1.00
7.00×10^7	2.33×10^7	4.89	1.27×10^1	2.96×10^5	7.61×10^2	1.09×10^3	1.01	1.00
1.00×10^8	3.33×10^7	5.66	1.50×10^1	4.70×10^5	9.61×10^2	1.37×10^3	1.01	1.00

Table 7.65: Results from section 5.2 with $\Delta T/T_0 = d/H_0 = 0.02$, Ek $= 10^{-3}$ with $N_x = 128$, $N_z = 256$.

Ra	Ra$_*$	Nu	Nu$_*$	E_{kin}	Pe	Re	$\rho_{\max}$	$\rho_{\min}$
1.00×10^5	3.33×10^4	1.36	2.09	1.01×10^2	1.42×10^1	2.03×10^1	1.01	1.00
2.00×10^5	6.67×10^4	1.27	1.81	1.43×10^2	1.68×10^1	2.40×10^1	1.01	1.00
4.00×10^5	1.33×10^5	1.46	2.37	4.60×10^2	3.02×10^1	4.32×10^1	1.01	1.00
7.00×10^5	2.33×10^5	1.61	2.82	1.01×10^3	4.47×10^1	6.38×10^1	1.01	1.00
1.00×10^6	3.33×10^5	1.74	3.21	1.67×10^3	5.75×10^1	8.22×10^1	1.01	1.00
2.00×10^6	6.67×10^5	2.45	5.34	5.08×10^3	9.60×10^1	1.37×10^2	1.01	1.00
4.00×10^6	1.33×10^6	2.87	6.62	1.17×10^4	1.48×10^2	2.11×10^2	1.01	1.00
7.00×10^6	2.33×10^6	3.23	7.69	2.18×10^4	2.04×10^2	2.91×10^2	1.01	1.00
1.00×10^7	3.33×10^6	3.42	8.27	3.23×10^4	2.48×10^2	3.55×10^2	1.01	1.00
2.00×10^7	6.67×10^6	3.86	9.59	7.04×10^4	3.69×10^2	5.27×10^2	1.01	1.00
4.00×10^7	1.33×10^7	4.29	1.09×10^1	1.55×10^5	5.50×10^2	7.85×10^2	1.01	1.00
7.00×10^7	2.33×10^7	4.90	1.27×10^1	2.97×10^5	7.62×10^2	1.09×10^3	1.01	1.00
1.00×10^8	3.33×10^7	5.63	1.49×10^1	4.68×10^5	9.59×10^2	1.37×10^3	1.01	1.00

Table 7.66: Results from section 5.2 with $\Delta T/T_0 = d/H_0 = 0.02$, Ek $= 10^{-4}$ with $N_x = 128$, $N_z = 256$.

Ra	Ra$_*$	Nu	Nu$_*$	E_{kin}	Pe	Re	$\rho_{\max}$	$\rho_{\min}$
4.00×10^5	1.33×10^5	1.56	2.69	3.33×10^2	2.57×10^1	3.67×10^1	1.01	1.00
7.00×10^5	2.33×10^5	1.94	3.82	1.12×10^3	4.71×10^1	6.73×10^1	1.01	1.00
1.00×10^6	3.33×10^5	2.10	4.30	1.94×10^3	6.21×10^1	8.87×10^1	1.01	1.00
2.00×10^6	6.67×10^5	2.36	5.07	4.90×10^3	9.87×10^1	1.41×10^2	1.01	1.00
4.00×10^6	1.33×10^6	2.61	5.84	1.11×10^4	1.49×10^2	2.12×10^2	1.01	1.00
7.00×10^6	2.33×10^6	2.81	6.44	2.02×10^4	2.00×10^2	2.86×10^2	1.01	1.00
1.00×10^7	3.33×10^6	3.47	8.41	3.23×10^4	2.46×10^2	3.52×10^2	1.01	1.00
2.00×10^7	6.67×10^6	3.85	9.56	6.76×10^4	3.61×10^2	5.15×10^2	1.01	1.00
4.00×10^7	1.33×10^7	4.27	1.08×10^1	1.51×10^5	5.42×10^2	7.74×10^2	1.01	1.00
7.00×10^7	2.33×10^7	4.82	1.25×10^1	2.87×10^5	7.50×10^2	1.07×10^3	1.01	1.00
1.00×10^8	3.33×10^7	5.63	1.49×10^1	4.70×10^5	9.60×10^2	1.37×10^3	1.01	1.00

Table 7.67: Results from section 5.2 with $\Delta T/T_0 = d/H_0 = 0.02$, Ek $= 10^{-5}$ with $N_x = 128$, $N_z = 256$.

Ek	$\Delta T/T_0 = 2.00 \times 10^{-2}$	1.00×10^{-1}	2.00×10^{-1}	1.00	2.00
1.00×10^{-1}					
7.00×10^{-2}	2.33×10^3	2.30×10^3	2.28×10^3	2.17×10^3	2.15×10^3
4.00×10^{-2}	2.33×10^3	2.30×10^3	2.28×10^3	2.21×10^3	2.26×10^3
2.00×10^{-2}	2.33×10^3	2.31×10^3	2.29×10^3	2.37×10^3	2.67×10^3
1.00×10^{-2}	2.33×10^3	2.32×10^3	2.33×10^3	2.88×10^3	3.79×10^3
7.00×10^{-3}	2.33×10^3	2.33×10^3	2.38×10^3	3.42×10^3	4.87×10^3
4.00×10^{-3}	2.33×10^3	2.39×10^3	2.57×10^3	4.91×10^3	7.72×10^3
2.00×10^{-3}	2.35×10^3	2.61×10^3	3.22×10^3	8.60×10^3	1.46×10^4
1.00×10^{-3}	2.39×10^3	3.29×10^3	4.82×10^3	1.61×10^4	2.87×10^4
7.00×10^{-4}	2.44×10^3	3.97×10^3	6.27×10^3	2.27×10^4	4.07×10^4
4.00×10^{-4}	2.65×10^3	5.80×10^3	9.96×10^3	3.91×10^4	6.96×10^4
2.00×10^{-4}	3.35×10^3	1.02×10^4	1.88×10^4		
1.00×10^{-4}	5.04×10^3	1.94×10^4	3.70×10^4		
7.00×10^{-5}	6.57×10^3	2.72×10^4	5.25×10^4		
4.00×10^{-5}	1.04×10^4	4.68×10^4	9.32×10^4		
2.00×10^{-5}	1.98×10^4				
1.00×10^{-5}	3.83×10^4				

Table 7.68: Critical Rayleigh number Ra_c for different Ek at specific $\Delta T/T_0 = d/H_0$ with periodic horizontal and free-slip vertical boundaries, and $L/d = 2$.

Ek	$\Delta T/T_0 = 1.00 \times 10^{-2}$	2.00×10^{-2}	1.00×10^{-1}	2.00×10^{-1}	1.00
1.00×10^{-1}					
7.00×10^{-2}	5.18×10^3	5.17×10^3	5.11×10^3	5.04×10^3	4.76×10^3
4.00×10^{-2}	5.18×10^3	5.17×10^3	5.11×10^3	5.05×10^3	4.81×10^3
2.00×10^{-2}	5.18×10^3	5.17×10^3	5.11×10^3	5.06×10^3	5.01×10^3
1.00×10^{-2}	5.18×10^3	5.17×10^3	5.13×10^3	5.11×10^3	5.74×10^3
7.00×10^{-3}	5.18×10^3	5.17×10^3	5.14×10^3	5.17×10^3	6.58×10^3
4.00×10^{-3}	5.18×10^3	5.18×10^3	5.21×10^3	5.42×10^3	9.18×10^3
2.00×10^{-3}	5.18×10^3	5.19×10^3	5.50×10^3	6.37×10^3	1.66×10^4
1.00×10^{-3}	5.20×10^3	5.24×10^3	6.50×10^3	9.12×10^3	2.79×10^4
7.00×10^{-4}	5.22×10^3	5.31×10^3	7.62×10^3	1.19×10^4	3.76×10^4
4.00×10^{-4}	5.29×10^3	5.58×10^3	1.10×10^4	1.97×10^4	6.22×10^4
2.00×10^{-4}	5.59×10^3	6.61×10^3	2.01×10^4	3.23×10^4	1.21×10^5
1.00×10^{-4}	6.62×10^3	9.55×10^3	3.31×10^4	5.88×10^4	
7.00×10^{-5}	7.79×10^3	1.25×10^4	4.46×10^4	8.16×10^4	
4.00×10^{-5}	1.13×10^4	2.05×10^4	7.39×10^4	1.39×10^5	
2.00×10^{-5}			1.43×10^5		
1.00×10^{-5}		6.21×10^4	2.81×10^5		

Table 7.69: Critical Rayleigh number Ra_c for different Ek at specific $\Delta T/T_0 = {}^d\!/_{H_0}$ with periodic horizontal and no-slip vertical boundaries, and $L/d = 2$.

Ek	$\Delta T/T_0 = 1.00 \times 10^{-1}$
1.00×10^{-1}	
7.00×10^{-2}	5.11×10^3
4.00×10^{-2}	5.12×10^3
2.00×10^{-2}	5.15×10^3
1.00×10^{-2}	5.27×10^3
7.00×10^{-3}	5.49×10^3
4.00×10^{-3}	6.17×10^3
2.00×10^{-3}	6.64×10^3
1.00×10^{-3}	8.05×10^3
7.00×10^{-4}	9.46×10^3
4.00×10^{-4}	1.34×10^4
2.00×10^{-4}	2.33×10^4
1.00×10^{-4}	4.63×10^4
7.00×10^{-5}	6.92×10^4
4.00×10^{-5}	1.30×10^5
2.00×10^{-5}	3.02×10^5
1.00×10^{-5}	

Table 7.70: Critical Rayleigh number Ra_c for different Ek at specific $\Delta T/T_0 = {}^d\!/_{H_0}$ with free-slip horizontal and no-slip vertical boundaries, and $L/d = 2$.

Ek	$\Delta T/T_0 = 1.00 \times 10^{-2}$	2.00×10^{-2}	1.00×10^{-1}	2.00×10^{-1}	1.00	2.00
1.00×10^{-1}						
7.00×10^{-2}	2.33×10^3		2.30×10^3	2.28×10^3	2.19×10^3	
4.00×10^{-2}	2.33×10^3	2.33×10^3	2.30×10^3	2.28×10^3	2.26×10^3	2.44×10^3
2.00×10^{-2}	2.33×10^3		2.31×10^3	2.30×10^3	2.61×10^3	
1.00×10^{-2}	2.33×10^3	2.34×10^3	2.33×10^3	2.37×10^3	4.58×10^3	7.05×10^3
7.00×10^{-3}	2.34×10^3		2.35×10^3	2.47×10^3		
4.00×10^{-3}	2.34×10^3	2.34×10^3	2.46×10^3	2.91×10^3	9.52×10^3	1.65×10^4
2.00×10^{-3}	2.34×10^3		2.98×10^3			
1.00×10^{-3}	2.36×10^3	2.45×10^3	6.54×10^3	9.25×10^3	3.88×10^4	8.22×10^4
7.00×10^{-4}	2.39×10^3		7.59×10^3			
4.00×10^{-4}	2.50×10^3	3.03×10^3	1.16×10^4	2.20×10^4	1.25×10^5	
2.00×10^{-4}	3.04×10^3		2.26×10^4			
1.00×10^{-4}		9.71×10^3	4.71×10^4	1.08×10^5		
7.00×10^{-5}			7.26×10^4			
4.00×10^{-5}		2.32×10^4	1.48×10^5	3.13×10^5		
2.00×10^{-5}			3.21×10^5			
1.00×10^{-5}				1.77×10^6		

Table 7.71: Critical Rayleigh number Ra_c for different Ek at specific $\Delta T/T_0 = d/H_0$ with free-slip horizontal and free-slip vertical boundaries, and $L/d = 1$.

Ek	PF2 $k_{x,c}$	PF2 $\omega_{x,c}$	PN2 $k_{x,c}$	PN2 $\omega_{x,c}$	FN2 $k_{x,c}$	FN2 $\omega_{x,c}$	FF1 $k_{x,c}$	FF1 $\omega_{x,c}$
1.00×10^{-1}	1.00		1.00		1.00	7.00×10^{-2}	1.00	2.80×10^{-1}
7.00×10^{-2}	1.00		1.00		1.00	1.40×10^{-1}	1.00	2.80×10^{-1}
4.00×10^{-2}	1.00		1.00		1.00	7.00×10^{-2}	1.00	2.80×10^{-1}
2.00×10^{-2}	1.00		1.00		1.00	7.00×10^{-2}	1.00	2.80×10^{-1}
1.00×10^{-2}	1.00		1.00		1.00	7.00×10^{-2}	1.00	2.80×10^{-1}
7.00×10^{-3}	1.00		1.00		1.00	3.50×10^{-2}	1.00	2.80×10^{-1}
4.00×10^{-3}	1.00		1.00		1.00	2.80×10^{-1}	1.00	2.80×10^{-1}
2.00×10^{-3}	1.00		1.00		1.00	8.00×10^{-1}	1.00	1.40×10^{-1}
1.00×10^{-3}	1.00		1.00		1.00	1.70	1.00	4.85×10^{-1}
7.00×10^{-4}	1.00		1.00		1.00	2.45	1.00	1.40
4.00×10^{-4}	1.00		1.00		2.00	4.10	1.00	2.90
2.00×10^{-4}	1.00		2.00		2.00	7.10	1.00	5.95
1.00×10^{-4}	1.00		2.00		2.00	1.12×10^{1}	1.00	1.03×10^{1}
7.00×10^{-5}	1.00		2.00		3.00	1.43×10^{1}	2.00	1.33×10^{1}
4.00×10^{-5}	1.00		2.00		3.00	2.03×10^{1}	2.00	2.04×10^{1}
2.00×10^{-5}			2.00		4.00	3.05×10^{1}	2.00	3.21×10^{1}
1.00×10^{-5}			2.00					

Table 7.72: Critical wave number $k_{x,c}/\pi$ and frequency $\omega_{x,c}$ for $\Delta T/T_0 = d/H_0 = 0.1$ and different boundary conditions: "PF2" horizontall periodic and vertical free slip with $L/d = 2$, "PN2" horozontally periodic and vertically no slip with $L/d = 2$, "FN2" horizontally free-slip and vertically no-slip with $L/d = 2$, and "FF1" horizontally free-slip and vertically free-slip with $L/d = 1$.

Bibliography

Abkarian, Manouk et al. (Oct. 2020). "Speech can produce jet-like transport relevant to asymptomatic spreading of virus". In: *Proceedings of the National Academy of Sciences* 117.41, pp. 25237–25245. DOI: 10.1073/pnas.2012156117.

Albin, E., Y. D'Angelo, and L. Vervisch (2012). "Using staggered grids with characteristic boundary conditions when solving compressible reactive Navier-Stokes equations". en. In: *International Journal for Numerical Methods in Fluids* 68.5, pp. 546–563. ISSN: 1097-0363. DOI: 10.1002/fld.2520.

Bayly, B. J. (Oct. 1986). "Three-Dimensional Instability of Elliptical Flow". In: *Physical Review Letters* 57.17. Publisher: American Physical Society, pp. 2160–2163. DOI: 10.1103/PhysRevLett.57.2160.

Brown, Benjamin P., Geoffrey M. Vasil, and Ellen G. Zweibel (Aug. 2012). "ENERGY CONSERVATION AND GRAVITY WAVES IN SOUND-PROOF TREATMENTS OF STELLAR INTERIORS. PART I. ANELASTIC APPROXIMATIONS". en. In: *The Astrophysical Journal* 756, p. 109. ISSN: 0004-637X. DOI: 10.1088/0004-637X/756/2/109.

Busse, Friedrich H. and Radostin D. Simitev (July 2014). "Quasi-geostrophic approximation of anelastic convection". en. In: *Journal of Fluid Mechanics* 751, pp. 216–227. ISSN: 0022-1120, 1469-7645. DOI: 10.1017/jfm.2014.293.

Chandrasekhar, Subrahmanyan (1961). *Hydrodynamic and hydromagnetic stability*. The international series of monographs in physics. Oxford: Clarendon Press.

Chorin, Alexandre Joel (Aug. 1967). "A numerical method for solving incompressible viscous flow problems". en. In: *Journal of Computational Physics* 2.1, pp. 12–26. ISSN: 0021-9991. DOI: 10.1016/0021-9991(67)90037-X.

Clausen, N. and A. Tilgner (Feb. 2014). "Elliptical instability of compressible flow in ellipsoids". en. In: *Astronomy & Astrophysics* 562, A25. ISSN: 0004-6361, 1432-0746. DOI: 10.1051/0004-6361/201322817.

Craik, A. D. D. (Jan. 1989). "The stability of unbounded two- and three-dimensional flows subject to body forces: some exact solutions". en. In: *Journal of Fluid Mechanics* 198, pp. 275–292. ISSN: 1469-7645, 0022-1120. DOI: 10.1017/S0022112089000133.

Craik, A. D. D., W. O. Criminale, and Michael Gaster (July 1986). "Evolution of wavelike disturbances in shear flows : a class of exact solutions of the Navier-Stokes equations". In: *Proceedings of the Royal Society of London. A. Mathematical and Physical Sciences* 406.1830, pp. 13–26. DOI: 10.1098/rspa.1986.0061.

Currie, Laura K. and Steven M. Tobias (Jan. 2016). "Mean flow generation in rotating anelastic two-dimensional convection". In: *Physics of Fluids* 28.1, p. 017101. ISSN: 1070-6631. DOI: 10.1063/1.4939300.

Ecke, Robert E. and Olga Shishkina (2023). "Turbulent Rotating Rayleigh–Bénard Convection". In: *Annual Review of Fluid Mechanics* 55.1, pp. 603–638. DOI: 10.1146/annurev-fluid-120720-020446.

Fletcher, Clive A. J. (2000). *Fundamental and general techniques*. 2nd ed., 4th print. Springer series in computational physics. Series Title: Springer series in computational physics. Berlin [u.a.]: Springer. ISBN: 978-3-540-53058-9.

Goepfert, O. and A. Tilgner (Oct. 2016). "Dynamos in precessing cubes". en. In: *New Journal of Physics* 18.10, p. 103019. ISSN: 1367-2630. DOI: 10.1088/1367-2630/18/10/103019.

Greenspan, Harvey P. (1968). *The theory of rotating fluids*. Cambridge monographs on mechanics and applied mathematics. Series Title: Cambridge monographs on mechanics and applied mathematics. London: Cambridge Univ. Pr. ISBN: 978-0-521-05147-7.

Griebel, Michael, Thomas Dornseifer, and Tilman Neunhoeffer (1998). *Numerical simulation in fluid dynamics: a practical introduction*. SIAM monographs on mathematical modeling and computation. - Philadelphia, Pa. : SIAM, 1997-2005 ; ZDB-ID: 2198776-2 3. Series Title: SIAM monographs on mathematical modeling and computation. - Philadelphia, Pa. : SIAM, 1997-2005 ; ZDB-ID: 2198776-2. Philadelphia, Pa.: SIAM.

Grossmann, Siegfried and Detlef Lohse (Mar. 2000). "Scaling in thermal convection: a unifying theory". en. In: *Journal of Fluid Mechanics* 407, pp. 27–56. ISSN: 1469-7645, 0022-1120. DOI: 10.1017/S0022112099007545.

– (Apr. 2001). "Thermal Convection for Large Prandtl Numbers". In: *Physical Review Letters* 86.15, pp. 3316–3319. DOI: 10.1103/PhysRevLett.86.3316.

– (July 2002). "Prandtl and Rayleigh number dependence of the Reynolds number in turbulent thermal convection". In: *Physical Review E* 66.1, p. 016305. DOI: 10.1103/PhysRevE.66.016305.

Hardenberg, J. von et al. (Sept. 2015). "Generation of Large-Scale Winds in Horizontally Anisotropic Convection". In: *Physical Review Letters* 115.13, p. 134501. DOI: `10.1103/PhysRevLett.115.134501`.

Jiang, Hechuan et al. (Oct. 2020). "Supergravitational turbulent thermal convection". In: *Science Advances* 6, eabb8676. DOI: `10.1126/sciadv.abb8676`.

Jones, Chris A., Krzysztof A. Mizerski, and Mouloud Kessar (Jan. 2022). "Fully developed anelastic convection with no-slip boundaries". en. In: *Journal of Fluid Mechanics* 930, A13. ISSN: 0022-1120, 1469-7645. DOI: `10.1017/jfm.2021.905`.

Jordan, Dominic W. and Peter Smith (2007). *Nonlinear ordinary differential equations: problems and solutions ; a sourcebook for scientists and engineers*. 1. publ. Oxford [u.a.]: Oxford Univ. Press. ISBN: 978-0-19-921203-3.

Kennedy, Christopher A., Mark H. Carpenter, and R. Michael Lewis (Nov. 2000). "Low-storage, explicit Runge-Kutta schemes for the compressible Navier-Stokes equations". In: *Applied Numerical Mathematics* 35.3, pp. 177–219. ISSN: 0168-9274. DOI: `10.1016/S0168-9274(99)00141-5`.

Kerswell, Richard R. (2002). "Elliptical Instability". In: *Annual Review of Fluid Mechanics* 34.1. _eprint: https://doi.org/10.1146/annurev.fluid.34.081701.171829, pp. 83–113. DOI: `10.1146/annurev.fluid.34.081701.171829`.

Kundu, Pijush K. and Ira M. Cohen (Aug. 2001). *Fluid Mechanics, Second Edition*. Englisch. 2nd ed. San Diego: Academic Press. ISBN: 978-0-12-178251-1.

Landman, M. J. and P. G. Saffman (Aug. 1987). "The three-dimensional instability of strained vortices in a viscous fluid". In: *The Physics of Fluids* 30.8, pp. 2339–2342. ISSN: 0031-9171. DOI: `10.1063/1.866124`.

Lüdemann, K. and A. Tilgner (May 2022). *Transition to three dimensional flow in thermal convection with spanwise rotation*. Tech. rep. arXiv:2205.05431. arXiv:2205.05431 [physics] type: article. arXiv. DOI: `10.48550/arXiv.2205.05431`.

Menaut, Rémi et al. (Mar. 2019). "Experimental study of convection in the compressible regime". In: *Physical Review Fluids* 4.3. Publisher: American Physical Society, p. 033502. DOI: `10.1103/PhysRevFluids.4.033502`.

Ogura, Yoshimitsu and Norman A. Phillips (Nov. 1961). "Scale analysis of deep and shallow convection in the Atmosphere". en. In:

Pandey, Ambrish et al. (June 2016). "Similarities between 2D and 3D convection for large Prandtl number". en. In: *Pramana* 87, p. 13. ISSN: 0973-7111. DOI: `10.1007/s12043-016-1204-z`.

Poel, Erwin P. van der et al. (July 2014). "Effect of velocity boundary conditions on the heat transfer and flow topology in two-dimensional Rayleigh-B\'enard convection". In: *Physical Review E* 90, p. 013017. DOI: `10.1103/PhysRevE.90.013017`.

Radko, Timour (2013). *Double-diffusive convection*. Cambridge: Cambridge University Press. ISBN: 978-0-521-88074-9.

Rein, Martin (2020). "Einführung in die Strömungsmechanik". ger. In: Accepted: 2021-02-02T11:01:31Z Artwork Medium: Print ISBN: 9783863954802 Interview Medium: Print. DOI: `10.17875/gup2020-1362`.

Rosenthal, A., K. Lüdemann, and A. Tilgner (Nov. 2022). "Staircase formation in unstably stratified double diffusive finger convection". In: *Physics of Fluids* 34.11. Publisher: American Institute of Physics, p. 116605. ISSN: 1070-6631. DOI: `10.1063/5.0122882`.

Rouhi, Amirreza et al. (Mar. 2021). "Coriolis effect on centrifugal buoyancy-driven convection in a thin cylindrical shell". en. In: *Journal of Fluid Mechanics* 910. ISSN: 0022-1120, 1469-7645. DOI: `10.1017/jfm.2020.959`.

Salby, Murry L. (1996). *Fundamentals of atmospheric physics*. International geophysics series. - New York, NY [u.a.] : Academic Press, 1959- ; ZDB-ID: 410944-2 61. San Diego [u.a.]: Academic Press. ISBN: 978-0-12-615160-2.

Schmalzl, J., M. Breuer, and U. Hansen (Aug. 2004). "On the validity of two-dimensional numerical approaches to time-dependent thermal convection". en. In: *EPL (Europhysics Letters)* 67, p. 390. ISSN: 0295-5075. DOI: `10.1209/epl/i2003-10298-4`.

Schmitz, S. and A. Tilgner (July 2009). "Heat transport in rotating convection without Ekman layers". In: *Physical Review E* 80, p. 015305. DOI: `10.1103/PhysRevE.80.015305`.

Shishkina, Olga et al. (July 2010). "Boundary layer structure in turbulent thermal convection and its consequences for the required numerical resolution". en. In: *New Journal of Physics* 12, p. 075022. ISSN: 1367-2630. DOI: `10.1088/1367-2630/12/7/075022`.

Tilgner, A. (Aug. 2011). "Convection in an ideal gas at high Rayleigh numbers". In: *Physical Review E* 84.2, p. 026323. DOI: `10.1103/PhysRevE.84.026323`.

– (Dec. 2012). "Transitions in Rapidly Rotating Convection Driven Dynamos". In: *Physical Review Letters* 109.24. Publisher: American Physical Society, p. 248501. DOI: `10.1103/PhysRevLett.109.248501`.

Verhoeven, Jan and Gary A. Glatzmaier (Jan. 2018). "Validity of sound-proof approaches in rapidly-rotating compressible convection: marginal stability versus turbulence". In: *Geophysical & Astrophysical Fluid Dynamics* 112.1, pp. 36–61. ISSN: 0309-1929. DOI: `10.1080/03091929.2017.1380800`.

Verhoeven, Jan and Stephan Stellmach (July 2014). "The compressional beta effect: A source of zonal winds in planets?" In: *Icarus* 237, pp. 143–158. ISSN: 0019-1035. DOI: 10.1016/j.icarus.2014.04.019.

Verhoeven, Jan, Thomas Wiesehöfer, and Stephan Stellmach (2015). "Anelastic versus Fully Compressible Turbulent Rayleigh–Bénard Convection". en. In: *The Astrophysical Journal* 805.1, p. 62. ISSN: 0004-637X. DOI: 10.1088/0004-637X/805/1/62.

Waleffe, Fabian (Jan. 1990). "On the three-dimensional instability of strained vortices". In: *Physics of Fluids A: Fluid Dynamics* 2.1. Publisher: American Institute of Physics, pp. 76–80. ISSN: 0899-8213. DOI: 10.1063/1.857682.

Wang, Qi et al. (Dec. 2020). "From zonal flow to convection rolls in Rayleigh–Bénard convection with free-slip plates". en. In: *Journal of Fluid Mechanics* 905. ISSN: 0022-1120, 1469-7645. DOI: 10.1017/jfm.2020.793.

Whitehead, Jared P. and Charles R. Doering (June 2011). "Ultimate State of Two-Dimensional Rayleigh-B\'enard Convection between Free-Slip Fixed-Temperature Boundaries". In: *Physical Review Letters* 106.24, p. 244501. DOI: 10.1103/PhysRevLett.106.244501.

– (Sept. 2012). "Rigid bounds on heat transport by a fluid between slippery boundaries". en. In: *Journal of Fluid Mechanics* 707, pp. 241–259. ISSN: 1469-7645, 0022-1120. DOI: 10.1017/jfm.2012.274.

Williamson, J. H (Mar. 1980). "Low-storage Runge-Kutta schemes". In: *Journal of Computational Physics* 35.1, pp. 48–56. ISSN: 0021-9991. DOI: 10.1016/0021-9991(80)90033-9.

Wood, T. S. and P. J. Bushby (Sept. 2016). "Oscillatory convection and limitations of the Boussinesq approximation". en. In: *Journal of Fluid Mechanics* 803, pp. 502–515. ISSN: 0022-1120, 1469-7645. DOI: 10.1017/jfm.2016.511.

Acknowledgements

First and above all, I would like to thank Andreas Tilgner[1] for the opportunity to work on this project and his continued support. Many problems outside the scientific part of my work have plagued this relation but we continued to work productively together. I also thank all of my TAC members as well as the members of my defence.

Secondly, I have to thank my colleagues. I thank Axel Rosenthal for the many great discussions as well as the opportunity to work on an experimental study in addition to my own, theoretical studies. Also, I thank Ulrich Einecke for his relentless support with all the computer, networking and data problems. Furthermore, I would like to thank Alexandra Lüttich for her assistance and guidance with the monstrous bureaucracy of this university, as well as the many helpful discussions in general.

Continuing, I have to thank all of the students that I assisted during their stay at the Institute. Specifically and above all, I have to thank Marie-Christine Volk who agreed to stay after finishing her Bachelors and help me with many simulations, which have been put to good use in this work. Additionally, I would like to thank Ole Merkes for prove reading many of the chapter of this work. Ultimately, I would like to thank all the others Maj-Britt, Florian, Enrico, Fabian and Julian for their general help in pitching ideas and the very pleasant company.

Lastly, but most importantly, I have to thank my parents Katja and Klaus as well as my brother Kilian who assisted me whatever happened. They were there to help me get back up and continue fighting, however I overworked myself.

What I learned from my time in academia, which is my most scaring takeaway, is: Don't work the system when you can work the people.[2]

I would like to close by quoting Rule #11.[3]

---

[1]"Darth Tilgner the wise", a Star Wars reference regarding Darth Plagueis the wise. It is meant as a tribute to his skill and cunning in creating ideas and calculations. Also, this would make me his apprentice and the second most intelligent being after him thanks to his teachings.

[2]Unnumbered rule of the Series: NCIS

[3]When the job is done, walk away (NCIS)

CV

Personal data

Name	Lüdemann
Firstname	Kevin
Date of birth	27.10.1993
Place of birth	Rotenburg (Wümme)
Nationality	German
Marital status	single

Educational background

25.08.2005 - 23.07.2010	**Realschulabschluss** Fintauschule, Lauenbrück
05.08.2010 - 21.06.2013	**Abitur** Berufsbildende Schule Roteburg (Wümme)
01.10.2013 - 30.09.2016	**Bachelor of Science** Georg-August-University Göttingen
	Numerical investigation of the spectral transport
	in kinetic energie for Rayleigh-Bénard convection
01.10.2016 - 31.03.2019	**Master of Science** Georg-August-University Göttingen
	Simulation of horizontally rotating compressible convection:
	Towards the Boussinesq limit
01.05.2019 - today	**Doctoral studies** Georg-August-University Göttingen